

Ministry of Education and Science of the Russian Federation
Saint Petersburg National Research University of Information
Technologies, Mechanics, and Optics

NANOSYSTEMS:
PHYSICS, CHEMISTRY, MATHEMATICS

2022, volume 13(3)

Наносистемы: физика, химия, математика

2022, том 13, № 3



NANOSYSTEMS:

PHYSICS, CHEMISTRY, MATHEMATICS

ADVISORY BOARD MEMBERS

Chairman: V.N. Vasiliev (*St. Petersburg, Russia*),
V.M. Buznik (*Moscow, Russia*); V.M. Ievlev (*Voronezh, Russia*), P.S. Kop'ev (*St. Petersburg, Russia*), N.F. Morozov (*St. Petersburg, Russia*), V.N. Parmon (*Novosibirsk, Russia*),
A.I. Rusanov (*St. Petersburg, Russia*),

EDITORIAL BOARD

Editor-in-Chief: I.Yu. Popov (*St. Petersburg, Russia*)

Section Co-Editors:

Physics – V.M. Uzdin (*St. Petersburg, Russia*),
Material science – V.V. Gusarov (*St. Petersburg, Russia*),
Chemistry – V.K. Ivanov (*Moscow, Russia*),
Mathematics – I.Yu. Popov (*St. Petersburg, Russia*).

Editorial Board Members:

V.M. Adamyan (*Odessa, Ukraine*); O.V. Al'myasheva (*St. Petersburg, Russia*);
A.P. Alodjants (*Vladimir, Russia*); S. Bechta (*Stockholm, Sweden*); J. Behrndt (*Graz, Austria*);
M.B. Belonenko (*Volgograd, Russia*); A. Chatterjee (*Hyderabad, India*); A.V. Chizhov
(*Dubna, Russia*); A.N. Enyashin (*Ekaterinburg, Russia*), P.P. Fedorov (*Moscow, Russia*);
E.A. Gudilin (*Moscow, Russia*); H. Jónsson (*Reykjavik, Iceland*); A.A. Kiselev (*Durham, USA*);
Yu.S. Kivshar (*Canberra, Australia*); S.A. Kozlov (*St. Petersburg, Russia*);
P.A. Kurasov (*Stockholm, Sweden*); A.V. Lukashin (*Moscow, Russia*); I.V. Melikhov
(*Moscow, Russia*); G.P. Miroshnichenko (*St. Petersburg, Russia*); I.Ya. Mittova (*Voronezh, Russia*);
Nguyen Anh Tien (*Ho Chi Minh, Vietnam*); V.V. Pankov (*Minsk, Belarus*);
K. Pankrashkin (*Orsay, France*); A.V. Ragulya (*Kiev, Ukraine*); V. Rajendran (*Tamil Nadu, India*);
A.A. Rempel (*Ekaterinburg, Russia*); V.Ya. Rudyak (*Novosibirsk, Russia*);
H.M. Sedighi (*Ahvaz, Iran*); D Shoikhet (*Karmiel, Israel*); P Stovicek (*Prague, Czech Republic*);
V.M. Talanov (*Novocherkassk, Russia*); A.Ya. Vul' (*St. Petersburg, Russia*);
A.V. Yakimansky (*St. Petersburg, Russia*), V.A. Zagrebnoy (*Marseille, France*).

Editors:

I.V. Blinova; A.I. Popov; A.I. Trifanov; E.S. Trifanova (*St. Petersburg, Russia*),
R. Simoneaux (*Philadelphia, Pennsylvania, USA*).

Address: ITMO University, Kronverkskiy pr., 49, St. Petersburg 197101, Russia.

Phone: +7(812)607-02-54, **Journal site:** <http://nanojournal.ifmo.ru/>,

E-mail: nanojournal.ifmo@gmail.com

AIM AND SCOPE

The scope of the journal includes all areas of nano-sciences. Papers devoted to basic problems of physics, chemistry, material science and mathematics inspired by nanosystems investigations are welcomed. Both theoretical and experimental works concerning the properties and behavior of nanosystems, problems of its creation and application, mathematical methods of nanosystem studies are considered.

The journal publishes scientific reviews (up to 30 journal pages), research papers (up to 15 pages) and letters (up to 5 pages). All manuscripts are peer-reviewed. Authors are informed about the referee opinion and the Editorial decision.

CONTENT

MATHEMATICS

M.I. Muminov, A.M. Khurramov, I.N. Bozorov
Conditions for the existence of bound states of a two-particle Hamiltonian on a three-dimensional lattice 237

I.V. Blinova, A.I. Popov, A.A. Bosova
Spectral gaps for star-like quantum graph and for two coupled rings 245

PHYSICS

V.D. Krevchik, A.V. Razumov, M.B. Semenov,
A.V. Levashov, A.V. Shorokhov
Influence of dissipative tunneling on the photodielectric effect associated with the excitation of impurity complexes $A^+ + e$ in a quasi-zero dimensional structure 250

Ayham Shaer, Mohammad K. Elsaid
The Gaussian impurity effect on the electronic and magnetic properties of an electron confined in a lateral quantum dot 265

A.V. Smirnov, A.M. Semenov, Yu.B. Porozov, B.A. Fedorov
Assessment of structural changes in proteins and surrounding water molecules in solution according to SAXS and MD data 274

I.V. Pleshakov, A.V. Prokof'ev, E.E. Bibik, Yu.I. Kuz'min
Investigation of structures formed by magnetic fluid nanoparticles in polymer matrices by static light scattering 285

R. Goncharov, E. Bolychev, I. Vorontsova, E. Samsonov, V. Egorov
Overview of device-independent continuous-variable quantum key distribution 290

G.V. Tushavin, A.I. Trifanov, E.V. Zaitseva
Ladder operators approach to representation classification problem for Jordan-Schwinger image of $su(2)$ algebra 299

CHEMISTRY AND MATERIAL SCIENCE

N.N. Chukavin, A.L. Popov, A.B. Shcherbakov,
O.S. Ivanova, A.D. Filippova, V.K. Ivanov
CeO₂-calcein nanoconjugate protective action against H₂O₂-induced oxidative stress *in vitro* 308

S.S. Kozlov, O.V. Alexeeva, A.B. Nikolskaia, O.I. Shevaleevskiy, D.D. Averkiev, P.V. Kozhuhovskaya, O.V. Almjasheva, L.L. Larina Double perovskite oxides $\text{La}_2\text{NiMnO}_6$ and $\text{La}_2\text{Ni}_{0.8}\text{Fe}_{0.2}\text{MnO}_6$ for inorganic perovskite solar cells	314
S. Kalaiarasi, S. Shyamala, M. Kavitha C. Vedhi, R.R. Muthuchudarkodi Electrochemical performance of r-graphene oxide based MnO_2 nanocomposite for supercapacitor	320
S.V. Kuznetsov, S.A. Burikov, A.A. Fedyanina, E.A. Filippova, V.Yu. Proydakova, V.V. Voronov, N.Yu. Tabachkova, P.P. Fedorov, T.A. Dolenko Impact of sensitizer Yb and activator Tm on luminescence intensity of $\beta\text{-NaYF}_4\text{:Yb/Tm}$ nanoluminophores	331
D.J. Kamothi, V. Kant, V. Kumar, V.G. Joshi, R. Chhabra Evaluation of antibacterial potential of bilirubin nanoparticles against <i>Staphylococcus aureus</i> and <i>Escherichia coli</i>	342
Information for authors	349

Conditions for the existence of bound states of a two-particle Hamiltonian on a three-dimensional lattice

M. I. Muminov^{1,2,a}, A. M. Khurramov^{1,b}, I. N. Bozorov^{1,c}

¹Samarkand State University, Samarkand, 140104, Uzbekistan

²V. I. Romanovskiy Institute of Mathematics, Uzbekistan Academy of sciences 100174, Tashkent, Uzbekistan

^ammuminov@mail.ru, ^bxurramov@mail.ru, ^cislomb@mail.ru

Corresponding author: M.I. Muminov, mmuminov@mail.ru

ABSTRACT The Hamiltonian h of the system of two quantum particles moving on a 3-dimensional lattice interacting via some attractive potential is considered. Conditions for the existence of eigenvalues of the two-particle Schrödinger operator $h_\mu(k)$, $k \in \mathbb{T}^3$, $\mu \in \mathbb{R}$, associated to the Hamiltonian h , are studied depending on the energy of the particle interaction $\mu \in \mathbb{R}$ and total quasi-momentum $k \in \mathbb{T}^3$ (\mathbb{T}^3 – three-dimensional torus).

KEYWORDS two-particle Hamiltonian, invariant subspace, unitary equivalent operator, virtual level, multiplicity of virtual level, eigenvalue.

ACKNOWLEDGEMENTS The authors express their kind gratitude to the referee for valuable remarks. The work was supported by the Fundamental Science Foundation of Uzbekistan, Grant No. FZ–20200929224.

FOR CITATION Muminov M.I., Khurramov A.M., Bozorov I.N. Conditions for the existence of bound states of a two-particle Hamiltonian on a three-dimensional lattice. *Nanosystems: Phys. Chem. Math.*, 2022, **13** (3), 237–244.

1. Introduction

To manipulate ultracold atoms and a unique setting for quantum simulations of interacting many-body systems, the coherent optical fields provide a strong tool because of their high-degree controllable parameters such as optical lattice geometry, dimension, particle mass, tunneling, two-body potentials, temperature etc. (See [1–4]). However, in such manipulations, due to diffraction, there is a fundamental limit for the length scale given by the wavelength of light [5] and therefore, the corresponding models are naturally restricted to a short-range case. The recent experimental and theoretical results show that integrating plasmonic systems with cold atoms, using optical potential fields formed from the near field scattering of light by an array of plasmonic nanoparticles, allows one to considerably increase the energy scales in the implementation of Hubbard models and engineer effective long-range interaction in many body dynamics [5–7].

In [8], the spectral properties of the two-particle operator depending on total quasi-momentum were investigated. In [9], the existence conditions and positiveness of eigenvalues of the two particle Hamiltonian with short range attractive perturbation was studied with respect to the quasi-momentum k and the virtual level at the lower edge of essential spectrum.

In [10], several numerical results for the bound state energies of one and two-particle systems was presented in two adjacent 3D layers, connected through a window. The authors investigated the relation between the shape of a window and energy levels, as well as number of eigenfunction's nodal domains.

In the recent work [11], the condition was obtained for the discrete two-particle Schrödinger operator with zero-range attractive potential to have an embedded eigenvalue in the essential spectrum depending on the dimension of the lattice. In [12], the discrete spectrum of the one-dimensional discrete Laplacian with short range attractive perturbation was studied.

In general, the Schrödinger operator $h(k)$, $k \in \mathbb{T}^d$, associated to the Lattice Hamiltonian h of two arbitrary particles with some dispersion relation and short range potential interaction acts in $L_2(\mathbb{T}^d)$ as (see [13])

$$h(k) = h_0(k) - \mathbf{v}, \quad k \in \mathbb{T}^d,$$

where $h_0(k)$ is a multiplication operator by $\mathcal{E}_k(p) = \frac{1}{m_1}\varepsilon(p) + \frac{1}{m_2}\varepsilon(p - k)$ and \mathbf{v} is integral operator with kernel $v(p, s) = v(p - s)$.

The existence and absence of eigenvalues of the family $h(k)$ depending on the energy of interaction and quasi-momentum k were investigated in [14] and [15] for the cases $\varepsilon(p) = \sum_{i=1}^3 (1 - \cos 2p_i)$, $v(p - s) = \sum_{\alpha=1}^3 \mu_\alpha \cos(p_\alpha - s_\alpha)$

and $\varepsilon(p) = \sum_{i=1}^3 (1 - \cos 2np_i)$, $v(p - q) = \sum_{l=1}^N \sum_{i=1}^3 \mu_{li} \cos l(p_i - q_i)$, respectively. The spectral properties of this operator $h(k)$ for the one dimensional case was studied in [16]. The general case when the function $\varepsilon(p)$ satisfies some conditions and $v(p - s) = \mu_0 + \sum_{\alpha=1}^d \mu_{\alpha} \cos(p_{\alpha} - q_{\alpha})$ was investigated in [17].

In [18], the Hamiltonian $\hat{h}_{\mu\lambda}$, $\mu, \lambda \geq 0$, describing the motion of one quantum particle on a three-dimensional lattice in an external field was considered. The authors completely investigated the dependence of the number of eigenvalues of this operator on the interaction energy for $\mu \geq 0$ and $\lambda \geq 0$. They showed that all eigenvalues arise either from the threshold virtual level (resonance) or from the threshold eigenvalues under a variation of the interaction energy.

In [19], the authors considered the two-particle Schrödinger operator $H(k)$, ($k \in \mathbb{T}^3 \equiv (-\pi, \pi]^3$ is the total quasi-momentum of a system of two particles) corresponding to the Hamiltonian of the two-particle system on the three-dimensional lattice \mathbb{Z}^3 . It was proved that the number $N(\mathbf{k}) \equiv N(k^{(1)}, k^{(2)}, k^{(3)})$ of eigenvalues below the essential spectrum of the operator $H(k)$ is a nondecreasing function in each $k^{(i)} \in [0, \pi]$, $i = 1, 2, 3$. Under some additional conditions on the potential \hat{v} , the monotonicity of each eigenvalue $z_n(\mathbf{k}) \equiv z_n(k^{(1)}, k^{(2)}, k^{(3)})$ of the operator $H(k)$ in $k^{(i)} \in [0, \pi]$ with other coordinates k being fixed was proved.

In this work we study the Hamiltonian h for a system of two particles on the lattice \mathbb{Z}^3 interacting through *attractive short-range potential* V . We investigate the existence conditions of eigenvalues and bound states of the Hamiltonians $h_{\mu}(k)$, $k \in \mathbb{T}^3$, associated to the Hamiltonian h . To study $h_{\mu}(k)$, we first construct the invariant subspaces $\mathcal{H}_l \subset L_2(\mathbb{T}^3)$, $l = \overline{1, 27}$ for the operator $h_{\mu}(k)$. Moreover, the investigation of spectral properties for $h_{\mu}(k)$ is reduced to study the operator $h_{\mu,l}(k) := h_{\mu}(k) : \mathcal{H}_l \rightarrow \mathcal{H}_l$, $l = \overline{1, 27}$. Further, eigenvalue problem for $h_{\mu,l}(k)$ is reduced to study of a compact equation of rank one, which allows one to analyze the spectrum of $h_{\mu,l}(k)$.

2. Statement of the main result

The two-particle Schrödinger operator $h_{\mu}(k)$, $k \in \mathbb{T}^3$, $\mu \in \mathbb{R}$, associated to the Hamiltonian h for a system of two particles on the lattice \mathbb{Z}^3 interacting via attractive short-range potential, is a self-adjoint operator which acts in $L_2(\mathbb{T}^3)$ as

$$h_{\mu}(k) = h_0(k) - \mu \mathbf{v}, \quad k = (k_1, k_2, k_3) \in \mathbb{T}^3, \quad \mu \in \mathbb{R},$$

where $h_0(k)$ is a multiplication operator by

$$\mathcal{E}_k(p) = \frac{1}{m_1} \varepsilon(p) + \frac{1}{m_2} \varepsilon(p - k), \quad \varepsilon(p) = \sum_{i=1}^3 (1 - \cos 2p_i),$$

with \mathbf{v} being an integral operator with kernel

$$v(p - s) = 1 + \sum_{\alpha=1}^3 \cos(p_{\alpha} - s_{\alpha}) + \sum_{\gamma=1}^3 \cos(p_{\alpha} - s_{\alpha}) \cos(p_{\beta} - s_{\beta}) + \prod_{\alpha=1}^3 \cos(p_{\alpha} - s_{\alpha}),$$

Note that by the Weyl theorem on the essential spectrum [20] the essential spectrum $\sigma_{ess}(h_{\mu}(k))$ of the operator $h_{\mu}(k)$ coincides with the spectrum of the unperturbed operator $h_0(k)$

$$\sigma_{ess}(h_{\mu}(k)) = \sigma(h_0(k)) = [m(k), M(k)],$$

where $m(k) = \min_{p \in \mathbb{T}^3} \mathcal{E}_k(p)$, $M(k) = \max_{p \in \mathbb{T}^3} \mathcal{E}_k(p)$.

Since $\mathbf{v} \geq 0$ for $\mu > 0$,

$$\sup_{\|f\|=1} (h_{\mu}(k)f, f) \leq \sup_{\|f\|=1} (h_0(k)f, f) = M(k)(f, f), \quad f \in L_2(\mathbb{T}^3).$$

Hence, $h_{\mu}(k)$ does not have eigenvalues lying to the right of the essential spectrum, i.e.,

$$\sigma(h_{\mu}(k)) \cap (M(k), \infty) = \emptyset.$$

Similarly, for $\mu < 0$

$$\inf_{\|f\|=1} (h_{\mu}(k)f, f) \geq \inf_{\|f\|=1} (h_0(k)f, f) = m(k)(f, f), \quad f \in L_2(\mathbb{T}^3).$$

Therefore, $h_{\mu}(k)$ does not have eigenvalues lying to the left of the essential spectrum, i.e.,

$$\sigma(h_{\mu}(k)) \cap (-\infty, m(k)) = \emptyset.$$

Let functions φ_l be defined as

$$\varphi_l(p) = \prod_{\alpha=1}^3 \eta_l(p_{\alpha}), \quad \{\eta_l(p_{\alpha})\} \in \{1, \cos p_{\alpha}, \sin p_{\alpha}\}, \quad \alpha \in \{1, 2, 3\}. \tag{1}$$

This system consists of a 27 orthogonal functions $\{\varphi_l\}$. The operator \mathbf{v} can be expressed via the functions $\{\varphi_l(\cdot)\}$, defined in (1), in the form

$$(\mathbf{v}f)(p) = \sum_{l=1}^{27} (\varphi_l, f)\varphi_l(p). \quad (2)$$

Below, we describe the conditions for the existence of eigenvalues of $h_\mu(k)$.

Let us denote by $n(\mu)$ the number of eigenvalues (with the multiplicities) lying outside the essential spectrum of the operator $h_\mu(k)$.

Remark that for the number $n(\mu)$ of eigenvalues of $h_\mu(k)$, $\mu > 0$ (resp. $\mu < 0$) and $k \in \mathbb{T}^3$, lying to the left (resp. to the right) of the essential spectrum the following estimate is true

$$0 \leq n(\mu) \leq 27.$$

Assumption 2.1. Assume that $m = m_1 = m_2$ and $k \in \Pi$, where Π is a set of $k = (k_1, k_2, k_3) \in \mathbb{T}^3$ with $k_\alpha = -\frac{\pi}{2}$ or $k_\alpha = \frac{\pi}{2}$ for some $\alpha \in \{1, 2, 3\}$.

We divide the set Π into three subsets Π_n , $n = 1, 2, 3$, defined as follows: Π_n contains elements $k \in \Pi$ such that precisely n of their coordinates are equal to $\pm\pi/2$.

Theorem 2.1. Let the Assumption 2.1 be fulfilled. Then the following statements are true

1. For any $\mu > 0$ (resp. $\mu < 0$) and $k \in \Pi_1$, the operator $h_\mu(k)$ has at least 12 eigenvalues lying to the left (resp. to the right) of the essential spectrum.
2. For any $\mu > 0$ (resp. $\mu < 0$) and $k \in \Pi_2$, the operator $h_\mu(k)$ has at least 18 eigenvalues lying to the left (resp. to the right) of the essential spectrum.
3. For any $\mu > 0$ (resp. $\mu < 0$) and $k \in \Pi_3$, the operator $h_\mu(k)$ has 27 eigenvalues lying to the left (resp. to the right) of the essential spectrum.

We introduce the following subspaces \mathcal{H}_l , $l = \overline{1, 27}$, of $L_2(\mathbb{T}^3)$ as

$$\begin{aligned} \mathcal{H}_1 &= \mathcal{H}_{000}^{eee}, \mathcal{H}_2 = \mathcal{H}_{\pi 00}^{eee}, \mathcal{H}_3 = \mathcal{H}_{0\pi 0}^{eee}, \mathcal{H}_4 = \mathcal{H}_{00\pi}^{eee}, \mathcal{H}_5 = \mathcal{H}_{0\pi\pi}^{eee}, \mathcal{H}_6 = \mathcal{H}_{\pi 0\pi}^{eee}, \mathcal{H}_7 = \mathcal{H}_{\pi\pi 0}^{eee}, \\ \mathcal{H}_8 &= \mathcal{H}_{\pi\pi\pi}^{eee}, \mathcal{H}_9 = \mathcal{H}_{\pi 00}^{oeo}, \mathcal{H}_{10} = \mathcal{H}_{\pi\pi 0}^{oeo}, \mathcal{H}_{11} = \mathcal{H}_{\pi 0\pi}^{oeo}, \mathcal{H}_{12} = \mathcal{H}_{\pi\pi\pi}^{oeo}, \mathcal{H}_{13} = \mathcal{H}_{0\pi 0}^{oeo}, \mathcal{H}_{14} = \mathcal{H}_{0\pi\pi}^{oeo}, \\ \mathcal{H}_{15} &= \mathcal{H}_{\pi\pi 0}^{oeo}, \mathcal{H}_{16} = \mathcal{H}_{\pi\pi\pi}^{oeo}, \mathcal{H}_{17} = \mathcal{H}_{0\pi 0}^{eoo}, \mathcal{H}_{18} = \mathcal{H}_{0\pi\pi}^{eoo}, \mathcal{H}_{19} = \mathcal{H}_{00\pi}^{eoo}, \mathcal{H}_{20} = \mathcal{H}_{0\pi\pi}^{eoo}, \mathcal{H}_{21} = \mathcal{H}_{\pi 0\pi}^{eoo}, \\ \mathcal{H}_{22} &= \mathcal{H}_{\pi\pi\pi}^{eoo}, \mathcal{H}_{23} = \mathcal{H}_{0\pi\pi}^{ooo}, \mathcal{H}_{24} = \mathcal{H}_{\pi 0\pi}^{ooo}, \mathcal{H}_{25} = \mathcal{H}_{\pi\pi\pi}^{ooo}, \mathcal{H}_{26} = \mathcal{H}_{\pi\pi\pi}^{ooo}, \mathcal{H}_{27} = \mathcal{H}_{\pi\pi\pi}^{ooo}, \end{aligned}$$

where $o, e, 0$ and π denote even, odd, π -even and π -odd notions of variable, respectively. For example $\mathcal{H}_{0\pi\pi}^{eoo}$ denotes a space of functions $f(p)$ which are even with respect to each variables p_1, p_2 and odd with respect to p_3 , and π -even with respect to p_1 , and π -odd with respect to each variables p_2, p_3 , i.e.,

$$\mathcal{H}_{0\pi\pi}^{eoo} = \{f \in L_2(\mathbb{T}^3) :$$

$$\begin{aligned} f(-p_1, p_2, p_3) &= f(p_1, p_2, p_3), \quad f(p_1, -p_2, p_3) = f(p_1, p_2, p_3), \quad f(p_1, p_2, -p_3) = -f(p_1, p_2, p_3), \\ f(p_1 + \pi, p_2, p_3) &= f(p_1, p_2, p_3), \quad f(p_1, p_2 + \pi, p_3) = -f(p_1, p_2, p_3), \quad f(p_1, p_2, p_3 + \pi) = -f(p_1, p_2, p_3)\}. \end{aligned}$$

Remark that the operator $h_\mu(k)$ is invariant with respect to \mathcal{H}_l , $l = \overline{1, 27}$ (See Lemma 3.1). We denote by $h_{\mu,l}(k)$ the restriction $h_\mu(k)|_{\mathcal{H}_l}$ of $h_\mu(k)$ to \mathcal{H}_l .

Note that $\varphi_l \in \mathcal{H}_l$, $l = \overline{1, 27}$. Therefore, the operator $h_{\mu,l}(k)$, $l = \overline{1, 27}$ acts in \mathcal{H}_l as

$$h_{\mu,l}(k) = h_0(k) - \mu \mathbf{v}_l,$$

where

$$(\mathbf{v}_l f)(p) = (\varphi_l, f)\varphi_l(p), \quad \varphi_l \in \mathcal{H}_l, \quad l = \overline{1, 27}.$$

Then we have

$$\sigma(h_\mu(k)) = \bigcup_{l=1}^{27} \sigma(h_{\mu,l}(k)).$$

Next, we study the operator $h_{\mu,l}(k)$, $l = \overline{1, 27}$.

We set

$$\xi_l(k; z) = \int_{\mathbb{T}^3} \frac{\varphi_l^2(s) ds}{\tilde{\mathcal{E}}_k(s) - z}, \quad \varphi_l \in \mathcal{H}_l, \quad l = \overline{1, 27}, \quad z \in \mathbb{C} \setminus [m(k), M(k)], \quad (3)$$

where

$$\tilde{\mathcal{E}}_k(p) = \sum_{i=1}^3 \left(\frac{1}{m_1} + \frac{1}{m_2} - \sqrt{\frac{1}{m_1^2} + \frac{2}{m_1 m_2} \cos 2k_i + \frac{1}{m_2^2} \cos 2p_i} \right).$$

If Assumption 2.1 is not fulfilled, then the integral (3) converges as $z = m(k)$ ($z = M(k)$) (see Lemma 3.2 below).

We set

$$\mu_l^0(m(k)) = \frac{1}{\xi_l(k; m(k))}, \quad \mu_l^0(M(k)) = \frac{1}{\xi_l(k; M(k))}, \quad l = \overline{1, 27}.$$

Let $C(\mathbb{T}^3)$ be the Banach space of continuous (periodic) functions on \mathbb{T}^3 and $G_l(z)$, $l \in \{1, 2, \dots, 27\}$ be the (Birman–Schwinger) integral operator with the kernel

$$G_l(p, q; z) = \frac{\varphi_l(p)\varphi_l(q)}{\tilde{\mathcal{E}}_0(q) - z}, \quad z \in (-\infty, m(\mathbf{0})] \cup [M(\mathbf{0}), +\infty), \quad m(\mathbf{0}) = 0, \quad M(\mathbf{0}) = 6\frac{m_1 + m_2}{m_1 m_2}.$$

Definition 2.1. If number 1 is an eigenvalue of the operator $G_l(0)$, (resp. $G_l(M(\mathbf{0}))$) and the corresponding eigenfunction ψ_l satisfies the condition

$$\frac{\psi_l(\cdot)}{\tilde{\mathcal{E}}_0(\cdot)} \in L_1(\mathbb{T}^3) \setminus L_2(\mathbb{T}^3), \quad \left(\text{resp. } \frac{\psi_l(\cdot)}{\tilde{\mathcal{E}}_0(\cdot) - M(\mathbf{0})} \in L_1(\mathbb{T}^3) \setminus L_2(\mathbb{T}^3)\right),$$

then it means that the operator $h_{\mu, l}(\mathbf{0})$ has a virtual level at the left edge (resp. at the right edge) of the essential spectrum.

Theorem 2.2. Suppose that Assumption 2.1 are not fulfilled. Then the following statements are true

1. For any $0 < \mu < \mu_l^0(k)$ (resp. $\mu_l^0(k) < \mu < 0$) the operator $h_{\mu, l}(k)$ has no eigenvalues lying to the left (resp. to the right) of the essential spectrum.
2. Let $0 < \mu = \mu_l^0(m(\mathbf{0}))$ (resp. $\mu_l^0(M(\mathbf{0})) = \mu < 0$). If $\varphi_l(\mathbf{0}) \neq 0$, then $h_{\mu, l}(\mathbf{0})$ has a virtual level at $z = 0$ (resp. at $z = 6\frac{m_1 + m_2}{m_1 m_2}$), if $\varphi_l(\mathbf{0}) = 0$, then the number $z = 0$ (resp. $z = 6\frac{m_1 + m_2}{m_1 m_2}$) is an eigenvalue of $h_{\mu, l}(\mathbf{0})$.
3. For any $k \in \mathbb{T}^3$ and $\mu > \mu_l^0(k) > 0$ (resp. $\mu < \mu_l^0(k) < 0$), the operator $h_{\mu, l}(k)$ has unique eigenvalue lying to the left (resp. to the right) of the essential spectrum.

Theorem 2.3. Let Assumption 2.1 be fulfilled. Then the following statements are true

1. For any $\mu > 0$ (resp. $\mu < 0$) and $k \in \Pi_1$, there exist $l_1, l_2, \dots, l_{12} \in \{1, 2, \dots, 27\}$ such that the operator $h_{\mu, l_i}(k)$, $i = \overline{1, 12}$ has a unique eigenvalue lying to the left (resp. to the right) of the essential spectrum.
2. For any $\mu > 0$ (resp. $\mu < 0$) and $k \in \Pi_2$, there exist $l_1, l_2, \dots, l_{18} \in \{1, 2, \dots, 27\}$ such that the operator $h_{\mu, l_i}(k)$, $i = \overline{1, 18}$ has a unique eigenvalue lying to the left (resp. to the right) of the essential spectrum.
3. For any $\mu > 0$ (resp. $\mu < 0$), $k \in \Pi_3$ and $l \in \{1, 2, \dots, 27\}$ the operator $h_{\mu, l}(k)$ has unique eigenvalue lying to the left (resp. to the right) of the essential spectrum.

Remark 2.1. Note that Theorem 2.2, 2) shows that the number $z = 0$ (respectively, $z = 6\frac{m_1 + m_2}{m_1 m_2}$) might be a virtual level or an eigenvalue or a virtual level and an eigenvalue for the operator $h_\mu(\mathbf{0})$. For the case $\mu = \mu_1^0(m(\mathbf{0}))$ or $\mu = \mu_8^0(m(\mathbf{0}))$, number $z = 0$ is a simple virtual level of $h_\mu(\mathbf{0})$ with

$$f_1(p) = \frac{1}{\tilde{\mathcal{E}}_0(p)} \in L_1(\mathbb{T}^3) \setminus L_2(\mathbb{T}^3) \quad \text{or} \quad f_8(p) = \frac{\cos p_1 \cos p_2 \cos p_3}{\tilde{\mathcal{E}}_0(p)} \in L_1(\mathbb{T}^3) \setminus L_2(\mathbb{T}^3).$$

For the case $\mu = \mu_2^0(m(\mathbf{0})) = \mu_3^0(m(\mathbf{0})) = \mu_4^0(m(\mathbf{0}))$ or $\mu = \mu_5^0(m(\mathbf{0})) = \mu_6^0(m(\mathbf{0})) = \mu_7^0(m(\mathbf{0}))$, number $z = 0$ is a virtual level of $h_\mu(\mathbf{0})$ with multiplicity 3 with

$$f_{1+i}(p) = \frac{\cos p_i}{\tilde{\mathcal{E}}_0(p)} \in L_1(\mathbb{T}^3) \setminus L_2(\mathbb{T}^3) \quad \text{or} \quad f_{4+i}(p) = \frac{\cos p_\alpha \cos p_\beta}{\tilde{\mathcal{E}}_0(p)} \in L_1(\mathbb{T}^3) \setminus L_2(\mathbb{T}^3),$$

$$\{i, \alpha, \beta\} = \{1, 2, 3\}.$$

3. Proof of the main results

Consider the operator $\tilde{h}_\mu(k)$ acting in $L_2(\mathbb{T}^3)$ by the formula

$$\tilde{h}_\mu(k) = \tilde{h}_0(k) - \mu \mathbf{v},$$

where $\tilde{h}_0(k)$ is the operator of multiplication by the function $\tilde{\mathcal{E}}_k(\cdot)$.

The operator $h_\mu(k)$ is unitary equivalent to the operator $\tilde{h}_\mu(k)$ (See Lemma 2 in [15]). The equivalence is performed by the unitary operator $U : L_2(\mathbb{T}^3) \rightarrow L_2(\mathbb{T}^3)$ as $\tilde{h}_\mu(k) = U^{-1}h_\mu(k)U$, where

$$(Uf)(p) = f\left(p - \frac{1}{2}\theta(k)\right),$$

$$\theta(k) = (\theta_1(k_1), \theta_2(k_2), \theta_3(k_3)), \quad \theta_i(k_i) = \arccos \frac{\frac{1}{m_1} + \frac{1}{m_2} \cos 2k_i}{\sqrt{\frac{1}{m_1^2} + \frac{2}{m_1 m_2} \cos 2k_i + \frac{1}{m_2^2}}}, \quad i = 1, 2, 3.$$

Lemma 3.1. 1. The following equality holds

$$L_2(\mathbb{T}^3) = \bigoplus_{l=1}^{27} \mathcal{H}_l. \quad (4)$$

2. The operator $h_\mu(k)$ is invariant with respect to \mathcal{H}_l , $l = \overline{1, 27}$, i.e., $h_\mu(k) : \mathcal{H}_l \rightarrow \mathcal{H}_l$.

Proof. 1. For brevity, let us introduce some notations: o , e , 0 and π denote even, odd, π -even and π -odd notions of variables, respectively. For example, \mathcal{H}^e denotes a space of functions $f(p)$ which are even with respect to variable p_1 , similarly, \mathcal{H}_0^{ee} denotes a space of functions $f(p)$ which are even with respect to each variables p_1, p_2 and π -even with respect to p_1 .

We represent $f \in L_2(\mathbb{T}^3)$ as

$$f(p_1, p_2, p_3) = f^e(p_1, p_2, p_3) + f^o(p_1, p_2, p_3),$$

where

$$f^e(p_1, p_2, p_3) = \frac{f(p_1, p_2, p_3) + f(-p_1, p_2, p_3)}{2} \in \mathcal{H}^e,$$

$$f^o(p_1, p_2, p_3) = \frac{f(p_1, p_2, p_3) - f(-p_1, p_2, p_3)}{2} \in \mathcal{H}^o.$$

It is clear that $L_2(\mathbb{T}^3) = \mathcal{H}^e \oplus \mathcal{H}^o$.

Similarly, we represent the functions f^e and f^o as

$$f^e(p_1, p_2, p_3) = f^{ee}(p_1, p_2, p_3) + f^{eo}(p_1, p_2, p_3)$$

and

$$f^o(p_1, p_2, p_3) = f^{oe}(p_1, p_2, p_3) + f^{oo}(p_1, p_2, p_3),$$

where

$$f^{ee}(p_1, p_2, p_3) = \frac{f^e(p_1, p_2, p_3) + f^e(p_1, -p_2, p_3)}{2} \in \mathcal{H}^{ee},$$

$$f^{eo}(p_1, p_2, p_3) = \frac{f^e(p_1, p_2, p_3) - f^e(p_1, -p_2, p_3)}{2} \in \mathcal{H}^{eo},$$

$$f^{oe}(p_1, p_2, p_3) = \frac{f^o(p_1, p_2, p_3) + f^o(p_1, -p_2, p_3)}{2} \in \mathcal{H}^{oe},$$

$$f^{oo}(p_1, p_2, p_3) = \frac{f^o(p_1, p_2, p_3) - f^o(p_1, -p_2, p_3)}{2} \in \mathcal{H}^{oo}.$$

Then $\mathcal{H}^e = \mathcal{H}^{ee} \oplus \mathcal{H}^{eo}$ and $\mathcal{H}^o = \mathcal{H}^{oe} \oplus \mathcal{H}^{oo}$.

Arguing similarly step by step we obtain the equality of the direct sum of subspaces

$$L_2(\mathbb{T}^3) = \mathcal{H}^{eee} \oplus \mathcal{H}^{eeo} \oplus \mathcal{H}^{eoe} \oplus \mathcal{H}^{oeo} \oplus \mathcal{H}^{ooo} \oplus \mathcal{H}^{oee} \oplus \mathcal{H}^{oeo} \oplus \mathcal{H}^{ooe} \oplus \mathcal{H}^{ooo}. \quad (5)$$

Each subspace in (5) is represented via the direct sum of subspaces defined as combination of π -even and π -odd functions

$$\mathcal{H}^{eee} = \mathcal{H}_{000}^{eee} \oplus \mathcal{H}_{\pi 00}^{eee} \oplus \mathcal{H}_{0\pi 0}^{eee} \oplus \mathcal{H}_{00\pi}^{eee} \oplus \mathcal{H}_{0\pi\pi}^{eee} \oplus \mathcal{H}_{\pi 0\pi}^{eee} \oplus \mathcal{H}_{\pi\pi 0}^{eee} \oplus \mathcal{H}_{\pi\pi\pi}^{eee},$$

$$\mathcal{H}^{eeo} = \mathcal{H}_{00\pi}^{eeo} \oplus \mathcal{H}_{0\pi\pi}^{eeo} \oplus \mathcal{H}_{\pi 0\pi}^{eeo} \oplus \mathcal{H}_{\pi\pi\pi}^{eeo}, \quad \mathcal{H}^{eoe} = \mathcal{H}_{0\pi 0}^{eoe} \oplus \mathcal{H}_{0\pi\pi}^{eoe} \oplus \mathcal{H}_{\pi 0\pi}^{eoe} \oplus \mathcal{H}_{\pi\pi\pi}^{eoe},$$

$$\mathcal{H}^{oeo} = \mathcal{H}_{\pi 00}^{oeo} \oplus \mathcal{H}_{\pi\pi 0}^{oeo} \oplus \mathcal{H}_{\pi 0\pi}^{oeo} \oplus \mathcal{H}_{\pi\pi\pi}^{oeo}, \quad \mathcal{H}^{ooo} = \mathcal{H}_{0\pi\pi}^{ooo} \oplus \mathcal{H}_{\pi\pi\pi}^{ooo},$$

$$\mathcal{H}^{oee} = \mathcal{H}_{\pi 0\pi}^{oee} \oplus \mathcal{H}_{\pi\pi\pi}^{oee}, \quad \mathcal{H}^{ooe} = \mathcal{H}_{\pi\pi 0}^{ooe} \oplus \mathcal{H}_{\pi\pi\pi}^{ooe}, \quad \mathcal{H}^{ooo} = \mathcal{H}_{\pi\pi\pi}^{ooo}.$$

Substituting these equalities into (5), we obtain (4).

2. By (2), the operator \mathbf{v} can be expressed via \mathbf{v}_l as

$$(\mathbf{v}f)(p) = \sum_{l=1}^{27} (\mathbf{v}_l f)(p), \quad (\mathbf{v}_l f)(p) = (\varphi_l, f)\varphi_l(p), \quad \varphi_l \in \mathcal{H}_l, \quad l = \overline{1, 27}.$$

Since $\{\varphi_l(\cdot)\}$, $l = \overline{1, 27}$ is an orthogonal system in $L_2(\mathbb{T}^3)$, $\mathbf{v} : \mathcal{H}_l \rightarrow \mathcal{H}_l$. One can see that $\tilde{\mathcal{E}}_k(p)\varphi_l(p) \in \mathcal{H}_l$. Hence, $h_\mu(k) : \mathcal{H}_l \rightarrow \mathcal{H}_l$. \square

The following lemma is proven in [14]

Lemma 3.2. Suppose Assumption 2.1 does not hold. Then the integral

$$\int_{\mathbb{T}^3} \frac{\varphi(s)ds}{\tilde{\mathcal{E}}_k(s) - m(k)}$$

converges for any $\varphi \in C(\mathbb{T}^3)$.

Lemma 3.3. A number z , $z \in \mathbb{C} \setminus [m(k), M(k)]$, is an eigenvalue of $h_{\mu,l}(k)$ iff $\Delta_l(\mu, k; z) = 0$, where

$$\Delta_l(\mu, k; z) = 1 - \mu\xi_l(k; z). \quad (6)$$

Proof of lemma 3.3. Let $z \in \mathbb{C} \setminus [m(k), M(k)]$ be an eigenvalue of $h_{\mu,l}(k)$ and $f_l, l = \overline{1, 27}$ be the corresponding eigenfunction, i.e., the equation

$$h_{\mu,l}(k)f_l = zf_l$$

has a nontrivial solution f_l . Then

$$f_l = \mu(r_0(k, z)\mathbf{v}_l)f_l, \quad l = \overline{1, 27}, \tag{7}$$

where $r_0(k, z)$ is a multiplication operator by the function $\frac{1}{\tilde{\mathcal{E}}_k(p) - z}$. Denote

$$\psi_l = (\varphi_l, f_l). \tag{8}$$

Then equation (7) can be represented as

$$f_l(p) = \frac{\mu\varphi_l(p)}{\tilde{\mathcal{E}}_k(p) - z}\psi_l. \tag{9}$$

By substituting (9) in (8), we obtain the following equation

$$\psi_l = \mu \int_{\mathbb{T}^3} \frac{\varphi_l^2(s)ds}{\tilde{\mathcal{E}}_k(s) - z}\psi_l, \quad l = \overline{1, 27}.$$

If $z \in \mathbb{C} \setminus [m(k), M(k)]$ is an eigenvalue of the operator $h_{\mu,l}(k)$ then $\Delta_l(\mu, k; z) = 0$. Conversely, let $\Delta_l(\mu, k; z) = 0$ with $z \in \mathbb{C} \setminus [m(k), M(k)]$, i.e.,

$$1 - \mu\xi_l(k; z) = 0.$$

Then the function

$$\psi_l(p) = \frac{\varphi_l(p)}{\tilde{\mathcal{E}}_k(p) - z}$$

is an eigenfunction of the operator $h_{\mu,l}(k)$ corresponding to the eigenvalue $z \in \mathbb{C} \setminus [m(k), M(k)]$. □

Lemma 3.3 gives the following result.

Corollary 3.1. A number $z, z \in \mathbb{C} \setminus [m(k), M(k)]$, is an eigenvalue of $h_{\mu}(k)$ iff $\Delta(\mu, k; z) = 0$, where

$$\Delta(\mu, k; z) = \prod_{l=1}^{27} \Delta_l(\mu, k; z).$$

Further we prove the main results for $\mu > 0$. The case $\mu < 0$ will be proven in a similar way.

Proof of Theorem 2.2. By Lemma 3.2, the integral

$$\int_{\mathbb{T}^3} \frac{\varphi_l^2(s)ds}{\tilde{\mathcal{E}}_k(s) - m(k)}$$

converges for any $\varphi_l \in \mathcal{H}_l, l = \overline{1, 27}$.

1. The function $\Delta_l(\cdot, k; \cdot)$ is monotonically decreasing for $z \in (-\infty, m(k))$ ($\mu \in (0, \infty)$) for any fixed $\mu > 0$ ($z < m(k)$). Then we have

$$\Delta_l(\mu, k; z) > \Delta_l(\mu, k; m(k)) > \Delta_l(\mu_l^0(k), k; m(k)) = 0 \quad \text{for all } \mu \in (0, \mu_l^0(k)).$$

According to Lemma 3.3, the operator $h_{\mu,l}(k), l = \overline{1, 27}$ has no eigenvalues lying to the left of the essential spectrum.

2. Let $z = 0$ and $\mu = \mu_l^0(m(\mathbf{0})), \mathbf{0} = (0, 0, 0) \in \mathbb{T}^3$. Then

$$\Delta_l(\mu_l^0(m(\mathbf{0})), \mathbf{0}; 0) = 1 - \mu_l^0(m(\mathbf{0})) \int_{\mathbb{T}^3} \frac{\varphi_l^2(s)ds}{\tilde{\mathcal{E}}_{\mathbf{0}}(s) - m(\mathbf{0})} = 0.$$

Then the function

$$f_l(p) = \frac{\varphi_l(p)}{\tilde{\mathcal{E}}_{\mathbf{0}}(p) - m(\mathbf{0})}, \quad l = \overline{1, 27}.$$

is a solution of the equation $h_{\mu,l}(\mathbf{0})f_l = 0$. Indeed,

$$h_{\mu,l}(\mathbf{0})f_l = \varphi_l(p) \left(1 - \mu_l^0(m(\mathbf{0})) \int_{\mathbb{T}^3} \frac{\varphi_l^2(s)ds}{\tilde{\mathcal{E}}_{\mathbf{0}}(s) - m(\mathbf{0})} \right) = 0.$$

Note that from the equation (1), we have

$$\varphi_l(\mathbf{0}) = \prod_{\alpha=1}^3 \eta_l(\mathbf{0}) \neq 0, \quad l = \overline{1, 8}, \quad \varphi_l(\mathbf{0}) = \prod_{\alpha=1}^3 \eta_l(\mathbf{0}) = 0, \quad l = \overline{9, 27}.$$

Therefore,

$$f_l \in L_1(\mathbb{T}^3) \setminus L_2(\mathbb{T}^3), \quad l = \overline{1, 8} \quad f_l \in L_2(\mathbb{T}^3), \quad l = \overline{9, 27}.$$

This yields that $h_{\mu, l}(\mathbf{0})$ has a virtual level at $z = 0$ for any $l = \overline{1, 8}$ and $z = 0$ is an eigenvalue of $h_{\mu, l}(\mathbf{0})$ for any $l = \overline{9, 27}$.

3. Let $\mu > \mu_l^0(k)$. Then

$$\lim_{z \rightarrow m(k)} \Delta_l(\mu, k; z) = \Delta_l(\mu, k; m(k)) = 1 - \frac{\mu}{\mu_l^0(k)} < 0.$$

Note that

$$\lim_{z \rightarrow -\infty} \Delta_l(\mu, k; z) = 1.$$

Then from the continuity and monotonicity of $\Delta_l(\mu, k; \cdot)$ in $(-\infty, m(k))$, we have that there exists unique $z_l \in (-\infty, m(k))$ such that

$$\Delta_l(\mu, k; z_l) = 0.$$

According to Lemma 3.3, the operator $h_{\mu, l}(k)$ has unique eigenvalue lying to the left of the essential spectrum. \square

Proof of Theorem 2.3. 1. We prove theorem for the case $k \in \Pi_1, k_1 = \pm \frac{\pi}{2}$. Then the function $\tilde{\mathcal{E}}_k(\cdot)$ does not depend of p_1 is expressed as

$$\tilde{\mathcal{E}}_k(p) = \frac{6}{m} - \sum_{i=2}^3 \frac{1}{m} \sqrt{2 + 2 \cos 2k_i \cos 2p_i}.$$

We separate the functions $\xi_l(k; \cdot)$ with $\varphi_l(p_1, 0, 0) \neq 0$. There are 12 such functions and after integrating them with respect to s_1 they can be represented as

$$\begin{aligned} \xi_1(k; z) &= 2\pi \int_{\mathbb{T}^2} \frac{ds}{\tilde{\mathcal{E}}_k(s) - z}, & \xi_2(k; z) = \xi_9(k; z) &= \pi \int_{\mathbb{T}^2} \frac{ds}{\tilde{\mathcal{E}}_k(s) - z}, \\ \xi_{i+1}(k; z) &= 2\pi \int_{\mathbb{T}^2} \frac{\cos^2 s_i ds}{\tilde{\mathcal{E}}_k(s) - z}, & \xi_{i+3}(k; z) = \xi_{i+8}(k; z) &= \pi \int_{\mathbb{T}^2} \frac{\cos^2 s_i ds}{\tilde{\mathcal{E}}_k(s) - z}, \quad i = 2, 3, \\ \xi_7(k; z) &= 2\pi \int_{\mathbb{T}^2} \frac{\cos^2 s_2 \cos^2 s_3 ds}{\tilde{\mathcal{E}}_k(s) - z}, & \xi_8(k; z) = \xi_{12}(k; z) &= \pi \int_{\mathbb{T}^2} \frac{\cos^2 s_2 \cos^2 s_3 ds}{\tilde{\mathcal{E}}_k(s) - z}. \end{aligned}$$

Since $(\tilde{\mathcal{E}}_k(p) - m(k)) = O(p^2)$ as $|p| \rightarrow 0$, the last equations give

$$\lim_{z \rightarrow m(k)} \Delta_l(\mu, k; z) = -\infty.$$

According to the continuity and monotonicity of $\Delta_l(\mu, k; \cdot)$ in $(-\infty, m(k))$ and

$$\lim_{z \rightarrow -\infty} \Delta_l(\mu, k; z) = 1,$$

there exists unique $z_l \in (-\infty, m(k))$ such that

$$\Delta_l(\mu, k; z_l) = 0, \quad l = \overline{1, 12}.$$

The cases $k_i = \pm \frac{\pi}{2}, i = 2, 3$ can be considered in a similar way.

2. We prove theorem for the case $k \in \Pi_2$ with $k_1 = k_2 = \pm \frac{\pi}{2}$. The function $\tilde{\mathcal{E}}_k(\cdot)$ does not depend of p_1, p_2 and is expressed as

$$\tilde{\mathcal{E}}_k(p) = \frac{6}{m} - \frac{1}{m} \sqrt{2 + 2 \cos 2k_3 \cos 2p_3}.$$

Then there exist 18 functions $\xi_l(k; \cdot), l = \overline{1, 18}$ with $\varphi_l(p_1, p_2, 0) \neq 0$. These functions are represented via integrals with respect to s_3 and contain a numerator function $\tilde{\varphi}_l(s_3)$ with $\tilde{\varphi}_l(0) \neq 0$. Since $(\tilde{\mathcal{E}}_k(p_3) - m(k)) = O(p_3^2)$ as $p_3 \rightarrow 0$, the last equations give

$$\lim_{z \rightarrow m(k)} \xi_l(k; z) = +\infty, \quad \lim_{z \rightarrow m(k)} \Delta_l(\mu, k; z) = -\infty, \quad l = \overline{1, 18}.$$

Hence there exists unique $z_l \in (-\infty, m(k))$ such that

$$\Delta_l(\mu, k; z_l) = 0, \quad l = \overline{1, 18}.$$

The remaining cases with $k \in \Pi_2$ are proved in a similar way.

3. The case $k \in \Pi_3$ can also be considered by similar discussions as in parts 1) and 2). \square

Theorem 2.3 leads to Theorem 2.1.

4. Conclusion

We investigate the existence conditions for eigenvalues of the two-particle Schrödinger operator $h_\mu(k)$, $k \in \mathbb{T}^3$, $\mu \in \mathbb{R}$ corresponding to the Hamiltonian of the two-particle system on the three-dimensional lattice, where $h_\mu(k)$ is considered as a perturbation of free Hamiltonian $h_0(k)$ by the potential operator μv with rank 27.

To study spectral properties of $h_\mu(k)$, we first constructed the invariant subspaces $\mathcal{H}_l \subset L_2(\mathbb{T}^3)$, $l = \overline{1, 27}$ for the operator $h_\mu(k)$. Moreover, investigation of the spectral properties of the operator $h_\mu(k)$ is reduced to the study of the operator $h_{\mu,l}(k) := h_\mu(k) : \mathcal{H}_l \rightarrow \mathcal{H}_l$, $l = \overline{1, 27}$. Further, eigenvalue problem for $h_{\mu,l}(k)f = zf$, $z \notin \sigma_{ess}(h_\mu(k))$ is reduced to the study of an integral operator $\mu G_l(z)$ of rank one. This allowed us to analyze the eigenvalue problem of $h_{\mu,l}(k)$ for any $\mu \in \mathbb{R}$.

Particularly, if $k = \mathbf{0}$, then there exist the numbers $\mu_l^0(m(\mathbf{0})) > 0$ and $\mu_l^0(M(\mathbf{0})) < 0$, $l = \overline{1, 27}$ such that

(i) for any μ with $0 < \mu < \mu_l^0(\mathbf{0})$ (resp. $\mu_l^0(\mathbf{0}) < \mu < 0$) the operator $h_{\mu,l}(\mathbf{0})$ has no eigenvalues lying to the left (resp. to the right) of the essential spectrum;

(ii) for $\mu = \mu_l^0(m(\mathbf{0}))$ (resp. $\mu_l^0(M(\mathbf{0})) = \mu$), if $\varphi_l(\mathbf{0}) \neq 0$, then $h_{\mu,l}(\mathbf{0})$ has a virtual level at $z = 0$ (resp. at $z = 6 \frac{m_1 + m_2}{m_1 m_2}$), if $\varphi_l(\mathbf{0}) = 0$, then the number $z = 0$ (resp. $z = 6 \frac{m_1 + m_2}{m_1 m_2}$) is an eigenvalue of $h_{\mu,l}(\mathbf{0})$;

(iii) for any μ , $\mu > \mu_l^0(\mathbf{0}) > 0$ (resp. $\mu < \mu_l^0(\mathbf{0}) < 0$), the operator $h_{\mu,l}(\mathbf{0})$ has unique eigenvalue lying to the left (resp. to the right) of the essential spectrum.

References

- [1] Bloch I., Dalibard J., and Nascimbene S. Quantum simulations with ultracold quantum gases, *Nature Physics*, 2012, **8**, P. 267–276.
- [2] Jaksch D., Zoller P. The cold atom Hubbard toolbox. *Annals of Physics*, 2005, **315**, P. 52–79.
- [3] Lewenstein M., Sanpera A., Ahufinger V. *Ultracold Atoms in Optical Lattices: Simulating Quantum Many-body Systems*. Oxford University, Press, 2012.
- [4] Gullans M., Tiecke T.G., Chang D.E., Feist J., Thompson J.D., Cirac J.I., Zoller P., Lukin M.D. Nanoplasmonic Lattices for Ultracold Atoms. *Phys. Rev. Lett.*, 2012, **109**, P. 235309.
- [5] Hecht E. *Optics*. Addison-Wesley, Reading, MA. 1998.
- [6] Murphy B., Hau L.V. Electro-optical nanotraps for neutral atoms. *Phys. Rev. Lett.*, 2009, **102**, P. 033003.
- [7] N.P. de Leon, Lukin M.D., and Park H. Quantum plasmonic circuits. *IEEE J. Sel. Top. Quantum Electron.*, 2012, **18**, P. 1781–1791.
- [8] Faria da Veiga P. A., Ioriatti L., O’Carroll M. Energy momentum spectrum of some two-particle lattice Schrödinger Hamiltonians. *Physical Review E*, 2006, **66**, 016130.
- [9] Muminov M. E. Positivity of the two-particle Hamiltonian on a lattice. *Theor. Math. Phys.*, 2007, **153**(3), P. 1671–1676.
- [10] Bagmutov A. S., Popov I. Y. Window-coupled nanolayers: window shape influence on one-particle and two-particle eigenstates. *Nanosystems: Physics, Chemistry, Mathematics*, 2020, **11**(6), P. 636–641.
- [11] Hiroshima F., Sasaki I., Shirai T., Suzuki A. Note on the spectrum of discrete Schrödinger operators. *Journal of Math-for-Industry*, 2012, **4**, P. 105–108.
- [12] Higuchi Y., Matsumoto T., Ogurisu O. On the spectrum of a discrete Laplacian on \mathbb{Z} with finitely supported potential. *Linear and Multilinear Algebra*, 2011, **8**, P. 917–927.
- [13] Albeverio S., Lakaev S. N., Makarov K. A., Muminov Z. I. The Threshold effects for the two-particle Hamiltonians. *Communications in Mathematical Physics*, 2006, **262**, P. 91–115.
- [14] Muminov M. E., Khurramov A. M. Spectral properties of a two-particle Hamiltonian on a lattice. *Theor. Math. Phys.*, 2013, **177**(3), P. 482–496.
- [15] Muminov M. E., Khurramov A. M. Multiplicity of virtual levels at the lower edge of the continuous spectrum of a two-particle Hamiltonian on a lattice. *Theor. Math. Phys.*, 2014, **180**(3), P. 329–341.
- [16] Bozorov I. N., Khurramov A. M. On the number of eigenvalues of the lattice model operator in one-dimensional case. *Lobachevskii Journal of Mathematics*, 2022, **43**(2), P. 353–365.
- [17] Muminov M. I., Khurramov A. M. Spectral properties of a two-particle hamiltonian on a d -dimensional lattice. *Nanosystems: Physics, Chemistry, Mathematics*, 2016, **7**(5), P. 880–887.
- [18] Lakaev S. N., Bozorov I. N. The number of bound states of a one-particle Hamiltonian on a three-dimensional lattice. *Theor. Math. Phys.*, 2009, **158**(3), P. 360–376.
- [19] Abdullaev J. I., Khalkhuzhaev A. M., Usmonov L. S. Monotonicity of the eigenvalues of the two-particle Schrödinger operator on a lattice. *Nanosystems: Physics, Chemistry, Mathematics*, 2021, **12**(6), P. 657–663.
- [20] Reed M., Simon B. *Methods of modern Mathematical Physics. Vol.4. Analysis of Operators*. Academic Press, London, 1980, 404 p.

Submitted 17 May 2022; accepted 26 May 2022

Information about the authors:

M. I. Muminov – Samarkand State University, University blv., 15, Samarkand, 140104, Uzbekistan; V. I. Romanovskiy Institute of Mathematics, Uzbekistan Academy of sciences 100174, Tashkent, Uzbekistan; mmuminov@mail.ru

A. M. Khurramov – Samarkand State University, University blv., 15, Samarkand, 140104, Uzbekistan; xurramov@mail.ru

I. N. Bozorov – Samarkand State University, University blv., 15, Samarkand, 140104, Uzbekistan; islomnb@mail.ru

Conflict of interest: the authors declare no conflict of interest.

Spectral gaps for star-like quantum graph and for two coupled rings

Irina V. Blinova^a, Anton I. Popov^b, Anna A. Bosova^c

ITMO University, St. Petersburg, 197101, Russia

^airin-a@yandex.ru, ^bpopov239@gmail.com, ^cbossandbosss@yandex.ru

Corresponding author: I. V. Blinova, irin-a@yandex.ru

ABSTRACT The spectral problems for two types of quantum graphs are considered. We deal with star-like graph and a graph consisting of two rings connected through a segment. The spectral gap, i.e. the difference between the second and the first eigenvalues of the free Schrödinger operator, is studied. The dependence of the gap on the geometric parameters of the graph is investigated. Particularly, it is shown that the maximal gap is observed for the symmetric quantum graph.

KEYWORDS spectral gap, quantum graph, Schrödinger operator, discrete spectrum.

FOR CITATION Blinova I.V., Popov A.I., Bosova A.A. Spectral gaps for star-like quantum graph and for two coupled rings. *Nanosystems: Phys. Chem. Math.*, 2022, **13** (3), 245–249.

1. Introduction

The most adequate models of quantum system (particularly, for nanosystems) is ab initio methods. But using of such approaches is not simple due to great computational complexity. The situation changes if a particle under consideration cannot leave a submanifold of less dimension [1–4]. It allows one to reduce the problem to a task on this manifold or several manifolds [5]. Correspondingly, an important point is a way of gluing of solutions on different manifolds. It can be made in the framework of the theory of self-adjoint extensions of symmetric operators [6–11]. The simplest model of such type is quantum graph. Rigorous mathematical theory of quantum graphs was constructed last decades [12–14]. Hybrid manifolds were studied in less extent [3, 15, 16]. It was shown that such models are effective for description of spectral properties of operators. Some approaches were developed in this field (Krein’s formula approach, boundary triplets method, spaces of boundary values).

In our paper, the spectral gap for a few simple quantum graphs is determined and a relation to graph surgery is discussed. One can mention recent results concerning to quantum graph problems related to the present paper [17–21].

The quantum graph is a set of vertices and edges. At each edge e_i , we consider the free Schrödinger operator

$$H_i = \frac{d^2}{dx^2}$$

with the domain $W_2^2(e_i)$ acting in the space $L_2(e_i)$. Here $W_2^2(e_i)$ is the Sobolev space. The state space for the whole graph is $\sum_i \oplus L_2(e_i)$. To determine the Hamiltonian for the graph, we consider the operator H_i at each edge and impose a coupling condition at the graph vertices. We choose the Kirchhoff condition. It means that a function from the operator domain should be continuous on the graph, particularly, at vertices, i.e. it should have the same boundary value at each edge e_{ji} , e_{pi} adjacent to the vertex v_i :

$$\psi_j(v_i) = \psi_p(v_i). \quad (1)$$

The second condition at the vertex v_i is vanishing of the algebraic sum over all adjacent vertices of derivatives:

$$\sum_{e_{ji}} (-1)^{\nu_{ji}} \psi_j(v_i) = 0, \quad (2)$$

where $\nu_{ji} = 1$ if the edge e_{ji} is outgoing from the vertex v_i and $\nu_{ji} = -1$ if the edge e_{ji} is incoming to the vertex v_i . As for the boundary vertices of the quantum graph, we assume the Dirichlet boundary condition here

$$\psi_j(v_i) = 0. \quad (3)$$

We consider quantum graphs with finite number of edges of finite lengths, correspondingly, the Hamiltonian has purely discrete spectrum. To solve the spectral problem, it is necessary to solve the equation

$$-\psi_i''(x) = \lambda \psi_i(x)$$

at each edge e_i and to satisfy the boundary conditions at all vertices.

2. Spectral gap

2.1. Star-like graph

Consider a star-type graph with 5 vertices and 4 edges and study the dependence of the spectral gap on the ratio of edge lengths.

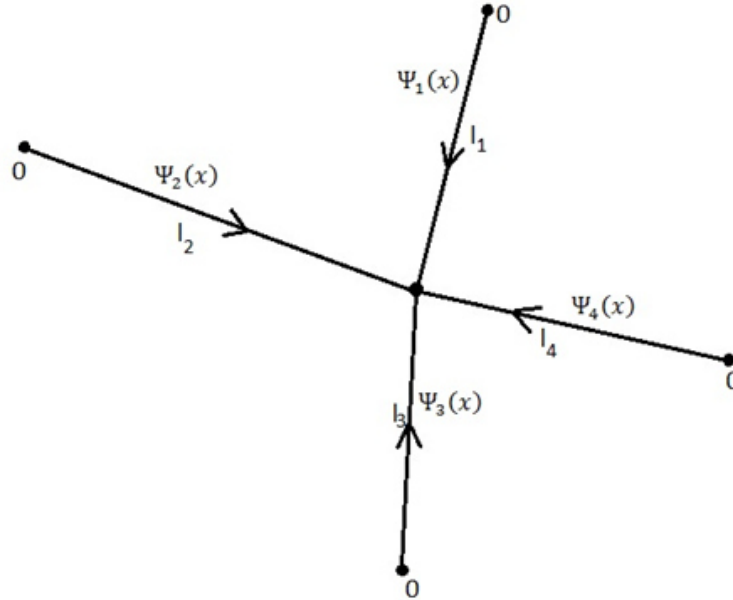


FIG. 1. Graph with 5 vertices and 4 edges

On each edge of the graph, the solution has a form $\psi = a \cos kx + b \sin kx$. The coefficients are determined from the conditions at the vertices. On the edges e_1, e_2, e_3, e_4 of lengths l_1, l_2, l_3, l_4 , correspondingly, functions $\psi_1(x), \dots, \psi_4(x)$ are given by the following expressions

$$\begin{cases} \psi_1(x) = A \cos kx + B \sin kx, \\ \psi_2(x) = C \cos kx + D \sin kx, \\ \psi_3(x) = E \cos kx + F \sin kx, \\ \psi_4(x) = H \cos kx + G \sin kx. \end{cases}$$

Let us write down the system of coupling conditions at the vertices. Boundary conditions (1), (2), (3)) lead to a system of homogeneous equations for the coefficients. The condition for the system to have a nontrivial solution is that its determinant is equal to zero. This gives us the spectral equation:

$$\sin kl_1 \sin kl_2 \sin kl_3 \cos kl_4 + \sin kl_1 \sin kl_4 \sin kl_3 \cos kl_2 + \sin kl_2 \sin kl_4 \sin kl_3 \cos kl_1 + \sin kl_1 \sin kl_2 \sin kl_4 \cos kl_3 = 0. \quad (4)$$

Eigenvalues $\lambda_i = k_i^2$, where k_i is the i -th root of the spectral equation (4), are positive and they are ordered increasingly. The spectral gap is the difference between the second and first eigenvalues. Let's see how the spectral gap changes if one varies the lengths of edges. To ensure the comparability of the gaps,, we preserve the total length of the graph L unchanged for all such transformations. Let us take the unit total length for simplicity: $L = 1$. Consider the following variation of lengths:

$$l_1 = L + \delta, \quad l_2 = L - \frac{\delta}{3}, \quad l_3 = L - \frac{\delta}{3}, \quad l_4 = L - \frac{\delta}{3}.$$

Figure 2. shows the dependence of the spectral gap on the value of δ . One can see that the maximal value of the spectral gap is observed for the symmetric case when all edges are equal ($\delta = 0$). The graph in Fig. 2 is not even in respect to δ because the perturbation is not symmetric: the length of one edge increases and the lengths of three edges decrease. In case of two increasing and two decreasing lengths, the graph is even, naturally.

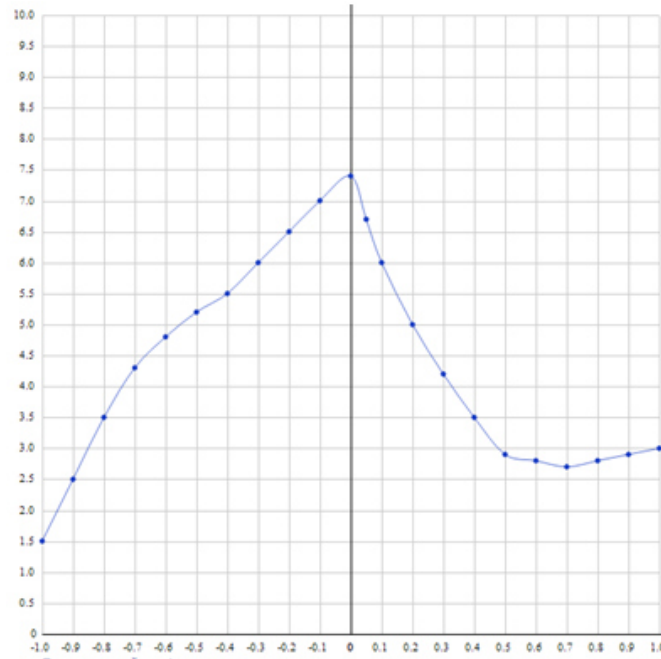


FIG. 2. Dependence of the spectral gap on the value of δ ; dimensionless units

2.2. Two coupled loops

Consider a graph with two loops coupled by one edge. It is shown in Fig. 3. Parameter x at the rings is the length of the arc starting from the vertex. It should be noted that in the considered case, the curvature of the edge does not play a role.

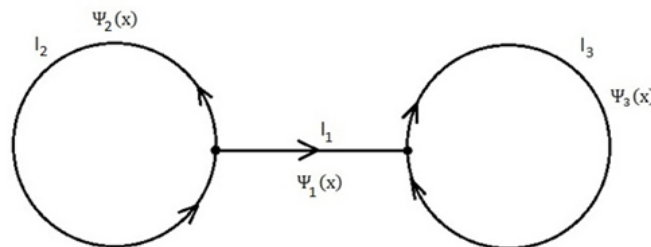


FIG. 3. Two coupled loops

On each edge of the graph, the solution has the following form $\psi(x) = a \cos kx + b \sin kx$. The coefficients are determined from the conditions at the vertices. In this case, the spectral equation has the form:

$$-\sin\left(\frac{kl_1}{2}\right) \sin\left(\frac{kl_3}{2}\right) \times \left(2 \sin(kl_2) \left(5 \cos\left(\frac{1}{2}k(l_1 + l_3)\right) - 3 \cos\left(\frac{1}{2}k(l_1 - l_3)\right)\right) + 8 \sin\left(\frac{1}{2}k(l_1 + l_3)\right) \cos(kl_2)\right) = 0.$$

We vary the lengths of the edges preserving the total length of the graph unchanged, i. e. $L = 1$. Consider the following symmetrical and asymmetrical length variations:

$$\begin{cases} 1) l_1 = L + \delta, l_2 = L - \frac{\delta}{2}, l_3 = L - \frac{\delta}{2}. \\ 2) l_1 = L + \delta, l_2 = L - \frac{5}{6}\delta, l_3 = L - \frac{\delta}{6}. \\ 3) l_1 = L - \frac{\delta}{4}, l_2 = L - \frac{3}{4}\delta, l_3 = L + \delta. \end{cases} \quad (5)$$

Figure 4 shows plots of the spectral gap versus δ for these three cases. One can see that curve 1 corresponding to the symmetric perturbation lies above curves 2,3. It is interesting that there are also such values of the perturbation which correspond to minima of the graph of this dependence.

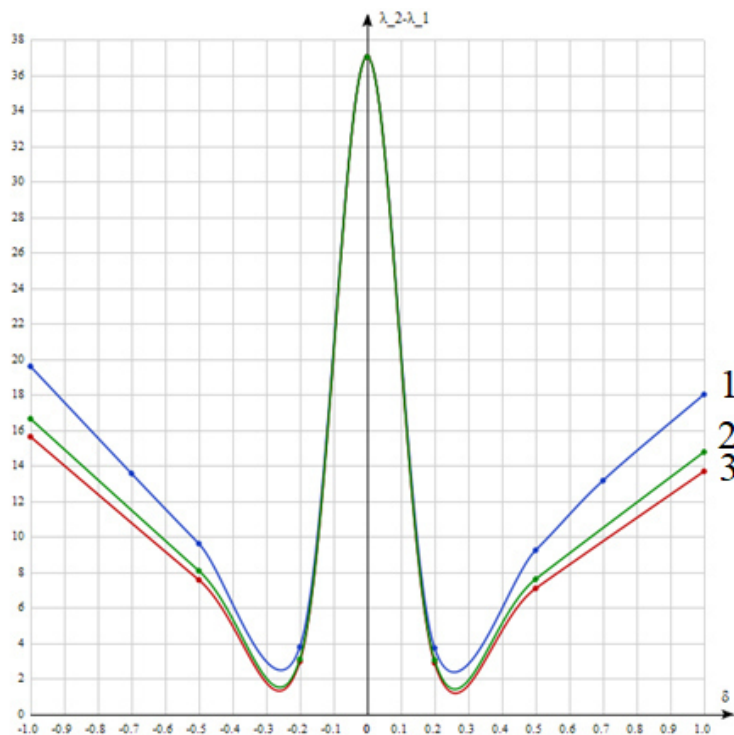


FIG. 4. Plots of the spectral gap versus δ ; curves 1, 2, 3 correspond to cases in (5); dimensionless units.

Thus, consideration of these two types of quantum graphs leads to the conclusion that the value of the spectral gap depends on the symmetry of the graph and the ratio of the lengths of the edges. The largest gap is obtained in a symmetrical situation. Any breaking of symmetry leads to the decreasing of the spectral gap.

References

- [1] Berkolaiko G. and Kuchment P. Dependence of the spectrum of a quantum graph on vertex conditions and edge lengths. *Spectral geometry. Proc. Sympos. Pure Math.*, Amer. Math. Soc., Providence, 2012, **84**, P. 117–137.
- [2] Lipovsky J. Quantum Graphs And Their Resonance Properties. *Acta Physica Slovaca*, 2016, **66**(4), P. 265–363.
- [3] Brüning J., Geiler V. and Lobanov I. Spectral properties of Schrödinger operators on decorated graphs. *Mat. notes*, 2005, **77**(6), P. 932–935.
- [4] Sobirov Z.A., Rakhimov K.U., Ergashov R.E. Green's function method for time-fractional diffusion equation on the star graph with equal bonds. *Nanosystems: Phys. Chem. Math.*, 2021, **12**(3), P. 271–278.
- [5] Post O. *Spectral Analysis on Graph-Like Spaces*. Springer, 2010.
- [6] Alberverio S., Gesztesy F., Høegh-Krohn R., Holden H. *Solvable models in quantum mechanics*. AMS Chelsea Publishing, Providence, RI, 2005.
- [7] Pavlov B.S. The theory of extensions, and explicitly solvable models. *Uspekhi Mat. Nauk*, 1987, **42**(6), P. 99–131.
- [8] Popov I.Y. The resonator with narrow slit and the model based on the operator extensions theory. *Journal of Mathematical Physics*, 1992, **33**(11), P. 3794–3801.
- [9] Popov I.Y. Model of point-like window for electromagnetic Helmholtz resonator. *Zeitschrift für Analysis und ihre Anwendungen*, 2013, **32**(2), P. 155–162.
- [10] Geyler V.A., Popov I.Yu. Ballistic transport in nanostructures: explicitly solvable model. *Theor. Math. Phys.*, 1996, **107**(1), P. 427–434.
- [11] Behrndt J., Frank R.L., Kühn Ch., Lotoreichik V., Rohlleder J. Spectral Theory for Schrödinger Operators with delta-Interactions Supported on Curves in R^3 . *Ann. Henri Poincaré*, 2017, **18**, P. 1305–1347.
- [12] Exner P., Keating P., Kuchment P., Sunada T. and Teplyaev A. *Analysis on graph and its applications*, AMS, Providence, 2008.
- [13] Berkolaiko G. and Kuchment P. *Introduction to Quantum Graphs*, AMS, Providence, 2012.
- [14] Exner P., Kostenko A., Malamud M., Neidhardt H. Spectral theory of infinite quantum graphs. *Ann. H. Poincaré*, 2018, **19**, P. 3457–3510.
- [15] Boitsev A.A., Neidhardt H., Malamud M., Brasche J., Popov I.Y. Boundary Triplets, Tensor Products and Point Contacts to Reservoirs. *Annales Henri Poincaré*, 2018, **19**(9), P. 2783–2837.
- [16] Popov I.Y., Popov A.I. Quantum Dot with Attached Wires: Resonant States Completeness. *Reports on Mathematical Physics*, 2017, **80**(1), P. 1–10.
- [17] Kurasov P., Malenová G. and Naboko S. Spectral gap for quantum graphs and their edge connectivity. *Journal of Physics A: Mathematical and Theoretical*, 2013, **46**(27), article id. 275309, 16 pp.
- [18] Kurasov P. and Naboko S. Rayleigh estimates for differential operators on graphs. *J. Spectr. Theory*, 2014, **4**(2), P. 211–219.
- [19] Kennedy J., Kurasov P. and Malenová G.; et al. On the Spectral Gap of a Quantum Graph. *Ann. Henri Poincaré*, 2016, **17**, P. 2439.
- [20] Exner P., Khrabustovskiy A. Gap control by singular Schrödinger operators in a periodically structured metamaterial. *Journal of Mathematical Physics, Analysis, Geometry*, 2018, **14**(3), P. 270–285.
- [21] Barseghyan D., Khrabustovskiy A. Gaps in the spectrum of a periodic quantum graph with periodically distributed δ' -type interactions. *J. Phys. A*, 2015, **48**, P. 255201.

Information about the authors:

Irina V. Blinova – ITMO University, Kronverkskiy, 49, St. Petersburg, 197101, Russia; irin-a@yandex.ru

Anton I. Popov – ITMO University, Kronverkskiy, 49, St. Petersburg, 197101, Russia; popov239@gmail.com

Anna A. Bosova – ITMO University, Kronverkskiy, 49, St. Petersburg, 197101, Russia; bossandbosss@yandex.ru

Conflict of interest: the authors declare no conflict of interest.

Influence of dissipative tunneling on the photodielectric effect associated with the excitation of impurity complexes $A^+ + e$ in a quasi-zero-dimensional structure

Vladimir D. Krevchik¹, Alexey V. Razumov¹, Mikhail B. Semenov¹, Alexander V. Levashov¹, Alexey V. Shorokhov^{1,2}

¹Penza State University, Physics Department, Penza, Russia

²University of Jyväskylä, Seminaarinkatu, Finland

^aalex.shorokhov@gmail.com, ^bmisha29.02.1@gmail.com

Corresponding author: Alexey Vladimirovich Shorokhov, alex.shorokhov@gmail.com

PACS 73.40.Gk, 03.65.Xp

ABSTRACT Effect of tunneling decay for the quasi-stationary A^+ -state, in an impurity complex $A^+ + e$ (a hole, localized on a neutral acceptor, interacting with an electron, localized in the ground state of a quantum dot) on the photodielectric effect, associated with the excitation of impurity complexes $A^+ + e$ in a quasi-zero-dimensional structure, has been studied in the zero-radius potential model in the one-instanton approximation. Calculation of the binding energy of a hole in an impurity complex $A^+ + e$ was performed in the zero radius potential model in the adiabatic approximation. It is shown that as the probability of dissipative tunneling increases, the binding energy of a hole in a complex $A^+ + e$ decreases, which is accompanied by an increase in the effective localization radius of the impurity complex and, accordingly, an increase in the magnitude of the photodielectric effect. The spectral dependence of the photodielectric effect has been calculated in the dipole approximation taking into account the dispersion of the quantum dot radius. A high sensitivity of the magnitude of the photodielectric effect to such parameters of dissipative tunneling as the frequency of the phonon mode, temperature, and coupling constant with the contact medium, has been revealed.

KEYWORDS photodielectric effect, quantum dot, adiabatic approximation, impurity complex, relative permittivity, dissipative tunneling, adiabatic potential, quasi-zero-dimensional structure

ACKNOWLEDGEMENTS The work was supported by a grant from the Ministry of Science and Higher Education of the Russian Federation 0748-2020-0012.

FOR CITATION Krevchik V.D., Razumov A.V., Semenov M.B., Levashov A.V., Shorokhov A.V. Influence of dissipative tunneling on the photodielectric effect associated with the excitation of impurity complexes $A^+ + e$ in a quasi-zero-dimensional structure. *Nanosystems: Phys. Chem. Math.*, 2022, **13** (3), 250–264.

1. Introduction

Dielectric permittivity, as a measure of polarizability, is a fundamental parameter that determines the properties of various materials. Reversible control of the permittivity of materials in a wide range is an urgent problem. In this regard, of interest is the photodielectric effect (PDE), associated with a change in the permittivity of a material under the action of photoirradiation. In recent years, interest in PDE in various materials has increased due to a wide range of practical applications [1–8]. Thus, in article [1], a photo sensor developed on the basis of PDE in CdS is presented, which changes its electrical capacitance upon photoirradiation. The significant change in photocapacitance discovered by the authors of [1] opens up certain prospects for photosensor applications. In [2], PDE was experimentally studied in the compound $\text{LaAl}_{0.99}\text{Zn}_{0.01}\text{O}_{3-\delta}$. It was found that photoirradiation significantly increases the dielectric permittivity in the compound under study in a wide frequency range. It is expected that the results of [2] will contribute to the development of photocapacitors that allow remote control of the dielectric response using photoirradiation. In article [3], the systematic tuning of the PDE in $\text{Ba}(\text{Al}_{1-x}\text{Zn}_x)_2\text{O}_{4-\delta}$ was experimentally studied by varying the Zn concentration (x) and the intensity of the incident light. Results of the study in [3] can form the basis for the development of innovative phototunable functional devices. From the point of view of the possibility of controlling the PDE in a wide range, semiconductor nanostructures with impurity centers are promising. The presence of the quantum size effect makes it possible to control the binding energy of impurity centers, as well as the energy spectrum of the nanostructure, by varying its characteristic size.

Interest in the photodielectric effect (PDE) associated with the excitation of impurity complexes $A^+ + e$ in quantum dots (QDs) (a hole, localized at the A^+ -center, forms a quasi-stationary A^+ -state; an electron is localized in the ground

state of the QD) is due to the possibility of its usage as a method for spectroscopic studies of impurities in quasi-zero-dimensional semiconductor structures [9]. Spectral studies of impurities using PDE, in contrast to photothermal ionization, do not require thermal ionization of excited states. Therefore, measurements can be carried out at arbitrarily low temperatures, which eliminates the effect of temperature on the width of the optical absorption line. From a fundamental point of view, PDE is of interest as a nonlinear optical effect with a lower threshold than conventional nonlinear optical effects, and in the case of QD, this threshold can be controlled by changing of its (QD's) characteristic size. The resonant frequencies ν_0 , which characterize the PDE dispersion, can be in the submillimeter range, for example, as estimates show, for InSb QDs with radius $R_0 \approx 70$ nm, $\nu_0 \sim 10^{11}$ c⁻¹. Consequently, when a semiconductor quasi-zero-dimensional structure is irradiated with energy quanta $h\nu_0$, the refractive index of submillimeter waves should change. Therefore, PDE is an effective mechanism for the influence of IR-radiation on the propagation of submillimeter waves in semiconductor quasi-zero-dimensional structures with impurity complexes $A^+ + e$. As will be shown below, the presence of tunneling decay of quasi-stationary A^+ - states in a QD provides additional degrees of freedom for controlling of the PDE. The purpose of this work is to study theoretically influence of the tunnel decay of a quasi-stationary A^+ -state on the PDE, associated with the excitation of impurity complexes $A^+ + e$ in a quasi-zero-dimensional structure with semiconductor QDs.

2. The binding energy of a quasi-stationary A^+ -state in an impurity complex $A^+ + e$ in a semiconductor quantum dot

Figure 1 shows the energy structure of the “quantum dot with an impurity complex $A^+ + e$ – external matrix” model under consideration. Quasi-stationary A^+ -state can be formed by attaching an additional hole to a neutral acceptor. The finite lifetime of a hole is associated with the decay of the A^+ -state.

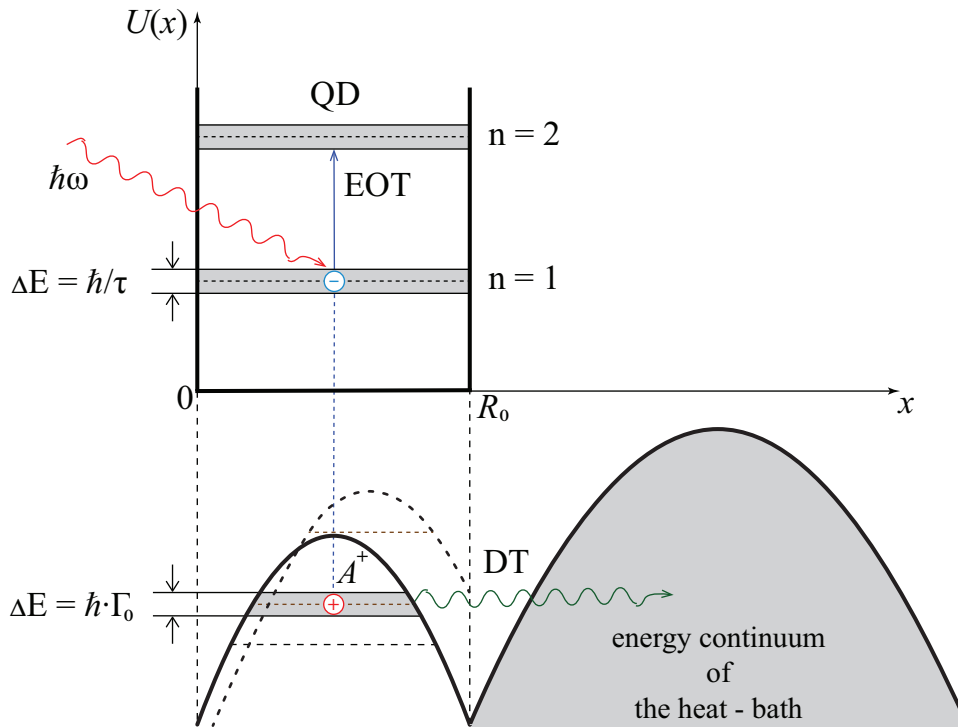


FIG. 1. Energy structure of the “quantum dot with an impurity complex $A^+ + e$ – external matrix” model. Electron is localized in the ground state of the quantum dot, the hole is in the quasi-stationary state of A^+ -center; $\Delta E = \hbar/\tau$ – magnitude of the broadening of the electronic energy level of the quantum dot, this broadening is associated with the radiative lifetime τ ; $\Delta E = \hbar\Gamma_0$ is the broadening of the impurity level, which is associated with the tunneling decay of the A^+ -state; DT – dissipative tunneling; the electron optical transition (EOT) is the optical transition of an electron from the ground state of the QD to the excited state; the dotted line shows the change in the potential profile of the adiabatic potential of the electron due to the change in its quantum state; R_0 is the QD radius.

We will assume that the process of decay of the quasi-stationary A^+ -state is mainly due to the dissipative tunneling of the hole. In the one-instanton approximation, the tunnel decay probability Γ_0 can be represented as $\Gamma_0 = B \exp(-S)$, where the action S and the pre-exponential factor B are defined as (in the Bohr units) [10]:

$$B = \frac{2\sqrt{U_0^*} E_h (1+b^*) \sqrt{\varepsilon_T^*}}{\sqrt{\pi} \hbar} \times \left\{ \frac{A^* \left[\beta_1^* \cosh\left(\frac{\beta_1^*}{2}\right) - 1 \right] + D^* \left[\beta_2^* \cosh\left(\frac{\beta_2^*}{2}\right) - 1 \right]}{\left\{ A^* \left[\frac{\beta_1^*}{2} \frac{\cosh\left(\frac{\beta_1^*}{2} - \tilde{\tau}_{01}^*\right)}{\sinh\left(\frac{\beta_1^*}{2}\right)} - 1 \right] + D^* \left[\frac{\beta_2^*}{2} \frac{\cosh\left(\frac{\beta_2^*}{2} - \tilde{\tau}_{02}^*\right)}{\sinh\left(\frac{\beta_2^*}{2}\right)} - 1 \right] \right\}^{\frac{1}{2}} + \frac{A^* \left[1 - \frac{\beta_1^*}{2} \frac{\cosh\left[\frac{\beta_1^*}{2} - \tilde{\tau}_{01}^*\right]}{\sinh\left[\frac{\beta_1^*}{2}\right]} \right] + D^* \left(\frac{\beta_2^*}{2} \frac{\cosh\left(\frac{\beta_2^*}{2} - \tilde{\tau}_{02}^*\right)}{\sinh\left(\frac{\beta_2^*}{2}\right)} - 1 \right)}{\left\{ A^* \left[\frac{\beta_1^*}{2} \frac{\cosh\left[\frac{\beta_1^*}{2} - \tilde{\tau}_{01}^*\right]}{\sinh\left[\frac{\beta_1^*}{2}\right]} - 1 \right] + D^* \left(\frac{\beta_2^*}{2} \frac{\cosh\left(\frac{\beta_2^*}{2} - \tilde{\tau}_{02}^*\right)}{\sinh\left(\frac{\beta_2^*}{2}\right)} - 1 \right) \right\}^{\frac{1}{2}}} \right\}, \quad (1)$$

and

$$S = a^* \sqrt{U_0^*} \left\{ \frac{1}{2} (b^* + 1)(3 - b^*) \tau_0^* - \frac{(b^* + 1)^2 (\tau_0^*)^2}{2\beta^*} - \frac{(b^* + 1)^2}{2\tilde{\gamma}'} \left\{ \frac{(1 - \tilde{x}'_2)}{\sqrt{\tilde{x}'_1}} \left[\coth(\beta^* \sqrt{\tilde{x}'_1}) - \frac{1}{\sinh(\beta^* \sqrt{\tilde{x}'_1})} \left\{ \cosh((\beta^* - \tau_0^*) \sqrt{\tilde{x}'_1}) - \cosh(\beta^* \sqrt{\tilde{x}'_1}) \right\} + \cosh((\beta^* - \tau_0^*) \sqrt{\tilde{x}'_1}) \right] - \frac{1 - \tilde{x}'_1}{\sqrt{\tilde{x}'_2}} \left[\coth(\beta^* \sqrt{\tilde{x}'_2}) - \frac{1}{\sinh(\beta^* \sqrt{\tilde{x}'_2})} \left\{ \cosh(\beta^* - \tau_0^*) \sqrt{\tilde{x}'_2} - \cosh(\beta^* \sqrt{\tilde{x}'_2}) \right\} + \cosh((\beta^* - \tau_0^*) \sqrt{\tilde{x}'_2}) \right] \right\} \right\}, \quad (2)$$

where

$$\begin{aligned} A^* &= \left(2\varepsilon_L^* a^{*2} - \gamma_{\delta.p.}^{(-)} \right) / \left(\gamma_{\delta.p.}^{(-)} - \gamma_{\delta.p.}^{(+)} \right) \gamma_{\delta.p.}^{(-)}, \\ D^* &= \left(2\varepsilon_L^* a^{*2} - \gamma_{\delta.p.}^{(+)} \right) / \left(\gamma_{\delta.p.}^{(-)} - \gamma_{\delta.p.}^{(+)} \right) \gamma_{\delta.p.}^{(+)}, \\ \beta_1^* &= \sqrt{\gamma_1} \beta = \sqrt{2U_0^* \gamma_{\delta.p.}^{(-)}} / a^* \varepsilon_T^*, \\ \beta_2^* &= \sqrt{\gamma_2} \beta = \sqrt{2U_0^* \gamma_{\delta.p.}^{(+)}} / a^* \varepsilon_T^*, \\ \tilde{\tau}_{01}^* &= 2\sqrt{\gamma_1} \tau_0 = \sqrt{\gamma_{\delta.p.}^{(-)} \tau_0'^*} / \sqrt{2}, \\ \tilde{\tau}_{02}^* &= 2\sqrt{\gamma_2} \tau_0 = \sqrt{\gamma_{\delta.p.}^{(+)} \tau_0'^*} / \sqrt{2}, \\ b^* &= b/a, \\ \beta^* &= \sqrt{U_0^*} / a^* \varepsilon_T^*, \\ \tau_0'^* &= \operatorname{arcsinh} \left((1 - b^*) \sinh \beta^* / (1 + b^*) \right) + \beta^*, \\ \tilde{\gamma}' &= \sqrt{(\varepsilon_L^* a^{*2} / 4U_0^* + 1 + \varepsilon_c^4 a^{*2} / 4\varepsilon_L^* U_0^*)^2 - \varepsilon_L^* a^{*2} / U_0^*}, \\ \varepsilon_T^* &= kT / E_h, \\ \varepsilon_c^* &= \hbar \sqrt{C} / E_h, \\ \varepsilon_L^* &= \hbar \omega_L / E_h, \end{aligned}$$

$$\begin{aligned} \tilde{x}'_1 &= \frac{1}{2} \left[\varepsilon_L^* a^{*2} / 4U_0^* + 1 + \varepsilon_c^4 a^{*2} / 4\varepsilon_L^* U_0^* - \sqrt{(\varepsilon_L^* a^{*2} / 4U_0^* + 1 + \varepsilon_c^4 a^{*2} / 4\varepsilon_L^* U_0^*)^2 - \varepsilon_L^* a^{*2} / 4U_0^*} \right], \\ \tilde{x}'_2 &= \frac{1}{2} \left[\varepsilon_L^* a^{*2} / 4U_0^* + 1 + \varepsilon_c^4 a^{*2} / 4\varepsilon_L^* U_0^* + \sqrt{(\varepsilon_L^* a^{*2} / 4U_0^* + 1 + \varepsilon_c^4 a^{*2} / 4\varepsilon_L^* U_0^*)^2 - \varepsilon_L^* a^{*2} / 4U_0^*} \right]. \end{aligned}$$

Figure 2 shows dependence of the probability of dissipative tunneling on the parameters ε_L^* , ε_T^* and ε_c^* , which characterize, respectively, frequency of the phonon mode, temperature, and constant of interaction with the contact medium. As it can be seen from Fig. 2, that, as the parameters ε_L^* and ε_T^* increase, the probability of dissipative tunneling of a hole increases too (due to approaching to the top of the potential barrier), and an increase in the parameter ε_c^* leads to blocking of the tunneling decay (due to an increase in the degree of viscosity of the contact medium (or of the heat-bath)).

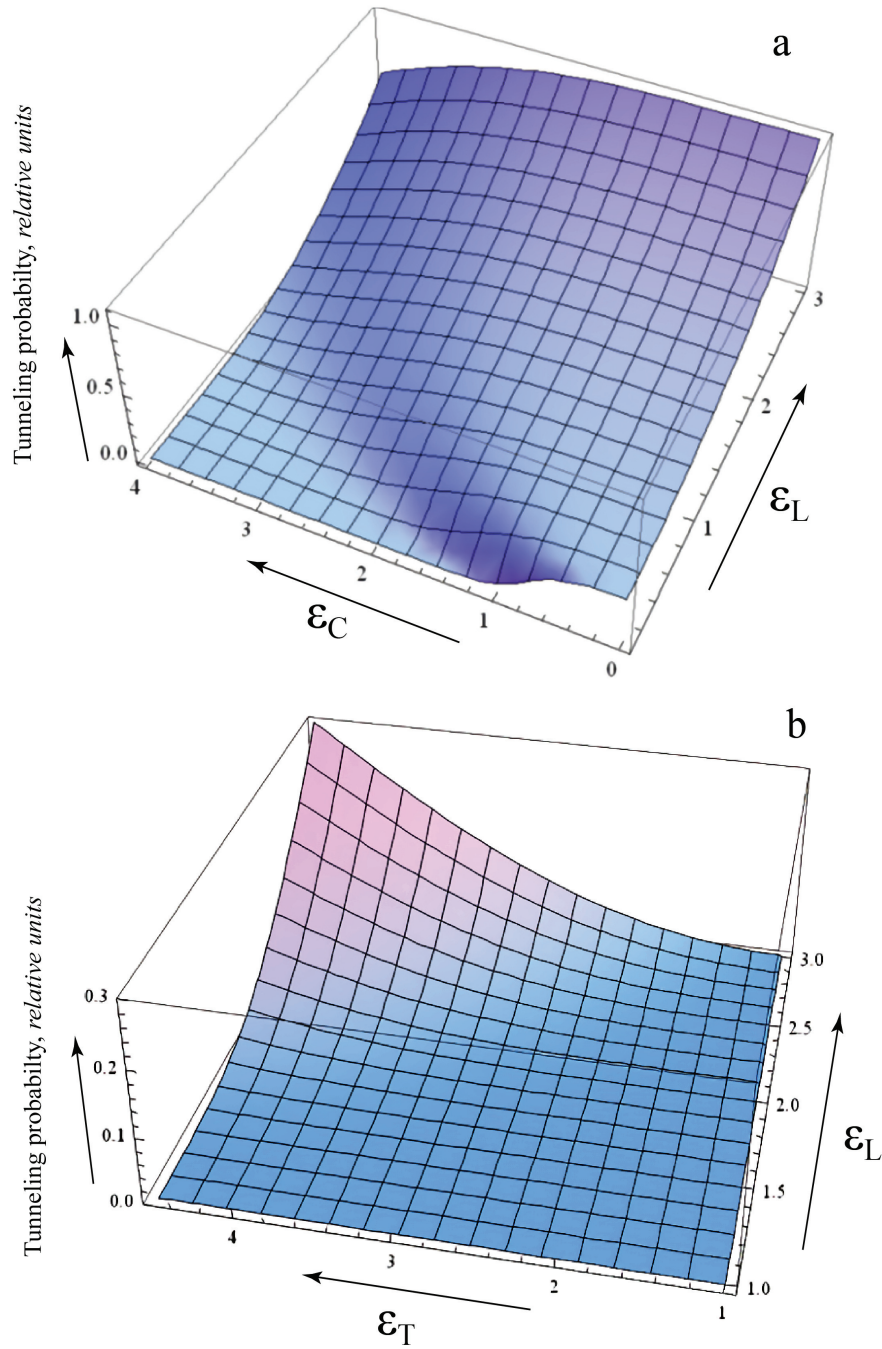


FIG. 2. Dependence of the probability of dissipative tunneling at $R_0 = 70$ nm, $\eta_i = 3.5$ on the next parameters (in relative units): a – ε_L and ε_C , under $\varepsilon_T = 1$; b – ε_L and ε_T , under $\varepsilon_C = 3$

Let the electron be initially in the s-state ($l = m = 0$), then the hole is acted upon by a spherically symmetric potential:

$$V_{n,l,m}(\vec{r}) = -\frac{e^2}{4\pi\varepsilon\varepsilon_0} \int_0^{R_0} \frac{|\psi_{n,l,m}(\vec{r}_e)|^2}{|\vec{r} - \vec{r}_e|} d\vec{r}_e, \quad (3)$$

where e – the electron charge; ε – permittivity of the QD material; ε_0 is the electric constant; $\Psi_{n,l,m}(\vec{r}_e)$ is the electron wave function in QD; n is the radial quantum number of an electron; $m = 0, \pm 1, \pm 2 \dots$ – magnetic quantum number; $l = 0, 1, 2 \dots$ is the orbital quantum number. In the first order of perturbation theory, for the ground state of an electron

($m = 0, l = 0$), potential (3) can be represented as:

$$V_{n,0,0}(r) = -\frac{e^2\beta_n^s}{4\pi\epsilon\epsilon_0R_0} + \frac{m_h^*\omega_n^2r^2}{2}, \quad (4)$$

where $\beta_n^s = \gamma_0 - Ci(2\pi n) + \ln(2\pi n)$, $\gamma_0 = 1.781$ is the Euler constant; $Ci(x)$ is the integral cosine; the frequency ω_n is determined by the following relation:

$$\hbar\omega_n = [(2\hbar^2\pi^2n^2e^2)/(3m_h^*R_0^3\epsilon)]^{1/2}. \quad (5)$$

The energy levels of such an oscillator are given in the form

$$E_{n_1, n_2, n_3}^{n, 0, 0} = -\frac{e^2}{4\pi\epsilon\epsilon_0R_0}\beta_n^s + \hbar\omega_n \left(n_1 + n_2 + n_3 + \frac{3}{2} \right), \quad (6)$$

and the corresponding one-particle wave functions are written as

$$\Psi_{n_1, n_2, n_3}^n(x, y, z) = C_n \exp\left(-\frac{x^2 + y^2 + z^2}{2a_n^2}\right) H_{n_1}\left(\frac{x}{a_n}\right) H_{n_2}\left(\frac{y}{a_n}\right) H_{n_3}\left(\frac{z}{a_n}\right), \quad (7)$$

where $C_n = [2^{n_1+n_2+n_3}n_1!n_2!n_3!\pi^{3/2}a_n^3]^{-1/2}$; $a_n = \sqrt{\hbar/(m_h^*\omega_n)}$; $H_n(x)$ are the Hermite polynomials; n_1, n_2, n_3 – quantum numbers, corresponding to the energy levels of a harmonic oscillator (6).

Using, further, the zero-radius potential procedure (see, for example, [11]), we obtain an equation, that determines dependence of the binding energy of a hole in a complex $A^+ + e$ on the QD and dissipative tunneling parameters.

The short-range impurity perturbation potential can be written correctly in the form of a pseudopotential [12] as The short-range potential can be represented as a boundary condition at the point (x_a, y_a, z_a) given by a pseudo-potential of the form

$$V_\delta(x, y, z; x_a, y_a, z_a) = \gamma\delta(x - x_a)\delta(y - y_a)\delta(z - z_a) \times \left[1 + (x - x_a)\frac{\partial}{\partial x} + (y - y_a)\frac{\partial}{\partial y} + (z - z_a)\frac{\partial}{\partial z} \right], \quad (8)$$

where $\gamma = 2\pi\hbar^2/(\alpha m_h^*)$ is the zero-range potential intensity; α is determined by the energy E_i of the bound state of the same A^+ -center in the bulk semiconductor; ρ_a, z_a are the coordinates of the A^+ -center in QD.

To determine the binding energy of a hole in the complex $A^+ + e$, it is necessary to construct a one-particle Green's function $G(r, R_a; E_{\lambda n})$ to the Schrödinger equation with a Hamiltonian, containing potential (8):

$$G(r, R_a; E_{\lambda n}) = - \sum_{n_1, n_2, n_3} \frac{\Psi_{n_1, n_2, n_3}^{n*}(x_a, y_a, z_a) \Psi_{n_1, n_2, n_3}^n(x, y, z)}{-E_{\lambda n} - \frac{e^2\beta_n^s}{\epsilon R_0} + \frac{i\Gamma_0}{\hbar\omega_n} + \hbar\omega_n \left(n_1 + n_2 + n_3 + \frac{3}{2} \right)}, \quad (9)$$

where $E_{\lambda n} = -\hbar^2\lambda_n^2/(2m_h^*)$.

For the Green's function, taking into account (7), we obtain

$$G(\vec{r}, \vec{R}_a, \varepsilon_{\lambda n}) = -\frac{1}{\pi^{3/2}a_n^2} e^{-\frac{r^2 + R_a^2}{2a_n^2}} \sum_{n_1, n_2, n_3} \frac{H_{n_1}\left(\frac{x}{a_n}\right) H_{n_1}\left(\frac{x_a}{a_n}\right) H_{n_2}\left(\frac{y}{a_n}\right) H_{n_2}\left(\frac{y_a}{a_n}\right)}{2^{n_1}n_1!} \frac{H_{n_2}\left(\frac{y}{a_n}\right) H_{n_2}\left(\frac{y_a}{a_n}\right)}{2^{n_2}n_2!} \times \\ \times \frac{H_{n_3}\left(\frac{z}{a_n}\right) H_{n_3}\left(\frac{z_a}{a_n}\right)}{2^{n_3}n_3!} \frac{1}{\hbar\omega_n \left(-\varepsilon_{\lambda n} - \frac{e^2\beta_n^s}{\epsilon R_0\hbar\omega_n} + \frac{i\Gamma_0}{\hbar\omega_n} + \frac{3}{2} + n_1 + n_2 + n_3 \right)}, \quad (10)$$

where $\varepsilon_{\lambda n} = E_{\lambda n}/\hbar\omega_n$.

Further, considering that

$$\frac{1}{-\varepsilon_{\lambda n} - \frac{e^2\beta_n^s}{\epsilon R_0\hbar\omega_n} + \frac{i\Gamma_0}{\hbar\omega_n} + \frac{3}{2} + n_1 + n_2 + n_3} = \\ = \int_0^\infty dt \exp \left[-t \left(-\varepsilon_{\lambda n} - \frac{e^2\beta_n^s}{\epsilon R_0\hbar\omega_n} + \frac{i\Gamma_0}{\hbar\omega_n} + \frac{3}{2} + n_1 + n_2 + n_3 \right) \right], \quad (11)$$

the expression for the Green's function will take the following form

$$G(\vec{r}, \vec{R}_a, \varepsilon_{\lambda n}) = -\frac{1}{\pi^{3/2} a_n^3 \hbar \omega_n} e^{-\frac{r^2 + R_a^2}{2a_n}} \int_0^\infty dt \exp \left[-t \left(-\varepsilon_{\lambda n} - \frac{e^2 \beta_n^s}{\varepsilon R_0 \hbar \omega_n} + \frac{i\Gamma_0}{\hbar \omega_n} + \frac{3}{2} \right) \right] \times \\ \times \sum_{n_1} \left(\frac{e^{-tn_1}}{2} \right) \frac{H_{n_1} \left(\frac{x}{a_n} \right) H_{n_1} \left(\frac{x_a}{a_n} \right)}{n_1!} \sum_{n_2} \left(\frac{e^{-tn_2}}{2} \right) \frac{H_{n_2} \left(\frac{y}{a_n} \right) H_{n_2} \left(\frac{y_a}{a_n} \right)}{n_2!} \times \\ \times \sum_{n_3} \left(\frac{e^{-tn_3}}{2} \right) \frac{H_{n_3} \left(\frac{z}{a_n} \right) H_{n_3} \left(\frac{z_a}{a_n} \right)}{n_3!}. \quad (12)$$

The summation in (12) over quantum numbers can be performed using the Moeller formula for the generating function of Hermite polynomials [13]

$$\sum_{k=0}^{\infty} \left(\frac{z}{2} \right)^k \frac{H_k(x) H_k(y)}{k!} = \frac{1}{\sqrt{1-z^2}} \exp \left(\frac{2xyz - (x^2 + y^2)z^2}{1-z^2} \right). \quad (13)$$

Finally, for the Green's function we will have

$$G(\vec{r}, \vec{R}_a, \varepsilon_{\lambda n}) = -\frac{1}{\pi^{3/2} a_n^3 \hbar \omega_n} \exp \left[-\frac{r^2 + R_a^2}{2a_n} \right] \int_0^\infty dt \exp \left[-t \left(-\varepsilon_{\lambda n} - \frac{e^2 \beta_n^s}{\varepsilon R_0 \hbar \omega_n} + \frac{i\Gamma_0}{\hbar \omega_n} + \frac{3}{2} \right) \right] \times \\ \times (1 - e^{-2t})^{-3/2} \exp \left[\frac{2e^{-t} (\vec{r} \vec{R}_a) - e^{-2t} (r^2 + R_a^2)}{a_n^2 (1 - e^{-2t})} \right]. \quad (14)$$

After separating the divergent part in (14) (see, for example, [11]), we obtain

$$G(\vec{r}, \vec{R}_a, \varepsilon_{\lambda n}) = \frac{1}{\pi^{3/2} a_n^3 \hbar \omega_n} \left\{ -\frac{a_n}{2\pi} \frac{\exp \left[\sqrt{2 \left(-\varepsilon_{\lambda n} - \frac{e^2 \beta_n^s}{\varepsilon R_0 \hbar \omega_n} + \frac{i\Gamma_0}{\hbar \omega_n} + \frac{3}{2} \right)} \frac{|\vec{r} - \vec{R}_a|}{a_n} \right]}{|\vec{r} - \vec{R}_a|} - \right. \\ \left. - \frac{1}{(2\pi)^{3/2}} \int_0^\infty dt \exp \left[-t \left(-\varepsilon_{\lambda n} - \frac{e^2 \beta_n^s}{\varepsilon R_0 \hbar \omega_n} + \frac{i\Gamma_0}{\hbar \omega_n} + \frac{3}{2} \right) \right] \times \right. \\ \left. \times \left[\exp \left\{ \frac{2e^{-t} (\vec{r} \vec{R}_a) - e^{-2t} (r^2 + R_a^2)}{a_n^2 (1 - e^{-2t})} \right\} e^{-\frac{r^2 + R_a^2}{2a_n}} \frac{(1 - e^{-2t})^{-3/2}}{2^{-3/2}} - \frac{1}{t\sqrt{t}} e^{-\frac{(\vec{r} - \vec{R}_a)^2}{2a_n^2 t}} \right] \right\}. \quad (15)$$

Acting on both sides of relation (15) by the operator \hat{T} , we obtain an equation, that determines dependence of the binding energy $E_{\lambda n}$ of a hole in a complex $A^+ + e$ on the parameters of the QD, as well as on the parameters of dissipative tunneling and the quantum number n .

$$\eta_i = \sqrt{-\eta_n^2 - \frac{2\beta_n^s}{R_0^*} + 4i\Gamma_0^* + 3\gamma_n^{s-1}} + \frac{2}{\sqrt{\gamma_n^s \pi}} \int_0^\infty dt \exp \left[-\frac{t}{2} \left(-\gamma_n^s \eta_n^2 + 4i\gamma_n^s \Gamma_0^* - \frac{2\gamma_n^s \beta_n^s}{R_0^*} + 3 \right) \right] \times \\ \times \left[\frac{1}{2t\sqrt{2t}} - \frac{\exp \left(-\frac{R_0^{*2} R_a^{*2}}{\gamma_n^s} \left(\frac{1-e^{-t}}{1+e^{-t}} \right) \right)}{(1 - e^{-2t})^{3/2}} \right], \quad (16)$$

where $\gamma_n^s = \sqrt{6R_0^* R_0^* / (2\pi n)}$; $\eta_i = \sqrt{|E_i|/E_h}$; $\eta_n = \sqrt{E_{\lambda n}/E_h}$; $\Gamma_0^* = \hbar\Gamma_0/(4E_h)$.

Further, it is necessary to find the explicit form of the potential $V_{n,l,m}(\vec{r}_h)$, defined by formula (3) in the case, when the electron is in the excited p-state ($l = 1, m = 0$) of QD. Expression (3) can be represented as

$$V_{n,l,m}(r_h) = \frac{-e^2}{4\pi\varepsilon\varepsilon_0} \int_0^\pi \sin\theta d\theta \int_0^{2\pi} d\varphi \left(\int_0^{r_h} \frac{|\Psi_{n,l,m}(r_e, \theta, \varphi)|^2 r_e^2 dr_e}{\sqrt{r_h^2 + r_e^2 - 2r_h r_e \cos\theta}} + \int_{r_h}^{R_0} \frac{|\Psi_{n,l,m}(r_e, \theta, \varphi)|^2 r_e^2 dr_e}{\sqrt{r_h^2 + r_e^2 - 2r_h r_e \cos\theta}} \right). \quad (17)$$

The wave function of an electron, in the p-state with $m = 0$, is given by the next expression

$$\psi_{n,1,0}(r_e, \theta, \varphi) = \frac{J_{\frac{3}{2}}\left(\frac{X_{n,1}r_e}{R_0}\right)}{\sqrt{\pi r_e R_0} J_{\frac{5}{2}}(X_{n,1})} \cos \theta, \quad (18)$$

then, after integration in (17) we obtain

$$\begin{aligned} V_{n,1,0}(r_h) = & \frac{e^2 X_{n,1}}{120\pi R_0^3 r_h^3 \varepsilon \varepsilon_0 (3X_{n,1} \cos(X_{n,1}) + (X_{n,1}^2 - 3) \sin(X_{n,1}))^2} \left[15R_0^3 (R_0^2 + X_{n,1}^2 r_h^2) \times \right. \\ & \times \sin\left(\frac{2X_{n,1}r_h}{R_0}\right) - 30X_{n,1}R_0^4 r_h \cos\left(\frac{2X_{n,1}r_h}{R_0}\right) + X_{n,1}r_h^3 \left(3r_h^2 (1 + 2X_{n,1}^2) - 5R_0^2 (8X_{n,1}^2 - 3) - \right. \\ & - 3 \cos(2X_{n,1}) (5R_0^2 + r_h^2) + 6X_{n,1} \left[5R_0^2 X_{n,1} \left(\text{Ci}(2X_{n,1}) - \text{Ci}\left(\frac{2X_{n,1}r_h}{R_0}\right) - \ln\left(\frac{R_0}{r_h}\right) \right) - \right. \\ & \left. \left. - \sin(2X_{n,1}) (5R_0^2 + r_h^2) \right] \right] \left. \right]. \quad (19) \end{aligned}$$

Note, that in the case of p-state with $m = 0$, the minimum of potential (19) is shifted relative to the QD center (see Fig. 1). Position of the minimum is determined from the solution of the following transcendental equation, which is obtained from the equality to zero of the derivative of expression (19) with respect to r_h :

$$\begin{aligned} 2X_{n,1}r_h \min \left[15R_0^4 \cos\left(\frac{2X_{n,1}r_h \min}{R_0}\right) + 5R_0^2 X_{n,1}^2 r_h \min^2 - \right. \\ \left. - \left(\cos(2X_{n,1}) + 2X_{n,1} \sin(2X_{n,1}) - 1 - 2X_{n,1}^2 \right) r_h \min^4 \right] - \\ - 15R_0^3 \sin\left(\frac{2X_{n,1}r_h \min}{R_0}\right) (R_0^2 - X_{n,1}^2 r_h \min^2) = 0. \quad (20) \end{aligned}$$

Expanding expression (19) into a Taylor series near $r_{h\min}$ and restricting ourselves to the quadratic term, we obtain

$$V_{n,1,0}(r_h) = -\frac{e^2}{\varepsilon R_0} \beta_n^{p,0} - \frac{m_h \omega_n^{p,0,2} (r_h - r_{h\min})^2}{2}, \quad (21)$$

where the quantities $\beta_n^{p,0}$ and $\omega_n^{p,0}$ are defined as follows

$$\begin{aligned} \beta_n^{p,0} = & \frac{X_{n,1}}{30R_0^2 r_h^3 \min (3X_{n,1} \cos(X_{n,1}) + (X_{n,1}^2 - 3) \sin(X_{n,1}))^2} \left[6r_h^5 \min X_{n,1}^3 - 3r_h^5 \min X_{n,1} - \right. \\ & - 15r_h^3 \min X_{n,1} R_0^2 + 40r_h^3 \min X_{n,1}^3 R_0^2 + 3r_h^5 \min X_{n,1} \cos(2X_{n,1}) + 15r_h^3 \min X_{n,1} R_0^2 \cos(2X_{n,1}) + \\ & + 30r_h \min X_{n,1} R_0^4 \cos\left(\frac{2r_h \min X_{n,1}}{R_0}\right) - 30r_h^3 \min X_{n,1}^3 R_0^2 \text{Ci}(2X_{n,1}) + 30r_h^3 \min X_{n,1}^3 R_0^2 \text{Ci}\left(\frac{2r_h \min X_{n,1}}{R_0}\right) - \\ & - 30r_h^3 \min X_{n,1}^3 R_0^2 \ln\left(\frac{r_h \min}{R_0}\right) + 6r_h^5 \min X_{n,1}^2 \sin(2X_{n,1}) + 30r_h^3 \min X_{n,1}^2 R_0^2 \sin(2X_{n,1}) - \\ & \left. - 15r_h^2 \min X_{n,1}^2 R_0^3 \sin\left(\frac{2r_h \min X_{n,1}}{R_0}\right) - 15R_0^5 \sin\left(\frac{2r_h \min X_{n,1}}{R_0}\right) \right]. \quad (22) \end{aligned}$$

The binding energy of a hole localized at the A^+ center, in the case when the electron is in the p-state with $m = 0$, is determined from the solution of the transcendental equation

$$\begin{aligned} \eta_i = & \sqrt{-\eta_n^p - \frac{2\beta_n^{p,0}}{R_0^*} + 4i\Gamma_0^* + 3\gamma_n^{p-1} +} \\ & + \frac{2}{\sqrt{\gamma_n^{p,0} \pi}} \int_0^\infty dt \exp \left[-\frac{\gamma_n^p t}{2} \left(-(\eta_n^p)^2 + 4i\Gamma_0^* - \frac{2\beta_n^p}{R_0^*} + \frac{3}{\gamma_n^p} \right) \right] \left[\frac{1}{2t\sqrt{2t}} - \frac{\exp\left(-\frac{R_0^{*2} R_a^{*2}}{\gamma_n^p} \left(\frac{1-e^{-t}}{1+e^{-t}}\right)\right)}{(1-e^{-2t})^{3/2}} \right], \quad (23) \end{aligned}$$

where

$$\gamma_n^{p,0} = \left[\frac{5r_{h \min}^{*5} R_0^{*3} (3X_{n,1} \cos(X_{n,1}) + (X_{n,1}^3 - 3) \sin(X_{n,1}))^2}{X_{n,1}} \left(r_{h \min}^{*5} X_{n,1} + 2r_{h \min}^{*5} X_{n,1}^3 - \right. \right. \\ \left. \left. - 5r_{h \min}^{*3} X_{n,1}^3 R_0^{*2} - r_{h \min}^{*5} X_{n,1} \cos(2X_{n,1}) + 15r_{h \min}^* X_{n,1} R_0^{*2} (r_{h \min}^{*2} X_{n,1}^2 - 4R_0^{*2}) \cos\left(\frac{2r_{h \min}^* X_{n,1}}{R_0^*}\right) - \right. \right. \\ \left. \left. - 2r_{h \min}^{*5} X_{n,1}^2 \sin(2X_{n,1}) - 15R_0^{*3} \sin\left(\frac{2r_{h \min}^* X_{n,1}}{R_0^*}\right) (3r_{h \min}^{*2} X_{n,1}^2 + 2R_0^{*2}) \right)^{-1} \right]^{1/2} \quad (24)$$

and correspondingly $r_{h \min}^*/r_{h \min}/a_h, \eta_n^{p,0} = \sqrt{|E^{p,0}, \lambda_n|/E_h}$.

The wave function of a hole localized at the A^+ -center in the p-state is defined as:

$$\Psi_{\lambda; n}^p(\vec{r}_h) = \sqrt{\frac{\Gamma\left(\frac{3}{4} + \frac{\varepsilon_{\lambda n}^p}{2}\right) \Gamma\left(\frac{1}{4} + \frac{\varepsilon_{\lambda n}^p}{2}\right)}{2\pi^2 a_{p,n}^3 \left(\psi\left(\frac{3}{4} + \frac{\varepsilon_{\lambda n}^p}{2}\right) - \psi\left(\frac{3}{4} + \frac{\varepsilon_{\lambda n}^p}{2}\right)\right)}} \left(\frac{r_h^2}{a_{p,n}^2}\right)^{-3/4} W_{-\frac{\varepsilon_{\lambda n}^p}{2}, \frac{1}{4}}\left(\frac{r_h^2}{a_{p,n}^2}\right), \quad (25)$$

where

$$\varepsilon_{\lambda n}^p = \left[\frac{5r_{h \min}^{*5} R_0^* (3X_{n,1} \cos(X_{n,1}) + (X_{n,1}^3 - 3) \sin(X_{n,1}))^2}{X_{n,1}} \times \right. \\ \times \left(r_{h \min}^{*5} X_{n,1} + 2r_{h \min}^{*5} X_{n,1}^3 - 5r_{h \min}^{*3} X_{n,1}^3 R_0^{*2} - r_{h \min}^{*5} X_{n,1} \cos(2X_{n,1}) + \right. \\ \left. + 15r_{h \min}^* X_{n,1} R_0^{*2} (r_{h \min}^{*2} X_{n,1}^2 - 4R_0^{*2}) \cos\left(\frac{2r_{h \min}^* X_{n,1}}{R_0^*}\right) - 2r_{h \min}^{*5} X_{n,1}^2 \sin(2X_{n,1}) - \right. \\ \left. \left. - 45r_{h \min}^{*2} X_{n,1}^2 R_0^{*3} \sin\left(\frac{2r_{h \min}^* X_{n,1}}{R_0^*}\right) + 30R_0^{*5} \sin\left(\frac{2r_{h \min}^* X_{n,1}}{R_0^*}\right) \right)^{-1} \right]^{1/2} \left(\frac{R_0^* \eta_i^2 - 2\beta_{p,n}^{p,0}}{2}\right), \quad (26)$$

where $a_{p,n}^2 = a_h^2 \gamma_n^p$.

Thus, the wave function of the excited state of the electron-hole pair will have the following form:

$$\Phi_{out}(r_e, r_h) = \psi_{n,1}^p(r_e) \Psi_{\lambda; n}^p(r_h). \quad (27)$$

Figures 3(a) and 3(b) show dependence of the binding energy of the quasi-stationary A^+ -state in the impurity complex $A^+ + e$ on the dissipative tunneling parameters $\varepsilon_L, \varepsilon_C$ and ε_T for InSb-based QDs at $R_0 = 70$ nm, calculated using formula (23).

It can be seen, that with an increase in the parameters ε_L and ε_T , which characterize the frequency of the phonon mode and temperature, respectively, the binding energy of the quasi-stationary A^+ -state decreases (see Fig. 3(b)) due to an increase in the probability of dissipative tunneling (see Fig. 2(a,b)), as a result, the wave function of the quasi-stationary A^+ -state “spreads”, which leads to an increase in the effective radius of the localized A^+ -state. An increase in the parameter ε_C , which characterizes the constant of interaction with the contact medium (with the heat-bath), is accompanied by the blocking of tunnel decay and a corresponding increase in the binding energy of the quasi-stationary A^+ -state (Fig. 3(a)).

The obtained relations (16), (23), and (25) will be used in the next section to calculate the process of photoexcitation of impurity complexes $A^+ + e$ in a quasi-zero-dimensional structure.

3. Photodielectric effect in a quasi-zero-dimensional structure with impurity complexes $A^+ + e$ in the presence of dissipative tunneling

Let us consider the process of photoexcitation for complexes $A^+ + e$ in QDs under conditions of dissipative tunneling. We will assume that the A^+ -center is localized at the point $\vec{R}_a = (0, 0, 0)$, (see Fig. 1). The energy spectrum of an electron in a size-quantized band will be determined by an expression of the next form

$$E_{n,l} = \frac{\tilde{X}_{n,l}^2 E_h}{R_0^{*2}}. \quad (28)$$

Here $\tilde{X}_{n,l} = X_{n,l}/\sqrt{E_h}$; $X_{n,l}$ is the root of the l -th order Bessel function.

The effective Hamiltonian H_{int} of interaction with the field of a light wave can be written as

$$H_{int} = -i \hbar \lambda_0 \sqrt{\frac{2\pi \hbar^2 \alpha^*}{m^* \omega}} I_0 \exp(i \vec{q}_s \vec{r}) (\vec{\epsilon}_{\lambda s} \nabla_{\vec{r}}), \quad (29)$$

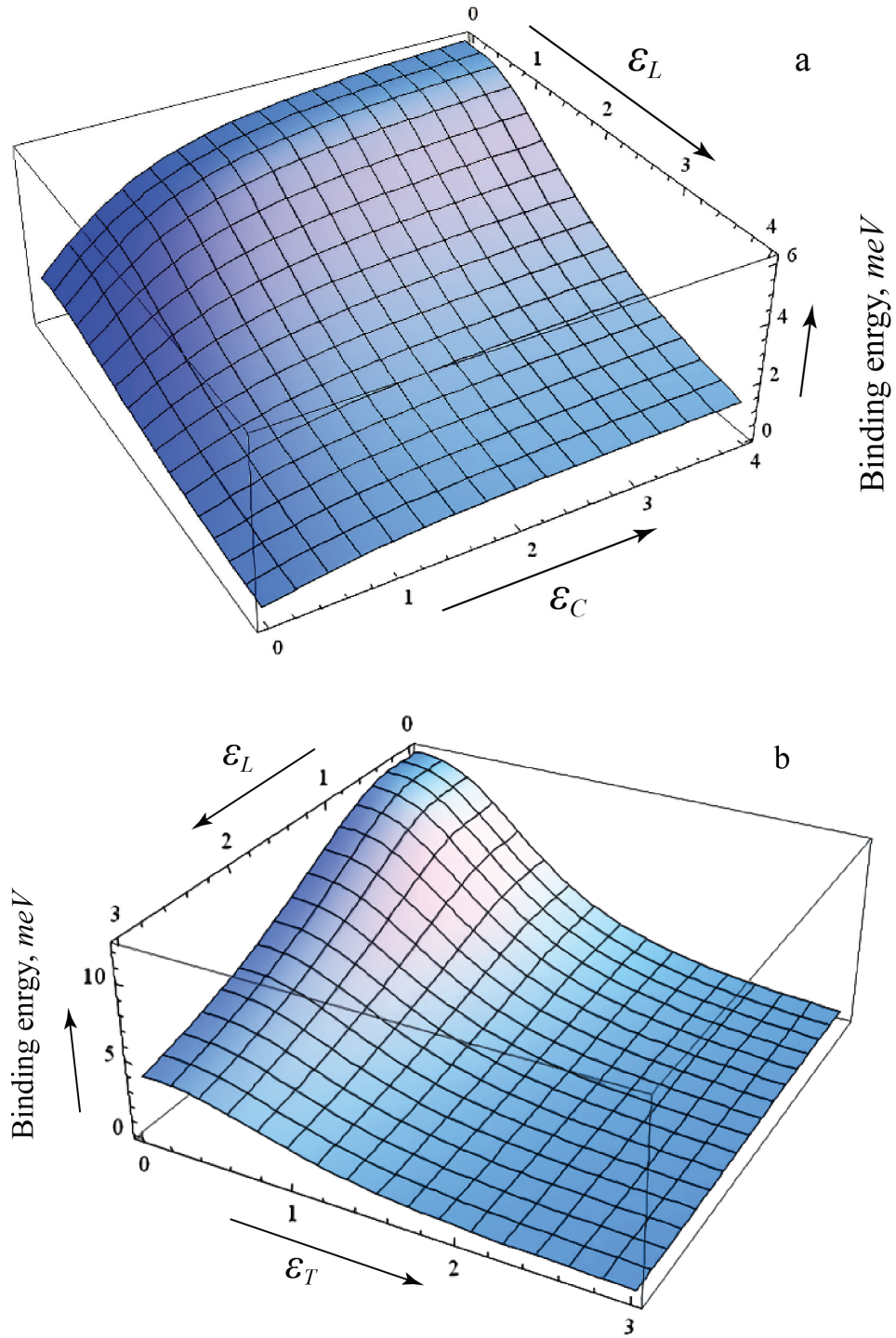


FIG. 3. Dependence of the binding energy of the quasi-stationary A^+ - state in the impurity complex $A^+ + e$ in InSb-based QDs on the parameters of dissipative tunneling at $R_0 = 70$ nm and $\eta_i = 3.5$: a – on the parameters ϵ_L and ϵ_C , at $\epsilon_T = 1$; b – from parameters ϵ_L and ϵ_T , at $\epsilon_c = 3$.

where λ_0 is the local field coefficient; α^* is the fine structure constant, taking into account the static relative permittivity ε ; I_0 is the intensity of light with frequency ω , wave vector \vec{q}_s and the unit polarization vector \vec{e}_{λ_s} ; $\nabla_{\vec{r}}$ is the Hamilton operator.

The matrix element $M_{f,\lambda}$, which determines the magnitude of the oscillator strength of the dipole optical transitions of an electron and a hole from the ground state $\Phi_{in}(\vec{r}_e, \vec{r}_h)$ to the excited states $\Phi_{out}(\vec{r}_e, \vec{r}_h)$ of the QD, is written as

$$M_{f,\lambda} = i \sqrt{\frac{2\pi\alpha^* I_0}{\omega}} \left(E_{n,1,\{0\}} - E_{1,1,0} - \left(E_{\lambda_n}^p \left\{ \begin{smallmatrix} 0 \\ \pm 1 \end{smallmatrix} \right\} - E_{\lambda_1}^s \right) \right) \times \\ \times \langle \Psi_{\lambda_n}^p(\vec{r}_h) | \Psi_{\lambda_1}^s(\vec{r}_h) \rangle \langle \psi_{n,1}(\vec{r}_e) | (\vec{e}_{\lambda_s}, \vec{r}_e) | \psi_{1,0}(\vec{r}_e) \rangle. \quad (30)$$

Taking into account the explicit form of the wave functions (18) and (25), the matrix element (30) can be written in the form

$$M_{f,\lambda} = i \sqrt{\frac{2\pi\alpha^* I_0}{\omega}} (E_{n,1,0} - E_{1,1,0} - (E_{\lambda_n}^p - E_{\lambda_1}^s)) \times \frac{8\pi}{R_0^2 J_{3/2}(X_{0,1}) J_{5/2}(X_{n,1})} \times \\ \times \sqrt{\frac{\Gamma\left(\frac{3}{4} + \frac{\varepsilon_{\lambda_1}^s}{2}\right) \Gamma\left(\frac{1}{4} + \frac{\varepsilon_{\lambda_1}^s}{2}\right)}{2\pi^2 a_{s,n}^3 \left(\psi\left(\frac{3}{4} + \frac{\varepsilon_{\lambda_1}^s}{2}\right) - \psi\left(\frac{3}{4} + \frac{\varepsilon_{\lambda_1}^s}{2}\right)\right)}} \sqrt{\frac{\Gamma\left(\frac{3}{4} + \frac{\varepsilon_{\lambda_n}^p}{2}\right) \Gamma\left(\frac{1}{4} + \frac{\varepsilon_{\lambda_n}^p}{2}\right)}{2\pi^2 a_{p,n}^3 \left(\psi\left(\frac{3}{4} + \frac{\varepsilon_{\lambda_n}^p}{2}\right) - \psi\left(\frac{3}{4} + \frac{\varepsilon_{\lambda_n}^p}{2}\right)\right)}} \times \\ \times \int_0^{R_0} W_{-\frac{\varepsilon_{\lambda_1}^s}{2}; \frac{1}{4}} \left(\frac{r_h^2}{a_{s,n}^2}\right) W_{-\frac{\varepsilon_{\lambda_n}^p}{2}; \frac{1}{4}} \left(\frac{r_h^2}{a_{p,n}^2}\right) \frac{dr_h}{r_h} \times \int_0^{R_0} dr_e r_e^2 J_{1/2}\left(\frac{r_e}{R_0} X_{1,0}\right) J_{\frac{3}{2}}\left(\frac{r_e}{R_0} X_{n,1}\right) \times \\ \times \int_0^\pi d\theta \sin\theta \int_0^{2\pi} d\varphi Y_{0,0}(\theta, \varphi) Y_{1,m}(\theta, \varphi) \cos\theta. \quad (31)$$

After calculating the integrals in (31) and taking into account the expression for the energy spectrum of charge carriers (23) for the matrix element (31), we obtain (in the Bohr units)

$$M_{f,\lambda}(X) = i a_h E_h (2^5 \pi)^{1/2} X_{n,1} \sqrt{\frac{\alpha^* I_0 E_h}{X}} \frac{\left(\frac{k(X_{n,1}^2 - \pi^2)}{R_0^{*2}} - (\eta_n^{p2} - \eta_1^{s2})\right)}{(3X_{n,1} \cos X_{n,1} + \sin X_{n,1} (X_{n,1}^2 - 3))} \times \\ \times \sqrt{\frac{\Gamma\left(\frac{3}{4} + \frac{\varepsilon_{\lambda_1}^s}{2}\right) \Gamma\left(\frac{1}{4} + \frac{\varepsilon_{\lambda_1}^s}{2}\right)}{\left(\psi\left(\frac{3}{4} + \frac{\varepsilon_{\lambda_1}^s}{2}\right) - \psi\left(\frac{3}{4} + \frac{\varepsilon_{\lambda_1}^s}{2}\right)\right)}} \frac{\Gamma\left(\frac{3}{4} + \frac{\varepsilon_{\lambda_n}^p}{2}\right) \Gamma\left(\frac{1}{4} + \frac{\varepsilon_{\lambda_n}^p}{2}\right)}{\left(\psi\left(\frac{3}{4} + \frac{\varepsilon_{\lambda_n}^p}{2}\right) - \psi\left(\frac{3}{4} + \frac{\varepsilon_{\lambda_n}^p}{2}\right)\right)} \times \\ \times \frac{(X_{n,1}^2 \cos X_{n,1} (X_{n,1}^2 - \pi^2) + \sin X_{n,1} (3X_{n,1}^2 - \pi^2)) (\gamma_n^s \gamma_n^p)^{-3/4}}{R_0^2 J_{3/2}(X_{0,1}) J_{5/2}(X_{n,1}) (\pi^2 - X_{n,1}^2)^2} \times \\ \times \sum_{i=0}^{\infty} \sum_{j=0}^{\infty} \frac{(-1)^j (\gamma_n^{s-1} + \gamma_n^{p-1})^j (\gamma_n^s)^{-i}}{2^j j! i!} \left(\frac{\Gamma\left(-\frac{1}{2}\right) \left(\frac{1}{4} + \frac{\varepsilon_{\lambda_n}^s}{2}\right)_i}{\Gamma\left(\frac{1}{4} + \frac{\varepsilon_{\lambda_n}^s}{2}\right) \left(\frac{3}{2}\right)_i} \left[\frac{R_0^{*2} \left(\frac{3}{2} + i + j\right) \Gamma\left(-\frac{1}{2}\right)}{\left(\frac{3}{2} + i + j\right) \Gamma\left(\frac{1}{4} + \frac{\varepsilon_{\lambda_n}^p}{2}\right)} \times \right. \right. \\ \times {}_2F_2\left(\frac{3}{2} + i + j, \frac{3}{4} + \frac{\varepsilon_{\lambda_n}^p}{2}; \frac{5}{2} + i + j, \frac{3}{2}; \frac{R_0^{*2}}{\gamma_n^p}\right) + \frac{\sqrt{\gamma_n^p} R_0^{*2} (1+i+j) \Gamma\left(\frac{1}{2}\right)}{\left(\frac{3}{2} + i + j\right) \Gamma\left(\frac{3}{4} + \frac{\varepsilon_{\lambda_n}^p}{2}\right)} \times \\ \times {}_2F_2\left(1 + i + j, \frac{1}{4} + \frac{\varepsilon_{\lambda_n}^p}{2}; \frac{1}{2}, 2 + i + j; \frac{R_0^{*2}}{\gamma_n^p}\right) \left. \right] + \frac{\sqrt{\gamma_n^s} \left(\frac{1}{4} + \frac{\varepsilon_{\lambda_n}^s}{2}\right)_i}{\Gamma\left(\frac{3}{4} + \frac{\varepsilon_{\lambda_n}^s}{2}\right) \left(\frac{1}{2}\right)_i} \times \\ \times \left[\frac{R_0^{*2} (1+i+j) \Gamma\left(-\frac{1}{2}\right)}{(1+i+j) \Gamma\left(\frac{1}{4} + \frac{\varepsilon_{\lambda_n}^p}{2}\right)} {}_2F_2\left(1 + i + j, \frac{3}{4} + \frac{\varepsilon_{\lambda_n}^p}{2}; 2 + i + j, \frac{3}{2}; \frac{R_0^{*2}}{\gamma_n^p}\right) + \right. \\ \left. + \frac{\sqrt{\gamma_n^p} R_0^{*2} \left(\frac{1}{2} + i + j\right) \Gamma\left(\frac{1}{2}\right)}{\left(\frac{1}{2} + i + j\right) \Gamma\left(\frac{3}{4} + \frac{\varepsilon_{\lambda_n}^p}{2}\right)} {}_2F_2\left(\frac{1}{2} + i + j, \frac{1}{4} + \frac{\varepsilon_{\lambda_n}^p}{2}; \frac{1}{2}, \frac{3}{2} + i + j; \frac{R_0^{*2}}{\gamma_n^p}\right) \right] \Bigg), \quad (32)$$

where $R_0^* = R_0/a_h$; $k = m_h/m_e$; $\eta_1^s = \sqrt{E_{\lambda_1}^s/E_h}$; $\eta_n^p = \sqrt{E_{\lambda_n}^p/E_h}$; ${}_pF_q(a_1, \dots, a_p; b_1, \dots, b_q; z)$ is the generalized hypergeometric function.

Let us further assume that the dispersion u of QD sizes arises during the phase decomposition of a supersaturated solid solution and is satisfactorily described by the Lifshitz–Slezov formula [14]

$$P(u) = \begin{cases} \frac{3^4 e u^2 \exp[-1/(1-2u/3)]}{2^{\frac{5}{3}} (u+3)^{\frac{7}{3}} (3/2-u)^{\frac{11}{3}}}, & u < \frac{3}{2}; \\ 0, & u > \frac{3}{2}, \end{cases} \quad (33)$$

where $u = R_0/\bar{R}_0$, R_0 and \bar{R}_0 – the QD radius and its average value, respectively; e is the base of the natural logarithm.

With relatively small changes in the permittivity ε ($\Delta\varepsilon \leq 3\varepsilon$), change in the value ε during photoexcitation in the dipole approximation, taking into account the dispersion of the QD radius, is determined from the following formula (see [15–17]):

$$\Delta\varepsilon(\omega) = \frac{4\pi N_0 I_0}{\hbar\omega} \sum_n \int_0^{3/2} \sigma_n(\omega) \tau_n \alpha_n P(u) du, \quad (34)$$

where I_0 is the radiation intensity; ω is the incident light frequency; α_n is the polarizability of excited states of an electron in QD; τ_n is the lifetime of excited electronic states; $\sigma_n(\omega)$ is the partial photon absorption cross section for QD with the complex $A^+ + e$.

Since the value $1/\tau_n$ determines the total probability, per unit time, for spontaneous emission of photons during quantum transitions of an electron from the p-state (with different quantum numbers n) to the ground state, then, assuming that the system is characterized only by the radiative lifetime, the expression for τ_n will be written as

$$\frac{1}{\tau_n} = \varpi, \quad (35)$$

where the total transition probability is given by an expression of the next form

$$\varpi = \frac{2\pi}{\hbar} \int \sum_{\sigma} |\langle \Phi_{out}(\vec{r}_e, \vec{r}_h) | \mathbf{V} | \Phi_{in}(\vec{r}_e, \vec{r}_h) \rangle|^2 d\rho(E_{out}), \quad (36)$$

the quantity $d\rho(E_{out})$ characterizes density of the final states number for the system and is defined as

$$d\rho(E_{out}) = \frac{V(\tilde{\omega})^2 d\Omega}{(2\pi)^3 \hbar c^3}, \quad (37)$$

where $\tilde{\omega} = (E_{in} - E_{out})/\hbar = (\hbar^2(X_{n,1}^2 - \pi^2)/2m_e^* a_h^2 R_0^{*2} - (E_{\lambda_n}^p - E_{\lambda_1}^s))/\hbar$; $d\Omega$ is an infinitesimal element of the solid angle, and the interaction operator of a particle with an electromagnetic field (in the one-photon approximation) has the next form

$$\mathbf{V} = -\frac{e}{m_e c} \mathbf{A}(\vec{r}) \mathbf{p}. \quad (38)$$

Here $\mathbf{A}(\vec{r})$ is the vector potential operator defined by the formula (in the Coulomb gauge)

$$\mathbf{A}(\vec{r}) = \sum_{k,\sigma} \left(\frac{2\pi\hbar c^2}{V\omega_k} \right)^{1/2} \vec{e}_{k,\sigma} \left(\mathbf{a}_{k,\sigma} e^{i\vec{k}\vec{r}} + \mathbf{a}_{k,\sigma}^\dagger e^{-i\vec{k}\vec{r}} \right). \quad (39)$$

Respectively, $\mathbf{a}_{k,\sigma}$ and $\mathbf{a}_{k,\sigma}^\dagger$ are the operators of annihilation and creation of a photon with a wave vector \vec{k} and polarization σ , respectively. In the case of the dipole approximation, the expression for the total probability, in the Bohr units, taking into account the QD size dispersion, will be determined as follows

$$\varpi = \frac{4e^2 E_h^3}{3\hbar^4 c^3} \left(\frac{k(X_{n,1}^2 - \pi^2)}{(\bar{R}_0^* u)^2} - (\eta_{\lambda_n}^p - \eta_{\lambda_h}^s) \right)^3 |P_{n,1,0}|^2, \quad (40)$$

where the value $P_{n,1,0}$ is determined by the next expression

$$P_{n,1,0}^p = \langle \Psi_{\lambda_h}^p(\vec{r}_h) | \Psi_{\lambda_h}(\vec{r}_h) \rangle \langle \Psi_{n,1,0}(\vec{r}_e) | (\vec{e}_{\lambda}^s, \vec{r}_e) | \Psi_{1,0}(\vec{r}_e) \rangle. \quad (41)$$

Taking into account the previously obtained expression for the matrix element (32), the expression for (41) can be written as

$$\begin{aligned}
P_n^p(\bar{R}_0^*u) &= \frac{4X_{n,1}(X_{n,1}^2 \cos X_{n,1}(X_{n,1}^2 - \pi^2) + \sin X_{n,1}(3X_{n,1}^2 - \pi^2))}{\bar{R}_0^*u J_{3/2}(X_{0,1}) J_{5/2}(X_{n,1})(\pi^2 - X_{n,1}^2)^2 (a_{s,n} a_{p,n})^{3/2}} \times \\
&\times \sqrt{\frac{\Gamma\left(\frac{3}{4} + \frac{\varepsilon_{\lambda 1}^s}{2}\right) \Gamma\left(\frac{1}{4} + \frac{\varepsilon_{\lambda 1}^s}{2}\right)}{\left(\psi\left(\frac{3}{4} + \frac{\varepsilon_{\lambda 1}^s}{2}\right) - \psi\left(\frac{3}{4} + \frac{\varepsilon_{\lambda 1}^s}{2}\right)\right)}} \left[\frac{\Gamma\left(\frac{3}{4} + \frac{\varepsilon_{\lambda n}^p}{2}\right) \Gamma\left(\frac{1}{4} + \frac{\varepsilon_{\lambda n}^p}{2}\right)}{\left(\psi\left(\frac{3}{4} + \frac{\varepsilon_{\lambda n}^p}{2}\right) - \psi\left(\frac{3}{4} + \frac{\varepsilon_{\lambda n}^p}{2}\right)\right)} \right]^{\frac{3}{2}} \times \\
&\times \sum_{i=0}^{\infty} \sum_{j=0}^{\infty} \frac{(-1)^j (a_{s,n}^{-2} + a_{p,n}^{-2})^j}{2^j a_{s,n}^{2i} j! i! (3X_{n,1} \cos X_{n,1} + \sin X_{n,1}(X_{n,1}^2 - 3))} \left(\frac{\Gamma(-\frac{1}{2}) \left(\frac{1}{4} + \frac{\varepsilon_{\lambda n}^s}{2}\right)_i}{\Gamma\left(\frac{1}{4} + \frac{\varepsilon_{\lambda n}^s}{2}\right) \left(\frac{3}{2}\right)_i} \right) \times \\
&\times \left[\frac{(\bar{R}_0^*u)^{2\left(\frac{3}{2}+i+j\right)} \Gamma\left(-\frac{1}{2}\right)}{\left(\frac{3}{2}+i+j\right) \Gamma\left(\frac{1}{4} + \frac{\varepsilon_{\lambda n}^p}{2}\right)} {}_2F_2\left(\frac{3}{2}+i+j, \frac{3}{4} + \frac{\varepsilon_{\lambda n}^p}{2}; \frac{5}{2}+i+j, \frac{3}{2}; \frac{(\bar{R}_0^*u)^2}{a_{p,n}^2}\right) + \right. \\
&+ \left. \frac{a_{p,n}(\bar{R}_0^*u)^{2(1+i+j)} \Gamma\left(\frac{1}{2}\right)}{\left(\frac{3}{2}+i+j\right) \Gamma\left(\frac{3}{4} + \frac{\varepsilon_{\lambda n}^p}{2}\right)} {}_2F_2\left(1+i+j, \frac{1}{4} + \frac{\varepsilon_{\lambda n}^p}{2}; \frac{1}{2}, 2+i+j; \frac{(\bar{R}_0^*u)^2}{a_{p,n}^2}\right) \right] + \\
&+ \frac{a_{s,n} \left(\frac{1}{4} + \frac{\varepsilon_{\lambda n}^s}{2}\right)_i}{\Gamma\left(\frac{3}{4} + \frac{\varepsilon_{\lambda n}^p}{2}\right) \left(\frac{1}{2}\right)_i} \left[\frac{(\bar{R}_0^*u)^{2(1+i+j)} \Gamma\left(-\frac{1}{2}\right)}{(1+i+j) \Gamma\left(\frac{1}{4} + \frac{\varepsilon_{\lambda n}^p}{2}\right)} {}_2F_2\left(1+i+j, \frac{3}{4} + \frac{\varepsilon_{\lambda n}^p}{2}; 2+i+j, \frac{3}{2}; \frac{(\bar{R}_0^*u)^2}{a_{p,n}^2}\right) + \right. \\
&+ \left. \frac{a_{p,n}(\bar{R}_0^*u)^{2\left(\frac{1}{2}+i+j\right)} \Gamma\left(\frac{1}{2}\right)}{\left(\frac{1}{2}+i+j\right) \Gamma\left(\frac{3}{4} + \frac{\varepsilon_{\lambda n}^p}{2}\right)} {}_2F_2\left(\frac{1}{2}+i+j, \frac{1}{4} + \frac{\varepsilon_{\lambda n}^p}{2}; \frac{1}{2}, \frac{3}{2}+i+j; \frac{(\bar{R}_0^*u)^2}{a_{p,n}^2}\right) \right] \Bigg). \quad (42)
\end{aligned}$$

Accordingly, for the lifetime of an electron at an excited level, taking into account the dispersion of the QD sizes, we obtain the following expression

$$\tau_n^p(\bar{R}_0^*u) = \frac{3\hbar^4 c^3}{4e^2 E_h^3 \left(\frac{k(X_{n,1}^2 - \pi^2)}{(\bar{R}_0^*u)^2} - (\eta_{\lambda n}^p)^2 - \eta_{\lambda 1}^s \right)^3 |P_n^p(\bar{R}_0^*u)|^2}. \quad (43)$$

The polarizability $\alpha_n^p(\bar{R}_0^*u)$ of electronic states in a QD with a complex $A^+ + e$ in the Bohr units is determined by an expression of the next form

$$\alpha_n^p(\bar{R}_0^*u) = \frac{4a_h^3}{E_h} \frac{|P_n^p|^2}{\frac{k(X_{n,1}^2 - \pi^2)}{(\bar{R}_0^*u)^2} - (\eta_{\lambda n}^p)^2 - \eta_{\lambda 1}^s}. \quad (44)$$

The partial photons absorption cross sections for QDs with the complex $A^+ + e$ are determined by the following formula

$$\sigma_n^p(\omega, R_0) = \frac{2\pi}{\hbar I_0} |M_{f,\lambda}(\omega, R_0)|^2 \frac{\Gamma_0}{\frac{\hbar^2 \Gamma_0^2}{4} + \left(\frac{\hbar^2 (X_{n,1}^2 - \pi^2)}{2m_e^* R_0^2} - (E_{\lambda n}^p - E_{\lambda 1}^s) - \hbar\omega \right)^2}, \quad (45)$$

Where $M_{f,\lambda}(\omega)$ is determined by formula (32). Rewriting (45) in the Bohr units, we obtain

$$\sigma_n^p(X, \bar{R}_0^*u) = \frac{2\pi}{\hbar^2 I_0 E_h} \frac{|M_{f,\lambda}(X)|^2 \Gamma_0^*}{\frac{\Gamma_0^{*2}}{4} + \left(\frac{k(X_{n,1}^2 - \pi^2)}{(\bar{R}_0^*u)^2} - (\eta_{\lambda n}^p)^2 - \eta_{\lambda 1}^s - X \right)^2}. \quad (46)$$

Thus, expression (34) takes the form

$$\begin{aligned}
\Delta\varepsilon(X) &= \frac{N_0 I_0 12\pi^2 \hbar^4 c^3 a_h^5 \alpha^*}{e^2 E_h^5 X^2} \sum_{n=1}^N \int_0^{3/2} P(u) du \frac{|P_n^p(\bar{R}_0^*u)|^2}{\left(\frac{k(X_{n,1}^2 - \pi^2)}{(\bar{R}_0^*u)^2} - (\eta_{\lambda n}^p)^2 - \eta_{\lambda 1}^s \right)^2} \times \\
&\times \frac{\Gamma_0^*}{\frac{\Gamma_0^{*2}}{4} + \left(\frac{k(X_{n,1}^2 - \pi^2)}{(\bar{R}_0^*u)^2} - (\eta_{\lambda n}^p)^2 - \eta_{\lambda 1}^s - X \right)^2}, \quad (47)
\end{aligned}$$

or, taking into account (32), for (47) we finally obtain

$$\begin{aligned}
\Delta\varepsilon(X) = & \frac{N_0 I_0 12 \pi^2 \hbar^4 c^3 a_h^5 \alpha^*}{e^2 E_h^5 X^2} \sum_{n=1}^N \int_0^{3/2} du \frac{P(u)}{\left(\frac{k(X_{n,1}^2 - \pi^2)}{(\bar{R}_0^* u)^2} - (\eta_{\lambda n}^p)^2 - \eta_{\lambda 1}^s \right)^2} \times \\
& \times \left| \frac{4X_{n,1} (X_{n,1}^2 \cos X_{n,1} (X_{n,1}^2 - \pi^2) + \sin X_{n,1} (3X_{n,1}^2 - \pi^2))}{\bar{R}_0^* u J_{3/2}(X_{0,1}) J_{5/2}(X_{n,1}) (\pi^2 - X_{n,1}^2)^2 (a_{s,n} a_{p,n})^{3/2}} \right| \times \\
& \times \sqrt{\frac{\Gamma\left(\frac{3}{4} + \frac{\varepsilon_{\lambda 1}^s}{2}\right) \Gamma\left(\frac{1}{4} + \frac{\varepsilon_{\lambda 1}^s}{2}\right)}{\left(\psi\left(\frac{3}{4} + \frac{\varepsilon_{\lambda 1}^s}{2}\right) - \psi\left(\frac{3}{4} + \frac{\varepsilon_{\lambda 1}^s}{2}\right)\right)} \left[\frac{\Gamma\left(\frac{3}{4} + \frac{\varepsilon_{\lambda n}^p}{2}\right) \Gamma\left(\frac{1}{4} + \frac{\varepsilon_{\lambda n}^p}{2}\right)}{\left(\psi\left(\frac{3}{4} + \frac{\varepsilon_{\lambda n}^p}{2}\right) - \psi\left(\frac{3}{4} + \frac{\varepsilon_{\lambda n}^p}{2}\right)\right)} \right]^{\frac{3}{2}}} \times \\
& \times \sum_{i=0}^{\infty} \sum_{j=0}^{\infty} \frac{(-1)^j (a_{s,n}^{-2} + a_{p,n}^{-2})^j}{2^j a_{s,n}^{2i} j! (3X_{n,1} \cos X_{n,1} + \sin X_{n,1} (X_{n,1}^2 - 3))} \left(\frac{\Gamma(-\frac{1}{2}) \left(\frac{1}{4} + \frac{\varepsilon_{\lambda n}^s}{2}\right)_i}{\Gamma\left(\frac{1}{4} + \frac{\varepsilon_{\lambda n}^s}{2}\right) \left(\frac{3}{2}\right)_i} \right) \times \\
& \times \left[\frac{(\bar{R}_0^* u)^{2(\frac{3}{2}+i+j)} \Gamma(-\frac{1}{2})}{\left(\frac{3}{2} + i + j\right) \Gamma\left(\frac{1}{4} + \frac{\varepsilon_{\lambda n}^p}{2}\right)} {}_2F_2\left(\frac{3}{2} + i + j, \frac{3}{4} + \frac{\varepsilon_{\lambda n}^p}{2}; \frac{5}{2} + i + j, \frac{3}{2}; \frac{(\bar{R}_0^* u)^2}{a_{p,n}^2}\right) + \right. \\
& \left. + \frac{a_{p,n} (\bar{R}_0^* u)^{2(1+i+j)} \Gamma\left(\frac{1}{2}\right)}{\left(\frac{3}{2} + i + j\right) \Gamma\left(\frac{3}{4} + \frac{\varepsilon_{\lambda n}^p}{2}\right)} {}_2F_2\left(1 + i + j, \frac{1}{4} + \frac{\varepsilon_{\lambda n}^p}{2}; \frac{1}{2}, 2 + i + j; \frac{(\bar{R}_0^* u)^2}{a_{p,n}^2}\right) \right] + \\
& + \frac{a_{s,n} \left(\frac{1}{4} + \frac{\varepsilon_{\lambda n}^s}{2}\right)_i}{\Gamma\left(\frac{3}{4} + \frac{\varepsilon_{\lambda n}^p}{2}\right) \left(\frac{1}{2}\right)_i} \left[\frac{(\bar{R}_0^* u)^{2(1+i+j)} \Gamma(-\frac{1}{2})}{(1+i+j) \Gamma\left(\frac{1}{4} + \frac{\varepsilon_{\lambda n}^p}{2}\right)} {}_2F_2\left(1 + i + j, \frac{3}{4} + \frac{\varepsilon_{\lambda n}^p}{2}; 2 + i + j, \frac{3}{2}; \frac{(\bar{R}_0^* u)^2}{a_{p,n}^2}\right) \right. \\
& \left. + \frac{a_{p,n} (\bar{R}_0^* u)^{2(\frac{1}{2}+i+j)} \Gamma\left(\frac{1}{2}\right)}{\left(\frac{1}{2} + i + j\right) \Gamma\left(\frac{3}{4} + \frac{\varepsilon_{\lambda n}^p}{2}\right)} {}_2F_2\left(\frac{1}{2} + i + j, \frac{1}{4} + \frac{\varepsilon_{\lambda n}^p}{2}; \frac{1}{2}, \frac{3}{2} + i + j; \frac{(\bar{R}_0^* u)^2}{a_{p,n}^2}\right) \right] \Bigg|^2 \times \\
& \times \frac{\Gamma_0^*}{\frac{\Gamma_0^{*2}}{4} + \left(\frac{k(X_{n,1}^2 - \pi^2)}{(\bar{R}_0^* u)^2} - (\eta_{\lambda n}^p)^2 - \eta_{\lambda 1}^s - X \right)^2}. \quad (48)
\end{aligned}$$

Figure 4(a,b,c) shows the spectral dependence of the relative change in permittivity $\Delta\varepsilon/\varepsilon$ for the quasi-zero-dimensional structure with InSb QDs for various dissipative tunneling parameters ε_L^* , ε_C^* and ε_T^* , calculated by formula (48). As can be seen from Fig. 4(a,b), an increase in the phonon mode value and temperature (respectively, parameters ε_L^* and ε_T^*) also leads to a significant increase in $\Delta\varepsilon/\varepsilon$, which is associated with an increase in the effective radius of the excited states of the impurity complex $A^+ + e$ under conditions of tunneling decay of the quasistationary A^+ state.

An increase in the degree of "viscosity" of the contact medium or of the heat-bath (parameter ε_C^*) leads to the suppression of the PDE due to an increase in the localization of the wave function of the quasi-stationary A^+ -state (see Fig. 4(c)). From Fig. 4(a,b,c) it is also seen that the PDE spectral dependence curves contain a peak that appears when the photon energy becomes comparable with the average energy of the optical transition. In this case, position of the peak depends on the parameters of dissipative tunneling, which, as shown above, have a significant influence on the effective localization radius of the quasi-stationary A^+ state.

4. Conclusion

Influence of dissipative tunneling on the PDE, associated with the excitation of impurity complexes $A^+ + e$ during intraband optical transitions of an electron in a QD, has been theoretically studied, taking into account change in the profile of the adiabatic potential of an electron.

In contrast to [15], where the case of a localized A^+ -state is considered, in this paper we consider the case of a quasi-stationary A^+ -state (the impurity level is located between the bottom of the adiabatic potential and the energy level of the ground state of the hole, see Fig. 1). In this case, the width of the potential barrier is finite, and the influence of the tunnel decay of the quasi-stationary-state should be taken into account. As a result, new possibilities appear for controlling the PDE in a quasi-zero-dimensional structure by varying such parameters of dissipative tunneling as temperature, the frequency of the phonon mode, and the constant of interaction with the contact medium, which differs significantly from the case of a localized A^+ -state [15], when the PDE is controlled only by changing the average quantum dot radius.

In the dipole approximation, an analytical formula is obtained for the spectral dependence of the change in the permittivity of a quasi-zero-dimensional structure upon photoexcitation of impurity complexes $A^+ + e$ under conditions

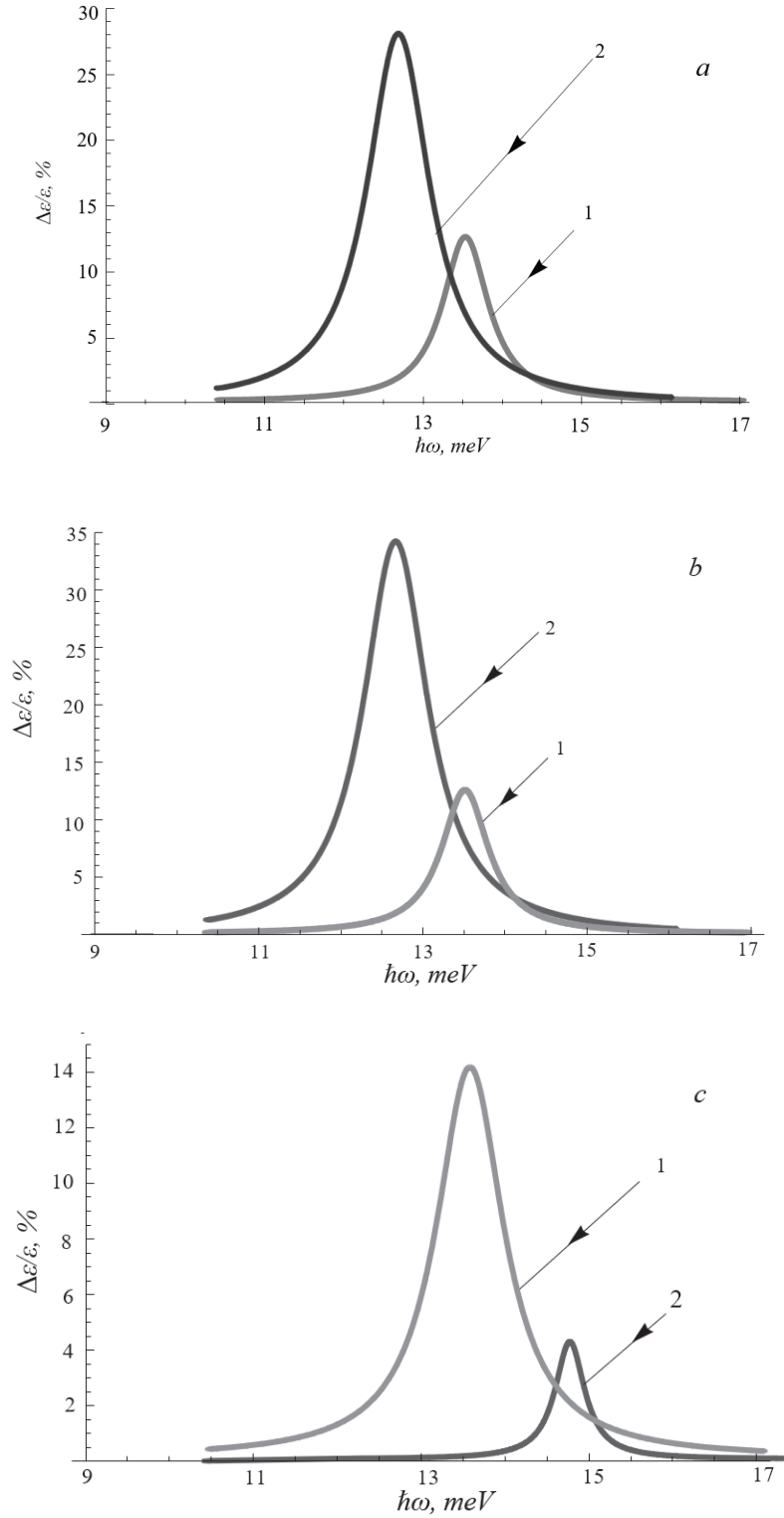


FIG. 4. Spectral dependence of the relative change in the permittivity of a quasi-zero-dimensional structure with InSb QDs at $E_i = 3.5$ meV; $\bar{R}_0 = 70$ nm, for different values of the dissipative tunneling parameters:

- a) 1 – $\varepsilon_L^* = 1$, $\varepsilon_T^* = 1$, $\varepsilon_C^* = 3$; 2 – $\varepsilon_L = 2$, $\varepsilon_T^* = 1$, $\varepsilon_C^* = 3$;
 b) 1 – $\varepsilon_L^* = 1$, $\varepsilon_T^* = 1$, $\varepsilon_C^* = 3$; 2 – $\varepsilon_L = 2$, $\varepsilon_T^* = 3$, $\varepsilon_C^* = 3$;
 c) 1 – $\varepsilon_L^* = 1$, $\varepsilon_T^* = 1$, $\varepsilon_C^* = 3$; 2 – $\varepsilon_L = 1$, $\varepsilon_T^* = 1$, $\varepsilon_C^* = 4$.

of tunnel decay of a quasi-stationary A^+ -state, taking into account the dispersion of the QD radius. It is found that varying the dissipative tunneling parameters leads to a change in the effective localization radius of the quasi-stationary A^+ -state in the QD and, as a consequence, to a noticeable change in the permittivity of the quasi-zero-dimensional structure. It is shown that the spectral dependence of the PDE is characterized by a peak that appears when the photon energy becomes comparable with the average energy of the optical transition. The position of the peak depends on the parameters of dissipative tunneling. It is revealed that an increase in the degree of “viscosity” of the contact medium is accompanied by the suppression of the PDE due to the strengthening of the localization of the wave function of the quasi-stationary A^+ -state. Thus, the controllability of the PDE in a quasi-zero-dimensional structure with impurity complexes $A^+ + e$ in the presence of dissipative tunneling has been demonstrated.

References

- [1] Kumari I. D., Jayasumana S., Attygalle D. Development of a photosensor based on photo dielectric effect of cadmium sulphide. *Moratuwa Engineering Research Conference (MERCCon)*, 2019, P. 349–353.
- [2] Nagai T., Takahashi H., et al. Optical control of dielectric permittivity in $LaAl_{0.99}Zn_{0.01}O_{3-\delta}$. *Appl. Phys. Lett.*, 2017, **110**, 172901.
- [3] Nagai T., Tanabe K., Terasaki I., Taniguchi H. Systematic tuning of the photo-dielectric effect in $Ba(Al_{1-x}Zn_x)_2O_{4-\delta}$. *Appl. Phys. Lett.*, 2018, **113**, 212902.
- [4] Avanesyan V.T., Puchkov M.Y. Photodielectric effect in thin-film structures of the poly[NiSalen] metallopolymer. *Phys. Solid State*, 2009, **51**, P. 2178–2181.
- [5] Shashin D.E., Sushentsov N.I. Development of manufacturing technology of photo-dielectric sensitive element of ultraviolet range on the basis of thin films of zinc oxide. *Herald of the Bauman Moscow State Technical University, Series Instrument Engineering*, 2019, **6**, P. 99–109.
- [6] Qasrawi A.F., Abu-Zaid S.F., Ghanameh S.A., Gasanly N.M. Dielectric and photo-dielectric properties of TlGaSeS crystals. *Bull. Mater. Sci.*, 2014, **37** (3), P. 505–509.
- [7] Nishikawa H., Sano K., Araoka F. Anisotropic fluid with phototunable dielectric permittivity. *Nature Communications*, 2022, **1142**.
- [8] Avanesyan V.T., Piskovatskova I.V. Photodielectric effect in $Bi_{12}SiO_{20}$ sillenite crystals. *Semiconductors*, 2020, **54**, P. 19–21.
- [9] Pillai P.K.C., Nath R. Photodielectric effect in photoconductors. *Phys. Stat. Sol. (a)*, 1976, **37** (2), P. 491–498.
- [10] Zhukovsky V.Ch., Dakhnovskii Yu.I., et al. Study of dissipative tunneling controllability in systems of interacting quantum molecules *Moscow University Physics Bulletin*, 2006, **62**, P. 73–77.
- [11] Krevchik V.D., Levashov A.V. Energy spectrum and optical properties of the quantum dot-impurity center complex *Semiconductors*, 2002, **36** (2), P. 208–212.
- [12] Demkov Yu.N., Ostrovskii V.N. *Zero-Range Potentials and Their Applications in Atomic Physics (Physics of Atoms and Molecules)*. Springer, New York, 1988, 296 p.
- [13] Bateman H. *Higher Transcendental Functions*. McGraw-Hill Book Company, 1953.
- [14] Lifshitz I.M., Slezov V.V. Kinetics of diffusion decomposition of supersaturated solid solutions. *Soviet Physics JETP*, 1959, **35** (2(8)), P. 331–339.
- [15] Krevchik V.D., Levashov A.V. Photodielectric effect associated with the excitation of the complex $A^+ + e$ in quasi-zero-dimensional structures. *Proceedings of the Volga region state universities. Physical and mathematical sciences*, 2007, **3**, P. 77–92.
- [16] Godik E.E., Kuznetsov A.I. Photodielectric effect associated with the excitation of impurities in semiconductors. *Proceedings of the Academy of Sciences of the USSR. (Physical series)*, 1978, **42** (6), 1206.
- [17] Krevchik V.D., Razumov A.V., Budyansky P.S. Features of the photodielectric effect associated with the excitation of impurity complexes $A^+ + e$ in quasi-zero-dimensional structures in an external magnetic field. *Proceedings of the Volga region state universities. Physical and mathematical sciences*, 2015, **4**, P. 114–144.

Submitted 26 April 2022; revised 16 May 2022; accepted 17 May 2022

Information about the authors:

Vladimir D. Krevchik – Penza State University, Physics Department, Krasnaya str., 40, Penza, 440026, Russia; ORCID 0000-0002-3522-8326; physics@pnzgu.ru

Alexey V. Razumov – Penza State University, Physics Department, Krasnaya str., 40, Penza, 440026, Russia; razumov_alex@mail.ru

Mikhail B. Semenov – Penza State University, Physics Department, Krasnaya str., 40, Penza, 440026, Russia; ORCID 0000-0003-4348-0000; misha29.02.1@gmail.com

Alexander V. Levashov – Penza State University, Physics Department, Krasnaya str., 40, Penza, 440026, Russia; physics@pnzgu.ru

A.V. Shorokhov – Penza State University, Physics Department, Krasnaya str., 40, Penza, 440026, Russia; University of Jyväskylä, Seminaarinkatu, 15, PO BOX 35, FI-40014, Finland; alex.shorokhov@gmail.com

Conflict of interest: the authors declare no conflict of interest.

The Gaussian impurity effect on the electronic and magnetic properties of an electron confined in a lateral quantum dot

Ayham Shaer, Mohammad K. Elsaid

Physics Department, An-Najah National University, Nablus, Palestine

Corresponding author: Ayham Shaer, ayham.shaer@najah.edu

ABSTRACT The Hamiltonian of a single electron trapped in a lateral quantum dot in the influence of an acceptor Gaussian impurity has been solved using a variational wavefunction as a superposition of a product of eigenfunctions of the harmonic oscillator in x and y coordinates. The effects of Gaussian impurity parameters on the system's spectra have been investigated as a function of the magnetic field. Furthermore, the electron probability has been displayed to investigate the impurity position effect on the energy levels. As a second step, the calculated energy spectra were utilized to compute and visualize the system's magnetic properties in the presence of the magnetic field and impurity. The obtained energy spectra show level crossings in the presence of acceptor impurity, which causes oscillations in the magnetic susceptibility and magnetization curves, resulting in an exciting diamagnetic–paramagnetic phase transition.

KEYWORDS lateral quantum dot, magnetic properties, Gaussian impurity, diamagnetic-paramagnetic transition

FOR CITATION Shaer A., Elsaid M.K. The Gaussian impurity effect on the electronic and magnetic properties of an electron confined in a lateral quantum dot. *Nanosystems: Phys. Chem. Math.*, 2022, **13** (3), 265–273.

1. Introduction

The electrical, thermal, optical, and magnetic properties in quantum-confined systems have recently got much attention. The advancements in semiconductor technology have made it feasible to develop structures with features that are particularly sensitive to heterostructure confinement, which has piqued interest. For example, by using an external magnetic field, the electronic states of the carriers confined in the quantum dot (QD) may be significantly altered [1–15]. This important topic has been well researched. Impurities also have an important influence in modifying the characteristics of semiconductor materials [13–16]. Since the ionized impurities comprise an extra attractive or repulsive electrostatic potential in the quantum dot's Hamiltonian, doping the quantum dot with acceptor and donor impurities alters the quantum confinement.

Various theoretical studies have been devoted to solving the Schrodinger equation for the QD system using various approaches such as the variational [13, 17, 18], the $1/N$ expansion [11, 12], and the exact diagonalization method [19–21].

The exact diagonalization method was used to study the magnetization and magnetic susceptibility of a donor impurity in a parabolic GaAs QD by Alia et al. [19]. The results of calculations have revealed that the electric field can modify the magnetic properties of the GaAs QD, causing its magnetic susceptibility to change from diamagnetic to paramagnetic.

The effect of the spin-orbit interaction (SOI) on the electron magnetic properties of a parabolic InAs QD has been investigated by Voskoboinikov et al. [22]. The work gives a theoretical investigation of the influence of SOI on the electron magnetic properties of tiny semiconductor QDs. At low temperatures, these properties exhibit quite exciting behavior. The sudden variations in magnetic properties at low magnetic fields are attributable to the alternate crossing of the spin-split electron levels in the energy spectrum, primarily caused by SOI. Hosseinpour [23] provided an investigation into the influence of Rashba SOI and Gaussian impurity on the heat capacity of an asymmetric QD. Madhav et al. [24] investigated the electronic properties of anisotropic QDs in a magnetic field. They also calculated a two-electron system's energy spectrum and pair-correlation function to examine the influence of inter-electron interaction on isotropic and anisotropic quantum dots.

The paper is organized as follows. Section II presents the Hamiltonian of a doped Gaussian impurity in an isotropic QD, the computation of energy spectra, and the magnetic properties of the QD. The numerical results and related discussions are given in section III, while the last section presents the conclusion.

2. Theory

This section contains the QD Hamiltonian under the effect of Gaussian impurity, the variational procedure, and the QD magnetic properties.

2.1. The quantum dot Hamiltonian

The Hamiltonian used to represent a two-dimensional QD with a single carrier in the presence of an external uniform magnetic field (\mathbf{B}), in addition to an impurity, can be given as:

$$\hat{H} = \frac{(\vec{p} - e\vec{\mathbf{A}})^2}{2m^*} + V_{\text{conf}}(x, y) + V_{\text{imp}}(x, y) + H_{\text{Zeeman}}. \quad (1)$$

The effective mass m^* for the electron depends on the QD material. $\vec{\mathbf{A}}$ is the potential vector that corresponds to the applied \mathbf{B} taken normal to QD plane, in the present work, the symmetric gauge, $\vec{\mathbf{A}} = \frac{B}{2}(-y, x, 0)$, has been used, where the confinement potential is taken to be anisotropic:

$$V_{\text{conf}}(x, y) = \frac{1}{2}m^* (\omega_x^2 x^2 + \omega_y^2 y^2). \quad (2)$$

The confinement potential's shape implies asymmetric electrostatic confinement of the electron in the x and y directions, which may be achieved using appropriate electrostatic gates. By choosing the appropriate values for ω_x and ω_y one can define the shape of the dot from a circle ($\omega_x = \omega_y$) to an ellipse ($\omega_x \neq \omega_y$).

A smooth changing form, finite depth, and range make the Gaussian impurity model an excellent approximation of the impurity potential in QDs. In our current investigation, we picked the impurity potential as:

$$V_{\text{imp}}(x, y) = V_0 e^{-\frac{(x-x_0)^2 + (y-y_0)^2}{d^2}}, \quad (3)$$

where $V_0 > 0$ signifies a repulsive impurity, and (x_0, y_0) specifies the impurity center's position. V_0 measures the impurity potential's strength, whereas d is a measure of the impurity's domain of influence. A large value of d shows that it is spatially distributed, whereas a small value of d accounts for one where the spatial extension of the impurity potential is minimal.

The final term in the Hamiltonian corresponds to the standard Zeeman energy,

$$\hat{H}_{\text{Zeeman}} = \frac{1}{2}g\mu_B\sigma_z. \quad (4)$$

The Schrödinger equation with full Hamiltonian in eq. (1) cannot be solved in an analytic form. As a consequence, the trial wave function has been described in x and y coordinates as a superposition of a product of eigenfunctions of harmonic oscillators,

$$\psi(x, y) = \sum_{n,m} C_{n,m} \phi_n(\alpha_x, x) \phi_m(\alpha_y, y). \quad (5)$$

Here

$$\phi_n(\alpha_x, x) = \frac{1}{\sqrt{2^n n!}} \left(\frac{\alpha_x}{\sqrt{\pi}} \right)^{\frac{1}{2}} e^{-\frac{\alpha_x^2 x^2}{2}} H_n(\alpha_x x), \quad \alpha_x = \left(\frac{m^* \omega_x}{\hbar} \right)^{\frac{1}{2}}; \quad (6)$$

$$\phi_n(\alpha_y, y) = \frac{1}{\sqrt{2^n n!}} \left(\frac{\alpha_y}{\sqrt{\pi}} \right)^{\frac{1}{2}} e^{-\frac{\alpha_y^2 y^2}{2}} H_n(\alpha_y y), \quad \alpha_y = \left(\frac{m^* \omega_y}{\hbar} \right)^{\frac{1}{2}}. \quad (7)$$

By solving the spectral equation $|\langle \Psi_{n_x n_y s} | \hat{H} | \Psi_{n'_x n'_y s'} \rangle - \lambda I| = 0$, the eigenvalues are obtained. Furthermore, eigenvectors are given by the Schrodinger equation with inserted eigenvalues as the energy.

2.2. The magnetic properties of the QD

From the numerical outputs, one can use sufficient energy spectra to calculate the partition function using canonical definition,

$$Z = \sum_n e^{-\beta E_n}, \quad (8)$$

where $\beta = 1/k_B T$, k_B is the Boltzmann constant.

The magnetization (M) of the QD, which indicates the response of the material to \mathbf{B} , is computed as follows [25]:

$$M = -\frac{\partial \langle E \rangle}{\partial B}, \quad (9)$$

where the average energy ($\langle E \rangle$) can be calculated as [10]:

$$\langle E \rangle = -\frac{\partial \text{Ln}(Z)}{\partial \beta}. \quad (10)$$

The magnetic susceptibility (χ) for the system can be computed by taking the derivative of M with respect to B [25] as:

$$\chi = \frac{\partial M}{\partial B}, \quad (11)$$

according to the χ sign, the material can be classified into paramagnetic ($\chi > 0$) and diamagnetic ($\chi < 0$).

3. Results and discussion

This work was done on the InAs anisotropic QD with parameters: $m^* = 0.0239m_0$ and $g = -15$ [26]. The basis-functions with n_x, n_y were taken from 0 – 30 for each direction in the linear variational calculation. The direct product of the basis gave a 30×30 -dimensional space. We confirmed that the basis functions completely cover the two-dimensional space, at least in expressing the observables under investigation. A larger number of basis functions were used in the convergence test. Table 1 shows the eigenenergies for the ground and the first two excited states for a range of basis functions.

TABLE 1. The low-lying states energies for different basis numbers at $V_0 = 32$ meV, $d = 10$ nm, $\omega_x = 4$ meV, $\omega_y = 6$ meV, and $B = 2T$

Space dimension	G. S (meV)	1st excited state (meV)	2nd excited state (meV)
5×5	10.2834	12.9467	20.3453
10×10	10.0443	11.0118	11.3830
15×15	10.0140	10.9043	11.3779
20×20	10.0025	10.8960	11.3750
25×25	9.9996	10.8938	11.3747
30×30	9.9995	10.8938	11.3746
35×35	9.9995	10.8938	11.3746
40×40	9.9995	10.8938	11.3746

In Fig. 1(a,b), we show the Fock-Darwin states of a single electron in the absence of impurity ($V_0 = 0$), for circular QD (Fig. 1(a)) and elliptical QD (Fig. 1(b)). The plots show quite similar behavior of the energies as a function of B , except that the degeneracies of the states are lifted at $B = 0$ due to different confinement strengths in x and y directions; this result has been previously reported in [27]. At $B \neq 0$ the most characteristic feature of the figures is that the Fock-Darwin levels are split due to Zeeman interaction into two substates corresponding to different spin orientations. This separation between the two sublevels shows linear increase with the applied field as $|\mu_B g B|$. Fig. 1(c,d) highlights the effect of on-center gaussian impurity on the state energies of the system as a function of B . An interesting level crossing between the ground state and the first excited state appeared at a particular B . In the isotropic (anisotropic) potential case, this crossing occurs at $B \approx 2.4 T$ ($2.8 T$).

We have studied the dependence of low-lying states on the impurity profiles (strength, influence domain, and position). Fig. 2(a,b,c) shows the effect of the impurity domain on the level crossing; as d increases, the intersection point occurs at a lower magnetic field value. Also, by comparing Figs. 1(d) and 2(a,d), it is revealed that increasing the impurity strength for a fixed influence domain moves the crossing to a lower B value.

In Fig. 3, we plot the low-lying states as a function of impurity strength (Fig. 3(a)) and impurity domain (Fig. 3(b)). The on-center impurity affects the ground state ($|0, 0\rangle$) more than other states, and this increase in the ground state energy makes the levels cross. As V_0 increases, the repulsive force between the impurity and the electron increases; as a result, the electron is pushed from the center to be at a higher energy point. In the same way, as d increases, the impurity effect is spread from the center, so the electron is being pushed further away. Another observation is that when d increases, the excited states are also significantly affected by the impurity potential.

To explain this observation, the electron probability density has been plotted in Fig. 4 for different impurity profiles. As the top panel shows, in the absence of impurity, the electron in state $|0, 0\rangle$ has a higher probability of being at the center of the QD. Since, $\omega_x < \omega_y$ the first excited state ($|1, 0\rangle$) has a node in the x -direction, while the state $|0, 1\rangle$ is the second excited state (which has a node in the y -direction). In the presence of an on-center impurity, the charge density distributes away due to electron-impurity repulsion, so the electron has a greater probability of being further from the center, while for the excited states $|1, 0\rangle$ and $|0, 1\rangle$ the electron probability at the center is zero, so the presence of the impurity has an insignificant effect on the probability, therefore a minor effect on the state's energy, especially for low values of d .

As the impurity strength or its stretch increases, the probability becomes less at the center, so the electron is obligated to be at a higher confined point due to the parabolic well in x and y directions. On the other hand, for a larger value of d (bottom panel of Fig. 4), the effects of impurity on the excited states are apparent, and the effects on the state $|1, 0\rangle$ and $|0, 1\rangle$ varies due to the isotropy of the QD.

From Fig. 5(a), it is clear that the $E_{G.S}$ increases as the impurity strength increases, and the cusp, which corresponds to the crossing, shifts to the left as the strength increases. In Fig. 5(b), the effect of the impurity domain on the $E_{G.S}$ has been displayed. As d increases, more cusps appear in the $E_{G.S}$. For example, two cusps for $d = 20$ nm correspond to the two crossings in Fig. 2(c).

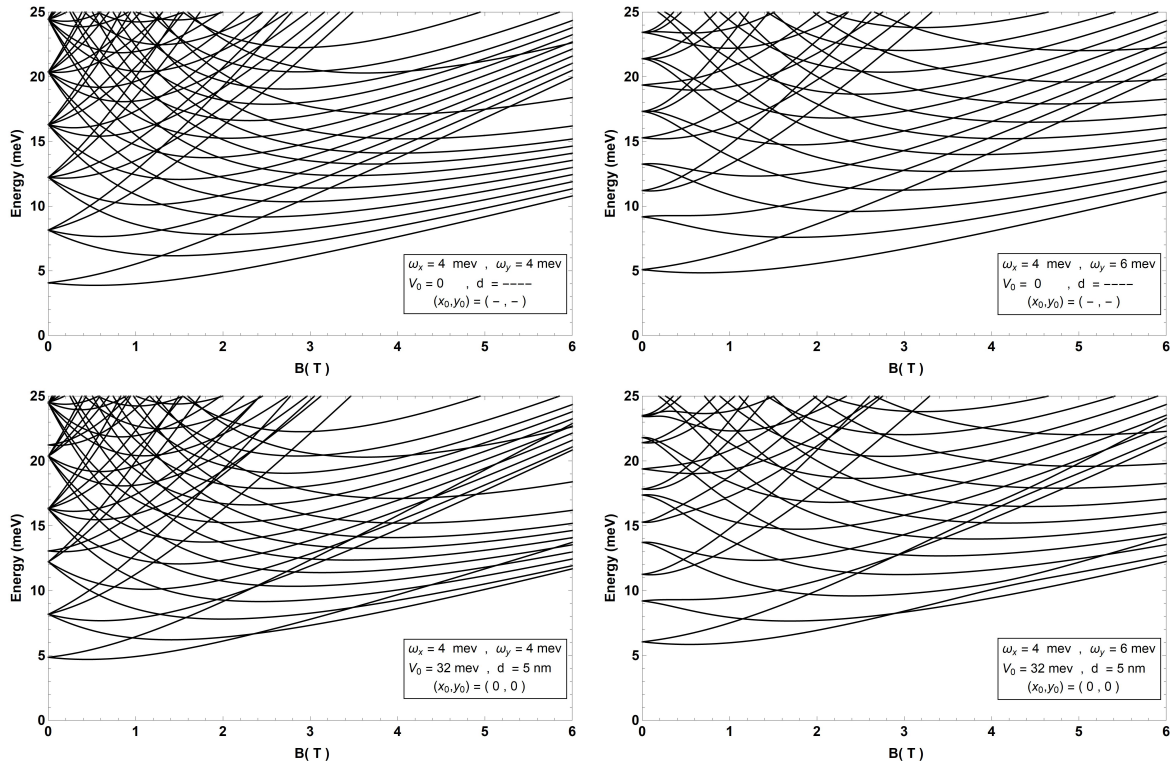


FIG. 1. Low-lying states energies of the QD as a function of B for isotropic (a and c) and anisotropic (b and d)

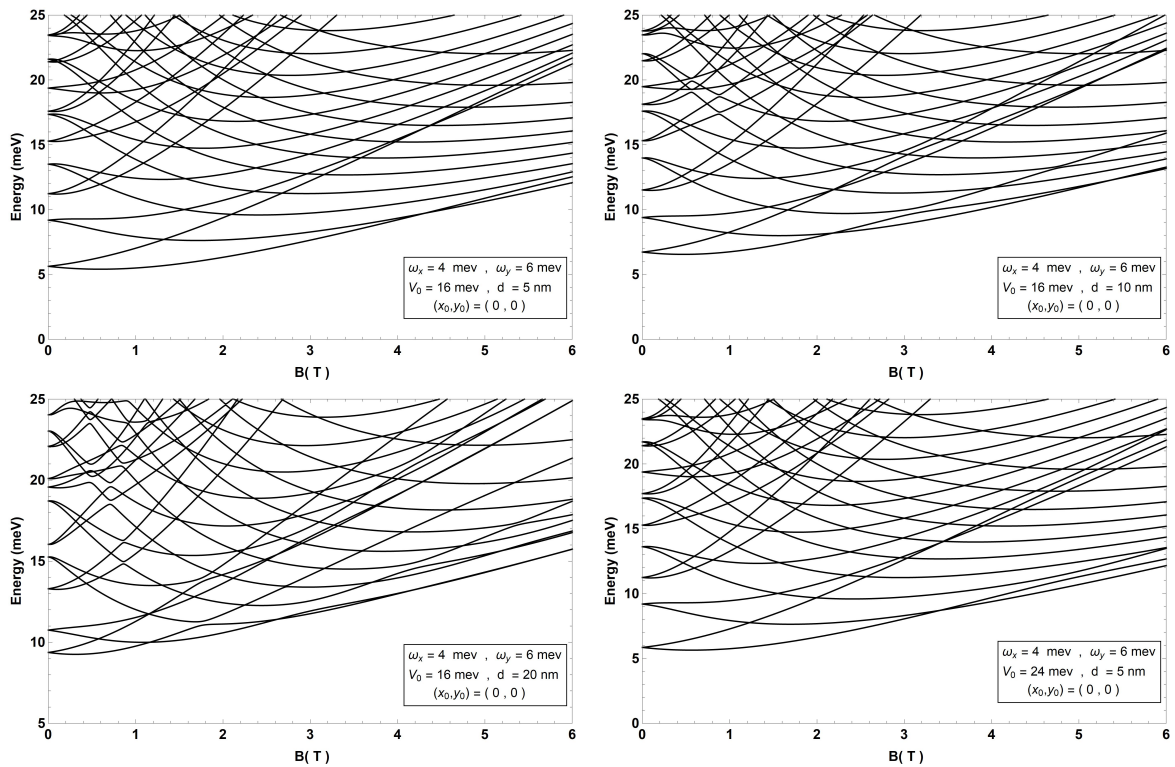


FIG. 2. Low-lying states energies as a function of B for different impurity

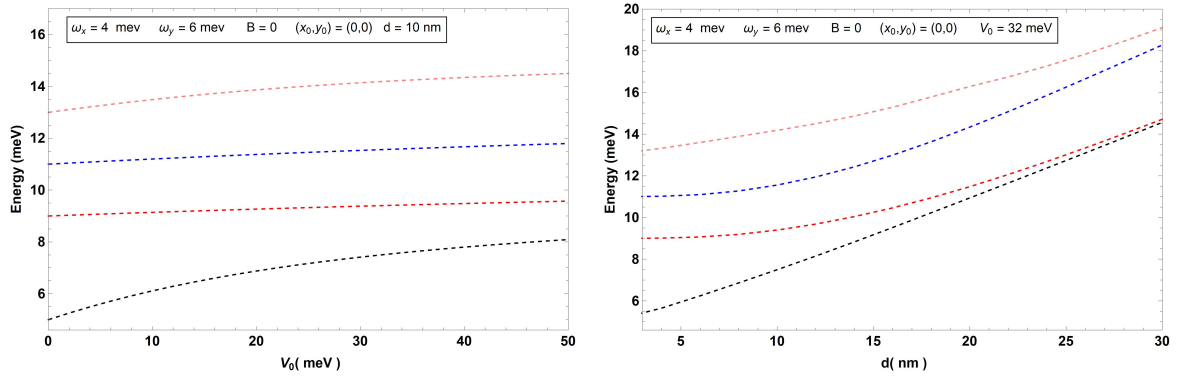


FIG. 3. Low-lying states energies as a function of a) V_0 , b) d for anisotropic potential

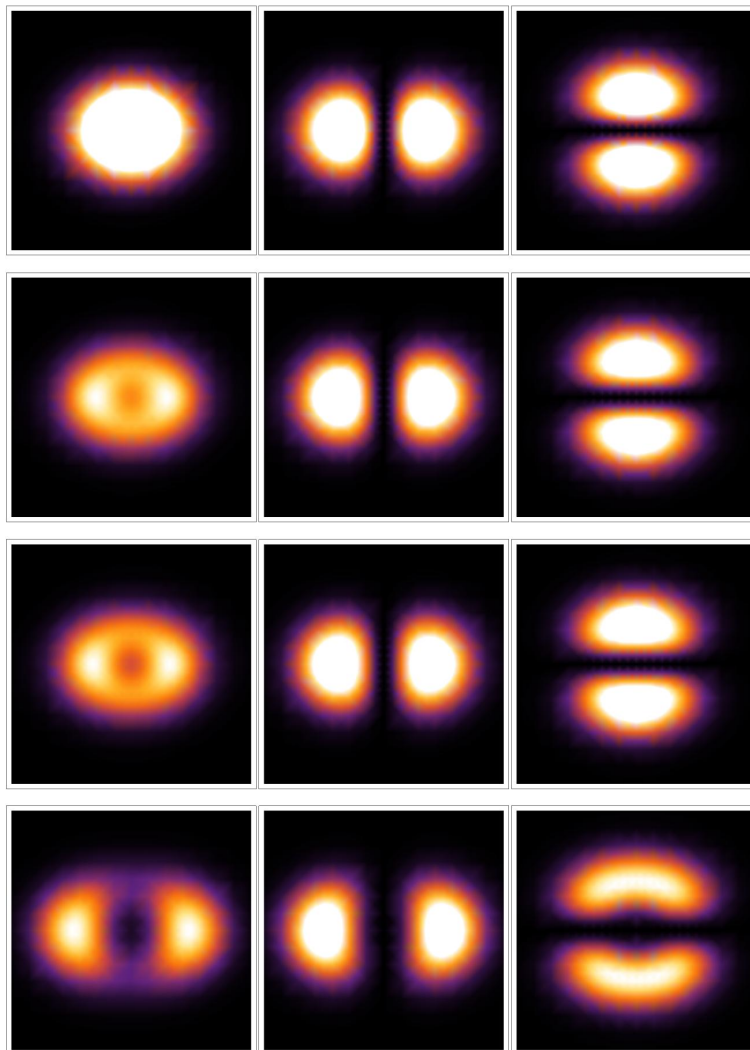


FIG. 4. Probability density $|\psi|^2$ for the wavefunctions of the low-lying states $|0, 0\rangle$, $|1, 0\rangle$, and $|0, 1\rangle$, in the presence of on-center impurity with profiles (from up to down) (V_0, d) : $(0, -)$, $(24, 10)$, $(32, 10)$ and $(32, 20)$ in meV and nm, respectively

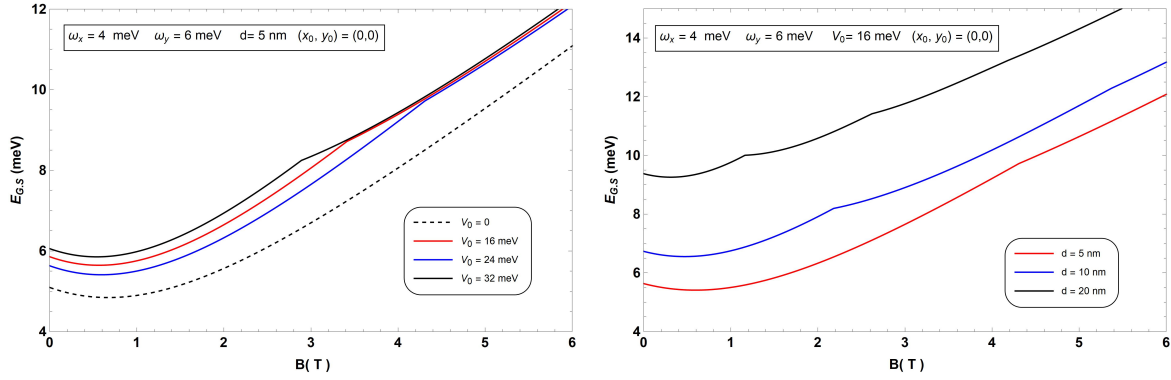


FIG. 5. $E_{G,S}$ as a function of B for different impurity profiles

In Fig. 6, we have displayed the effect of impurity position on the energy level for the four low-lying states. From these two plots, we can conclude that the off-center impurity position affects the states with a larger probability of the electron being at the impurity position; when the impurity is located at $x(y) = 22$ nm from the origin, the energy of the state $|1, 0\rangle$ ($|0, 1\rangle$) is significantly affected, while the states $|0, 1\rangle$ ($|1, 0\rangle$) are minorly affected due to their node at $x(y) = 0$, whereas the third excited state $|2, 0\rangle$ is more affected by the on-center impurity than the lower excited states due to its electron probability at $x = 0$.

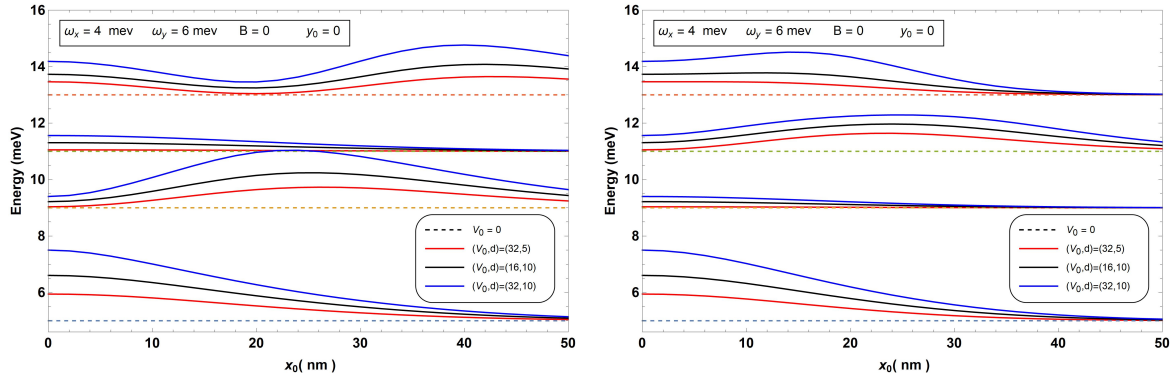


FIG. 6. Impurity position effect on the low-lying energy state

The electron's probability density was calculated and plotted in Fig. 7 for the previous four orbits to support the result of Fig. 6 and make it more understandable. The density extends perpendicular to the axis, which contains the impurity. As a consequence, the energy value increases.

The average statistical energy has been plotted in Fig. 8 in the presence of on-center impurity for different temperatures, and the figure shows that $\langle E \rangle$ is very similar to the ground state energy at low temperatures $T \rightarrow 0$, $E_{G,S}$ has cusps at the level crossings, where the states are degenerate.

The dependence of the magnetization on the magnetic field and the impurity profile was studied in Fig. 9. The results show the presence of oscillation in the magnetization curve due to the intersection of the low-lying states energies. In Fig. 9(a), the effect of the impurity strength is shown; the increase in the impurity strength pulls the intersection in the energy levels shown in previous figures towards a lower value of the magnetic field.

The influence of impurity expansion has been investigated in Fig. 9(b). It is noticed that there are numerous peaks in the magnetization curve at larger values of d due to the occurrence of multiple changes in the ground state energy, which can be observed by referring to Fig. 5(b).

The influence of the impurity position was investigated in Fig. 9(c) since most of the effect on magnetization is attributable to the ground state at temperatures near zero. As a result, the impurity existence away from the center reduces the oscillation peaks height.

In Fig. 9(d), the effect of the temperature has been illustrated. For $T \rightarrow 0$, at the level crossings, the magnetization is discontinuous; consequently, the susceptibility diverges. At finite temperatures, thermal excitations make the magnetization a continuous and smooth function, and the susceptibility then has the spectral line form with a temperature dependence linewidth, as presented in Fig. 10(a). The number and position of the peaks depend on the impurity profile, as shown in Fig. 10(b).

The full width at half maximum of the spectral line of the susceptibility (FWHM) is shown as a function of temperature in Fig. 11. One can see that the temperature changes the spectral linewidth linearly.

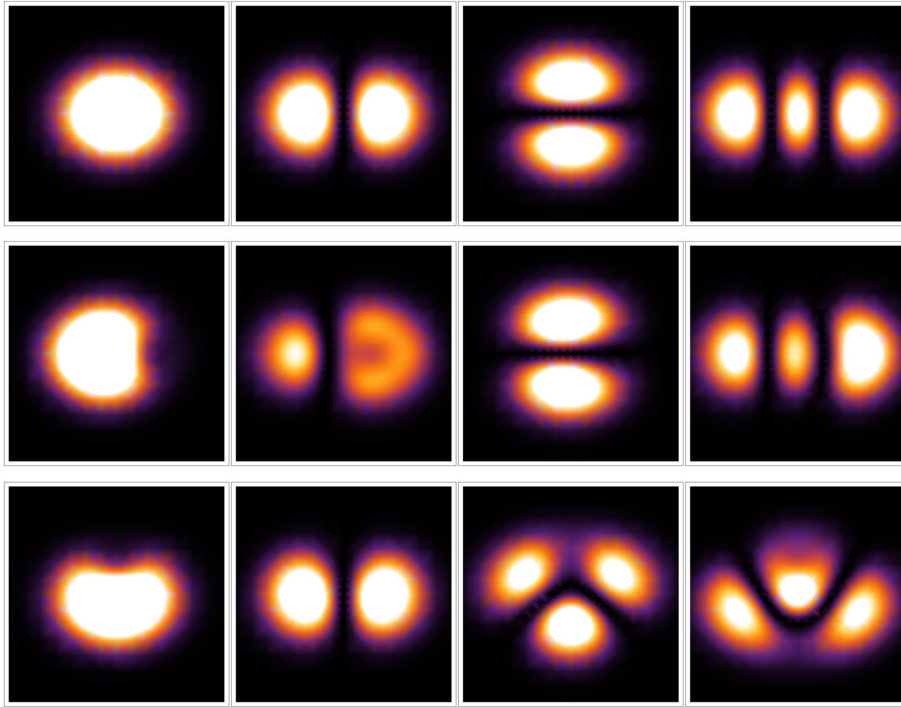


FIG. 7. Probability density $|\psi|^2$ for the wavefunctions of the low-lying states, the top panel for $V_0 = 0$ and the other two panels in the presence of an off-center impurity with $V_0 = 32$ meV and $d = 10$ nm, located at (x_0, y_0) : $(22, 0)$, $(0, 22)$ from up to down respectively

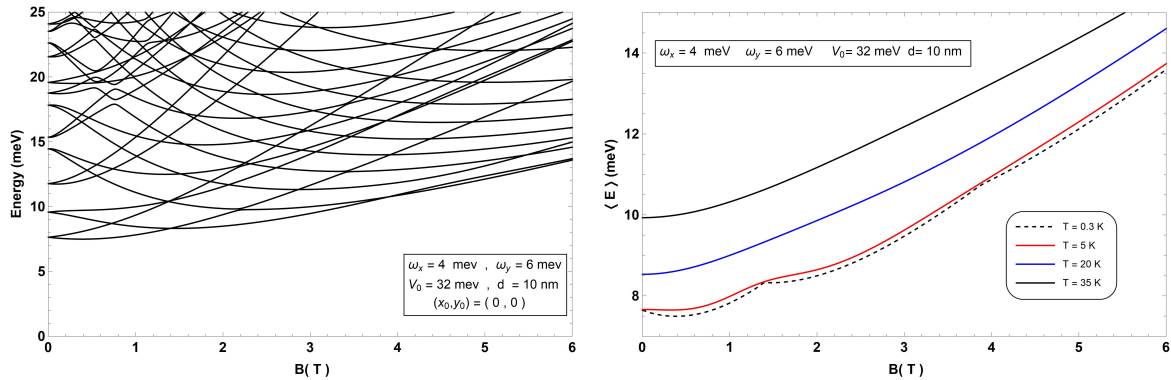


FIG. 8. a) the energy spectra; b) $\langle E \rangle$ vs. the magnetic field for fixed impurity profiles

4. Conclusion

Finally, the Hamiltonian of an electron confined in a 2D anisotropic quantum dot in the presence of acceptor Gaussian impurity has been studied. The obtained numerical energies have been used to investigate the system statistical energies, magnetization, and magnetic susceptibility. This work has concentrated on the low-lying energy levels crossings corresponding to the ground state transitions. These transitions cause cusps in the statistical average energy and oscillations in the magnetization curve. In addition, the magnetic susceptibility of InAs QD has been shown to have a diamagnetic-paramagnetic phase transition due to the impurity presence. This transition is strongly correlated with the impurity profiles (strength, position, and influence domain), magnetic field, and temperature. In applications, the magnetic phase transition (diamagnetic to paramagnetic transition) should be taken into account when estimating the applicability of material to be involved in future technologies as switching devices, magnetic sensors, and magnetic shielding.

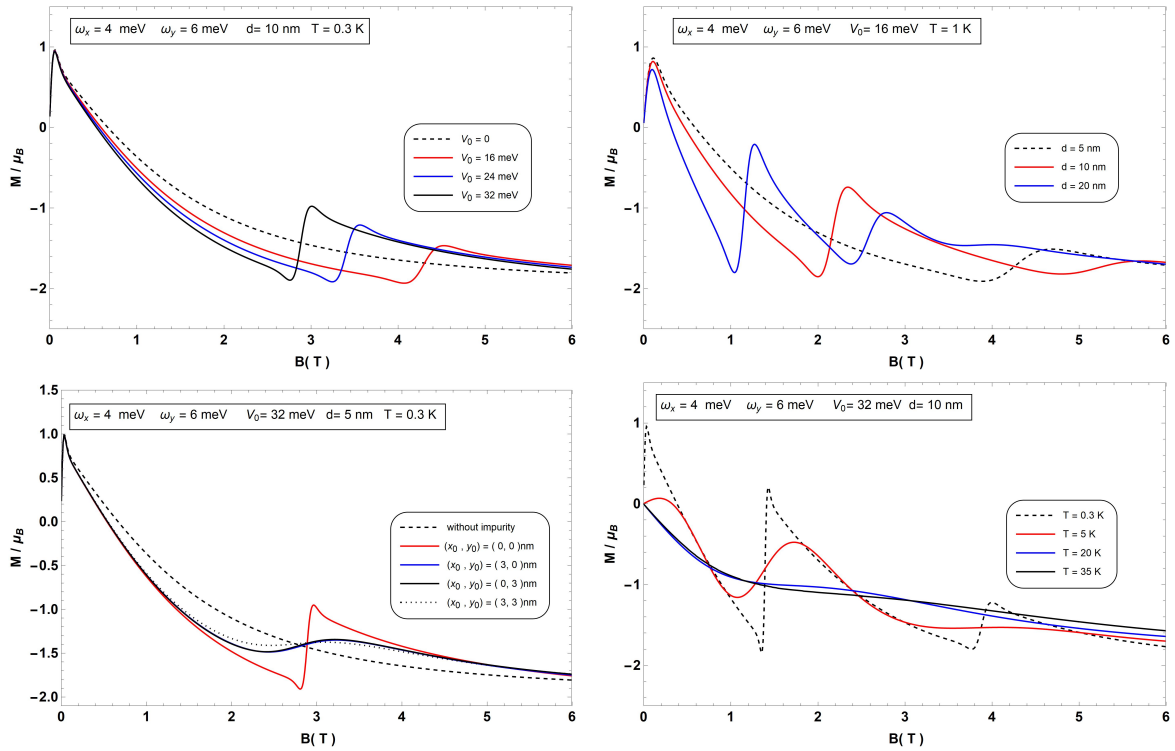


FIG. 9. M vs. B for a) different impurity strengths; b) different impurity stretches; c) different impurity position; and d) different temperature, where all other parameters have been fixed

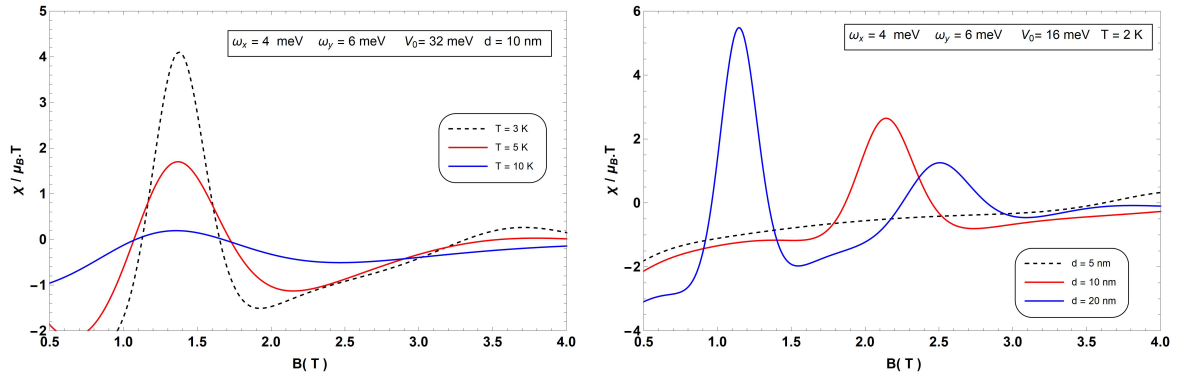


FIG. 10. χ vs. B for a) different temperatures; b) different impurity stretches

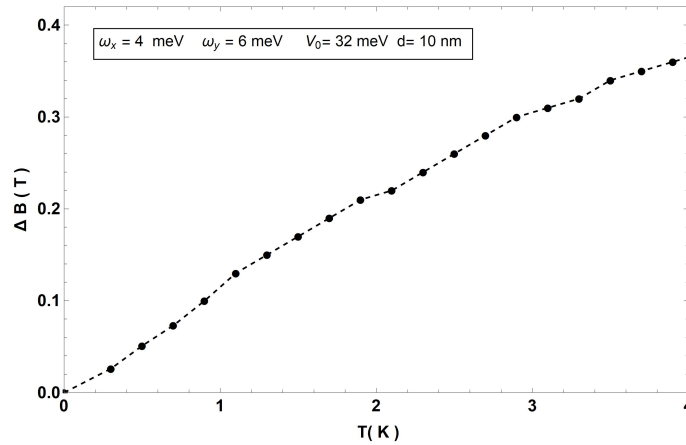


FIG. 11. The full width at half maximum of the spectral linewidth of the susceptibility as a function of temperature

References

- [1] Chakraborty T., Pietiläinen P. Optical signatures of spin-orbit interaction effects in a parabolic quantum dot. *Phys. Rev. Lett.*, 2005, **95** 136603.
- [2] Stufler S., Ester P., Zrenner A., Bichler M. Quantum optical properties of a single $\text{In}_x\text{Ga}_{1-x}\text{As}$ -GaAs quantum dot two-level system. *Phys. Rev. B*, 2005, **72**, 121301.
- [3] Jha P.K., Kumar M., et al. Rashba spin orbit interaction effect on nonlinear optical properties of quantum dot with magnetic field. *Superlattices Microstructures*, 2014, **65**, P. 71–78.
- [4] Gumber S., Kumar M., et al. Thermal and magnetic properties of cylindrical quantum dot with asymmetric confinement. *Canadian J. of Physics*, 2015, **93**, P. 1264–1268.
- [5] Avetisyan S., Chakraborty T., Pietiläinen P. Magnetization of interacting electrons in anisotropic quantum dots with Rashba spin-orbit interaction. *Physica E: Low-dimensional Systems Nanostructures*, 2016, **81**, P. 334–338.
- [6] Gumber S., Kumar M., Jha P.K., Mohan M. Thermodynamic behaviour of Rashba quantum dot in the presence of magnetic field. *Chinese Physics B*, 2016, **25**, 056502.
- [7] Khordad R. The effect of Rashba spin-orbit interaction on electronic and optical properties of a double ring-shaped quantum dot. *Superlattices Microstructures*, 2017, **110**, P. 146–154.
- [8] Baghdasaryan D., Hayrapetyan D., Kazaryan E., Sarkisyan H. Thermal and magnetic properties of electron gas in toroidal quantum dot. *Physica E: Low-dimensional Systems Nanostructures*, 2018, **101**, P. 1–4.
- [9] Castano-Yepes J.D., Amor-Quiroz D., Ramirez-Gutierrez C., Gómez E.A. Impact of a topological defect and Rashba spin-orbit interaction on the thermo-magnetic and optical properties of a 2D semiconductor quantum dot with Gaussian confinement. *Physica E: Low-dimensional Systems Nanostructures*, 2019, **109**, P. 59–66.
- [10] Shaer A., Hjaz E., Elsaid M. The heat capacity of a semiconductor quantum dot in magnetic fields. *Nanosystems: Phys. Chem. Math.*, 2019, **10**, P. 530–535.
- [11] Yahyah N.S., Elsaid M.K., Shaer A. Heat capacity and entropy of Gaussian spherical quantum dot in the presence of donor impurity. *J. of Theor. and Appl. Phys.*, 2019, **13**, P. 277–288.
- [12] Yaseen A., Shaer A., Elsaid M.K. The magnetic properties of GaAs parabolic quantum dot in the presence of donor impurity, magnetic and electric fields. *Chinese J. of Physics*, 2019, **60**, P. 598–611.
- [13] Kandemir B., Cetin A. Impurity magnetopolaron in a parabolic quantum dot: the squeezed-state variational approach. *J. of Phys.: Condensed Matter*, 2005, **17**, 667.
- [14] Datta N.K., Ghosh M. Impurity strength and impurity domain modulated frequency-dependent linear and second nonlinear response properties of doped quantum dots. *Physica Status Solidi*, 2011, **248**, P. 1941–1948.
- [15] Boda A., Chatterjee A. Transition energies and magnetic properties of a neutral donor complex in a Gaussian GaAs quantum dot. *Superlattices Microstructures*, 2016, **97**, P. 268–276.
- [16] Krevchik V.D., Razumov A.V., et al. Temperature dependence of recombination radiation in semiconductor nanostructures with quantum dots containing impurity complexes. *Nanosystems: Phys. Chem. Math.*, 2021, **12**, P. 680–689.
- [17] Shaer A., Elsaid M.K., Elhasan M. Variational calculations of the heat capacity of a semiconductor quantum dot in magnetic fields. *Chinese Journal of Physics*, 2016, **54**, P. 391–397.
- [18] Ciftja O., Faruk M.G. Two-dimensional quantum-dot helium in a magnetic field: Variational theory. *Phys. Rev. B*, 2005, **72**, 205334.
- [19] Alia A.A., Elsaid M.K., Shaer A. Magnetic properties of GaAs parabolic quantum dot in the presence of donor impurity under the influence of external tilted electric and magnetic fields. *J. of Taibah University for Science*, 2019, **13**, P. 687–695.
- [20] Ali M., Elsaid M., Shaer A. Magnetization and magnetic susceptibility of GaAs quantum dot with Gaussian confinement in applied magnetic field. *Jordan J. of Physics*, 2019, **12**, P. 247–254.
- [21] Sharma H.K., Boda A., Boyacioglu B., Chatterjee A. Electronic and magnetic properties of a two-electron Gaussian GaAs quantum dot with spin-Zeeman term: A study by numerical diagonalization. *J. of Magnetism Magnetic Materials*, 2019, **469**, P. 171–177.
- [22] Voskoboynikov O., Bauga O., Lee C., Tretyak O. Magnetic properties of parabolic quantum dots in the presence of the spin-orbit interaction. *J. of Applied Physics*, 2003, **94**, P. 5891–5895.
- [23] Hosseinpour P. The role of Rashba spin-orbit interaction and external fields in the thermal properties of a doped quantum dot with Gaussian impurity. *Physica B: Condensed Matter*, 2020, **593**, 412259.
- [24] Madhav A., Chakraborty T. Electronic properties of anisotropic quantum dots in a magnetic field. *Phys. Rev. B*, 1994, **49**, 8163.
- [25] Shaer A., Elsaid M., Elhasan M. The magnetic properties of a quantum dot in a magnetic field. *Turkish J. of Physics*, 2016, **40**, P. 209–218.
- [26] Prabhakar S., Reynolds J.E., Melnik R. Manipulation of the Landé g factor in InAs quantum dots through the application of anisotropic gate potentials: Exact diagonalization, numerical, and perturbation methods. *Phys. Rev. B*, 2011, **84**, 155208.
- [27] Avetisyan S., Pietiläinen P., Chakraborty T. Strong enhancement of Rashba spin-orbit coupling with increasing anisotropy in the Fock-Darwin states of a quantum dot. *Phys. Rev. B*, 2012, **85**, 153301.

Submitted 30 April 2022; revised 7 May 2022; accepted 8 May 2022

Information about the authors:

Ayham Shaer – Physics Department, An- Najah National University, Nablus, Palestine; ORCID 0000-0002-6518-6470; ayham.shaer@najah.edu

Mohammad K. Elsaid – Physics Department, An- Najah National University, Nablus, Palestine; ORCID 0000-0002-1392-3192; mkelsaid@najah.edu

Conflict of interest: the authors declare no conflict of interest.

Assessment of structural changes in proteins and surrounding water molecules in solution according to SAXS and MD data

Alexander V. Smirnov^{1,a}, Andrei M. Semenov^{2,3}, Yuri B. Porozov^{4,5}, Boris A. Fedorov¹

¹ITMO University, Saint Petersburg 197101, Russia

²Alferov University Russian Academy of Sciences, Saint Petersburg 194021, Russia

³Voronezh State University, Voronezh 394018, Russia

⁴Sechenov First Moscow State Medical University, Moscow 119991, Russia

⁵Sirius University of Science and Technology, Sochi 354340, Russia

^asmirnav_2@mail.ru

Corresponding author: A.V. Smirnov, smirnav_2@mail.ru

PACS 61.05.cf, 71.15. Pd, 87.15.B-

ABSTRACT The SASPAR program for calculation of SAXS of proteins in solution uses trajectories of molecular dynamics (MD) and an explicit solvent model. The program allows one to take into account real interactions of solvent molecules both between each other and with the protein molecule. The previously developed SAS-CUBE program (the “cube method”) is also used, it assumes that the protein structures in crystal and in solution coincide, and the water surrounding the proteins is considered as a homogeneous continuum. Using these programs, SAXS curves were calculated for 18 proteins of different molecular weights and then compared with one another and with the corresponding experimental scattering curves. “Vacuum” SAXS curves (i.e., without taking into account the surrounding water) were also calculated for each protein for two approaches: a) based on the coordinates of protein atoms in crystal and b) based on the coordinates of protein atoms for each MD frame with further averaging of the intensities from all the frames. 1) It was shown that for the 14 single-domain proteins considered, the “vacuum” scattering curves calculated by two methods coincide well for almost each protein. Hence, the structure of the studied proteins in a solution is similar to their structure in a crystal and, therefore, the presence of the surrounding water molecules does not alter the protein structure itself significantly. The SASPAR- and SASCUBE-curves coincide well only in two cases (i.e., water is only slightly structured near the protein surface), but in the other cases these curves are markedly different, which indicates the structuredness of the water near the protein surface, although to a different extent. 2) It was shown that for the 4 multi-domain proteins considered, their “vacuum” scattering curves, calculated with the two methods indicated above, differ noticeably, which is an evidence that their crystalline and “water” structures are different. It was also shown that the most of the calculated curves coincide well with the experimental ones.

KEYWORDS small-angle X-ray solution scattering, molecular dynamics, protein structure in solution, water structure.

ACKNOWLEDGEMENTS The authors are grateful to Dr. Alexander Grishaev for providing the experimental SAXS scattering curves of the GB3 protein and to the Master’s student K. S. Mazokha for the assistance with research.

FOR CITATION Smirnov A.V., Semenov A.M., Porozov Yu.B., Fedorov B.A. Assessment of structural changes in proteins and surrounding water molecules in solution according to SAXS and MD data. *Nanosystems: Phys. Chem. Math.*, 2022, **13** (3), 274–284.

1. Introduction

Studies of the proteins structure in a solution is known to be one of the most relevant tasks of molecular biophysics. Among various methods of this research, small-angle X-ray and neutron scattering play an essential role. Numerous works presented over the past fifty years have been dedicated to the development of algorithms that allow one to calculate scattering intensities of proteins in solution based on the information on their structure in crystal. The works of the Luzzati school [1], in which the internal volume of proteins was modelled by closely packed large-sized cubes with a 3Å edge, are considered pioneering in this field. However, in works [2, 3], the edge size was ten times less and the developed “cube method” allowed one to obtain an agreement of calculated curves with quite a few experimental scattering curves of proteins in solutions that was acceptable that time. The poor performance of computers significantly limited the application for this method. Today, the above-mentioned limitations are virtually eliminated. The speed of modern

computers dramatically exceeds the capabilities of the computers from 1970–1980s. Moreover, advances in protein extraction and purification together with the progress in X-ray equipment (primarily, the use of synchrotron radiation) allow one to create a vast database of experimental scattering curves of proteins in solution (SASBDB [4] and BioSis [5] databases). Recently, a new program recreating the “cube method” was presented by [6] The program uses the method which is considerably modified, better justified from the physical point of view and requires essentially less computation time (see [7]).

An important step in the development of this area was made in work [8]. The authors presented the CRY SOL program based on the assumption that there is homogeneous layer of water near the protein surface. The layer electron density differs from the electron density of water in which the protein is immersed. This program uses the method of expansion of exponential functions in spherical harmonics. This is an effective approach for the calculation of spherically symmetric pattern of scattering by free-oriented particles, as it considerably reduces the computation time. It was shown that the CRY SOL program with two adjustment parameters provides a good description of experimental scattering curves for many proteins in solution. This method with a number of different modifications has become widely used in the world ([9–12]).

Until recently, almost all works on improved methods of calculation of scattering intensity of protein in solution were based on the assumption that the structure of the protein in solution is identical to its structure in crystal. Therefore, the chi-square factor was chosen as a quality criterion for the newly developed programmes. It allows one to assess the degree of similarity between the calculated curves based on this assumption and the experimental scattering curves. However, a question arises: to which extent the specified assumption is correct. During the transition of protein into solution, structural changes may occur in the macromolecule itself caused by its interaction with the solvent molecules, as well as changes in the mutual arrangement of molecules of the solvent itself, especially in the areas close to the surface of the protein. These changes can significantly influence on the shape of the scattering curve.

For this reason, works [13–18] can be considered as the next step in the development of calculation methods for the scattering curves of proteins in solutions. Based on the methods of molecular dynamics, these studies consider real interactions between the solvent molecules themselves and with the protein atoms. Using MD allows one to monitor the changes in the protein structure and in the position of the solvent molecules over time, *i.e.*, to obtain a set of coordinates of protein atoms and solvent molecules (frame) at any chosen moment of time. The rigorous formulas presented in works [18] and [13] allow one to calculate the scattering intensity for each frame for specified protein conformation and specified positions of the solvent molecules. These formulas also take into account the free rotation of the whole system in relation with the primary X-ray beam. The last step is averaging the scattering curves over all the chosen frames. Compared with the previously presented methods, the method developed in [18] and later applied in [13] in WAXSIS server is evidently much closer to the realistic description of scattering intensity of proteins in solution.

The present work proposes a new program (SASPAR, see [19]) based on the same principles of joint use of the MD simulations results and strict formulas for the calculation of scattering intensities of proteins in solution. However, the program algorithm, which uses a parallelepiped as the volume containing the protein and the surrounding water molecules, significantly distinguishes the program SASPAR from the WAXSIS algorithm [13]. Another key difference is the method of averaging the scattering intensity in the reciprocal space. Nevertheless, we should note that for a few proteins presented in work [18], the scattering intensities calculated with WAXSIS and SASPAR methods are almost the same.

The further discussion is entirely based on the results of the SASPAR and SASCUBE programs with the use of numerous experimental scattering curves adopted mainly from the SASBDB [4].

Thus, we use the two programs that allow one to calculate the scattering intensity of protein in solution. The first one (SASPAR), based on the MD simulation data, takes into account the mobility of the protein itself and the mobility of the water molecules surrounding the protein. The second program (SASCUBE) considers the protein structure to be fixed, while the water surrounding the protein is regarded as a medium with homogeneous electron density. Further, “vacuum” SAS curves (without taking into account the surrounding water) were calculated for each protein for two approaches: a) based on the coordinates of protein atoms in a crystal from the Protein Data Bank (PDB [20, 21]), and b) based on the coordinates of protein atoms for each MD frame with further averaging of scattering intensities over all the frames.

The main goal of the present work is to answer the following two questions through the comparison of the above-mentioned scattering curves: a) to what extent does the protein structure change during its transition from crystal to solution, and b) to what extent does the structure of water surrounding the protein differ from the homogeneous continuum.

The logic of the presented discussion is as follows. Using the two programmes listed above, the scattering intensities of each protein in solution are calculated, as well as “vacuum” intensity for the crystal structure and “vacuum” intensity averaged over all frames. Then, the comparison of two corresponding “vacuum” curves and two curves obtained with SASPAR and SASCUBE programmes is performed in order to achieve the following conclusions.

1. If the “vacuum” curves are rather similar and the curves obtained with the SASPAR and SASCUBE programs are similar, then a) the protein structures in crystal and in solution are similar and b) the structure of water near the protein surface is close to the homogeneous continuum (protein of type I).

2. If the “vacuum” curves are rather similar while the curves calculated using the SASPAR and SASCUBE programmes are markedly different, then a) the protein structures in crystal and in solution are similar and b) the structure of water near the protein surface is considerably different from the homogeneous continuum (protein of type II).

3. If the “vacuum” curves are markedly different and the curves from the SASPAR and SASCUBE programs also differ substantially, then a) the protein structures in crystal and in solution are essentially different and b) the structure of water near the protein surface can differ from the homogeneous continuum or cannot (protein of type III).

The chi-factor is used for the quantitative assessment of the similarity of both scattering curves and protein structures.

This work considers 18 proteins for which experimental intensities in solution are available in literature. Each protein was analysed as described above. All scattering curves obtained from the SASCUBE and SASPAR programs were also compared with the experimental scattering curves.

2. Calculation methods

2.1. Molecular dynamic simulation

The initial configurations of proteins are from the PDB. The time step of the simulation was 2 fs, the total simulation time was 10 ns, the coordinates were recorded every 10 ps. The simulation was performed at a temperature of 298 K and a pressure of 1 atm. As a solvent, water from the TIP4P model [22] was used. According to [18], this model provides the best balance between speed and accuracy of the calculation. The simulation was performed in an orthorhombic cell of such size that the minimal distance from the protein to the cell boundary is 2.3 nm in all directions. This gap was selected so that the protein stays inside the cell throughout the entire simulation and yet the time of calculation does not grow due to the excessive number of solvent molecules in the cell. The MD simulation for the solvent without protein was carried out in a cubic cell of size 9.0×9.0×9.0 nm. This volume was sufficient to isolate the required volume of pure solvent when calculating the scattering intensities for all proteins. The authors used periodic boundary conditions to correctly describe the aqueous environment of a protein. However, the use of periodic boundary conditions can lead to the interaction of the protein with itself (the “head” of the protein may interact with its “tail”). To eliminate this effect, large enough cells were used.

The simulation was performed using the Desmond program from the software package Schrödinger Biologic Suite 2017-3 [23] and Gromacs 2019-3 software packages [24].

2.1.1. Molecular dynamic simulation in the Desmond program. The simulation was performed in the Desmond program using the OPLS2005 force field [25]. During the simulation, the NPT isobaric-isothermal ensemble was used together with the Nose-Hoover thermostat [26] and the Martyna-Tobias-Klein barostat [27]. Before the simulation, the system relaxation was carried out according to Desmond’s embedded protocol. All settings, except for the simulation time and temperature, were not changed, and the default settings of Desmond were used.

2.1.2. Molecular dynamic simulation in the Gromacs 2019-3 package. In the case of multi-domain proteins with a relatively high molecular weight, the Gromacs 2019-3 package was used, because there are difficulties with large-cell calculations in the Desmond program. In the Gromacs package, molecular dynamics modeling was performed with the AMBER99SB-ILDN force field [28]. The Nose-Hoover thermostat [26] and the Parrinello-Rahman barostat [29] were used to maintain the temperature and pressure. Before the simulation, the relaxation and equilibration of the system was performed in the NVT isochoric-isothermal ensemble as recommended by [30]. Configuration and command files are published at [31] (for proteins) and at [32] (for water solvent).

2.2. Programmes for calculation of scattering intensities of proteins in solutions

2.2.1. SASPAR. The SASPAR program is designed to calculate the scattering intensities of proteins in solutions taking into account the MD simulation data. The protein structure in crystal from the PDB was used as the initial structure. The coordinates of hydrogen atoms were not considered, and their presence was introduced by adding hydrogen electrons to the nearest non-hydrogen atom. The same is true for the water molecule: only the coordinates of oxygen, to which 10 electrons are attributed, were recorded.

2.2.1.1. Geometrical construction of the scattering system. In each frame, the minimum and maximum values of the protein atoms coordinates are selected for each coordinate axis, and the average coordinate, equal to the arithmetic mean of these two values, is determined. A set of three average coordinates is considered the centre of the molecule. A right parallelepiped whose faces are perpendicular to the coordinate axes is circumscribed around the protein molecule. The parallelepiped dimensions are chosen so that the distance from any atom of the protein to the parallelepiped faces is no less than d . This procedure is repeated for all the frames; the sizes of the edges along each coordinate axis are compared, and the maximum edge length is chosen for all the parallelepipeds: A – along x-axis; B – along y-axis; C – along z-axis. The volume of the parallelepiped constructed on the selected edges (ABC parallelepiped) is obviously larger than the volume of the parallelepiped from any frame. Then, the ABC parallelepiped is cut out from each frame so that its centre coincides with the centre of the protein molecule. This parallelepiped, with all the atoms contained in it, is translated until the indicated centre coincides with the coordinate origin.

It is necessary to know the scattering from the protein-free solvent to calculate the intensity of a protein in solution. For this purpose, the MD simulation of the solvent is considered. As before, the ABC parallelepiped is cut out from each frame, and the average electron density (ρ_0) of the solvent is calculated in the volume of each parallelepiped and then averaged over all frames.

The above-mentioned value d is highly important for the determination of the ABC parallelepiped size. It determines the size of the protein border layer, outside of which water no longer influences on the scattering curve of a protein in a solution. In other words, at distance d or farther from the protein surface, the real structure of water can be replaced with a homogeneous continuum with electron density ρ_0 . This value is assessed in [13] as $d \sim 0.7$ nm, which we adhere to in this work.

Thus, two sets of frames are considered as the basis for the calculation of scattering intensity of a protein in solution. Each frame of the first set is represented by the ABC parallelepiped filled with protein and water molecules. Outside the parallelepiped, there is structureless water (homogeneous continuum) with electron density ρ_0 . The centres of the parallelepiped and the protein are located in the coordinate origin. Each frame of the second set is represented by the same ABC parallelepiped that is filled only with water molecules. Its centre is located at the coordinate origin. It is also surrounded by structureless water with the electron density of ρ_0 . (Fig. 1b).

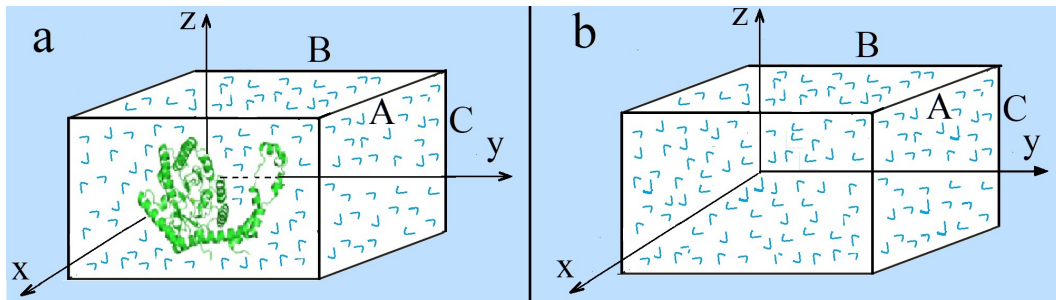


FIG. 1. The ABC parallelepiped cut from the cell with MD simulation: a) for solvent with protein; b) for pure solvent. The solvent outside the parallelepiped is considered a homogeneous medium

2.2.1.2. Calculation of scattering intensity. The scattering intensity $I(\mathbf{q})$ of a protein in a weak solution can be considered as the difference between the scattering intensities of the protein solution and the solvent. In the most general form, based on the model presented above, this intensity $I_{SP}(\mathbf{q})$ can be presented as follows:

$$I_{SP}(q) = \left\langle \left| \sum_k f_k(q) \exp(i\mathbf{r}_k \mathbf{q}) - \rho_0 P_0(\mathbf{q}) \right|^2 \right\rangle_{Fr, \Omega} - \left\langle \left| \sum_l f_l(q) \exp(i\mathbf{r}_l \mathbf{q}) - \rho_0 P_0(\mathbf{q}) \right|^2 \right\rangle_{Fr, \Omega}, \quad (1)$$

where

$$P_0(\mathbf{q}) = 8 \frac{\sin(q_x A/2) \sin(q_y B/2) \sin(q_z C/2)}{q_x q_y q_z}. \quad (2)$$

In this formula, index k numbers all non-hydrogen atoms in the ABC parallelepiped in the current frame of the first set, and l numbers the atoms in the ABC parallelepiped in the current frame of the second set; q_x , q_y , and q_z are the projections of the reciprocal space vector \mathbf{q} on the coordinate axes, $|\mathbf{q}| = q = 4\pi \sin \theta / \lambda$, λ is the X-ray wavelength, 2θ is the scattering angle; $P_0(\mathbf{q})$ is the scattering amplitude from the homogeneous ABC parallelepiped [33], whose centre is at the coordinate origin, with $P_0(0) = 1$. The amplitudes $f_k(q)$ required for the calculation were taken from the periodictable library [34]. If there are only one or several hydrogen atoms and an atomic group is formed (for example, CH_n group), the scattering amplitude of this group is calculated by the following formula

$$f_{\text{CH}_n}(q) = f_C(q) + n f_H(q). \quad (3)$$

Angle brackets $\langle \dots \rangle_{Fr, \Omega}$ in formula (1) indicate two types of averaging of scattering intensity: $\langle \dots \rangle_{Fr}$ is over all frames and $\langle \dots \rangle_{\Omega}$ is over all possible orientations of the parallelepiped with respect to the scattering vector direction. Fedorov et al [6] give a detailed description of the latter algorithm of averaging.

The first term in formula (1) is the scattering intensity of a protein in solution, and the second component is the scattering intensity of a pure solvent. In accordance with Babinet's principle, the term $\rho_0 P_0(\mathbf{q})$ in this formula describes the contribution to the scattering amplitude of the homogeneous solvent with density ρ_0 . This homogeneous solvent fills the entire space except for the volume of the ABC parallelepiped. The ρ_0 parameter is calculated in the following way. For each frame in pure solvent, an ABC parallelepiped is cut out; the electron density is calculated inside it and then averaged over all frames.

The scattering intensity for every single frame has the same weight, but then the number of frames used is $N = 300 - 1000$ both for the protein with solvent and for the solvent itself. The frames are selected with the same step along the timeline. These factors enable to take into account different protein conformations with their real weight.

Formula (1) is another representation of the formula for the scattering intensity proposed in [18] and it is more transparent from the physical point of view.

The computation time essentially depends on the computer capacity. It is possible to speed up the calculations by several orders when using multi-core computers and graphics cards. In our case, SASPAR calculations were performed using one graphics card, 1280 graphics processors and a 4-core computer. The time required to calculate the scattering intensity for one frame is ~ 0.5 s, and this time is virtually independent on the protein size.

After downloading the SASPAR (and SASCUBE) programs to a PC, they can be used “standalone”, i.e. without the Internet. Moreover, SASPAR has an open source code, which can be studied and modified. The “standalone” use of the SASPAR program is its advantage; without access to online services, calculations based on, for example, WAXSIS and AXIS programs are not possible.

One disadvantage of standalone programs (including SASPAR) is that higher computer performance is required. Another probable disadvantage of the SASPAR program is the necessity of using the NVIDIA graphics card that is supported by PyCUDA library.

2.2.2. SASCUBE program. The program is intended for the calculation of scattering intensities of proteins in a structureless solvent, with coordinates of protein atoms from the PDB data. In [6], the algorithm of this program is described in details.

Briefly, the principle of the program operation is as follows. A parallelepiped is circumscribed around the protein molecule with the known coordinates of atoms and is divided into closely packed small cubes (with an edge length of 0.03 nm), and from the coordinates of each cube, it is determined whether it is within the protein molecule or outside of it. Thus, the system of cubes can describe the volume and the form of the protein molecule with high accuracy. The formula for calculation of the scattering intensity $I_{sc}(q)$ by such a system is comparatively simple (it is similar to the first term of formula (1) in the present work) and only requires the knowledge of the effective radii of the atoms of the protein and water molecules. However, it was shown in the work [6] that the variation of these radii within reasonable limits [35, 36] leads to small change of the scattering curve only.

We repeat the remark that the SASCUBE program (as opposed to the SASPAR program) calculates the scattering intensity of a protein that always keeps the crystal structure listed in the PDB. The protein is immersed in a structureless solvent. It means that no specific features of the water structure near the protein surface are taken into account.

2.3. Calculation of “vacuum” scattering intensities and radii of gyration of proteins

For further analysis of the structure of proteins in solvent and their scattering curves, we also need to know their “vacuum” curves $I_{vac}(q)$ and “vacuum” radii of gyration R_g . The corresponding calculations can be performed using the known formulas [37, 38]:

$$I_{vac}(q) = \sum_{i,j=1}^N f_i(q)f_j(q) \frac{\sin(qr_{ij})}{qr_{ij}}, \quad (4)$$

and

$$R_g = \sqrt{\frac{\sum_{i,j=1}^N f_i(0)f_j(0)r_{ij}^2}{2 \sum_{i,j=1}^N f_i(0)f_j(0)}}. \quad (5)$$

Here, r_{ij} is the distance between atoms i and j , while $f_i(q)$ is the scattering amplitude (described above) for the i -th atom of protein, and N is the number of non-hydrogen atoms in the protein.

To calculate “vacuum” scattering intensity $I_{vac}^{crys}(q)$ for the protein crystal structure, formula (4) is used once, but to obtain intensity $I_{vac}^{MD}(q)$ based on the MD data, it is necessary to perform the calculation by this formula for each frame, average the received scattering intensities over all frames, and then calculate the dispersion for each value of q .

The same procedure is used to obtain the values of the radius of gyration: $R_{g,vac}^{crys}$ is calculated by formula (5) once, and $R_{g,vac}^{MD}$ is calculated for each frame and then averaged over all frames.

3. Quantitative assessment of the similarity of scattering curves

For each protein, the calculated curves $I_{SP}(q)$ and $I_{SC}(q)$ were compared using the following formula from [18]

$$\chi_{\log}^{water} = \sqrt{N^{-1} \sum_{i=1}^N [\log I_{SP}(q_i) - \log(f \times I_{SC}(q_i) + c)]^2}, \quad (6)$$

where N is the number of the selected values of q , \log is the decimal logarithm, and f and c are adjustment parameters ensuring the best coincidence of the two curves. In formula (6) and subsequent formulas (7)–(9), parameters f and c are determined by minimizing the value of the corresponding χ . It should be noted that f is not an adjustment parameter in the accepted sense. It only ensures the best coincidence of the curves without distorting them.

A similar formula is used to compare “vacuum” curves $I_{vac}^{crys}(q)$ and $I_{vac}^{MD}(q)$:

$$\chi_{log}^{vac} = \sqrt{N^{-1} \sum_{i=1}^N [\log I_{vac}^{MD}(q_i) - \log(f \times I_{vac}^{crys}(q_i) + c)]^2} \quad (7)$$

In formulas (6) and (7), a logarithmic scale allows one to more effectively take into account the contribution to χ_{log}^{water} and χ_{log}^{vaA} of the medium-angle part of the curve, where the scattering intensity can take value of several orders lower than the intensity in the small-angle part.

The term “medium-angle part of the curve” denotes the region of the curve starting immediately after the relatively abrupt (depending on the protein size) fall of the curve that continues up to $q \sim 10 \text{ nm}^{-1}$; moreover, at larger q , the curve is not very specific to the protein structure [39].

According to the goals of the present work, the medium-angle part of the curve is the most interesting one for the comparison of two scattering curves, as the shape of the scattering curve in the medium-angle part, in accordance with the Bragg formula, is mainly determined by the nature of electron density distribution over relatively short distances. It is these distances that define the internal structure and its change in the protein molecule and in the surrounding water to a large extent.

The scattering intensities obtained from the SASPAR and SASCUBE programmes were compared with the corresponding experimental intensities using the following formulas

$$\chi_{SP} = \sqrt{N^{-1} \sum_{i=1}^N \left(\frac{I_{exp}(q_i) - (f \times I_{SP}(q_i) + c)}{\sigma_{exp}(q_i)} \right)^2} \quad (8)$$

and, respectively,

$$\chi_{SC} = \sqrt{N^{-1} \sum_{i=1}^N \left(\frac{I_{exp}(q_i) - (f \times I_{SC}(q_i) + c)}{\sigma_{exp}(q_i)} \right)^2}, \quad (9)$$

where $\sigma_{exp}(q_i)$ are standard deviations, while f and c , the same as above, are the parameters that provide the best coincidence of the scattering curves.

The similarity of the radii of gyration $R_{g,vac}^{crys}$ and $R_{g,vac}^{MD}$ can be assessed using the following formula

$$\delta R_g = \frac{R_{g,vac}^{MD} - R_{g,vac}^{crys}}{R_{g,vac}^{crys}}, \quad (10)$$

4. Analysis of scattering curves of proteins. Comparison with the experimental curves

The following proteins were considered: the third IGG-binding domain (“GB3”, 1IGD); ubiquitin (1UBQ); cytochrome C (1CRC); neurotrypsin Scavenger receptor cysteine-rich domain 3 (“mmNT-SRCR3”, 6H8M); lysozyme (193L, 6LYZ); ribonuclease pancreatic (1C0B); myoglobin (1WLA); EAL/GGDEF domain (3ICL); truncated alpha-DsbN (6EEZ); carbonic anhydrase (5A25); sensory box/GGDEF domain (3LYX); filamin A Ig-like domains 3–5 P637Q mutant (“FLNa3-5 P637Q”, 6EWL); bovine serum albumin (“BSA”, 4F5S monomer, 4F5S dimer); alcohol dehydrogenase (5ENV, tetramer); glucose isomerase (1OAD, tetramer); apoferritin (1IER, 24-mer). Representative curves for four of these proteins are shown in Fig. 2. Curves for all proteins are presented in supplementary materials.

Five scattering curves are presented for each of the studied proteins in a separate graph: experimental curve $I_{exp}(q)$; SASPAR program curve $I_{SP}(q)$; SASCUBE program curve $I_{SC}(q)$; “vacuum” curve $I_{vac}^{MD}(q)$, calculated with MD and averaged over all frames; and “vacuum” curve $I_{vac}^{crys}(q)$, calculated based on a crystalline structure.

Vertical lines in each graph show the borders within which the corresponding scattering curves were matched with each other. There were certain difficulties with the choice of the left border, so it was selected individually for each protein. As we know, the shape of the experimental curve in the region of the smallest scattering angles can be distorted by interference effects [40] and, probably, by residual impurities of oligomers, while the $I_{SP}(q)$ intensity, apparently, provides the best description of the curve across the entire range of scattering angles for a *single* molecule of protein. Therefore, the q value to the left of which a systematic divergence between the experimental curve and the calculated curve $I_{SP}(q)$ is observed can be considered as the criterion for the choice of the left border.

As for the choice of the right border, generally, it either coincided with the maximum values of scattering angles on the experimental curve or was limited by $q = 15 \text{ nm}^{-1}$, although the experimental curve could be continued further. As mentioned above, for globular proteins, the region of scattering angles with $q > 15 \text{ nm}^{-1}$ (and even with $q > 10 \text{ nm}^{-1}$) is weakly specific to the internal structure of the protein and is defined only by the fact that the polypeptide chains are sufficiently closely packed. In [40], it was shown that the maximum itself at $q \sim 14 \text{ nm}^{-1}$ depends only on the average van der Waals distance between the neighbouring closely packed atoms of protein and disappears during its denaturation.

The values of the above-described parameters for proteins with various molecular weights W are presented in the Table 1. The following information is presented in the table: the protein codes from the PDB (column 1), references to the

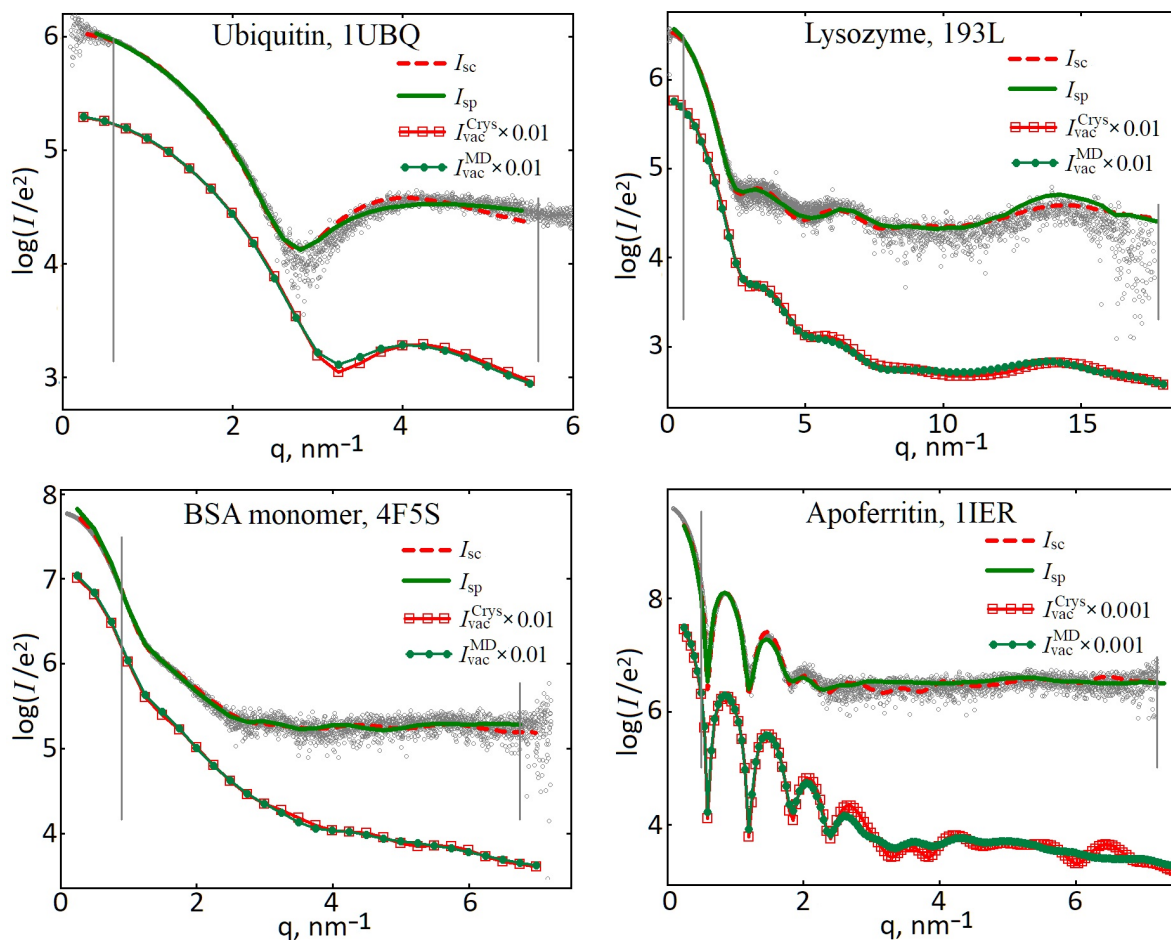


FIG. 2. Experimental and calculated scattering curves for 4 from 18 considered proteins. Experimental curves: $I_{exp}(q)$ (circles); calculated curves: $I_{SP}(q)$ are the SASPAR curves; $I_{SC}(q)$ are the SASCUBE curves; $I_{vac}^{MD}(q)$ are the “vacuum curves” averaged for all MD simulation frames; $I_{vac}^{Crys}(q)$ are the “vacuum curves” for proteins in crystalline form. Hereinafter, the experimental curves were shifted in a logarithmic scale, using a scale factor, to align them with the calculated curves. For each protein, its name and its PDB code are given. The vertical lines mark the boundaries of the region where the calculated and experimental curves are compared

records in SASBDB and references to the SAS experiment (column 2), and the molecular weights of the proteins (column 3). The numerical evaluations of similarity listed in the other columns and their analysis are given in the text of the article.

First, let us consider column 7 listing values χ_{log}^{vaA} (formula 7) that determine the similarity of the “vacuum” scattering curves calculated both from the MD data and for the crystal forms of proteins. If we introduce the criterion of similarity of the curves: $\chi_{log}^{vac} \leq 3\%$, then these curves can be considered “sufficiently similar” for all the 14 single-domain proteins indicated in the first 14 lines of the table. Qualitatively, the similarity of these curves is clearly visible on the respective graphs. Therefore, the first important conclusion is that all the considered single-domain proteins only slightly change their structure during the transition from crystal to solution. At the same time, for the 4 considered multi-domain proteins the following inequality holds: $\chi_{log}^{vac} > 3\%$, which is an evidence that their structure changes to a greater or lesser degree. It should also be noted that all these 18 proteins do not exhibit significant changes in their sizes (column 10), judging by the comparison of the gyration radii of crystal structures (column 9) and the averaged structures according to MD data (column 8). The Lysozyme C protein was considered for two modifications of its structure presented in the PDB (193L and 6LYZ), and each modification has its own line.

Let us now study column 6 presenting the χ_{log}^{water} values that determine the similarity of the scattering curves calculated by the SASPAR and SASCUBE programs (“water” curves). It is evident that the similarity of these curves is a rarer event. If the same criterion of “sufficient similarity” is still to be used ($\chi_{log}^{vac} \leq 3\%$), only two of the studied proteins meets this criterion: 3ICL and 4F5S. Only these proteins can be categorised as type I, i.e., we can assume that if there is the similarity of its structure in crystal and in solution, then the structure of water in the layer adjacent to the protein is only slightly distorted as compared to the homogeneous continuum. As for the other proteins with a “sufficient similarity” of the “vacuum” curves, they show a considerable increase in value χ_{log}^{water} . This indicates that for these proteins,

TABLE 1. The numerical evaluation of the similarity both for “water” and “vacuum” SAXS curves of the studied proteins

protein	ref	W kDa	χ_{SP}	χ_{SC}	χ_{log}^{water} %	χ_{log}^{vac} %	$R_{g,vac}^{MD}$ nm	$R_{g,vac}^{crys}(q)$ nm	δR_g %	Type of protein
1	2	3	4	5	6	7	8	9	10	11
IIGD	(private message) Grishaev <i>et al.</i> (2010)	6.2	2.395	2.875	5.9	2.1	1.076	1.056	1.9	II
1UBQ	SASDAQ2, St. Prot. ¹	9	1.198	1.685	4.4	2.5	1.165	1.173	-0.7	II
1CRC	SASDAB2, St. Prot. ²	12.5	1.092	1.577	9.8	2.2	1.299	1.296	0.2	II
6H8M	SASDES5, [41]	13	1.811	2.228	4.2	2.8	1.304	1.295	0.7	II
193L	SASDAG2, St. Prot. ¹	14	0.942	0.726	4.6	2.6	1.422	1.385	2.7	II
6LYZ	SASDAG2, St. Prot. ¹	14	0.951	0.884	4.6	1.7	1.411	1.398	0.9	II
1C0B	SASDAN2 St. Prot. ¹	16	2.138	1.178	6.1	2.5	1.497	1.455	2.9	II
1WLA	SASDAK2, St. Prot. ¹	17	2.480	1.993	8.2	1.9	1.550	1.532	1.2	II
3ICL	SASDCG6, [42]	19	2.120	2.348	1.2	1.0	1.575	1.526	3.2	I
6EEZ	SASDC38, [43]	21	2.638	2.454	5.6	2.1	1.632	1.616	1.0	II
5A25	SASDFP8, [44]	29	2.097	3.017	6.8	2.7	1.771	1.741	1.7	II
3LYX	SASDCE6, [42]	30	3.100	2.512	4.3	0.9	1.911	1.884	1.4	II
6EWL	SASDEP7, [45]	31	1.440	1.550	5.0	1.5	2.117	2.086	1.5	II
4F5S	SASDFQ8, St. Prot. ³	66	1.099	1.156	3.0	2.3	2.707	2.674	1.2	I
4F5S dimer	SASDFR8, [44]	133	1.625	1.915	3.5	3.5	3.940	3.851	2.3	III
5ENV	SASDFS8, [44]	147	1.707	2.335	8.0	3.5	3.351	3.331	0.6	III
1OAD	SASDCK2, [46]	174	2.531	1.874	6.0	4.3	3.200	3.174	0.8	III
1IER	SASDFN8, [44]	479	5.360	3.726	12.8	9.4	5.300	5.264	0.7	III.

¹Standard proteins Darja Ruskule²Standard proteins Cy M Jeffries³Standard proteins Melissa Graewert, Cy M Jeffries

the differences between the “water” curves are mainly conditioned by the changes (to a greater or lesser degree) in the structure of water in the area adjacent to the protein, as compared to the homogeneous continuum. These 12 proteins are categorised as type II.

Finally, a considerable discrepancy is observed between the “vacuum” curves as well as between the “water” curves for all the studied multi-domain proteins. Thus, the structures of these proteins in solution are different from their structures in crystal and, probably, the water near their surfaces is structured (proteins of type III). The interdomain mobility is a possible reason leading to the difference in their structures in solution and in crystal, while the overall dimensions remain the same.

Column 11 shows the type of the protein according to the classification suggested in the Introduction.

Now let us compare the curves from the SASPAR and SASCUBE programs with the experimental scattering curves. Using formulas (8) and (9) and taking into account the errors specified in the experimental works, chi-factors were calculated for both programs: column 4 (SASPAR) and column 5 (SASCUBE). As one can see, for most of the 18 studied proteins, the obtained chi-factors are indicative of a sufficient similarity between the experimental and the calculated scattering curves. It is also visible in the graphs.

Noteworthy, we did not intend to develop a method that would allow making the calculated curves as close as possible to the experiment. As the table and graphs show, a significant difference between the SASPAR and experimental scattering curves is observed for at least two proteins (1IER and 3LYX). On the one hand, this can be explained by an imperfect theory. Indeed, the use of different packages for the MD simulation (see Fig. 2s in Supplementary) and the use of different water models [18] within the SASPAR programme can result in different scattering curves of proteins if q values are large enough.

On the other hand, the comparison of the calculated scattering curves with the experimental ones has certain difficulties. As it was noted in the review by Hub [47], “the quality of SWAXS data has greatly benefited from better light sources, single-photon counting detectors, and from set-ups coupled to size-exclusion chromatography which have led to reduced statistical noise”. Further, “Common sources for systematic errors in SWAXS are aggregation, inter-particle repulsion, and poor buffer-matching”, as well as vibrations of atoms. Therefore, according to Hub, “the overall uncertainty of the data is by now often dominated by systematic errors”. Nevertheless, as it was mentioned in recent work [48] “noise has the greatest impacts on low signal in the high- q region”.

It can only be assumed that the significant differences between the experimental and calculated curves for some proteins are related either to the factors specified in [47] and [48] or to the errors of subtraction of the buffer scattering from the solution scattering curve at relatively wide angles, at which the solution and buffer scattering intensities are rather similar.

We compared the scattering intensities calculated using the SASPAR program and another program (WAXSIS) with a similar algorithm. We also compared the intensities calculated with the SASPAR program based on the MD simulations performed both with the MD Gromacs 2019-3 software package and the Desmond MD program. Comparison results are presented in supplementary materials. In both cases, there are small discrepancies in the wide-angle range that are within the limits of an experimental error.

5. Conclusion

The main conclusion from the present analysis is that most of the studied one-domain proteins only slightly change their structure during the transition from crystal to solution using the experimental conditions as described for the SAXS experiments. This statement is also confirmed by the similarity of their radii of gyration. However, this does not mean that for some frames, the protein structure in solution cannot significantly differ from its structure in crystal; it is stated only that the average protein structure in a solution is similar to the crystal one. Although this statement follows from the study of the protein structures not in the real space but in the reciprocal one, this conclusion seems quite reasonable, considering the unambiguous relation between these spaces in terms of the Fourier transform. Certainly, this is not the first time the problem of the protein structures’ similarity in crystal and in solution is discussed. There is an extensive literature confirming the indicated similarity of structures using NMR [48–50]. However, our work provides *quantitative evidence* of this statement during the analysis of the considered single-domain proteins based on the combination of two methods: MD and SAXS.

As for the considered multi-domain proteins, their crystalline and “water” structures might differ significantly. A possible reason for this difference is the relative movement of domains. This issue requires additional research, which can be done within the framework of the approach described in this article.

The second important conclusion is that the structure of water in the layer adjacent to the protein surface is usually significantly different from its structure far from the surface. Based on the almost full coincidence of the SASPAR and SASCUBE curves, only one (3icl) of the studied proteins does not have this layer, and all the water surrounding this protein can be considered a homogeneous continuum. However, this protein can be considered an exception. This layer definitely exists for the other proteins, and it is apparently associated with the interaction between the water molecules and the surface atoms of a protein. The electron density within this layer is non-homogeneous, which can significantly influence on the profile of the SASPAR curves. The conclusion about the presence of a hydration layer near a protein

surface is also not new, and many authors introduce this effect into the intensity calculations in some way or another (see, e.g., [8, 52–55]). Our contribution is that we directly confirm the existence of this hydrated layer using the fact that the SASPAR and SASCUBE scattering curves clearly *diverge* from one another.

As for the comparison of the calculated scattering curves with the experimental data, the table and graphs show that for most proteins, especially for their SASPAR curves, there is good agreement with the experiment in the “middle” q -area, which is the most sensitive to intraprotein rearrangements and rearrangements of the water molecules structure near the protein surface. At the same time, for some of the proteins, while there is a sufficiently good qualitative coincidence of their scattering curves, their quantitative coincidence based on the selected criteria is not good enough. The possible reasons for this difference were discussed in the work.

References

- [1] Ninio J., Luzzati V., Yaniv M. Comparative Small-Angle X-Ray Scattering Studies on Unacylated, Acylated and Cross-Linked Escherichia Coli Transfer RNAIVal. *Journal of Molecular Biology*, 1972, **71**(2), P. 217–229.
- [2] Fedorov B.A., Denesyuk A.I. Large-Angle X-Ray Diffuse Scattering, a New Method for Investigating Changes in the Conformation of Globular Proteins in Solutions. *J. Appl. Cryst.*, 1978, **11**(5), P. 473–477.
- [3] Pavlov M.Yu., Fedorov B.A. Improved Technique for Calculating X-Ray Scattering Intensity of Biopolymers in Solution: Evaluation of the Form, Volume, and Surface of a Particle. *Biopolymers*, 1983, **22**(6), P. 1507–1522.
- [4] Valentini E., Kikhney A.G., Previtali G., Jeffries C.M., Svergun D.I. SASBDB, a Repository for Biological Small-Angle Scattering Data. *Nucleic Acids Res.*, 2015, **43**(D1), P. D357–D363.
- [5] Hura G.L., Menon A.L., Hammel M., Rambo R.P., Poole II F.L., Tsutakawa S.E., Jenney Jr F.E., Classen S., Frankel K.A., Hopkins R.C., Yang S., Scott J.W., Dillard B.D., Adams M.W.W., Tainer J.A. Robust, High-Throughput Solution Structural Analyses by Small Angle X-Ray Scattering (SAXS). *Nat Methods*, 2009, **6**(8), P. 606–612.
- [6] Fedorov B.A., Smirnov A.V., Yaroshenko V.V., Porozov Yu.B. SASCUBE: An Updated Method of Cubes for Calculation of the Intensity of X-Ray Scattering by Biopolymers in Solution. *BIOPHYSICS*, 2019, **64**(1), P. 38–48.
- [7] <https://sourceforge.net/projects/sascube>
- [8] Svergun D., Barberato C., Koch M.H.J. CRY SOL – a Program to Evaluate X-Ray Scattering of Biological Macromolecules from Atomic Coordinates. *J. Appl. Cryst.*, 1995, **28**(6), P. 768–773.
- [9] Bardhan J., Park S., Makowski L. SoftWAXS: A Computational Tool for Modeling Wide-Angle X-Ray Solution Scattering from Biomolecules. *Journal of applied crystallography*, 2009, **42**, P. 932–943.
- [10] Liu H., Hexemer A., Zwart P.H. The Small Angle Scattering ToolBox (SASTBX): An Open-Source Software for Biomolecular Small-Angle Scattering. *J. Appl. Cryst.*, 2012, **45**(4), P. 587–593.
- [11] Svergun D.I., Richard S., Koch M.H.J., Sayers Z., Kuprin S., Zaccai G. Protein Hydration in Solution: Experimental Observation by x-Ray and Neutron Scattering. *PNAS*, 1998, **95**(5), P. 2267–2272.
- [12] Schneidman-Duhovny D., Hammel M., Tainer J.A., Sali A. FoXS, FoXSDock and MultiFoXS: Single-State and Multi-State Structural Modeling of Proteins and Their Complexes Based on SAXS Profiles. *Nucleic Acids Research*, 2016, **44**(W1), P. W424–W429.
- [13] Park S., Bardhan J.P., Roux B., Makowski L. Simulated X-Ray Scattering of Protein Solutions Using Explicit-Solvent Models. *J. Chem. Phys.*, 2009, **130**(13), 134114.
- [14] Oroguchi T., Ikeguchi M. MD–SAXS Method with Nonspherical Boundaries. *Chemical Physics Letters*, 2012, **541**, P. 117–121.
- [15] Köfinger J., Hummer G. Atomic-Resolution Structural Information from Scattering Experiments on Macromolecules in Solution. *Phys. Rev. E*, 2013, **87**(5), 052712.
- [16] Knight C.J., Hub J.S. WAXSiS: A Web Server for the Calculation of SAXS/WAXS Curves Based on Explicit-Solvent Molecular Dynamics. *Nucleic Acids Research*, 2015, **43**(W1), P. W225–W230.
- [17] Grishaev A., Guo L., Irving T., Bax A. Improved Fitting of Solution X-Ray Scattering Data to Macromolecular Structures and Structural Ensembles by Explicit Water Modeling. *J. Am. Chem. Soc.*, 2010, **132**(44), P. 15484–15486.
- [18] Chen P., Hub J.S. Validating Solution Ensembles from Molecular Dynamics Simulation by Wide-Angle X-Ray Scattering Data. *Biophysical Journal*, 2014, **107**(2), P. 435–447.
- [19] <https://github.com/andy-biochem/saspar2>
- [20] Berman H., Battistuz T., Bhat T., Bluhm W., Bourne P., Burkhardt K., Feng Z., Gilliland G., Iype L., Jain S., Fagan P., Marvin J., Padilla D., Ravichandran V., Schneider B., Thanki N., Weissig H., Westbrook J., Zardecki, C. The Protein Data Bank. *Acta crystallographica. Section D, Biological crystallography*, 2002, **58**, P. 899–907.
- [21] Berman H.M., Westbrook J., Feng Z., Gilliland G., Bhat T. N., Weissig H., Shindyalov I.N., Bourne P.E. The Protein Data Bank. *Nucleic Acids Research*, 2000, **28**(1), P. 235–242.
- [22] Jorgensen W.L., Chandrasekhar J., Madura J.D., Impey R.W., Klein M.L. Comparison of Simple Potential Functions for Simulating Liquid Water. *J. Chem. Phys.*, 1983, **79**(2), P. 926–935.
- [23] Bowers K.J., Chow E., Xu H., Dror R.O., Eastwood M.P., Gregersen B.A., Klepeis J.L., Kolossvary I., Moraes M.A., Sacerdoti F.D., Salmon J.K., Shan Y., Shaw D.E. Scalable Algorithms for Molecular Dynamics Simulations on Commodity Clusters. In *In SC '06: Proceedings of the 2006 ACM/IEEE Conference on Supercomputing*, ACM Press, 2006.
- [24] Abraham M.J., Murtola T., Schulz R., Páll S., Smith J.C., Hess B., Lindahl E. GROMACS: High Performance Molecular Simulations through Multi-Level Parallelism from Laptops to Supercomputers. *SoftwareX*, 2015, **1–2**, P. 19–25.
- [25] Banks J.L., Beard H.S., Cao Y., Cho A.E., Damm W., Farid R., Felts A.K., Halgren T.A., Mainz D.T., Maple J.R., Murphy R., Philipp D.M., Repasky M.P., Zhang L.Y., Berne B.J., Friesner R.A., Gallicchio E., Levy R.M. Integrated Modeling Program, Applied Chemical Theory (IMPACT). *Journal of Computational Chemistry*, 2005, **26**(16), P. 1752–1780.
- [26] Hoover W.G. Canonical Dynamics: Equilibrium Phase-Space Distributions. *Phys. Rev. A*, 1985, **31**(3), P. 1695–1697.
- [27] Martyna G.J., Tobias D.J., Klein M.L. Constant Pressure Molecular Dynamics Algorithms. *J. Chem. Phys.*, 1994, **101**(5), P. 4177–4189.
- [28] Lindorff-Larsen K., Piana S., Palmo K., Maragakis P., Klepeis J.L., Dror R.O., Shaw D.E. Improved Side-Chain Torsion Potentials for the Amber Ff99SB Protein Force Field. *Proteins: Structure, Function, and Bioinformatics*, 2010, **78**(8), P. 1950–1958.
- [29] Parrinello M., Rahman A. Polymorphic Transitions in Single Crystals: A New Molecular Dynamics Method. *Journal of Applied Physics*, 1981, **52**(12), P. 7182–7190.

- [30] Gureev M.A., Kadochnikov V.V. Porozov Yu.B. *Molekulyarnyi doking i ego verifikatsiya v kontekste virtual'nogo skringinga* [Molecular docking and its verification in the context of virtual screening]. St. Petersburg: ITMO University, 2018 (In Russ.)
- [31] https://github.com/andy-biochem/saspar2/tree/master/gmx_prot
- [32] https://github.com/andy-biochem/saspar2/tree/master/gmx_water
- [33] Vainshtein B.K., Vainshtein B.K. *Diffraction of X-Rays by Chain Molecules*. Elsevier, 1966.
- [34] P.A. Kienzle Periodictable V1.5.0. Zenodo. <https://doi.org/10.5281/zenodo.840347>
- [35] Lee B., Richards F.M. The Interpretation of Protein Structures: Estimation of Static Accessibility. *J. Mol. Biol.*, 1971, **55**(3), P. 379–400.
- [36] Bondi A.A. *Physical Properties of Molecular Crystals, Liquids, and Glasses*. Wiley, 1968.
- [37] Debye P. Zerstreuung von Röntgenstrahlen. *Annalen der Physik*, 1915, **351**(6), P. 809–823.
- [38] Guinier A. La diffraction des rayons X aux très petits angles: application à l'étude de phénomènes ultramicroscopiques. *Ann. Phys.*, 1939, **11**(12), P. 161–237.
- [39] Fedorov B.A., Ptitsyn O.B., Voronin L.A. X-Ray Diffuse Scattering of Globular Protein Solutions: Consideration of the Solvent Influence. *FEBS Lett*, 1972, **28**(2), P. 188–190.
- [40] Guinier A., Fournet G., Yudowitch K.L. *Small-Angle Scattering of X-Rays*, 1955.
- [41] Canciani A., Catucci G., Forneris F. Structural Characterization of the Third Scavenger Receptor Cysteine-Rich Domain of Murine Neurotrophin. *Protein Science*, 2019, **28**(4), P. 746–755.
- [42] Grant T.D., Luft J.R., Wolfley J.R., Tsuruta H., Martel A., Montelione G.T., Snell E.H. Small Angle X-Ray Scattering as a Complementary Tool for High-Throughput Structural Studies. *Biopolymers*, 2011, **95**(8), P. 517–530.
- [43] Walden P.M., Whitten A.E., Premkumar L., Halili M.A., Heras B., King G.J., Martin J.L. The Atypical Thiol–Disulfide Exchange Protein α -DsbA2 from *Wolbachia Pipientis* Is a Homotrimeric Disulfide Isomerase. *Acta Cryst. D*, 2019, **75**(3), P. 283–295.
- [44] Graewert M.A., Da Vela S., Gräwert T.W., Molodenskiy D.S., Blanchet C.E., Svergun D.I., Jeffries C.M. Adding Size Exclusion Chromatography (SEC) and Light Scattering (LS) Devices to Obtain High-Quality Small Angle X-Ray Scattering (SAXS) Data. *Crystals*, 2020, **10**(11), P. 975.
- [45] Haataja T.J.K., Bernardi R.C., Lecointe S., Capoulade R., Merot J., Pentikäinen U. Non-Syndromic Mitral Valve Dysplasia Mutation Changes the Force Resilience and Interaction of Human Filamin A. *Structure*, 2019, **27**(1), P. 102–112.e4
- [46] Trehwella J., Duff A.P., Durand D., Gabel F., Guss J.M., Hendrickson W.A., Hura G.L., Jacques D.A., Kirby N.M., Kwan A.H., Pérez J., Pollack L., Ryan T.M., Sali A., Schneidman-Duhovny, D., Schwede T., Svergun D.I., Sugiyama M., Tainer J.A., Vachette P., Westbrook J., Whitten A.E. Publication Guidelines for Structural Modelling of Small-Angle Scattering Data from Biomolecules in Solution: An Update. *Acta Cryst D*, 2017, **73**(9), P. 710–728.
- [47] Hub J.S. Interpreting Solution X-Ray Scattering Data Using Molecular Simulations. *Current Opinion in Structural Biology*, 2018, **49**, P. 18–26.
- [48] Brosey C.A., Tainer J.A. Evolving SAXS Versatility: Solution X-Ray Scattering for Macromolecular Architecture, Functional Landscapes, and Integrative Structural Biology. *Curr Opin Struct Biol*, 2019, **58**, P. 197–213.
- [49] Sikic K., Tomic S., Carugo O. Systematic Comparison of Crystal and NMR Protein Structures Deposited in the Protein Data Bank. *Open Biochem J*, 2010, **4**, P. 83–95.
- [50] Everett J.K., Tejero R., Murthy S.B.K., Acton T.B., Aramini J.M., Baran M.C., Benach J., Cort J.R., Eletsky A., Forouhar F., Guan R., Kuzin A.P., Lee H.W., Liu G., Mani R., Mao B., Mills J.L., Montelione A.F., Pederson K., Powers R., Ramelot T., Rossi P., Seetharaman J., Snyder D., Swapna G.V.T., Vorobiev S.M., Wu Y., Xiao R., Yang Y., Arrowsmith C.H., Hunt J.F., Kennedy M.A., Prestegard J.H., Szyperski T., Tong L., Montelione G.T. A Community Resource of Experimental Data for NMR / X-Ray Crystal Structure Pairs. *Protein Science*, 2016, **25**(1), P. 30–45.
- [51] Leman J.K., D'Avino A.R., Bhatnagar Y., Gray J.J. Comparison of NMR and Crystal Structures of Membrane Proteins and Computational Refinement to Improve Model Quality. *Proteins*, 2018, **86**(1), P. 57–74.
- [52] Tjioe E., Heller W.T. ORNL_SAS: Software for Calculation of Small-Angle Scattering Intensities of Proteins and Protein Complexes. *J. Appl. Cryst.*, 2007, **40**(4), P. 782–785.
- [53] Poitevin F., Orland H., Doniach S., Koehl P., Delarue M. AquaSAXS: A Web Server for Computation and Fitting of SAXS Profiles with Non-Uniformly Hydrated Atomic Models. *Nucleic Acids Research*, 2011, **39**(suppl.2), P. W184–W189.
- [54] Schneidman-Duhovny D., Hammel M., Tainer J.A., Sali A. Accurate SAXS Profile Computation and Its Assessment by Contrast Variation Experiments. *Biophysical Journal*, 2013, **105**(4), P. 962–974.
- [55] Virtanen J.J., Makowski L., Sosnick T.R., Freed K.F. Modeling the Hydration Layer around Proteins: Application to Small- and Wide-Angle X-Ray Scattering. *Biophysical Journal*, 2011, **101**(8), P. 2061–2069.

Submitted 12 April 2022; accepted 14 April 2022

Information about the authors:

Alexander V. Smirnov – ITMO University, Kronverksky Pr. 49, bldg. A, Saint Petersburg 197101, Russian Federation; smirnav_2@mail.ru

Andrei M. Semenov – Alferov University Russian Academy of Sciences, Chlopina ul., 8, Saint Petersburg 194021, Russian Federation; Voronezh State University, Universitetskaya pl. 1, Voronezh 394018, Russian Federation; andy_semenov@mail.ru

Yuri B. Porozov – Sechenov First Moscow State Medical University, Trubetskaya ul. 8, Moscow 119991, Russian Federation; Sirius University of Science and Technology, Olympic ave. 1, Sochi 354340, Russian Federation; yuri.porozov@gmail.com

Boris A. Fedorov – ITMO University, Kronverksky Pr. 49, bldg. A, Saint Petersburg 197101, Russian Federation; borfedorov1@gmail.com

Conflict of interest: the authors declare no conflict of interest.

Investigation of structures formed by magnetic fluid nanoparticles in polymer matrices by static light scattering

Ivan V. Pleshakov^{1,a}, Andrey V. Prokof'ev¹, Efim E. Bibik², Yuriy I. Kuz'min¹

¹Ioffe Institute, St. Petersburg, 194021, Russia

²St. Petersburg State Institute of Technology (Technical University), 190013, St. Petersburg, Russia

^aivanple@yandex.ru

Corresponding author: Ivan V. Pleshakov, ivanple@yandex.ru

PACS 42.70.-a; 42.70.Jk; 75.50.Mm

ABSTRACT In this work, nanostructured composites in the form of polymer matrices with inclusions of magnetic particles were studied by the method of static scattering of laser radiation. The particles were embedded into polyvinyl alcohol and epoxy resin from magnetite-containing ferrofluid. It is shown that in a magnetic field they form a system of extended aggregates acting as light scatterers and established that optical technique based on this provides important information about the properties of such nanomaterial.

KEYWORDS nanocomposite, magnetite nanoparticles, ferrofluid, polymer matrix.

ACKNOWLEDGEMENTS The authors are grateful to A. V. Varlamov, I. V. Ilyichev and T. A. Kostitsyna for their help in the experiments.

FOR CITATION Pleshakov I.V., Prokof'ev A.V., Bibik E.E., Kuz'min Yu.I. Investigation of structures formed by magnetic fluid nanoparticles in polymer matrices by static light scattering. *Nanosystems: Phys. Chem. Math.*, 2022, **13** (3), 285–289.

1. Introduction

Among many nanostructured materials representing a system of small particles dispersed in an optical matrix, a special place is occupied by those in which the particles consist of magnetically ordered substance [1]. The interest in them is due to the fact that here there is an additional opportunity to control their properties by applying an external magnetic field. Besides, structures created by the field and fixed in a solid medium can be studied by various methods which is important, taking into account that the probing of the texture of such aggregates is still an urgent physical problem.

As an example of a magnet-containing nanocomposite of this type, one can point to a material made by introducing magnetite, Fe_3O_4 , into a transparent polyvinyl alcohol (PVA) matrix [2]. Its samples were obtained in a simple and convenient way – by mixing an aqueous solution of PVA and containing particles water colloid of Fe_3O_4 , i.e. the so-called magnetic fluid (MF). The aim of this work was to study the characteristics of structures formed by a magnetic field in composites prepared by the same approach using the light scattering technique.

2. Experiment

2.1. Samples preparing

The samples were fabricated as films of thicknesses of 40–80 μm by deposition of the initial liquid mixture onto glass wafer, with its subsequent drying in or without external magnetic field H .

In the case of PVA matrix the mixture was prepared by blending of two solutions: 5 wt. % aqueous solution of powdered PVA and water-based MF in such a proportion that provided of about 0.5 vol. % concentration of solid phase in mixture. The MF was the same as in [2] with the colloidal particles of Fe_3O_4 of the diameter approximately 10 nm, stabilized by double layer surfactant with hydrophobic (inner) and hydrophilic (outer) molecules (oleic acid salts). Mixing was carried out at a temperature of about 90°C, and then the resulting liquid was sonified in an ultrasonic bath for one hour.

The samples with the epoxy matrix were made by slightly different way because at this point the use of water as impossible. Here, magnetite-containing ionic-stabilized aqueous MF was dried on glass, and the resulting paste-like precipitate in an amount corresponding to about 0.25 mg/ml per full volume of the matrix substance was diluted in a hardener and sonified for one hour. After mixing with the resin, short-term sonification was also carried out, and then the film was made in the same way as in the case of PVA. For this purpose, commercially available Artline Crystal Epoxy material with high transparency was used.

2.2. Micrography of samples

Micrographs of several samples based on PVA are shown in Fig. 1. The values of H here do not exceed the saturation field H_s of MF, which in order of magnitude is of 1 kOe [3]. At zero field, as can be seen from Fig. 1a, inclusions of MF are present in the sample in the form of dispersed micro-droplet aggregates with dimensions of the order of several microns, composing an emulsion. This is usual for complex environment in which the MF is being embedded [2, 4]. The application of even a small field leads to the appearance of a preferred direction in which extended aggregates are oriented, and their thicknesses d indicate that they arose as a result of the fusion of many droplets. Note that, at least for small fields, not so much the thicknesses of the aggregates depend on H as their lengths, which is well traced from Fig. 1b to Fig. 1d (from 40 to 750 Oe).

Attention should also be paid to the presence of structures that are not related to the MF. They look like some kind of dendrite formations, and in one amount or another are present in all PVA-based films. At higher zoom, it is possible to establish that they consist of many small crystallites. By assumption, these elements are associated with the partial crystallization, typical for polyvinyl alcohol [5]. As it will be seen below, they have not a significant effect on the scattering of optical radiation, which in our case was almost entirely determined by MF-containing objects.

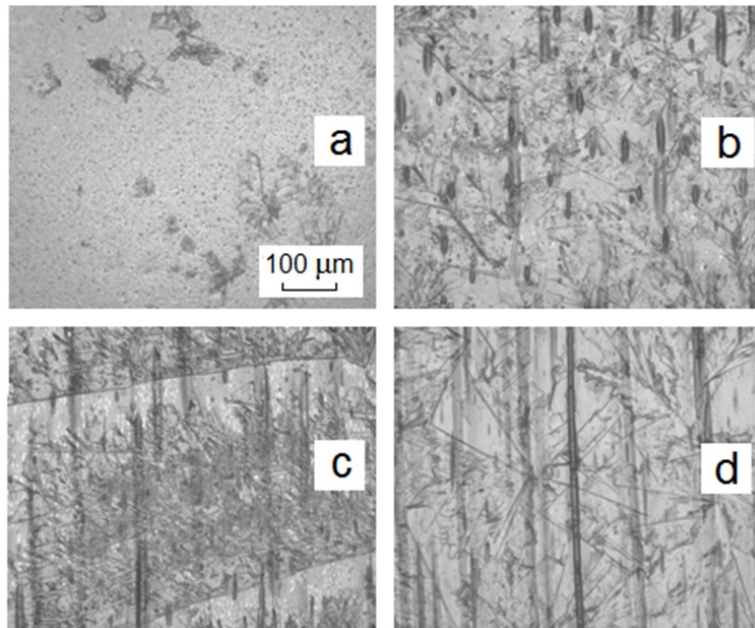


FIG. 1. Micrographs of PVA-based samples for: (a) $H = 0$, (b) $H = 40$ Oe, (c) $H = 115$ Oe, (d) $H = 750$ Oe. The common scale is indicated in the first image

For comparison, Fig. 2 shows examples of microphotographs of samples obtained using an epoxy resin and large fields. In this case, very long columnar aggregates with varying thicknesses are formed, among which, however, those with a diameter of the order of several tens of microns predominate. Of course, there is no here any dendritic structure. The results on light scattering for epoxy-based specimens turn out to be qualitatively similar to those obtained for PVA-based materials.

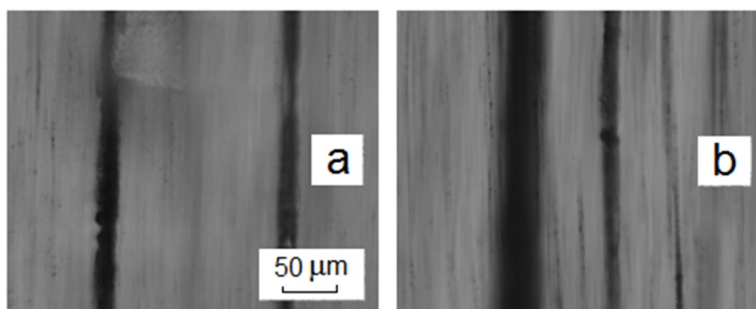


FIG. 2. Micrographs of epoxy-based samples for: (a) $H = 4$ kOe, (b) $H = 6$ kOe

2.3. Light scattering measurements

Static light scattering experiments were carried out according to the standard technique: a semiconductor laser beam ($\lambda = 650$ nm) was directed at the sample (illuminated from the side of the glass plate), which could be positioned in such a way that the direction of the field applied during its manufacture was either parallel or perpendicular to the polarization of the input radiation, and the scattered light was recorded in the plane orthogonal to the plane of polarization by a photodetector mounted on a rotating limb. A polarizer was placed in front of the photodetector, allowing to separate the different components of the scattered light. The measurement consisted in determining the dependence of the scattered light intensity I on the angle between the direction to the photodetector and the optical axis of the system θ , that is, the indicatrix $I(\theta)$ (in experiment the readings of the photodetector U_{ph} , proportional to I were recorded).

The experimental results for PVA-based samples at some values of H are shown in Fig. 3 and Fig. 4 (polarizer in the state of maximum incident light transmission). According to Fig. 2a, which demonstrates the dependence $U_{ph}(\theta)$ at the direction of the laser beam polarization along the field, one can see a rapid increase in the width of the diagram with H increasing from zero to several hundred oersteds (the case of a zero field is not depicted in the figures, since at $H = 0$ the density of the scattered radiation, due to its symmetrical distribution in a large solid angle, greatly reduced). In contrast, when the field is oriented perpendicular to the light polarization, the indicatrix narrows (Fig. 2b). The difference in the widths of these lines becomes very significant already at $H = 500$ Oe, which is illustrated in Fig. 4 representing the functions $U_{ph}(\theta)$ for the two indicated geometries of experiment. An important fact should be noted: at H approaching the saturation field, the change in the indicatrices practically stops, so the function $U_{ph}(\theta)$ measured at $H = 5$ kOe almost coincides with the function $U_{ph}(\theta)$ corresponding to 500 Oe.

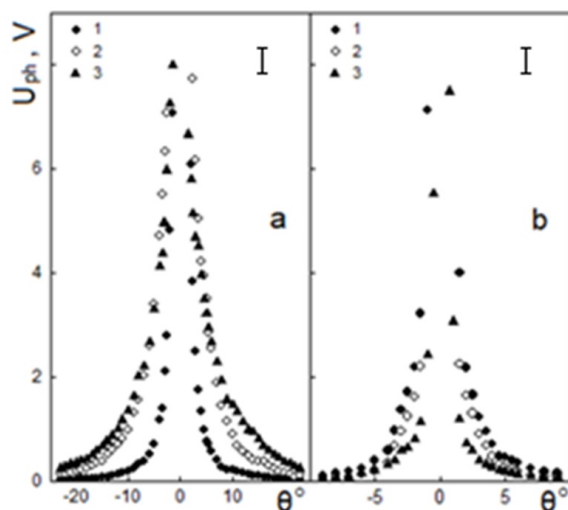


FIG. 3. Light scattering indicatrices of PVA-based samples for parallel (a) and orthogonal (b) orientations of magnetic field and incident light polarization. 1 – $H = 40$ Oe, 2 – $H = 250$ Oe, 3 – $H = 500$ Oe

Since measurements at angles θ close to zero are impossible in scattering experiments, the value of the width of the indicatrix at the half of its maximum intensity was not determined. As a criterion reflecting the properties of the indicatrix, its width $\delta\theta$ at the level $U_{ph} = 1$ V was chosen. Fig. 5 shows the dependences of $\delta\theta$ on H (Fig. 5a), as well as the field dependence of the ratio of the widths measured at parallel and perpendicular mutual orientations of the field and polarization (Fig. 5b).

Obviously, the considered effects can be associated only with the magnetic fraction of the composite. Thus, the dendritic inclusions mentioned above do not make any noticeable contribution to the measurement results, although in some cases a very weak pattern was visually recorded in the scattered radiation, reflecting, apparently, the symmetry of the crystallites.

The degree of polarization of scattered light P , determined from the intensities of its vertical and horizontal polarization components, in all cases, except for the case with $H = 0$, coincided with the degree of polarization of the incident laser radiation with an accuracy of at least 1%. In the zero field, an extremely insignificant depolarization, which, nevertheless, lied outside the error limits, was observed (a decrease in P by 2% from the initial one).

3. Discussion

Since the scattering centers in the samples under study are large objects with transverse dimensions of the order of several tens of microns (Fig. 1, Fig. 2), that is, with $d \gg \lambda$, it is acceptable to consider the obtained results in the framework of the concept of Fraunhofer diffraction. This is additionally confirmed by the fact that, despite the rather

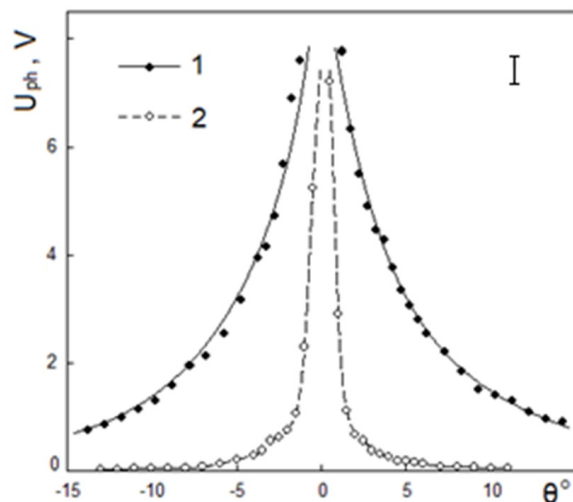


FIG. 4. Light scattering indicatrices of PVA-based sample for parallel (1) and orthogonal (2) orientations of magnetic field and incident light polarization at $H = 500$ Oe

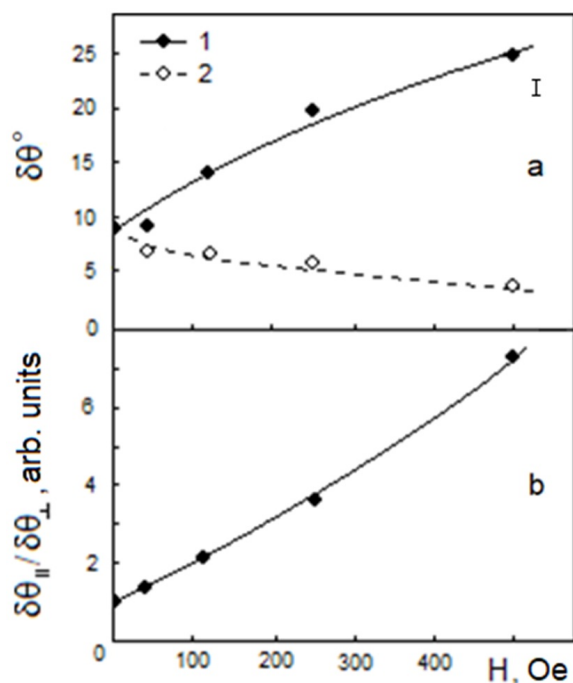


FIG. 5. The width of the scattering indicatrix depending on the magnetic field for different geometries of the experiment: 1 – parallel orientation, 2 – perpendicular orientation (a); the ratio of widths corresponding to these orientations (b)

large width of the indicatrices, for all films manufactured at $H \neq 0$ the value P does not depend on θ and, as mentioned above, does not differ from P of incident light. The classical diffraction pattern from individual aggregates isolated by laser focusing has been observed previously in MF with a complex solvent [6]. In the present work, a similar effect was also recorded, for example, it was clearly manifested on a well-formed structure in an epoxy resin matrix, similar to the one shown in Fig. 2.

Most of the experiments, however, were performed without focusing. Assuming the diameter of the laser spot to be 1 mm and using the images in the microphotographs of Fig. 1, it is possible to estimate the average number of scattered radiation sources in several tens. Consequently, the indicatrix should be a result of summation of a set of diffraction patterns with different parameters. We emphasize that this idea implies a simple scattering. This condition can be considered fulfilled a fairly good, since at small (not much larger than d) film thicknesses, overlapping aggregates practically do not occur. (At the same time, the attenuation of the passing laser beam is quite significant, but this is probably due to the fact that the main contribution to extinction comes not from absorption in magnetic nanoparticles, but namely from scattering). Accordingly, a further increase in the width of the indicatrix, measured when the polarization plane of incident light

coincides with the direction of the field, stops with increasing H . It should be mentioned that the growth of aggregates begins from the emulsion, i.e., they combine mainly microdroplets, in which the field induces a magnetic moment, rather than individual nanoparticles. This state itself ($H = 0$, Fig. 1a) is somewhat different in its effect from all the others in that the shading elements here can be quite small, perhaps, in some part approaching individual particles in size. This is confirmed by a very weak, but still noticeable, dependence of P on θ , suggesting a possible admixture of scattering by the Mie mechanism [8].

Thus, the data of light scattering experiments reflect the internal structure of the studied samples and allow us to draw certain conclusions about their magnetic behavior.

4. Conclusion

It was shown in present work that in a composite nanomaterial prepared on the basis of a polymer matrix with inclusions of nanoparticles of magnetically ordered material, a strongly anisotropic structure appears under the influence of a magnetic field, and its formation is mainly completed close to the saturation field. When using magnetic liquids as a filler, aggregates arising in samples during their manufacture are fixed in a solid medium, representing a system that is convenient to study by optical methods, using, in particular, the light scattering technique.

References

- [1] McHenry M.E., Laughlin D.E. Nano-scale materials development for future magnetic applications. *Acta Mater.*, 2000, **1**, P. 223–238.
- [2] Pleshakov I.V., Prokof'ev A.V., Bibik E.E., Nepomnyashchaya E.K., Velichko E.N., Kostitsyna T.A., Seliutin D.M. Spectral characteristics of composite obtained by embedding of magnetic nanoparticles into polymer matrix. *Nanosystems: physics, chemistry, mathematics*, 2021, **12**(3), P. 279–282.
- [3] Chikazumi S., Taketomi S., Ukita M., Mizukami M., Miyajima H., Setogawa M., Kurihara Y. Physics of magnetic fluids. *J. Magn. Magn. Mat.*, 1987, **65**, P. 245–251.
- [4] Zakinyan A.R., Dikansky Yu.I. Effect of microdrops deformation on electrical and rheological properties of magnetic fluid emulsion. *J. Magn. Magn. Mat.*, 2017, **431**, P. 103–106.
- [5] Thomas D., Cebe P. Self-nucleation and crystallization of polyvinyl alcohol. *J. Therm. Anal. Calorim.*, 2017, **127**, P. 885–894.
- [6] Prokof'ev A.V., Pleshakov I.V., Bibik E.E., Kuz'min Yu.I. An optical investigation of the geometric characteristics of aggregates formed by particles of magnetic fluid. *Tech. Phys. Lett.*, 2017, **43**(2), P. 194–196.
- [7] Stuart W.C. Aggregation in magnetic fluids and magnetic fluid composites. *Chem. Eng. Commun.*, 1988, **67**(1), P. 145–180.
- [8] Bohren C.F., Huffman D.R. *Absorption and scattering of light by small particles*. John Wiley & Sons, Inc., NY, 1998, 544 p.

Submitted 15 May 2022; revised 26 May 2022; accepted 27 May 2022

Information about the authors:

Ivan V. Pleshakov – Ioffe Institute, 26 Politechnicheskaya str., St. Petersburg, 194021, Russian Federation;
ivanple@yandex.ru

Andrey V. Prokof'ev – Ioffe Institute, 26 Politechnicheskaya str., St. Petersburg, 194021, Russian Federation;
Andrey.prokofyev@algo-spb.com

Efim E. Bibik – 2St. Petersburg State Institute of Technology (Technical University), 26 Moskovsky ave., 190013, St. Petersburg, Russian Federation; eefimovich@yandex.ru

Yuriy I. Kuz'min – Ioffe Institute, 26 Politechnicheskaya str., St. Petersburg, 194021, Russian Federation; iourk@yandex.ru

Conflict of interest: the authors declare no conflict of interest.

Overview of device-independent continuous-variable quantum key distribution

Roman Goncharov^a, Egor Bolychev, Irina Vorontsova, Eduard Samsonov, Vladimir Egorov

ITMO University, St. Petersburg, 197101, Russia

^arkgoncharov@itmo.ru

Corresponding author: R. Goncharov, rkgoncharov@itmo.ru

PACS 03.67.-a, 42.50.-p

ABSTRACT The objects of study of this paper are quantum key distribution (QKD) protocols and systems, in particular, continuous variable (CV) ones with untrusted devices (measurement devices or light sources). The present work is devoted to the consideration of such systems, namely, device-independent CV-QKD, and to the discussion of their performance.

KEYWORDS device-independent, quantum key distribution, continuous variables.

ACKNOWLEDGEMENTS The work was done by Leading Research Center “National Center for Quantum Internet” of ITMO University by order of JSCo Russian Railways.

FOR CITATION Goncharov R., Bolychev E., Vorontsova I., Samsonov E., Egorov V. Overview of device-independent continuous-variable quantum key distribution. *Nanosystems: Phys. Chem. Math.*, 2022, **13** (3), 290–298.

1. Introduction

Nowadays, the secure exchange of information plays an increasingly important role. Modern developments in the field of quantum communications help to solve a large number of relevant problems. One of them, quantum key distribution (QKD) [1], is a key transfer method that uses quantum phenomena to guarantee secure stable communication. This technology allows two parties connected via an open classical authenticated and imitated communication channel to create a common random key known only to them and use it to encrypt and decrypt messages transmitted over the classical channel.

Currently, there are a huge number of works (see, for example, [2–4]) devoted to QKD protocols, each of them has its own advantages, disadvantages, and a certain area of application. In a typical QKD protocol, two users, Alice (sender) and Bob (receiver), share a quantum channel to transmit information, and it is always assumed that this channel is being attacked by a third party, in other words, the eavesdropper (Eve) is trying to access the encoded quantum information. But her intervention creates various kinds of disturbances in the system, which leads to additional noise. Legitimate parties, in turn, can quantify the noise (parameter estimation) introduced by Eve, carry out error correction and security amplification procedures to minimize information potentially available to the intruder. They can then use the resulting key in symmetric encryption protocols, such as the one-time pad. The fundamental mechanism of QKD operation is clearly preserved in more complex communication configurations.

The most modern QKD systems are based on the point-to-point principle and the assumption of trust between sender and receiver nodes. The latter circumstance opens up the possibility for an intruder to carry out certain attacks on equipment [5] and, as a result, to extract information not only through a quantum channel. There are a number of countermeasures against such attacks, but the most effective way to get rid of them is to develop and implement new schemes based on the presence of untrusted equipment in the system. The present work is devoted to the consideration of such systems.

Several approaches can be distinguished against attacks on legitimate users' equipment. The first approach to solving the problem involves using a measurement-device-independent (MDI) protocol [6] and lies in the fact that the measuring node is available to Eve. In addition, she has information about which detectors clicked and at what time frame, but does not know which quantum state was used in the sender and receiver blocks. The latter is implemented due to the interference of weak coherent pulses on the beam splitter inside the untrusted registration node. At the post-selection stage, legitimate users identify the result of single-photon interference that led to the trigger and the corresponding states that were used. This approach is very difficult to implement in practice and is almost never used in conditions close to real.

Twin-Field (TF) protocol [7] can be considered a development of the MDI approach using phase encoded states with the announcement by the measuring node (available to Eve) of the result of the interference of coherent states on the beam splitter, leading to the operation of single photon detectors. In the TF protocol, in contrast to MDI, to minimize the phase correlation of the pulse train from each of the sources, the result of the interference of coherent states is used

with the definition of sectors on the phase plane and the rejection of phase states corresponding to different sectors in the post-processing, while the MDI protocol implies their randomization, that is, changing the phase in a random way.

The concept of the MDI protocol can be implemented on the base of CV-QKD. This version of the MDI protocol allows the parties to recover each other's variables based on the knowledge of the parameter relating the coherent states of the sender and receiver via detectable quadratures, which is open, so that they can locally rebuild the sender-receiver covariance matrix without disclosing any information.

Among the independent approaches, one can also single out the source-device-independent (SDI) one, where it is assumed that there is not a detector, but a light source on an untrusted node, which distributes the signal over several quantum channels to legitimate parties.

The paper is organized as follows. In the Section 2, we briefly describe CV-QKD protocols. In Section 3, we review the concept of MDI CV-QKD and discuss the results of numerical investigations. In section 4, we review an alternative approach to implementing a DI CV-QKD scheme with an untrusted source in a relay. In section 5 we present conclusions and discuss the prospects of the described technologies.

2. CV-QKD

For the first time QKD was presented with single photons as information carriers, sometimes called discrete variable QKD (DV-QKD). In such protocols, the quantum state is encoded by the polarization, phase, or time interval in finite degrees of freedom of the transmitted qubits, and Bob receives the secret key after detecting individual photons via single-photon detector.

The first of the QKD protocols, BB84, was proposed by Bennett and Brassard in 1984 [8]. This protocol was based on the use of two mutually unbiased photon polarization states.

Fifteen years after the first DV-QKD protocol, CV-QKD was considered as a promising alternative the hallmark of which is the ease of implementation and better compatibility with modern telecommunication systems, as the usage of compact balanced receivers instead of large single-photon ones.

First proposed with discrete [9] and Gaussian [10] encoding of squeezed states, this concept was soon developed further by CV-QKD with coherent states [11]. CV-QKD with Gaussian modulation (GG02) of coherent states is currently considered to be the most successfully implemented in practice [3, 11, 12].

The advantage of the coherent-state protocols over the squeezed-state ones lies mainly in the absence of the need to generate squeezed light (which is quite technically difficult). A comprehensive theoretical overviews of the CV-QKD are presented in [1, 13, 14]. To date, a lot of papers have been written on the experimental applications of CV-QKD, and they emphasize the possibility of practical implementation of exactly with coherent states.

Of course, the experimental results should be considered in the context of various assumptions. In the end, the CV-QKD setup is primarily evaluated by secure key rate that can be achieved at a given channel losses. The security, however, largely depends on the capabilities of a potential eavesdropper, the effectiveness of reconciliation, accounting for finite key effects, the classification of the so-called trusted noise, the security of a given modulation alphabet, etc. Moreover, different experimental demonstrations show different vulnerabilities to side-channel attacks.

For example, several papers have successfully demonstrated the CV-QKD at large distances with a non-zero key rate for a channel length of 80–100 km [15] and 200 km [16]. The presence of security assumptions is disclosed by the authors in part.

It should be noted that unconditional security of the discrete modulation protocols of CV-QKD against general (coherent) attacks is considered only in the case of infinite or close to infinite keys [17, 18]. However, the papers devoted to the CV-QKD GG02 offer a proof that gives non-zero secret key rates even for practical block sizes [19–23].

3. MDI CV-QKD

Despite theoretically provable security of QKD protocols, it is still a problem [24] to achieve it in real devices. In fact, before any security proof can be applied to practical scenarios, the various disadvantages of the devices used must be carefully examined. For example, a mismatch in the efficiency of a detector which can be used by Eve to implement an eponymous attack [25] or attacks with a time shift [26].

More recently, other flaws such as detector post-gate pulses and dead time have also been exploited in quantum hacking strategies. Although certain countermeasures have been proposed in each case, in order to completely eliminate such attacks, it is necessary to deal with the problem at the root. Referring to recent advances in the field of MDI QKD, alternative practical schemes have been proposed that are resistant to loopholes in detection, thus protecting against all the above-mentioned attacks in QKD systems [4, 27].

Security gaps in QKD systems essentially stem from existing problems in Bell's inequalities. There are three main loopholes corresponding to the three assumptions:

- a locality loophole that involves the assumption that two communicating parties are separated in a space,
- an efficiency loophole, which is related to the assumption of sample fairness,
- a loophole of randomness, which is related to the assumption that the bases of the dimension are chosen randomly.

In the context of the QKD, some of these loopholes have been more damaging than others. For example, it is reasonable to assume that the information in the two sides of the QKD, Alice and Bob, is protected from Eve. Thus, the locality loophole does not necessarily lead to hacking strategies. Given the recent developments in quantum random number generators, the randomness loophole may not pose a problem either. However, the efficiency loophole opens up many opportunities for quantum attacks. In fact, all of the aforementioned attacks fall into this category.

One of the approaches to overcome the drawbacks of the devices used is the applying of DI QKD schemes. Unfortunately, such schemes impose serious restrictions on the physical devices used. For example, the allowable quantum bit error rate (QBER) is 7.1%, and the minimum required transmittance is 92.4%, which makes the experimental demonstration an extremely difficult task. In order to reduce the above limitations, several QKD schemes with softer restrictions have been proposed, i.e. MDI QKD schemes.

3.1. Common MDI QKD protocol

This section discusses the MDI QKD scheme with phase coding [28]. The key component of the scheme is a partial Bell state measurement (BSM) module, implemented using 50/50 beam splitters and single-photon detectors, which we will hereafter refer to as a “relay” (Charlie). It is assumed that Alice and Bob are using improved single photon sources. Fig. 1 illustrates how the scheme works. The MDI QKD coding scheme works as follows. Both Alice and Bob prepare the single photon state and pass them through 50:50 beam splitters. The two resulting modes are called the reference and signal modes, denoted respectively by a_r and a_s on Alice’s side and b_r and b_s on Bob’s side.

To generate the four states of the BB84 protocol, the phase modulators respectively introduce relative phase shifts θ_a and θ_b between the reference and signal modes of Alice and Bob. To comply with the BB84 protocol, Alice and Bob randomly select θ_a and θ_b from two basis sets $\{0, \pi\}$ and $\{\pi/2, 3\pi/2\}$. The phase values 0 and $\pi/2$ represent bit “1” and the other two represent bit “0”. When single-photon sources are used, the common phase does not affect the final result and will not be taken into account.

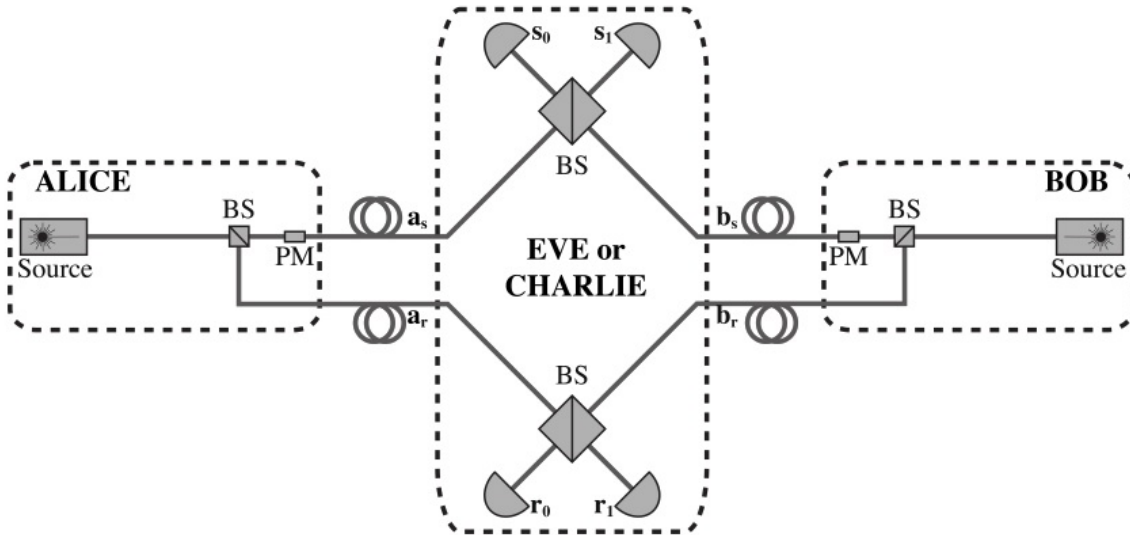


FIG. 1. Common MDI QKD scheme. BS is a beam splitter and PM is a phase modulator

In this implementation of MDI QKD, channel losses and dark counting effects are not taken into account. It is also assumed that the relative phase between the reference and signal modes is maintained. A successful partial BSM occurs when one and only one of r_0 and r_1 and one and only one of s_0 and s_1 are clicked. All other events, such as the case when r_0 and r_1 are clicked at the same time, are discarded.

If $\theta_a - \theta_b = \pm\pi$, then detectors r_0 and s_0 , and only these detectors, click or r_1 and s_1 click. Otherwise, if $\theta_a - \theta_b = 0$, then detectors r_0 and s_1 , or r_1 and s_0 click. In all other cases, when $\theta_a - \theta_b = \pm\pi/2$, two random detectors out of four will work, and then Alice’s and Bob’s qubits will not be correlated. Such events will be eliminated using a standard screening procedure. Clicks only on the reference (signal) detectors will also be excluded. Eventually, Alice’s and Bob’s bits, determined by the relative phases θ_a and θ_b , will be correlated or anticorrelated depending on the detection results at the central relay.

Then, in the case of a single-photon MDI scheme, the secure key fraction can be calculated as follows [28]

$$r > Y_{11}[1 - fh(e_{11}) - h(e_{11})], \quad (1)$$

where $h(x) = -x \log_2(x) - (1-x) \log_2(1-x)$, Y_{11} is a detector efficiency, e_{11} is a QBER, and f is an error correction efficiency.

3.2. MDI CV-QKD

Recently, several strategies for attacking real detectors have also been proposed in the CV-QKD systems. For example, the short pulse attack [29] and the LO calibration [30] attack manipulate measurement results, which provokes Alice and Bob to overestimate the security of the key. A saturation attack [31] can cause Alice and Bob to underestimate the excess noise by saturating the homodyne detector, which can hide the intercept-resend attack.

The most logical option to eliminate these attacks in the CV-QKD system was to characterize each specific loophole and find countermeasures. However, it is quite difficult to fully characterize real detectors and account for all loopholes. That is why it is so important to figure out how to defend against all the attacks on detectors in practical MDI CV-QKD systems.

Taking into account all the problems in the field of detection, the corresponding CV-QKD protocol was proposed, which can also prevent leakage through side channels [4, 32]. The basic idea, as in standard MDI QKD, is that both Alice and Bob are senders, and an untrusted third party (Charlie) is introduced to perform the measurement. The measurements on Charlie's relay will be used by Alice and Bob in post-processing to generate secure keys.

3.3. MDI CV-QKD protocol description

It is easier to describe the security analysis against arbitrary collective attacks by introducing the entanglement-based (EB) scheme of this protocol. It is based on the fact that the MDI CV-QKD scheme (Fig. 2) is equivalent to the prepare-and-measure (PM) scheme of CV-QKD with coherent states and heterodyne detection (Fig. 3). Moreover, the effectiveness of such a protocol against collective attacks is presented using numerical simulation methods.

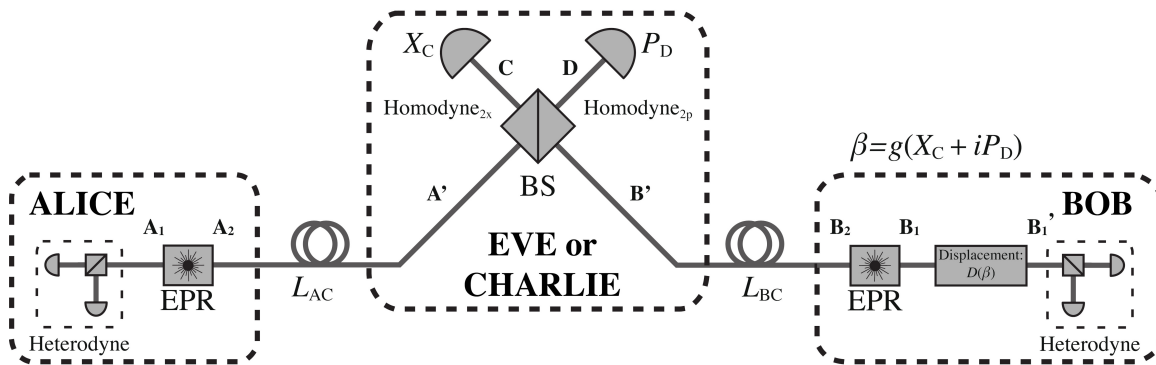


FIG. 2. EB MDI CV-QKD scheme

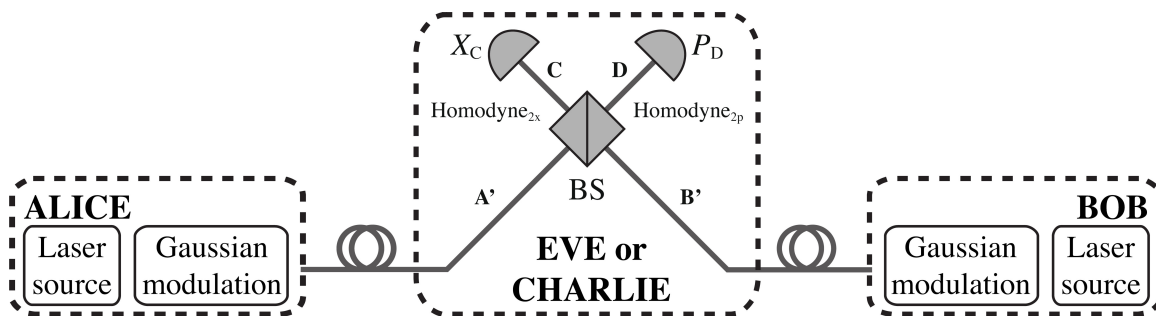


FIG. 3. PM MDI CV-QKD scheme

The MDI CV-QKD in the EB scenario (see Fig. 2) is executed according to the following steps:

- (1) Both Alice and Bob generate a two-mode squeezed vacuum state, keeping one mode each (A_1 , B_1), and the other sent over a quantum channel to a third untrusted party Charlie (A_2 , B_2);
- (2) Alice's and Bob's modes (A' , B') obtained by Charlie interfere in a beam splitter with two output modes C and D. The x -quadrature of the C mode and the p -quadrature of the D mode are measured via homodyning. Charlie then publicly announces the result $\{X_C, P_D\}$;
- (3) Bob displace his state B_1 using the displacement operator $\hat{D}(\beta)$ (with $\beta = g(X_C + iP_D)$, where g is a bias factor). After all the operations, Alice and Bob measure their states B'_1 and A_1 via heterodyning. After the displacement, the final states of Alice and Bob become entangled, that is, their final received information is correlated;

- (4) Alice and Bob use the authenticated public channel to complete the parameter estimation, information reconciliation, and privacy amplification.

It should be borne in mind that Charlie is an untrusted party and can be completely under the control of Eve. It is also necessary to consider a scheme more convenient for practical implementation (see Fig. 3), in this embodiment, where Alice and Bob prepare coherent states modulated in accordance with a two-dimensional Gaussian distribution (GG02), which are easier to generate than a two-mode squeezed vacuum state:

- (1) Alice and Bob generate a coherent state $|x_A + ip_A\rangle$ and $|x_B + ip_B\rangle$, where the quadratures x and p have variance $V_A - 1$ ($V_B - 1$) in shot noise units (SNU). Both Alice and Bob send their states to Charlie's untrusted relay via quantum channels;
- (2) Alice's and Bob's modes interfere at the beam splitter. The quadratures of Charlie's C and D modes are measured on a homodyne detectors. After that, Charlie announces publicly the resulting state $\{X_C, P_D\}$;
- (3) At the end, as in the case of the EB scheme, only Bob changes his state in the following way: $X_B = x_B + kX_C$, $P_B = p_B - kP_D$ (k is the gain associated with channel losses), while Alice preserves her state unchanged;
- (4) legitimate parties perform standard procedures for parameter estimation, information reconciliation, and privacy amplification;

As described above, the EB and PM scenarios are equivalent in proving the security of the CV-QKD protocols against collective attacks [3, 33] and are reduced to one another by transforming the covariance matrix.

3.4. Security proof for MDI CV-QKD protocol

From the point of view of the theoretical security proof, Eve can have access to almost the entire QKD system, including relays, quantum channels, and even Bob's state displacement operation in the EB scheme. In this case, one can consider the MDI CV-QKD protocol as a special case of a typical one-way CV-QKD protocol [12].

Then the secure key fraction can be estimated in accordance with the Devetak-Winter bound [34, 35]

$$r = \beta I(X_A, P_A : X_B, P_B) - \chi(X_B, P_B : E), \quad (2)$$

where β is reconciliation efficiency, I is a mutual information Alice-Bob, $\chi(X_B, P_B : E) = S(\hat{\rho}_E) - S(\hat{\rho}_E|X_B, P_B)$ is a Holevo bound, and $S(\hat{\rho}_E)$ is a von Neumann entropy of quantum state $\hat{\rho}_E$.

Based on the assumption that Eve can attack through a full purge, which means $\chi(X_B, P_B : E) = \chi(X_B, P_B : A_1, B'_1)$, one can obtain the final expression for the secret fraction

$$r = \beta I(X_A, P_A : X_B, P_B) - S(\hat{\rho}_{A_1 B'_1}) - S(\hat{\rho}_{A_1 B'_1}|X_B, P_B). \quad (3)$$

Moreover, the upper bound $\chi(X_B, P_B : A_1, B'_1)$ is determined only using the covariance matrix $\gamma_{A_1 B'_1}$.

3.5. Estimation of covariance matrix

The whole system is supposed to be under two independent entangling cloner attacks [11]. Then the covariance matrix has the form

$$\Xi = \begin{pmatrix} V_A I_2 & \sqrt{(T(V_A^2 - 1)\sigma_z)} \\ \sqrt{(T(V_A^2 - 1)\sigma_z)} & [(V_A - 1) + 1 + T\xi'] I_2 \end{pmatrix}, \quad (4)$$

$$T = \frac{\eta_A}{2} g^2, \quad (5)$$

$$\xi' = 1 + \frac{1}{\eta_A} [\eta_B (\Xi_B - 1) + \eta_A \Xi_A] + \frac{1}{\eta_A} \left(\frac{\sqrt{2}}{g} \sqrt{V_B - 1} - \sqrt{\eta_B} \sqrt{V_B + 1} \right)^2, \quad (6)$$

$$\Xi_A = \frac{1 - \eta_A}{\eta_A} + \xi_A, \quad \Xi_B = \frac{1 - \eta_B}{\eta_B} + \xi_B, \quad (7)$$

$$\eta_A = 10^{-\alpha L_{AC}/10}, \quad \eta_B = 10^{-\alpha L_{BC}/10}, \quad (8)$$

where η_A (η_B) is a channel (Alice-Charlie or Bob-Charlie) transmittance, ξ_A (ξ_B) is an excess noise, g is an offset factor, I_2 is an identity matrix, and σ is a Pauli z -matrix.

To minimize excess noise, the offset factor is set as

$$g = \sqrt{\frac{2}{\eta_B}} \sqrt{\frac{V_B - 1}{V_B + 1}}. \quad (9)$$

Then the excess noise is expressed as

$$\xi' = \xi_A + \frac{1}{\eta_A} [\eta_B (\xi_B - 2) + 2]. \quad (10)$$

3.6. MDI CV-QKD system performance

The symmetrical implementation in MDI CV-QKD schemes seems to be the most logical when the distance between Alice and the relay is equal to the distance between the relay and Bob. The system parameters in this implementation are [4]: $\beta = 1$, $L_{AC} = L_{BC}$. Security is evaluated in the presence of collective attacks for keys of finite length. The dotted line in Figure 4 denotes the ideal case of high modulation dispersion ($V_A = V_B = 10^5$) with almost no excess noise. The black solid line indicates the case when $V_A = V_B = 40$, $\xi_A = \xi_B = 0.002$.

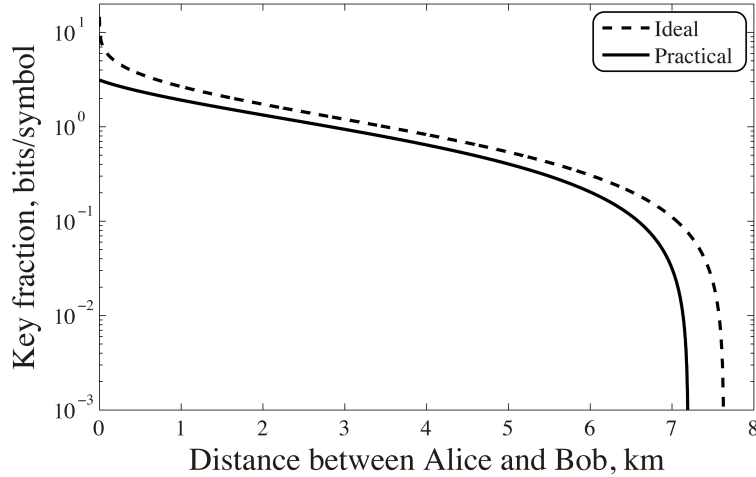


FIG. 4. Secure key fraction versus the distance between Alice and Bob in the symmetrical MDI CV-QKD implementation.

As can be seen, the maximum achievable transmission distance for the symmetrical case is only 7 km. Key transmission over long distances in this configuration is not possible. However, the symmetrical case can be used for MDI communication over short distances.

However, there is a way to increase the key transmission distance. Considering that only Bob changes his state, it becomes clear that ξ' is not symmetrical. In this case, consider the situation where $L_{AC} \neq L_{BC}$. The results of such an implementation are shown in Figure 5. Again, the dotted line represents the ideal case ($V_A = V_B = 10^5$, $\xi_A = \xi_B = 0$),

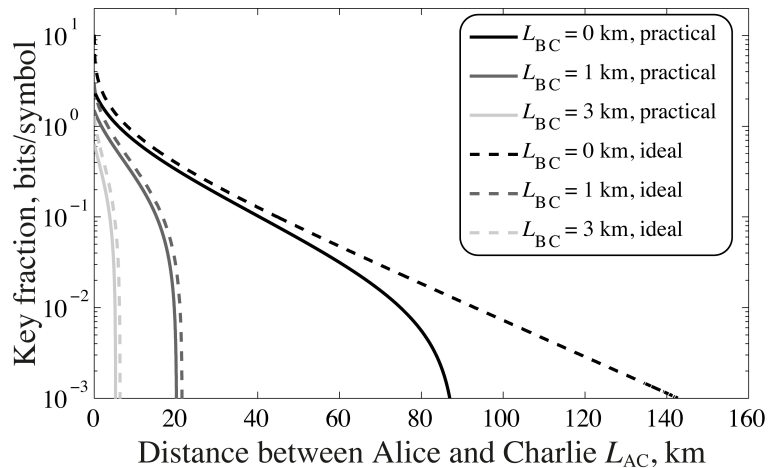


FIG. 5. Secure key fraction versus the distance between Alice and Bob in the symmetrical MDI CV-QKD implementation

and the parameters for the solid line, in turn, are as follows: $V_A = V_B = 40$, $\xi_A = \xi_B = 0.002$.

Obviously, in the asymmetric case, the results obtained are much superior to the symmetric one. The maximum achievable transmission distance is 80 km when the relay is as close to Bob as possible.

Thus, in accordance with the MDI CV-QKD protocols, it is possible to distribute the secure key with a generation rate comparable to one-way QKD protocols. Moreover, such systems are resistant to all collective attacks on the detectors, fluctuation attacks on the LO, and calibration attacks.

An ideal reconciliation ($\beta = 1$) was also assumed in all cases. In real systems, this is a difficult task, but some scientific groups demonstrate efficiency up to $\beta = 0.99$ [16]. But if we take a more typical value of efficiency for CV-QKD systems $\beta = 0.95$ [4], the maximum distance at which a key distribution session is possible will be halved.

3.7. Finite key aspects

Another obvious problem of CV-QKD getting in the way of integration into the telecommunications infrastructure is taking into account the finite size of the distributed key. Indeed, in real systems, parties cannot exchange an infinite number of bits to generate a key. And it is logical to assume that by creating keys of a finite size, it is impossible to achieve the same security results as in the asymptotic case of infinite keys.

To fill this gap, it is necessary to evaluate the effects of finite size effects on the security parameter of MDI CV-QKD protocol that has been done in [36].

The parameters of Gaussian quantum channel (transmittance and excess noise) are determined within the confidence intervals. Confidence intervals are used to select the worst case scenario by selecting the lowest channel bandwidth and highest excess noise. The secure key fraction is then numerically calculated using the estimated transmittance and noise values

$$r = \frac{n}{N} (r^\infty(\xi, V_A, \tau_A^{\text{low}}, \tau_B^{\text{low}}, V_{q,\xi}^{\text{up}}, V_{p,\xi}^{\text{up}}) - \Delta(n)), \quad (11)$$

where $n = \tilde{N} - m$ is a number of signals used for key generation, \tilde{N} is a total number of signals exchanged, $\tau_A^{\text{low}}, \tau_B^{\text{low}}$ are the smallest possible values of Alice's and Bob's channel transmittance coefficients, $V_{q,\xi}^{\text{up}}, V_{p,\xi}^{\text{up}}$ are the most pessimistic values for excess noise variance, $\Delta(n) \sim \sqrt{\frac{1}{n} \log_2(2\varepsilon_{\text{pa}}^{-1})}$, and ε_{pa} is a privacy amplification security parameter.

As expected, by increasing the key block size, one can achieve performance comparable to the ideal conditions of the asymptotic case. The final results show that with a block size in the range of $10^6 \div 10^9$ signals, it is possible to provide a positive secure key generation rate of about 10^{-2} bits/symbol in the presence of high excess noise $\xi = 0.01$ and attenuation caused by using standard optical fiber over long distances

4. SDI CV-QKD

Alternative DI CV-QKD systems of KKNKP are also worth mentioning. One example of such schemes is SDI QKD [27]. The main idea, just as in the case of MDI, is the ability to protect against attacks associated with non-ideal equipment used in QKD systems.

As in MDI, three independent modules are involved in communication: Alice, Bob and Charlie relay. The main difference is how the relay is used as a source in this system (see Fig. 6). After all, it is Charlie who prepares the two-mode squeezed vacuum state and sends it to Alice and Bob. Since the modes are entangled, Alice and Bob receive correlated information. However, it is still assumed that Charlie is a completely untrusted party that can be completely under the control of Eve in the same way as both quantum channels.

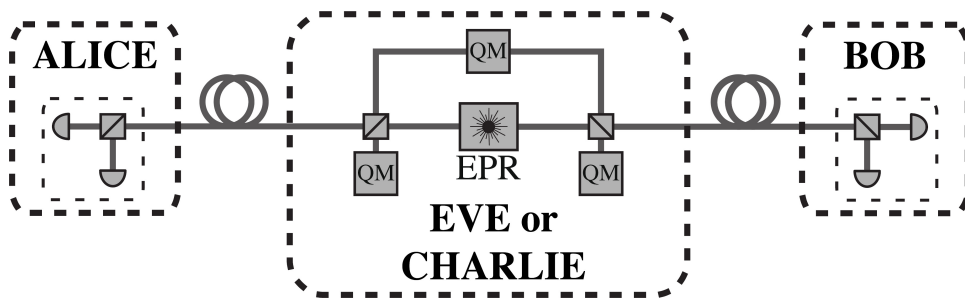


FIG. 6. SDI CV-QKD Scheme. QM is a quantum memory needed to carry out an attack

For SDI CV-QKD system, security to both collective attacks and coherent attacks was proved due to an additional energy test. But the maximum key distribution distance, even in a situation of collective attacks, does not exceed 20 km. While in the presence of coherent it is below 5 km.

5. Conclusion

In this review, we have considered DI CV-QKD protocols. Numerical simulations in the presence of entangling cloner attacks on MDI CV-QKD show that the transmission distance between Alice and Bob is severely limited in the symmetrical case ($L_{AC} = L_{BC}$). In addition, this QKD protocol requires only minor modifications to existing QKD systems and thus can be easily implemented in practice. SDI CV-QKD protocol is also of interest for further study, but does not show the proper level of performance at the moment.

References

- [1] Pirandola S., Andersen U.L., Banchi L., Berta M., Bunandar D., Colbeck R., Englund D., Gehring T., Lupo C., Ottaviani C., Pereira J.L., Razavi M., Shamsul Shaari J., Tomamichel M., Usenko V.C., Vallone G., Villoresi P., and Wallden P. Advances in quantum cryptography, *Advances in Optics and Photonics*, 2020, **12**, P. 1012.
- [2] Shor P.W. and Preskill J. Simple Proof of Security of the BB84 Quantum Key Distribution Protocol, *Physical Review Letters*, 2000, **85**, P. 441–444.
- [3] Laudenbach F., Pacher C., Fung C.-H. F., Poppe A., Peev M., Schrenk B., Hentschel M., Walther P., and Hübel H., Continuous-Variable Quantum Key Distribution with Gaussian Modulation-The Theory of Practical Implementations. *Advanced Quantum Technologies*, 2018 **1**(8), P. 1800011.
- [4] Li Z., Zhang Y.-C., Xu F., Peng X., and Guo H. Continuous-variable measurement-device-independent quantum key distribution. *Physical Review A*, 2014, **89**(5), P. 052301.
- [5] Xu F., Ma X., Zhang Q., Lo H.-K., and Pan J.-W. Secure quantum key distribution with realistic devices. *Reviews of Modern Physics*, 2020, **92**(5), P. 025002.
- [6] Lo H.-K., Curty M., and Qi B. Measurement-Device-Independent Quantum Key Distribution. *Physical Review Letters*, 2012, **108**(3), P. 130503.
- [7] Lucamarini M., Yuan Z.L., Dynes J.F., and Shields A.J. Overcoming the rate–distance limit of quantum key distribution without quantum repeaters. *Nature*, 2018, **557**(5), P. 400–403.
- [8] Bennett C.H. and Brassard G. Quantum cryptography: Public key distribution and coin tossing. *Theoretical Computer Science*, 2014, **560**(12), P. 7–11.
- [9] Hillery M. Quantum cryptography with squeezed states. *Physical Review A*, 2000, **61**(1), P. 22309.
- [10] Cerf N.J., Lévy M., and Assche G.V. Quantum distribution of Gaussian keys using squeezed states. *Physical Review A*, 2001, **63**(4), P. 052311.
- [11] Grosshans F., Van Assche G., Wenger J., Brouri R., Cerf N.J., and Grangier P. Quantum key distribution using gaussian-modulated coherent states. *Nature*, 2003, **421**(1), P. 238–241.
- [12] Weedbrook C., Lance A.M., Bowen W.P., Symul T., Ralph T.C., and Lam P.K. Quantum Cryptography Without Switching. *Physical Review Letters*, 2004, **93**(10), P. 170504.
- [13] Goncharov R., Kiselev A.D., Samsonov E., and Egorov V. Security proof for continuous-variable quantum key distribution with trusted hardware noise against general attacks. *arXiv preprint arXiv:2205.05299*, 5 2022.
- [14] Diamanti E. and Leverrier A. Distributing secret keys with quantum continuous variables: Principle, security and implementations. *Entropy*, 2015, **17**(8), P. 6072–6092.
- [15] Huang D., Huang P., Lin D., and Zeng G. Long-distance continuous-variable quantum key distribution by controlling excess noise. *Scientific Reports*, 2016, **6**(5), P. 19201.
- [16] Zhang Y., Chen Z., Pirandola S., Wang X., Zhou C., Chu B., Zhao Y., Xu B., Yu S., and Guo H. Long-Distance Continuous-Variable Quantum Key Distribution over 202.81 km of Fiber. *Physical Review Letters*, 2020, **125**(6), P. 010502.
- [17] Ghorai S., Grangier P., Diamanti E., and Leverrier A. Asymptotic Security of Continuous-Variable Quantum Key Distribution with a Discrete Modulation. *Physical Review X*, 2019, **9**(6), P. 021059.
- [18] Lin J., Upadhyaya T., and Lütkenhaus N. Asymptotic Security Analysis of Discrete-Modulated Continuous-Variable Quantum Key Distribution. *Phys. Rev. X*, 2019, **9**(12).
- [19] Leverrier A. Composable Security Proof for Continuous-Variable Quantum Key Distribution with Coherent States. *Physical Review Letters*, 2015, **114**(2), P. 070501.
- [20] Leverrier A. Security of Continuous-Variable Quantum Key Distribution via a Gaussian de Finetti Reduction. *Physical Review Letters*, 2017, **118**(5), P. 200501.
- [21] Hosseini N., Walk N., and Ralph T.C. Optimal realistic attacks in continuous-variable quantum key distribution. *Physical Review A*, 2019, **99**(5), P. 1–11.
- [22] Pirandola S. Limits and security of free-space quantum communications. *Physical Review Research*, 2021, **3**(3), P. 013279.
- [23] Pirandola S. Composable security for continuous variable quantum key distribution: Trust levels and practical key rates in wired and wireless networks. *Physical Review Research*, 2021, **3**(10), P. 043014.
- [24] Koashi M. and Preskill J. Secure Quantum Key Distribution with an Uncharacterized Source. *Physical Review Letters*, 2003, **90**(2), P. 057902.
- [25] Makarov V., Anisimov A., and Skaar J. Effects of detector efficiency mismatch on security of quantum cryptosystems. *Physical Review A*, 2006, **74**(2), P. 22313.
- [26] Zhao Y., Fung C.H.F., Qi B., Chen C., and Lo H.K. Quantum hacking: Experimental demonstration of time-shift attack against practical quantum-key-distribution systems. *Physical Review A*, 2008, **78**(4), P. 42333.
- [27] Zhang Y., Chen Z., Weedbrook C., Yu S., and Guo H. Continuous-variable source-device-independent quantum key distribution against general attacks. *Scientific Reports*, 2020, **10**(12), P. 6673.
- [28] Ma X. and Razavi M. Alternative schemes for measurement-device-independent quantum key distribution. *Physical Review A*, 2012, **86**(6), P. 62319.
- [29] Qin H., Huang A., and Makarov V. Short pulse attack on continuous-variable quantum key distribution system. in *QCrypt 2017*, 2017.
- [30] Jouguet P., Kunz-Jacques S., and Diamanti E. Preventing calibration attacks on the local oscillator in continuous-variable quantum key distribution. *Physical Review A - Atomic, Molecular, and Optical Physics*, 2013, **87**(6), P. 1–6.
- [31] Qin H., Kumar R., and Alléaume R. Quantum hacking: Saturation attack on practical continuous-variable quantum key distribution. *Physical Review A*, 2016, **94**(7), P. 012325.
- [32] Pirandola S., Ottaviani C., Spedalieri G., Weedbrook C., Braunstein S.L., Lloyd S., Gehring T., Jacobsen C.S., and Andersen U.L. High-rate measurement-device-independent quantum cryptography. *Nature Photonics*, 2015, **9**(6), P. 397–402.
- [33] Grosshans F., Cerf N.J., Wenger J., Tualle-Brouri R., and Grangier P. Virtual Entanglement and Reconciliation Protocols for Quantum Cryptography with Continuous Variables. *Quantum Information and Computation*, 2003, **3**(7), P. 535–552.
- [34] Devetak I. and Winter A. Distillation of secret key and entanglement from quantum states. *Proceedings of the Royal Society A: Mathematical, Physical and Engineering Sciences*, 2005, **461**(1), P. 207–235.
- [35] Pirandola S., Mancini S., Lloyd S., and Braunstein S.L. Continuous-variable quantum cryptography using two-way quantum communication. *Nature Physics*, 2008, **4**(9), P. 726–730.
- [36] Papanastasiou P., Ottaviani C., and Pirandola S. Finite-size analysis of measurement-device-independent quantum cryptography with continuous variables. *Physical Review A*, 2017, **96**(10), P. 042332.

Information about the authors:

Roman Goncharov – ITMO University, Kronverkskiy, 49, St. Petersburg, 197101, Russia; rkgoncharov@itmo.ru

Egor Bolychev – ITMO University, Kronverkskiy, 49, St. Petersburg, 197101, Russia; 285799@niuitmo.ru

Irina Vorontsova – ITMO University, Kronverkskiy, 49, St. Petersburg, 197101, Russia; viovorontsova@niuitmo.ru

Eduard Samsonov – ITMO University, Kronverkskiy, 49, St. Petersburg, 197101, Russia; Edi.samsonov@gmail.com

Vladimir Egorov – ITMO University, Kronverkskiy, 49, St. Petersburg, 197101, Russia; egorovvl@gmail.com

Conflict of interest: the authors declare no conflict of interest.

Ladder operators approach to representation classification problem for Jordan–Schwinger image of $su(2)$ algebra

Gleb V. Tushavin, Alexander I. Trifanov, Ekaterina V. Zaitseva

ITMO University, Saint Petersburg, Russia

Corresponding author: Gleb V. Tushavin, gleb@tushavin.ru

ABSTRACT The eigenvalues of the complete commuting set of self-adjoint operators determine the classification of states. We construct a classification for the image of the Jordan–Schwinger mapping of the $su(2)$ algebra. We use the ladder operator approach to construct a canonical basis of irreducible representations and define the self-adjoint operators of the complete commuting set.

KEYWORDS Ladder operators, $su(2)$, Jordan–Schwinger map, representation theory

FOR CITATION Tushavin G.V., Zaitseva E.V., Trifanov A.I. Ladder operators approach to representation classification problem for Jordan–Schwinger image of $su(2)$ algebra. *Nanosystems: Phys. Chem. Math.*, 2022, **13** (3), 299–307.

1. Introduction

The study of dynamics of some quantum systems can be reduced to the study of the dynamic group of the Hamiltonian. Generators of the dynamical group form an algebra. The structures of invariant spaces of the algebra and the group are similar. Eigenvalues of self-adjoint operators of the complete commuting set are used to the state classification. The ladder operator approach used to build the complete set and obtain eigenbasis. In articles [1–4], ladder operators are constructed for different algebras, which are obtained in consequence of modification of quantum harmonic oscillator model. In our work, we have formulated a general approach to the analysis of such systems.

The Lie algebra of the dynamic group of the Hamiltonian of the quantum harmonic oscillator model is the Heisenberg–Weyl algebra [5, 6] – $w(1)$. Generators of this algebra are Hermitian-conjugate boson creation/annihilation operators – a and a^\dagger which obey the following commutation relations

$$[a, a^\dagger] = \hat{I}, \quad [a, \hat{I}] = 0 = [a^\dagger, \hat{I}]. \quad (1)$$

Here \hat{I} is the identity operator of algebra $w(1)$. By introducing a particle number operator $\hat{N} = a^\dagger a$, the mentioned Hamiltonian can be expressed as

$$\hat{H} = \hbar\omega(\hat{N} + \frac{1}{2}). \quad (2)$$

The complete commuting set of operators for this Hamiltonian contains only one operator \hat{N} , which spectrum determines the observed energy levels. Operators a and a^\dagger are ladder operators for the operator \hat{N} . They satisfy the commutation relations

$$[\hat{N}, a^\dagger] = a^\dagger, \quad [\hat{N}, a] = -a. \quad (3)$$

Action of ladder operators a and a^\dagger transforms an eigenvector of operator \hat{N} into another eigenvector

$$\begin{aligned} \hat{N}|n\rangle &= n|n\rangle, \quad \hat{N}(a^\dagger|n\rangle) = a^\dagger(\hat{N} + \hat{I})|n\rangle = (n+1)(a^\dagger|n\rangle), \\ \hat{N}(a|n\rangle) &= a(\hat{N} - \hat{I})|n\rangle = (n-1)(a|n\rangle), \quad a|0\rangle = 0 = \hat{N}|0\rangle, \end{aligned} \quad (4)$$

The annihilation operator a (unlike the creation operator a^\dagger) has a non-trivial kernel corresponding to the vacuum state of the quantum oscillator. The corresponding eigenvector $|0\rangle$ is called vacuum vector. Thus, the spectrum of operator \hat{N} consists of integer non-negative numbers $\mathbb{N} \cup \{0\}$, and an arbitrary eigenvector can be obtained by the action of ladder operators on any particular eigenvector, e.g. the vacuum vector. In the canonical basis of the eigenvectors $\{|n\rangle\}$ the operators a and a^\dagger have the form

$$a^\dagger|n\rangle = \sqrt{n+1}|n+1\rangle, \quad a|n+1\rangle = \sqrt{n+1}|n\rangle, \quad a|0\rangle = 0, \quad (5)$$

and vector $|n\rangle$ is expressed as

$$|n\rangle = \frac{1}{\sqrt{n!}}(a^\dagger)^n|0\rangle. \quad (6)$$

In this way, dynamics of multidimensional harmonic oscillator can be described by an algebra which generators are represented through the bosonic polynomials resulting from Jordan–Schwinger mapping [7, 8] of generator matrices into $w(1)^{\otimes m}$ for certain m :

$$X = (x_{ij}) \mapsto \check{X} = \sum_{i,j=1}^m x_{i,j} a_i^\dagger a_j, \quad [\check{X}, \check{Y}] = [X, Y]. \quad (7)$$

The image of the identity matrix is the total particle number operator

$$\check{I} = N = \sum_{\mu=1}^m a_\mu^\dagger a_\mu = \sum_{\mu=1}^m N_\mu. \quad (8)$$

In our paper [10], we consider the image of the algebra $su(2)$ [9] represented by the operators N, J_z, J_+, J_- , which are expressed using bosonic operators a_i, a_i^\dagger by the Jordan–Schwinger mapping of generator matrices of the irreducible representation of dimension $(2s + 1)$ of $su(2)$ algebra [8]:

$$J_z = \sum_{\mu=-s}^s \mu a_\mu^\dagger a_\mu, \quad J_+ = \sum_{\mu=-s}^{\mu=s-1} \sqrt{(s + \mu + 1)(s - \mu)} a_{\mu+1}^\dagger a_\mu = (J_-)^\dagger. \quad (9)$$

We denote this algebra as $su^j(2)$ Bosonic operators for each degree of freedom obey the following commutation relations:

$$[a_i, a_j] = [a_i^\dagger, a_j^\dagger] = 0, \quad [a_i, a_j^\dagger] = \delta_{ij}. \quad (10)$$

The Fock basis, defined by eigenvalues of particle number operators of each degree of freedom, is complete and consists of vectors of the form $|n_{-s}, n_{-s+1}, \dots, n_s\rangle$.

The Jordan–Schwinger mapping is a Lie algebras homomorphism, thus the matrix images obey the same commutation relations as their pre-images. The operators J_z, J_+, J_- are generators of the algebra $su(2)$. They satisfy the corresponding commutative relations

$$[J_z, J_\pm] = \pm J_\pm, \quad [J_+, J_-] = 2J_z. \quad (11)$$

In $su(2)$ algebra, the Casimir operator commuting with all generators exists and by Schur’s lemma, in the space of irreducible representation, such an operator is proportional to the identity operator. Recall that the image of the unit matrix in the Jordan–Schwinger mapping is operator N . Hence,

$$[N, J_z] = 0, \quad [N, J_\pm] = 0. \quad (12)$$

The Casimir operator J^2 for generators J_z, J_+, J_- is defined as follows

$$J^2 = J_z^2 + \frac{1}{2}(J_+ J_- + J_- J_+). \quad (13)$$

The image of the canonical basis of an irreducible representation has standard form

$$\begin{aligned} J_z |j, j_z\rangle &= j_z |j, j_z\rangle, \quad J^2 |j, j_z\rangle = j(j+1) |j, j_z\rangle, \\ J_+ |j, j_z = j\rangle &= 0, \quad J_- |j, j_z = -j\rangle = 0, \\ J_+ |j, j_z\rangle &= \sqrt{(j - j_z)(j + j_z + 1)} |j, j_z + 1\rangle, \\ J_- |j, j_z + 1\rangle &= \sqrt{(j - j_z)(j + j_z + 1)} |j, j_z\rangle. \end{aligned}$$

The commuting set of operators $\{N; J^2, J_z\}$ is complete in the cases $s = \frac{1}{2}$ and $s = 1$. In these cases, the eigenvalues of operators N, J^2, J_z uniquely determine the basis vectors $|n; j, j_z\rangle$. In other cases within a fixed eigenvalue n of the operator N , the eigenvalues $j(j+1)$ of the operator J^2 are nontrivially degenerate. Note that if s is a non-negative integer, then j is also a non-negative integer. The arbitrary Fock vector will be an eigenvector for the operators $\{N; J^2, J_z\}$, but not for the operator J^2 .

The aim of our work is to augment the existing commutative set $N; J^2, J_z$ to a complete one. In our paper, we propose a method for constructing generalized ladder operators, which are used for classification and construction of the canonical basis.

2. Generalized ladder operators

Let us consider the self-adjoint operator $H = H^\dagger$. We will call an operator p^\dagger a *right ladder operator* (hereafter, RLO) if there exists a nonzero selfadjoint operator $P = P^\dagger \neq 0$ commuting with H , such that one of the following commutation relations is satisfied

$$[H, p^\dagger] = p^\dagger P \quad \text{or} \quad H p^\dagger = p^\dagger (P + H). \quad (14)$$

The expression conjugated to (14) is the definition of the *left ladder operator* (LLO)

$$[p, H] = P p. \quad (15)$$

For RLO p^\dagger , we will call the operator P a *right function* in the case when the operator P is represented as a function of $P(H, H_1, \dots, H_n)$ of the commuting set of self-adjoint operators H, H_1, \dots, H_n .

For an arbitrary polynomial of the operator H the operator p is a ladder operator. In view of the bilinearity of the commutator it suffices to show that for any degree of H the following property holds

$$[H^n, p^\dagger] = p^\dagger((H + P)^n - H^n) \quad \text{or} \quad H^n p^\dagger = p^\dagger(H + P)^n. \quad (16)$$

Proof. To prove this statement it is enough to use the recurrent property

$$[H^n, p^\dagger] = [H, p^\dagger]H^{n-1} + H[H^{n-1}, p^\dagger] = p^\dagger P H^{n-1} + [H^{n-1}, p^\dagger](H + P), \quad (17)$$

which can be proved by applying the method of mathematical induction, where the base of induction is the definition of the ladder operator.

Also, one can show that the result of multiplying the RLO by the self-adjoint operator A which commutes with operators H and P is again the RLO of operator H :

$$[H, pA] = pAP. \quad (18)$$

2.1. Ladder operators construction

Let the system of the self-adjoint operator H and the set of operators $\{T_\mu\}_{\mu=1}^n$ have the following properties

$$[H, T_\eta] = \sum_{\mu=1}^n T_\mu \alpha_{\mu\eta}, \quad \alpha_{\mu\eta}^\dagger = \alpha_{\mu\eta}, \quad [\alpha_{\mu\eta}, H] = 0. \quad (19)$$

We are looking for a nontrivial set of self-adjoint operators $\sigma_\eta = \sigma_\eta^\dagger$ which commute with H and $\{\alpha_{\mu\eta}\}$ and the operator $\sum_{\eta=1}^n T_\eta \sigma_\eta$ is the RLO for H again:

$$[H, \sum_{\eta=1}^n T_\eta \sigma_\eta] = \sum_{\eta=1}^n T_\eta \sigma_\eta P, \quad [P, \sigma_\eta] = 0.$$

Substituting (19) into the previous expression, we obtain the following equation

$$\sum_{\mu=1}^n T_\mu \left(\sum_{\eta=1}^n \alpha_{\mu\eta} \sigma_\eta - \sigma_\mu P \right) = 0, \quad (20)$$

which can be represented in matrix form

$$\begin{pmatrix} T_1 & T_2 & \dots & T_n \end{pmatrix} (A - P) \begin{pmatrix} \sigma_1 \\ \sigma_2 \\ \dots \\ \sigma_n \end{pmatrix} = 0, \quad (21)$$

where we use $(A - P)$ instead of matrix

$$(A - P) = \begin{pmatrix} \alpha_{11} - P, & \alpha_{12}, & \dots, & \alpha_{1n} \\ \alpha_{21}, & \alpha_{22} - P, & \dots, & \alpha_{2n} \\ \vdots & \vdots & \ddots & \vdots \\ \alpha_{n1}, & \alpha_{n2}, & \dots, & \alpha_{nn} - P \end{pmatrix}.$$

One of many solutions (21) is the solution to the equation

$$(A - P) \begin{pmatrix} \sigma_1 \\ \sigma_2 \\ \dots \\ \sigma_n \end{pmatrix} = 0. \quad (22)$$

Since all elements of the matrix $(A - P)$ commute with each other, we can consider the determinant of the matrix $(A - P)$, which must be equal to zero, since the coefficients $\{\sigma^\eta\}$ are in the nontrivial kernel of the matrix $(A - P)$. Hence, the equation for the right functions of RLO arises

$$\det(A - P) \equiv 0. \quad (23)$$

The determinant is a polynomial of the operator P of degree n , and its roots are various right-hand functions of RLO. Then, by substituting the obtained roots into equation (21), we can find their corresponding coefficients $\{\sigma_\eta\}$ of the RLO's.

3. Irreducible representations of the $su^J(2)$ algebra

3.1. Ladder operators of the Casimir operator

In this section, we construct ladder operators for the Casimir operator in the case of integer s . If s is integer, then irreducible representations with integer weights only are implemented, and the kernel of operator J_z is always nontrivial for any number of particles. Thus, any irreducible representation can be recovered by ladder operators of the algebra $su(2)$ from its state lying in the kernel of operator J_z . Thus, it suffices to solve the classification problem within the kernel of J_z . When s is half-integer, the irreducible representations of all possible weights are realized. However, the proposed approach can be easily applied to this case: the only difference is that the resulting ladder operators will not commute with the operator J_z but its ladder operators will be.

Let s be a non-negative integer. Consider the set of operators $\{p_k^\dagger\}_{k=0}^s$ and $\{m_k^\dagger\}_{k=1}^s$ commuting with operator J_z

$$\begin{aligned} p_0^\dagger &= 2a_0^\dagger, \\ p_k^\dagger &= \frac{1}{\prod_{i=1}^k \sqrt{(s+i)(s-i+1)}} \left(a_{-k}^\dagger J_+^k + a_k^\dagger J_-^k \right), \\ m_k^\dagger &= \frac{1}{\prod_{i=1}^k \sqrt{(s+i)(s-i+1)}} \left(a_{-k}^\dagger J_+^k - a_k^\dagger J_-^k \right). \end{aligned} \quad (24)$$

All operators from the sets $\{p_k^\dagger\}$ and $\{m_k^\dagger\}$ are ladder operators of operator N

$$[N, p_k^\dagger] = p_k^\dagger, \quad [N, m_k^\dagger] = m_k^\dagger.$$

The operators p_k^\dagger and m_k^\dagger are closed with respect to the action of the Casimir operator J^2 in the sense of definition (19)

$$\begin{aligned} [J^2, p_0^\dagger] &= s(s+1)p_0^\dagger + 2s(s+1)p_1^\dagger, \\ [J^2, p_k^\dagger] &= ((s+k+1)(s-k) - k(k-1))p_k^\dagger + (s+k+1)(s-k)p_{k+1}^\dagger + \\ &\quad + p_{k-1}^\dagger((\hat{j} + J_z + 1)(\hat{j} - J_z) - k(k-1)) + 2k(m_k^\dagger + m_{k-1}^\dagger)J_z, \\ [J^2, m_k^\dagger] &= ((s+k+1)(s-k) - k(k-1))m_k^\dagger + (s+k+1)(s-k)m_{k+1}^\dagger + \\ &\quad + m_{k-1}^\dagger((\hat{j} + J_z + 1)(\hat{j} - J_z) - k(k-1)) + 2k(p_k^\dagger + p_{k-1}^\dagger)J_z, \end{aligned} \quad (25)$$

where the operator \hat{j} is defined as

$$\hat{j} = \frac{1}{2} \left(\sqrt{\hat{I} + 4J^2} - \hat{I} \right). \quad (26)$$

Let us find the right-hand functions of the ladder operators from equation (21). We will construct ladder operators for the kernel J_z since the whole basis of the irreducible representation can be restored by the action of operators J_\pm . For this reason, we can replace the operator J_z in equation (25) by zero $J_z = 0$

$$\begin{aligned} [J^2, p_0^\dagger] &= s(s+1)p_0^\dagger + 2s(s+1)p_1^\dagger, \\ [J^2, p_k^\dagger] &= ((s+k+1)(s-k) - k(k-1))p_k^\dagger + (s+k+1)(s-k)p_{k+1}^\dagger + p_{k-1}^\dagger((\hat{j} + 1)\hat{j} - k(k-1)), \\ [J^2, m_k^\dagger] &= ((s+k+1)(s-k) - k(k-1))m_k^\dagger + (s+k+1)(s-k)m_{k+1}^\dagger + m_{k-1}^\dagger((\hat{j} + 1)\hat{j} - k(k-1)). \end{aligned} \quad (27)$$

Let us construct matrix $(A - P)$. The matrix A is a block-diagonal one

$$A = \begin{pmatrix} P & 0 \\ 0 & M \end{pmatrix},$$

consisting of two tridiagonal matrices P and M of dimensions $\dim P = s + 1$ and $\dim M = s$, respectively,

$$P = \begin{pmatrix} s(s+1) & \hat{j}(\hat{j}+1), & 0, & \dots & 0 & 0 \\ 2s(s+1) & s(s+1) - 4 & (\hat{j}-1)(\hat{j}+2) & \dots & 0 & 0 \\ 0 & (s-1)(s+2) & s(s+1) - 8 & \dots & 0 & 0 \\ \vdots & \vdots & \vdots & \ddots & \vdots & \vdots \\ 0 & 0 & 0 & \dots & -s^2 + 5s - 2 & \hat{j}(\hat{j}+1) - s^2 + s \\ 0 & 0 & 0 & \dots & 2s & -s^2 + s \end{pmatrix}.$$

Matrix M is obtained from matrix P by crossing out the first row and column.

The choice of coefficients at $\{p_k^\dagger\}_{k=0}^s$ and $\{m_k^\dagger\}_{k=1}^s$ makes it symmetric, hence, the matrices P and M have different eigenvalues, which are expressed using the operator \hat{j} . The traces of matrices P and M are equal to the sum of their eigenvalues. The matrix A corresponds to the following set of eigenvalues

$$\left\{ \theta(\theta + 2\hat{j} + 1)\hat{I} \right\}_{\theta=-s}^s,$$

and the matrix P is matched by θ of the same parity as s , and the matrix M by all others.

We will look for the coefficients recurrently, starting with σ_s . For matrices P and M , the equations on the ladder operator will be almost identical. It allows us to obtain a common result for them. Let us find the solution of the following equation

$$(P - \theta(\theta + 2\hat{j} + 1)\hat{I}) \begin{pmatrix} \sigma_0^\theta \\ \sigma_1^\theta \\ \vdots \\ \sigma_s^\theta = \hat{I} \end{pmatrix} = 0.$$

The coefficient σ_{s-1}^θ is found at $\sigma_s^\theta = \hat{I}$:

$$\sigma_{s-1}^\theta = \hat{j} \frac{\theta}{s} + \frac{\theta^2 + \theta + s^2 - s}{2s}. \quad (28)$$

Consider the k -th string:

$$(s-k)(s+k+1)\sigma_{k-1}^\theta + ((s-k)(s+k+1) - k(k-1) - \theta(\theta + 2\hat{j} + 1))\sigma_k^\theta + (\hat{j} - k)(\hat{j} + k + 1)\sigma_{k+1}^\theta = 0$$

and express σ_{k-1}^θ through σ_k^θ and σ_{k+1}^θ :

$$\sigma_{k-1}^\theta = \frac{\theta^2 + \theta + k^2 + k}{(s+k)(s-k+1)}\sigma_k^\theta + \hat{j} \frac{2\theta\sigma_k^\theta}{(s+k)(s-k+1)} - \sigma_k^\theta - \frac{(\hat{j} + k + 1)(\hat{j} - k)}{(s+k)(s-k+1)}\sigma_{k+1}^\theta, \quad (29)$$

where σ_k^θ is a polynomial of the operator \hat{j} of degree $(s-k)$.

Denote the obtained ladder operators as $\{\tau_\theta^\dagger\}_{\theta=-s}^s$

$$\tau_\theta^\dagger = \begin{cases} \sum_{k=0}^s p_k^\dagger \sigma_k^\theta, & \text{for } \theta \text{ of the same parity as } s, \\ \sum_{k=1}^s m_k^\dagger \sigma_k^\theta, & \text{otherwise.} \end{cases} \quad (30)$$

Ladder operators have the following commutative relations with the J^2 operator

$$[J^2, \tau_\theta^\dagger] = \tau_\theta^\dagger \theta(\theta + 2\hat{j} + 1). \quad (31)$$

Since the Casimir operator J^2 is represented as a polynomial $J^2 = \hat{j}(\hat{j} + 1)$ of operator \hat{j} , we obtain commutation relations between \hat{j} and $\{\tau_\theta^\dagger\}$ from the solution of the following equation

$$[\hat{j}^2 + \hat{j}, \tau_\theta^\dagger] = \tau_\theta^\dagger X(X + 2\hat{j} + 1) = \tau_\theta^\dagger \theta(\theta + 2\hat{j} + 1).$$

Hence, $X = \theta\hat{I}$ and

$$[j, \tau_\theta^\dagger] = \theta\tau_\theta^\dagger. \quad (32)$$

Operators $\{\tau_\theta^\dagger\}$ are also ladder operators for operators $\frac{1}{2\hat{j} + (2k+1)\hat{I}}$, where k is non-negative:

$$\left[\frac{1}{2\hat{j} + (2k+1)\hat{I}}, \tau_\theta^\dagger \right] = \tau_\theta^\dagger \left(\frac{1}{2\hat{j} + (2k+1)\hat{I}} - \frac{1}{2\hat{j} + (2(k-\theta)+1)\hat{I}} \right). \quad (33)$$

There is similar expression with the left-hand function:

$$\left[\frac{1}{2\hat{j} + (2k+1)\hat{I}}, \tau_\theta^\dagger \right] = \left(\frac{1}{2\hat{j} + (2k+1)\hat{I}} - \frac{1}{2\hat{j} + (2(k-\theta)+1)\hat{I}} \right) \tau_\theta^\dagger. \quad (34)$$

For an arbitrary polynomial of functions $\{\hat{j}^k\}_{k=0}^n$ and $\left\{ \left(\frac{1}{2\hat{j} + (1+2k)\hat{I}} \right)^k \right\}_{k=0}^n$ commutative relations with $\{\tau_\theta\}$ or $\{\tau_\theta^\dagger\}$ can be obtained.

Single-particle Fock states belongs to the irreducible representation of the algebra $su(2)$ corresponding to the eigenvalue $s(s+1)$ of the Casimir operator J^2

$$J^2 |0, 0, \dots, n_k = 1, \dots, 0\rangle = s(s+1) |0, 0, \dots, n_k = 1, \dots, 0\rangle,$$

and the kernel J_z is one-dimensional and consists of the following vector

$$J_z |0, 0, \dots, n_0 = 1, \dots, 0\rangle = 0.$$

The action of the ladder operators $\{\tau_\theta^\dagger\}$ allows us to construct the canonical basis of the kernel J_z . At these, it is easy to show that

$$[\tau_\theta^\dagger \tau_\theta, J^2] = 0 = [\tau_\theta^\dagger \tau_\theta, J_z] = [\tau_\theta^\dagger \tau_\theta, N].$$

Thus, the commuting set $\{N; J^2, j_z\}$ can be augmented to complete set of commuting operators by some self-adjoint polynomials of ladder operators.

3.2. The annihilated states of the ladder operators of the Casimir operator

The geometry of the Fock space allows us to find annihilated states of ladder operators $\left\{\tau_\theta^\dagger, \tau_\theta\right\}_{\theta=-s}^s$. Consider the vectors of the operators \hat{j} and N lying in the kernel of the operator J_z

$$|n, j, j_z = 0\rangle,$$

Given n the eigenvalues of the operator \hat{j} are in the range $0 \leq j \leq ns$. The action of operators within the J_z kernel can be represented by the following scheme for $\omega = 1 \dots s$:

$$\begin{aligned} \tau_\omega^\dagger |n, j\rangle &\Rightarrow |n+1, j+\omega\rangle, & \tau_{-\omega}^\dagger |n, j+\omega\rangle &\Rightarrow |n+1, j\rangle, \\ \tau_\omega |n+1, j+\omega\rangle &\Rightarrow |n, j\rangle, & \tau_{-\omega} |n+1, j\rangle &\Rightarrow |n, j+\omega\rangle. \end{aligned} \quad (35)$$

Operators τ_ω^\dagger have a trivial kernel if ω is the same parity, as s . If ω differs in parity from s , then all one-particle state lies in the kernel of τ_ω^\dagger . This is due to the antisymmetric definition of the operator τ_ω^\dagger for ω other than s parity.

The operators τ_ω transforms all states $j < \omega$ and the vacuum state $n = 0$ into zero, Thus, implementing ω of different representations of the algebra. The algebra of the pair of operators τ_ω^\dagger and τ_ω itself is a deformation of the Weyl algebra $w(1)$. Its different representations are defined by the number $r_\theta = j \bmod \omega$ and the eigenvalues of the self-adjoint operators $\tau_\omega^\dagger \tau_\omega$.

The operators $\tau_{-\omega}^\dagger$ annihilate all states $j < \omega$, and the operators $\tau_{-\omega}$ annihilate all states $j > ns - \omega$ and vacuum state $n = 0$. Thus, we can say that the operators $\tau_{-\omega}^\dagger$ and $\tau_{-\omega}$ represent a deformation of the algebra $su(2)$, where the representations differ by the number $r_\theta = j \bmod \omega$ and the eigenvalues of the self-adjoint operators

$$L_z^\omega = [\tau_{-\omega}^\dagger, \tau_{-\omega}], \quad L_\omega^2 = (L_z^\omega)^2 + \frac{1}{2} (\tau_{-\omega}^\dagger \tau_{-\omega} + \tau_{-\omega} \tau_{-\omega}^\dagger).$$

The operators τ_0^\dagger and τ_0 do not change the eigenvalues of the Casimir operator J^2

$$\tau_0^\dagger |n, j\rangle \Rightarrow |n+1, j\rangle, \quad \tau_0 |n+1, j\rangle \Rightarrow |n, j\rangle. \quad (36)$$

4. Case $s = 1$

In this case, the classification problem is of small interest because of all subspaces of kernel J_z are one-dimensional and the set of commuting operators $N; J^2, J_z$ is complete. However, the use of ladder operators can be well demonstrated by the following example. For the case of $s = 1$, the generators of the $su(2)$ algebra are represented as follows

$$J_z = \sum_{\mu=-1}^1 \mu a_\mu^\dagger a_\mu, \quad J_+ = (J_-)^\dagger = \sum_{\mu=-1}^{\mu=0} \sqrt{(\mu+2)(1-\mu)} a_{\mu+1}^\dagger a_\mu. \quad (37)$$

Consider the following operators

$$p_0^\dagger = 2a_0^\dagger, \quad \sqrt{2}p_1^\dagger = a_1^\dagger J_- + a_{-1}^\dagger J_+, \quad (38)$$

with the following commutation relations

$$\begin{aligned} [p_0, p_0^\dagger] &= 4, & [p_1, p_1^\dagger] &= 2\hat{j}(\hat{j}+1) - J_z(2J_z+1) + (N-N_0)(J_z-2), \\ [p_1, p_0^\dagger] &= 2(N-N_0), & [p_0, p_1^\dagger] &= 2(N-N_0), \end{aligned} \quad (39)$$

where $N_0 = a_0^\dagger a_0$.

The m_1^\dagger operator annihilates the J_z kernel (this is trivially checked) if we consider the action of the m_1^\dagger operator on arbitrary Fock state $|n_{-1} = m, n_0 = k, n_1 = m\rangle$. However, outside the kernel J_z the operator m_1^\dagger acts nontrivially, which is important in the construction of ladder operators on the whole Fock space. In our case it is important to obtain

canonical basis inside the kernel of J_z , because the whole basis can be reconstructed by the action of the operators J_+ and J_- .

Consider commutative relations of operators p_i^\dagger with operator J^2

$$[J^2, p_0^\dagger] = 2p_0^\dagger + 4p_1^\dagger, \quad [J^2, p_1^\dagger] = p_0^\dagger J_- J_+ = p_0^\dagger (\hat{j} - J_z)(\hat{j} + J_z + 1).$$

Assume $J_z \equiv 0$ and rewrite the commutation relations

$$[J^2, p_0^\dagger] = 2p_0^\dagger + 4p_1^\dagger, \quad [J^2, p_1^\dagger] = p_0^\dagger \hat{j}(\hat{j} + 1). \quad (40)$$

The solution of the equation for the right functions of the ladder operators is given by the operators $-2\hat{j}$ and $2(\hat{j} + 1)$.

Denote the ladder operators τ_{-1}^\dagger and τ_1^\dagger . They have the following commutative relations with the operator J^2

$$[J^2, \tau_{-1}^\dagger] = -\tau_{-1}^\dagger 2\hat{j}, \quad [J^2, \tau_1^\dagger] = \tau_1^\dagger 2(\hat{j} + 1). \quad (41)$$

They are expressed using the operators p_0^\dagger and p_1^\dagger as follows

$$\tau_{-1}^\dagger = p_0^\dagger \hat{j} - 2p_1^\dagger, \quad \tau_1^\dagger = p_0^\dagger (\hat{j} + 1) + 2p_1^\dagger. \quad (42)$$

Commutative relations for the operator \hat{j} :

$$[\hat{j}, \tau_{-1}^\dagger] = -\tau_{-1}^\dagger, \quad [\hat{j}, \tau_1^\dagger] = \tau_1^\dagger. \quad (43)$$

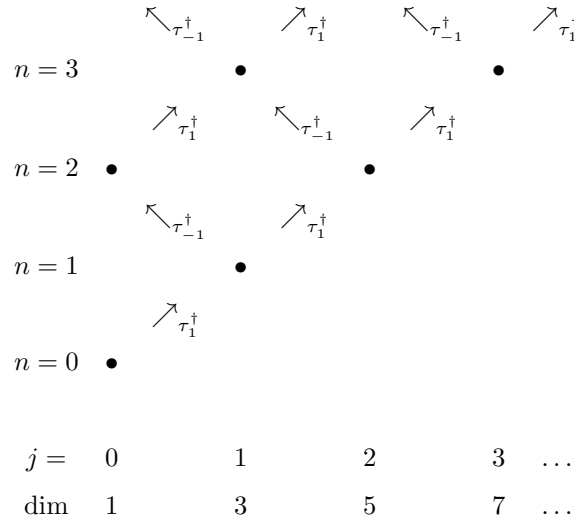
From the Jacobi relation we also obtain that the commutator $[\tau_1^\dagger, \tau_{-1}^\dagger]$ is a ladder operator \hat{j} :

$$[\hat{j}, [\tau_1^\dagger, \tau_{-1}^\dagger]] = 2[\tau_1^\dagger, \tau_{-1}^\dagger].$$

Any vector of the canonical basis can be obtained by the joint action of the ladder operators

$$|n, j, j_z\rangle_{su2} = \alpha(n, j, j_z) \begin{cases} J_+^{j_z} (\tau_{-1}^\dagger)^{\frac{n-j}{2}} (\tau_1^\dagger)^{\frac{n+j}{2}} |000\rangle_F, & j_z > 0 \\ (\tau_{-1}^\dagger)^{\frac{n-j}{2}} (\tau_1^\dagger)^{\frac{n+j}{2}} |000\rangle_F, & j_z = 0 \\ J_-^{j_z} (\tau_{-1}^\dagger)^{\frac{n-j}{2}} (\tau_1^\dagger)^{\frac{n+j}{2}} |000\rangle_F, & j_z < 0. \end{cases}$$

The action of ladder operators and the structure of irreducible representations of the algebra $su(2)$ can be visualized by the following scheme for $j_z = 0$:



Now, consider again the operators p_0^\dagger and p_1^\dagger which can be expressed using the operators τ_{-1}^\dagger and τ_1^\dagger

$$p_0^\dagger = \left(\tau_1^\dagger + \tau_{-1}^\dagger \right) \frac{1}{2\hat{j} + 1}, \quad p_1^\dagger = \frac{1}{4} \left((\tau_1^\dagger - \tau_{-1}^\dagger) - (\tau_1^\dagger + \tau_{-1}^\dagger) \frac{1}{2\hat{j} + 1} \right),$$

where we find commutative relations with the operator \hat{j} . We obtain

$$[\hat{j}, p_0^\dagger] = (p_0^\dagger + 4p_1^\dagger) \frac{1}{2\hat{j} + 1}, \quad [\hat{j}, p_1^\dagger] = (p_0^\dagger J^2 - p_1^\dagger) \frac{1}{2\hat{j} + 1}. \quad (44)$$

Define new operators, which will also be RLOs of the operator \hat{K}

$$A^\dagger = \tau_1^\dagger \frac{1}{2\sqrt{\hat{j}+1}} \frac{1}{\sqrt{(N+1)+\hat{j}+1+1}} \frac{\sqrt{2(\hat{j}+1)+1}}{\sqrt{2(\hat{j}+1)-1}}, \quad (45)$$

$$L_+ = \tau_{-1}^\dagger \frac{1}{2\sqrt{2}\sqrt{\hat{j}+1}} \frac{\sqrt{2(\hat{j}+1)-1}}{\sqrt{2(\hat{j}+1)+1}}. \quad (46)$$

The operators A and A^\dagger , defined above, satisfy the commutation relations of the Weyl algebra $w(1)$

$$[A, A^\dagger] = \hat{I}.$$

Self-adjoint operator $A^\dagger A$ has the same eigenvalues as the operator \hat{j} . The action of the operator on the state $|n, j j_z\rangle$ is defined by the formula

$$A^\dagger A |n, j j_z\rangle = j |n, j j_z\rangle.$$

Using the operators L_\pm as self-adjoint polynomials, the operators L_z and L^2 are defined as follows

$$L_z = \frac{1}{2}[L_+, L_-], \quad L^2 = L_z^2 + L_z + L_- L_+.$$

They satisfy the commutation relations of the algebra $su(2)$. Their action on the eigenstates is given by the following expression

$$L_z |n, j j_z\rangle = \left(\frac{n-j}{2} - \frac{n+j}{4} \right) |n, j j_z\rangle,$$

$$L^2 |n, j j_z\rangle = \frac{n+j}{4} \left(\frac{n+j}{4} + 1 \right) |n, j j_z\rangle.$$

The operators $A^\dagger A$, L_z and L^2 form a complete commutative set and can be used to classify the states of such a system on a par with the sets N_{-1} , N_0 , N_1 and K , J_z , N .

By constructing left-hand ladder operators for J^2 , we obtain another form of ladder operators

$$\bar{\tau}_1 = [a_0, \hat{j}] + a_0, \quad \bar{\tau}_{-1} = -[a_0, \hat{j}] + a_0,$$

$$\bar{\tau}_1^\dagger = [\hat{j}, a_0^\dagger] + a_0^\dagger, \quad \bar{\tau}_{-1}^\dagger = -[\hat{j}, a_0^\dagger] + a_0^\dagger. \quad (47)$$

From which, in particular, an interesting expression emerges

$$[\hat{j}[\hat{j}, a_0^\dagger]] = a_0^\dagger.$$

5. Conclusion

A method of classification and construction of invariant spaces corresponding to various irreducible representations of the $su(2)$ algebra is proposed for $su^j(2)$ algebra. We obtained a set of the ladder operators for the Casimir operator of the $su^j(2)$ algebra, which is used to find the canonical basis of the algebra. Algebras formed by ladder operators are deformations of known algebras, which eigenvalues determine persistent states of the Hamiltonian. In this paper we considered the simplest case for the algebra $su^j(2)$ and applied the ladder operator approach to demonstrate the method. The ladder operator approach is based on commutative algebra relations and can be applied to the analysis of irreducible representations of various Lie algebras. In this paper, we obtained an infinite basis of a complex structure which can be recovered from any chosen element of basis by the action of the ladder operators.

References

- [1] Williams C.L., Pandya N.N., Bodmann B.G., Kouri D.J. Coupled supersymmetry and ladder structures beyond the harmonic oscillator. *Molecular Physics*, 2018, **116** (19–20), P. 2599–2612.
- [2] Hoffmann S.E., Hussin V., Marquette I., Zhang Y.-Z. Ladder operators and coherent states for multi-step supersymmetric rational extensions of the truncated oscillator. *J. Math. Phys.*, 2019, **60**, 052105.
- [3] Bosso P., Das S. Generalized ladder operators for the perturbed harmonic oscillator. *Ann. of Phys.*, 2018, **396**, P. 254–265.
- [4] Aouda K., Kanda N., Naka S., Toyoda H. Ladder Operators in Repulsive Harmonic Oscillator with Application to the Schwinger Effect. *Phys. Rev. D*, 2020, **102**, 025002.
- [5] Weyl H., Robertson H.P. *The theory of groups and quantum mechanics*, Dover Publications, New York, 1950.
- [6] Perelomov A.M. *Generalized Coherent States and Their Applications*, Springer, Berlin, 1986.
- [7] Biedenharn L.C., Louck J.D. *Angular momentum in quantum physics*, Cambridge university press, Cambridge, 1984.
- [8] Miroshnichenko G.P., Kiselev A.D., Trifanov A.I., Gleim A.V. Algebraic approach to electro-optic modulation of light: exactly solvable multimode quantum model. *J. Opt. Soc. Am. B*, 2017, **34** (6), P. 1177–1190.

- [9] Gelfand I.D., Shapiro Z.Ya., Minlos R.A. *Representations of the Rotation and Lorentz Groups and Their Applications*, The Pergamon Press, Oxford, 1963.
- [10] Tushavin G.V., Trifanov A.I., Trifanova E.S., Shipitsyn I.A. Structure of invariant subspaces of the rotation group image under the Jordan mapping. *2019 Days on Diffraction (DD)*, 2019, St. Petersburg, Russia, P. 216–220.

Submitted 1 May 2022; revised 12 June 2022; accepted 13 June 2022

Information about the authors:

Gleb V. Tushavin – Faculty of Control Systems and Robotics, ITMO University, St. Petersburg, 197101, Russia;
ORCID 0000-0002-6482-0951; gleb@tushavin.ru

Alexander I. Trifanov – Faculty of Control Systems and Robotics, ITMO University, St. Petersburg, 197101, Russia;
alextrifanov@gmail.com

Ekaterina V. Zaitseva – Faculty of Control Systems and Robotics, ITMO University, St. Petersburg, 197101, Russia;
ORCID 0000-0003-3982-3592; zaytceva.workmail@gmail.com

Conflict of interest: the authors declare no conflict of interest.

CeO₂-calcein nanoconjugate protective action against H₂O₂-induced oxidative stress *in vitro*

Nikita N. Chukavin^{1,2,a}, Anton L. Popov^{1,b}, Alexander B. Shcherbakov^{3,c}, Olga S. Ivanova^{4,d}, Arina D. Filippova⁴, Vladimir K. Ivanov^{4,e}

¹Institute of Theoretical and Experimental Biophysics, Pushchino, Russia

²Moscow Region State University, Moscow, Russia

³Zabolotny Institute of Microbiology and Virology, Kyiv, Ukraine

⁴Kurnakov Institute of General and Inorganic Chemistry, Moscow, Russia

^achukavinnik@gmail.com, ^bantonpopovleonid@gmail.com, ^cceroform@gmail.com, ^drunetta05@mail.ru, ^evan@igic.ras.ru

Corresponding author: Vladimir K. Ivanov, van@igic.ras.ru

PACS 68.65.-k, 81.20.-n, 82.70. Dd, 87.80.-y

ABSTRACT We studied cerium oxide-calcein nanoconjugate, which is capable of providing intracellular detection and simultaneous inactivation of reactive oxygen species (ROS). The synthesized nanoconjugate is easily uptaken by human mesenchymal stem cells (MSCs) and demonstrates antioxidant properties, protecting cells from H₂O₂-induced oxidative stress *in vitro*. Cerium oxide-calcein nanoconjugate neutralizes hydrogen peroxide, meanwhile releasing brightly fluorescent calcein from its surface, which is easily detected by fluorimeter or fluorescent microscope. This nanoconjugate is biocompatible and non-toxic to MSCs in concentrations below 2 mM. Such a theranostic agent can be considered as a promising tool for tracking the redox status of human MSCs *in vivo*.

KEYWORDS cerium oxide, calcein, bioimaging, cell uptake, oxidative stress, theranostics

ACKNOWLEDGEMENTS The work was supported by the Russian Science Foundation (project 20-74-00086).

FOR CITATION Chukavin N.N., Popov A.L., Shcherbakov A.B., Ivanova O.S., Filippova A.D., Ivanov V.K. CeO₂-calcein nanoconjugate protective action against H₂O₂-induced oxidative stress *in vitro*. *Nanosystems: Phys. Chem. Math.*, 2022, **13** (3), 308–313.

1. Introduction

Nanomedicine is a modern branch of medicine that uses a nanotechnological approach in creating new formulations of medical and diagnostic agents. Such agents are able to detect and to treat more effectively various neoplasms or pathological processes in the body. Cerium oxide (CeO₂) nanoparticles are among the most promising biomedical agents of modern nanotechnology [1–3]. CeO₂ nanoparticles are metal oxide-based nanoparticles that have an outstanding ability of reactive oxygen species (ROS) scavenging [4]. It was found that CeO₂ nanoparticles are able to effectively inhibit the development of a number of diseases caused by oxidative stress, including diabetes, cancer, atherosclerosis, etc. [5–7]. It has been shown that CeO₂ nanoparticles are able to mimic enzyme activity such as catalase [8], SOD [9], oxidase [10], peroxidase [11] phosphatase [12], which distinguish them from the other metal oxide nanoparticles. The biological activity of CeO₂ nanoparticles depends strongly on the scheme of their synthesis, the type of stabilizer and the microenvironment in which they perform their biological function. Dar et al. demonstrated size-dependent antibacterial activity of CeO₂ nanoparticles against the gram-negative strain of *Escherichia coli* (*E. coli*) HB101 K-12 [13]. It was found that the inhibition of bacterial growth depends on the average size and the concentration of cerium oxide nanoparticles. It has been shown that dextran-stabilized CeO₂ nanoparticles exhibit selective anticancer activity against MG-63 human osteosarcoma cells [14]. It was also demonstrated that CeO₂ nanoparticles are much more cytotoxic to human osteosarcoma cells in a slightly acidic environment (pH = 6) compared to physiological and basic pH values (pH = 7 and pH = 9, respectively). On the contrary, minimal toxicity was observed to non-transformed cells when cultured with CeO₂ nanoparticles at pH = 6 in the concentration range of 10 – 1000 μg/mL. Using various methods and approaches for the synthesis of bioactive CeO₂ nanoparticles, it is possible to control the mode of their activity. In addition, the catalytic activity of CeO₂ nanoparticles seems to depend on the chemical composition of their surface, which can be regulated using various ligands. For example, it has been shown that doping of the cerium oxide crystal lattice with gadolinium provides an increase in their catalytic activity and their suitability for MRI imaging [15]. Various functional agents are used to enhance the therapeutic effect of CeO₂ nanoparticles. Indocyanine green conjugated CeO₂ nanoparticles were used as anti-inflammatory agent in collagen-induced arthritis (CIA) mouse model [16]. It was found that functionalized

CeO₂ nanoparticles could be delivered systemically with accumulation in synovial tissues of joints through the SPARC-mediated mechanism, and they effectively inhibit inflammation *via* reducing hypoxia, scavenging excessive ROS, and restoring the disbalance of M1/M2 macrophages.

Thus, the design of new functional cerium oxide-based nanomaterials with specific therapeutic or diagnostic activity is an urgent task. Here we propose a new cerium oxide-based nanoconjugate with calcein that is capable of simultaneously inactivating and detecting ROS in the cell *in vitro*.

2. Materials and methods

2.1. Synthesis and characterization of CeO₂-calcein nanoconjugate

CeO₂-calcein nanoconjugate was synthesized by the method described earlier [17]. The hydrodynamic diameter and the ζ -potential values of CeO₂-calcein nanoconjugate were measured using a Zetasizer Nano ZS analyzer (Malvern Instruments Ltd., UK). Transmission electron microscopy (TEM) analysis was performed using a Libra 200 MC microscope (Zeiss, Germany).

2.2. Cell culture

The experiments were performed using a culture of primary human mesenchymal stem cells derived from the third molar bud, extracted in a healthy 16-year-old patient by orthodontic indications. Cells were cultured in DMEM/F12 (1:1) medium containing 10 % fetal calf serum and 200 units of penicillin/streptomycin at 37 °C in an atmosphere with 5 % CO₂. Cells were removed from culture flasks using 0.25 % trypsin-EDTA solution after washing them three times with Hanks' solution and then were seeded in 96-well plates at a density of $2.5 \cdot 10^4/\text{cm}^2$. The cytotoxicity of the CeO₂-calcein nanoconjugate was analyzed by replacing the initial cell culture medium with a medium, containing different concentrations of the conjugate.

2.3. MTT assay

Analysis of the cell viability after incubation with CeO₂-calcein nanoconjugate was performed after 24, 48 and 72 hours of incubation using the MTT assay. Cells were seeded in 96 well plates at a density of $2.5 \cdot 10^4/\text{cm}^2$ in a DMEM/F12 culture medium containing 10 % fetal calf serum. After 8 hours, CeO₂-calcein nanoconjugate (10 μM – 10 mM) were added by changing the culture medium. Then, after 24, 48 and 72 hours, the medium was replaced with a solution of the MTT reagent (0.5 mg/mL) and further analysis was carried out according to the standard method [18].

2.4. Fluorescent microscopy

Intracellular visualization of CeO₂-calcein nanoconjugate was performed using an inverted fluorescence microscope Zeiss Axiovert 200. Cells were seeded in 35 mm Petri dishes with a central hole (Ibidi, Germany) at a density of $2.5 \cdot 10^4/\text{cm}^2$ in a DMEM/F12 culture medium containing 10 % fetal calf serum. Afterwards, CeO₂-calcein nanoconjugate were added to the cells at a concentration of 1 – 10 mM. After 24 hours, microphotography of cell cultures was carried out after washing three times with a Hanks solution. The viability of MSCs after incubation with nanoconjugate was analyzed by Live/Dead assay using an inverted fluorescence microscope Zeiss Axiovert 200. LIVE/DEAD BacLight Bacterial Viability Kit (Invitrogen) was used containing SYTO 9 (stains all cells, $\lambda = 485/498$ nm) and propidium iodide (stains the nuclei of dead cells, $\lambda = 535/617$ nm) dyes. Microphotography was performed using a Power Shot A620 digital camera (Canon).

2.5. Oxidative stress model

The biological action of CeO₂-calcein nanoconjugate was analyzed using an experimental model of oxidative stress: treatment by 1 mM hydrogen peroxide for 30 minutes. Cell viability analysis was performed using MTT assay after 24 hours.

2.6. ROS and MMP monitoring *in vitro*

Detection of the free calcein fluorescence in the cells was carried out at excitation/emission wavelengths 501/521 nm using a Synergy H1 Hybrid multi-mode microplate reader (Biotek, USA) for 3 hours after 1 mM hydrogen peroxide addition. Membrane mitochondrial potential (MMP) was monitored using the fluorescent dye tetramethylrhodamine ethyl ester perchlorate (TMRE) at excitation/emission wavelengths 553/557 nm.

2.7. Statistical analysis

Data are presented as standard deviation from the mean value. The significance of differences between experimental groups was assessed by the Mann-Whitney U test.

3. Results

Zeta potential of the nanoparticles diluted in distilled water was -26.7 ± 6.6 mV. According to the TEM data, nanoconjugate particle size was about 4 – 5 nm (Fig. 1a). The hydrodynamic diameter of the nanoconjugate particles dispersed in water was about 7 – 10 nm (Fig. 1b). The synthesized CeO₂-calcein nanoconjugate demonstrating good colloidal stability and can be stored for at least 1 year without sedimentation.

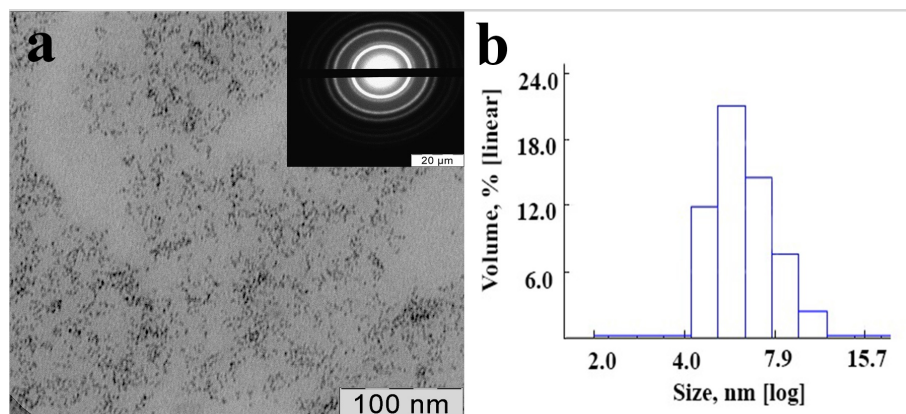


FIG. 1. Transmission electron microscopy of CeO₂-calcein nanoconjugate (a) and dynamic light scattering in MQ water (b)

At the first stage, biocompatibility of the CeO₂-calcein nanoconjugate was analyzed using the MTT assay. This assay determines the enzymatic activity of intracellular mitochondrial NADPH-dependent oxidoreductases, and reflects cells viability after their interaction with the test substance. The results of the MTT assay on human MSCs incubated with various concentrations of CeO₂-calcein nanoconjugate for 24, 48 and 72 hours are shown in Fig. 2. CeO₂-calcein nanoconjugate at a concentration of 200 μ M and 1 mM ($p = 0.004$) significantly reduces the level of metabolic activity after 24 hours of incubation. There is also a significant decrease in cell viability in comparison with the untreated control (without the addition of a nanoconjugate) after 48 and 72 hours of incubation at concentrations of 1 – 10 mM ($p = 0.016$). A promoting effect of the CeO₂-calcein nanoconjugate is observed after 72 hours of incubation with 20 μ M of nanoconjugate ($p = 0.016$). Such stimulating activity may be associated with the promoting effect of CeO₂ nanoparticles on the proliferative and migratory activity of human MSCs [19, 20]. Thus, according to the MTT assay, a high degree of biocompatibility of CeO₂-calcein nanoconjugate is observed in sufficiently low concentrations (below 1 mM) to human MSCs.

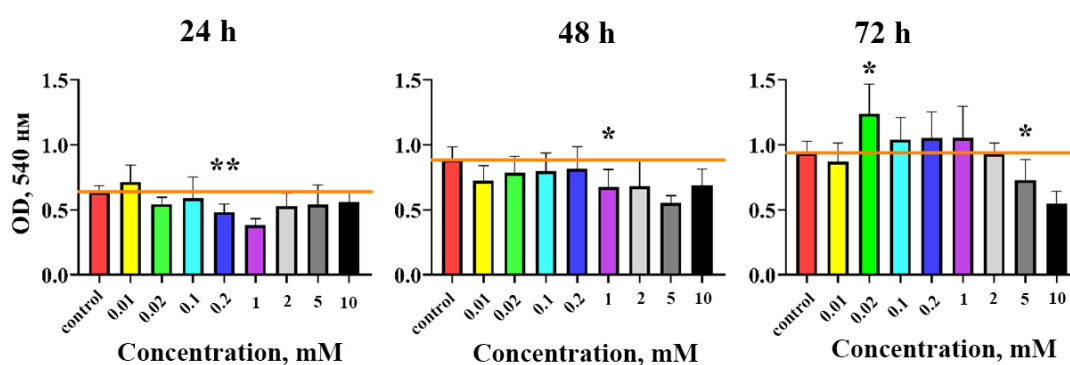


FIG. 2. MTT assay data for human MSCs after 24, 48 and 72 hours of incubation with CeO₂-calcein nanoconjugate in various concentrations (0.01 – 10 mM)

The effect of the CeO₂-calcein nanoconjugate on the morphofunctional state of human MSCs and the viability was analyzed by fluorescence microscopy. Fig. 3 shows micrographs of human MSCs stained with SYTO9/propidium iodide fluorescent dyes after their incubation with nanoconjugate in various concentrations (1 – 10 mM) for 24, 48 and 72 hours. 100 % absence of dead cells is confirmed in all the cases. This may simultaneously indicate both the absence of a pronounced toxic effect of the nanocomposite on mesenchymal stem cells, and the possible removal of dead cells at the

sample preparation stage. Also, excessive fluorescence is observed for nanoconjugate concentrations of 5 and 10 mM, that may be due to the luminescence of calcein, which has not entered the cells but has localized in the culture medium and on the cell surface [21].

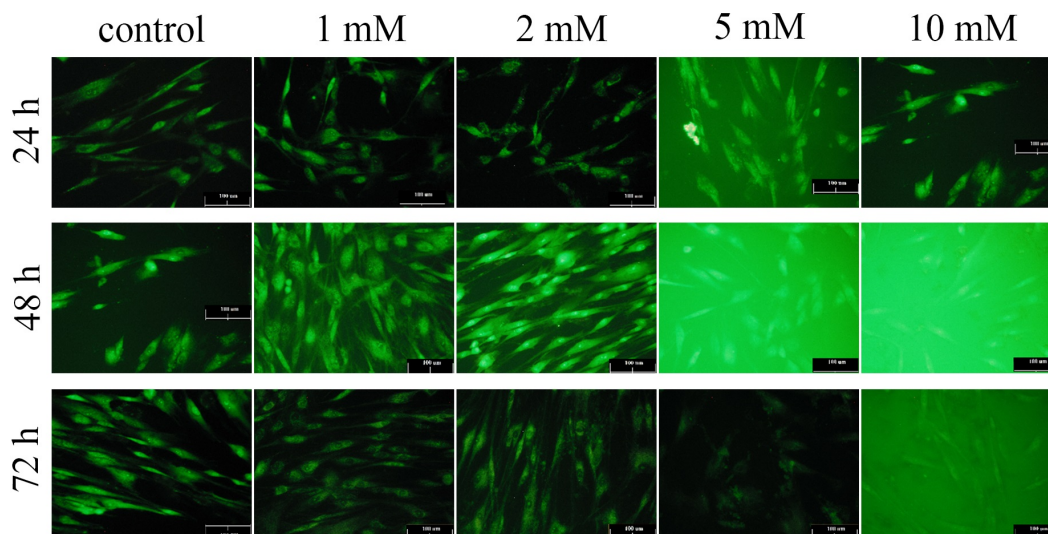


FIG. 3. Micrographs of human MSCs stained with SYTO9/propidium iodide fluorescent dyes after their incubation for 24, 48 and 72 hours with CeO₂-calcein nanoconjugate in concentrations from 1 to 10 mM. All cells are coloured green, and only dead cells are coloured both green and red. The scale is 100 μ m

The micrographs of human MSCs incubated with hydrogen peroxide at concentration of 0.125 – 1 mM are presented on the top panel of Fig. 4. The microphotographs show that the morphology of cells changes significantly under the action of H₂O₂ at concentrations of 500 μ M and 1 mM. Human MSCs lose focal contacts and reduce the degree of spreading after incubation with hydrogen peroxide. Moreover, in both cases, there is a statistically significant decrease in the metabolic activity of cells (Fig. 4, bottom panel). This indicates the cytotoxicity of hydrogen peroxide in both concentrations [22]. Thus, we selected a hydrogen peroxide concentration of 1 mM for further modeling of oxidative stress *in vitro*.

The antioxidant activity of the CeO₂-calcein nanoconjugate was analyzed in the model of H₂O₂-induced oxidative stress (Fig. 5). The dynamics of the calcein fluorescence intensity change (Fig. 5a) shows that the nanoconjugate at concentrations of 1 mM, 200 μ M and 100 μ M neutralizes readily exogenous ROS, that is confirmed by an increase in the fluorescence intensity. Therefore, CeO₂-calcein nanoconjugate can be used to detect the intracellular level of ROS and also to inactivate them locally. Next, the level of the membrane mitochondrial potential (MMP) of human MSCs after incubation with nanoconjugate was analyzed. MMP is an indirect indicator of intracellular oxidative stress [23]. An increase in the MMP compared to the control value was revealed in the cells which were pre-incubated with nanoconjugate (Fig. 5b). This confirms the antioxidant activity of the CeO₂-calcein nanoconjugate, which provides a high level of MMP, while maintaining the antioxidant status of human MSCs.

4. Conclusions

Here, we synthesized, characterized and investigated the CeO₂-calcein nanoconjugate, which can be considered as a promising theranostic agent for *in situ* monitoring of oxidative stress in the cells. It has been shown that the CeO₂-calcein nanoconjugate is biocompatible even in high concentrations (up to 1 mM). The CeO₂-calcein nanoconjugate does not cause any changes in morphofunctional characteristics of human MSCs. Also, CeO₂-calcein nanoconjugate is able to detect the level of ROS in cells *in vitro* at concentration of 0.1 – 1 mM. It has been shown that the nanoconjugate is capable of efficient inactivation of hydrogen peroxide, maintaining a high level of viability and mitochondrial potential of human MSCs under oxidative stress conditions. Thus, cerium-containing nanocomposites can be considered as a basis for the creation of new multifunctional theranostic agents.

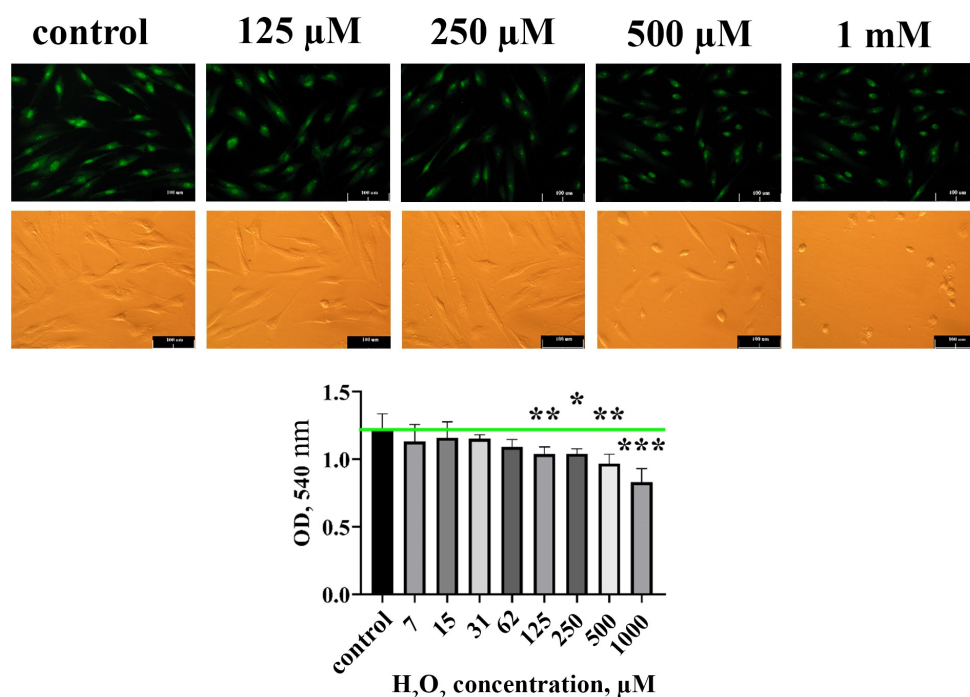


FIG. 4. Validation of the model of oxidative stress induced by the injection of exogenous hydrogen peroxide to human MSCs. Top panel: micrographs recorded in phase contrast and fluorescence modes. Bottom panel: a graph of the optical density of formazane according to the MTT assay 24 hours after the treatment of the cells with hydrogen peroxide

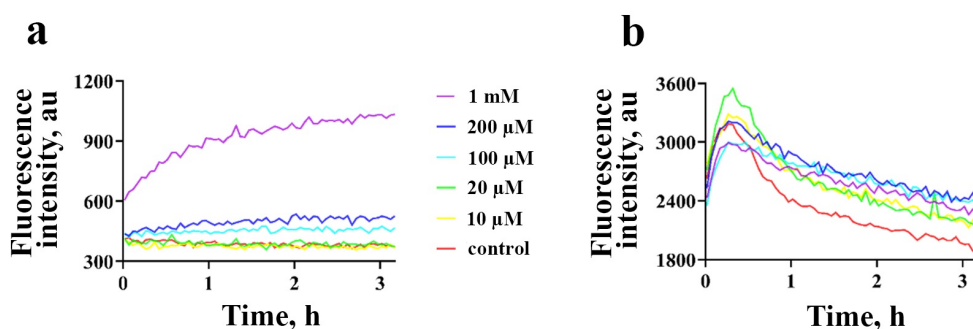


FIG. 5. Dynamics of fluorescence intensity change of CeO₂-calcein nanoconjugate in human MSCs after 24 hours of their incubation and further H₂O₂-induced oxidative stress for 3 hours. The excitation wavelength is 485 nm, the emission wavelength is 528 nm (a). Dynamics of MMP change (fluorescence of TMRE dye) in human MSCs after 24 hours of their incubation and further H₂O₂-induced oxidative stress for 3 hours. The excitation wavelength is 552 nm, the emission wavelength is 580 nm (b)

References

- [1] Shcherbakov A.B., Reukov V., et al. CeO₂ nanoparticle-containing polymers for biomedical applications: A review. *Polymers*, 2021, **13** (6), 924.
- [2] Dhall A., Self W. Cerium Oxide Nanoparticles: A Brief Review of Their Synthesis Methods and Biomedical Applications. *Antioxidants*, 2018, **7** (8), 97.
- [3] Rajeshkumar S., Naik P. Synthesis and biomedical applications of Cerium oxide nanoparticles – A Review. *Biotechnol. Rep. (Amst)*, 2017, **17**, P. 1–5.
- [4] Lord M.S., Berret J.F., et al. Redox Active Cerium Oxide Nanoparticles: Current Status and Burning Issues. *Small*, 2021, **17** (51), e2102342.
- [5] Chai W.F., Tang K.S. Protective potential of cerium oxide nanoparticles in diabetes mellitus. *J. Trace Elem. Med. Biol.*, 2021, **66**, 126742.
- [6] Gao Y., Chen K., Ma J.L., Gao F. Cerium oxide nanoparticles in cancer. *Onco Targets Ther.*, 2014, **7**, P. 835–840.
- [7] Hu X., Zhao P., Lu Y., Liu Y. ROS-Based Nanoparticles for Atherosclerosis Treatment. *Materials*, 2021, **14** (22), 6921.
- [8] Pirmohamed T., Dowding J.M., et al. Nanoceria exhibit redox state-dependent catalase mimetic activity. *Chem. Commun.*, 2010, **46** (16), P. 2736–2738.
- [9] Heckert E.G., Karakoti A.S., Seal S., Self W.T. The role of cerium redox state in the SOD mimetic activity of nanoceria. *Biomaterials*, 2008, **29** (18), P. 2705–2709.

- [10] Asati A., Santra S., et al. Oxidase-like activity of polymer-coated cerium oxide nanoparticles. *Angew Chem. Int. Ed. Engl.*, 2009, **48** (13), P. 2308–2312.
- [11] Xu C., Qu X. Cerium oxide nanoparticle: a remarkably versatile rare earth nanomaterial for biological applications. *NPG Asia Mater.*, 2014, **6**, e90.
- [12] Dhall A., Burns A., et al. Characterizing the phosphatase mimetic activity of cerium oxide nanoparticles and distinguishing its active site from that for catalase mimetic activity using anionic inhibitors *Environ. Sci.: Nano*, 2017, **4**, P. 1742–1749.
- [13] Dar M.A., Gul R., et al. Size-Dependent Effect of Nanoceria on Their Antibacterial Activity Towards Escherichia coli. *Science of Advanced Materials*, 2017, **9** (7), P. 1248–1253.
- [14] Alpaslan E., Yazici H., et al. pH-Dependent Activity of Dextran-Coated Cerium Oxide Nanoparticles on Prohibiting Osteosarcoma Cell Proliferation. *ACS Biomater. Sci. Eng.*, 2015, **1** (11), P. 1096–1103.
- [15] Popov A., Abakumov M., et al. Biocompatible dextran-coated gadolinium-doped cerium oxide nanoparticles as MRI contrast agents with high T1 relaxivity and selective cytotoxicity to cancer cells. *J. Mater. Chem. B*, 2021, **9**, P. 6586–6599.
- [16] Kalashnikova I., Chung S.J., et al. Ceria-based nanotheranostic agent for rheumatoid arthritis. *Theranostics*, 2020, **10** (26), P. 11863–11880.
- [17] Zholobak N.M., Shcherbakov A.B., et al. Direct monitoring of the interaction between ROS and cerium dioxide nanoparticles in living cells. *RSC Adv.*, 2014, **4**, P. 51703–51710.
- [18] Popov A.L., Zaichkina S.I., et al. Radioprotective effects of ultra-small citrate-stabilized cerium oxide nanoparticles. *RSC Advances*, 2016, **6**, P. 106141–106149.
- [19] Xiang J., Li J., et al. Cerium Oxide Nanoparticle Modified Scaffold Interface Enhances Vascularization of Bone Grafts by Activating Calcium Channel of Mesenchymal Stem Cells. *ACS Appl. Mater. Interfaces*, 2016, **8** (7), P. 4489–4499.
- [20] Zuo L., Feng Q., et al. Therapeutic effect on experimental acute cerebral infarction is enhanced after nanoceria labeling of human umbilical cord mesenchymal stem cells. *Ther. Adv. Neurol. Disord.*, 2019, **12**, 1756286419859725.
- [21] Holló Z., Homolya L., Davis C.W., Sarkadi B. Calcein accumulation as a fluorometric functional assay of the multidrug transporter. *Biochim. Biophys. Acta*, 1994, **1191** (2), P. 384–388.
- [22] Whittemore E.R., Loo D.T., Watt J.A., Cotman C.W. A detailed analysis of hydrogen peroxide-induced cell death in primary neuronal culture. *Neuroscience*, 1995, **67** (4), P. 921–932.
- [23] Fang X., Zhang X., Li H. Oxidative stress and mitochondrial membrane potential are involved in the cytotoxicity of perfluorododecanoic acid to neurons. *Toxicol. Ind. Health*, 2020, **36** (11), P. 892–897.

Submitted 8 February 2022; accepted 12 May 2022

Information about the authors:

Nikita N. Chukavin – Institute of Theoretical and Experimental Biophysics of the Russian Academy of Sciences, Institutskaya str., 3, Pushchino, 142290, Russia; Moscow Region State University, 141014, Moscow, Russia; ORCID 0000-0001-8431-4485; chukavinnik@gmail.com

Anton L. Popov – Institute of Theoretical and Experimental Biophysics of the Russian Academy of Sciences, Institutskaya str., 3, Pushchino, 142290, Russia; ORCID 0000-0003-2643-4846; antonpopovleonid@gmail.com

Alexander B. Shcherbakov – Zabolotny Institute of Microbiology and Virology, National Academy of Sciences of Ukraine, Kyiv D0368, Ukraine; ORCID 0000-0002-0020-0913; ceroform@gmail.com

Olga S. Ivanova – Kurnakov Institute of General and Inorganic Chemistry of the Russian Academy of Sciences, Leninskiy prosp., 31, Moscow, 119991, Russia; runetta05@mail.ru

Arina D. Filippova – Kurnakov Institute of General and Inorganic Chemistry of the Russian Academy of Sciences, Leninskiy prosp., 31, Moscow, 119991, Russia; arifilippova@yandex.ru

Vladimir K. Ivanov – Kurnakov Institute of General and Inorganic Chemistry of the Russian Academy of Sciences, Leninskiy prosp., 31, Moscow, 119991, Russia; ORCID 0000-0003-2343-2140; van@igic.ras.ru

Conflict of interest: the authors declare no conflict of interest.

Double perovskite oxides $\text{La}_2\text{NiMnO}_6$ and $\text{La}_2\text{Ni}_{0.8}\text{Fe}_{0.2}\text{MnO}_6$ for inorganic perovskite solar cells

Sergey S. Kozlov¹, Olga V. Alexeeva¹, Anna B. Nikolskaia¹, Oleg I. Shevaleevskiy^{1,a}, Denis D. Averkiev², Polina V. Kozhuhovskaya^{2,3}, Oksana V. Almjasheva^{2,3,b}, Liudmila L. Larina¹

¹Solar Photovoltaic Laboratory, Emanuel Institute of Biochemical Physics, Moscow, Russia

²St. Petersburg State Electrotechnical University “LETI”, St. Petersburg, Russia

³Ioffe Physical-Technical Institute, St. Petersburg, Russia

^ashevale2006@yahoo.com, ^balmjasheva@mail.ru

Corresponding author: Anna B. Nikolskaia, anickolskaya@mail.ru

PACS 84.60.Jt

ABSTRACT Nanopowders of $\text{La}_2\text{Ni}_{0.8}\text{Fe}_{0.2}\text{MnO}_6$ and $\text{La}_2\text{NiMnO}_6$ double perovskite oxides were synthesized by glycine-nitrate combustion method. The obtained materials were characterized using X-ray diffraction, scanning electron microscopy and optical measurements. Thin nanostructured layers based on the prepared materials were used as light absorbing layers for fabrication of inorganic perovskite solar cells (PSCs). Electron transport layers for the PSCs were prepared using TiO_2 and ZrO_2 nanostructured layers. The best performance of 3.7 % under AM1.5G illumination was obtained for the PSC structure glass/FTO/ $\text{ZrO}_2/\text{La}_2\text{Ni}_{0.8}\text{Fe}_{0.2}\text{MnO}_6/\text{Spiro-MeOTAD}/\text{Au}$.

KEYWORDS nanostructures, double perovskite oxides, perovskite solar cells, solar photovoltaics

ACKNOWLEDGEMENTS This work was supported by the Russian Science Foundation under grant No. 20-69-47124.

FOR CITATION Kozlov S.S., Alexeeva O.V., Nikolskaia A.B., Shevaleevskiy O.I., Averkiev D.D., Kozhuhovskaya P.V., Almjasheva O.V., Larina L.L. Double perovskite oxides $\text{La}_2\text{NiMnO}_6$ and $\text{La}_2\text{Ni}_{0.8}\text{Fe}_{0.2}\text{MnO}_6$ for inorganic perovskite solar cells. *Nanosystems: Phys. Chem. Math.*, 2022, **13** (3), 314–319.

1. Introduction

Nanostructured materials are widely used for the development of next-generation *solar cells* since they allow one to fabricate *high efficiency* and low-cost devices which are promising for mass production *photovoltaic technologies* [1, 2]. In the last decade, numerous studies in the area of solar photovoltaics were focused on the development of perovskite solar cells (PSCs) [3]. In PSCs an organic-inorganic hybrid material with perovskite-like structure ABX_3 ($\text{A} - \text{CH}_3\text{NH}_3^+$, $\text{HC}(\text{NH}_2)_2^+$, $\text{B} - \text{Pb}^{2+}$, Sn^{2+} , $\text{X} - \text{I}^-$, Br^- , Cl^-) is used as a light absorbing layer which is deposited on the surface of a nanostructured electron transport layer (ETL) [3–5]. Over a short period of time the power conversion efficiency (PCE) of lab-scale PSCs was increased from 3–5 % to 20–25 % that is comparable to the performance of conventional crystalline silicon solar cells [6, 7]. Low production costs make PSCs the most promising candidates for the future photovoltaic technologies. At the same time, conventional perovskite materials are not stable and degrade under high humidity conditions, light irradiation and increased temperatures [8, 9]. Yet another issue is the presence of the toxic lead cation Pb^{2+} in the B-site position of conventional hybrid perovskites [10, 11]. Therefore, the search for the new environmentally friendly and stable perovskite materials with the improved parameters is an essential task of the modern photovoltaics.

Recently it was reported that the $\text{A}_2\text{B}'\text{B}''\text{O}_6$ type double perovskite oxides (A is alkaline earth or rare-earth species and B'/B'' are 3d transition species) can be used as a light absorbing photoactive material in PSCs [12, 13]. Such inorganic compounds as $\text{Ln}_2\text{NiMnO}_6$, where $\text{Ln} = \text{La}$, Eu , Dy or Lu , are characterized by a narrow energy band gap, long carrier lifetime, and good stability under high temperatures and humidity levels [14, 15]. The first attempts to fabricate $\text{Ln}_2\text{NiMnO}_6$ -based PSCs resulted in poor photovoltaic parameters where the efficiency was less than 1 % [14]. To improve the performance, cation doping was used that caused the increase of the transport characteristics of double perovskite oxides [16, 17]. A significant increase of the PCE was reached with the introduction of metal atom in the B' -site position that improved the electronic properties of $\text{La}_2\text{NiMnO}_6$ material by increasing the concentration of charge carriers [18].

In this work, nanoparticles of $\text{La}_2\text{Ni}_{1-x}\text{Fe}_x\text{MnO}_6$ ($x = 0, 0.2$) double perovskite oxides were synthesized by glycine-nitrate combustion method and their structures were investigated using X-ray diffraction (XRD), X-ray fluorescence analysis (XRF), energy dispersive X-ray microanalysis (EDXMA) and scanning electron microscopy (SEM). Using the

obtained materials for the preparation of the light absorbing layers, we fabricated a series of PSC samples with the following architectures: (1) glass/FTO/ TiO_2 / $\text{La}_2\text{NiMnO}_6$ /Spiro-MeOTAD/Au, (2) glass/FTO/ TiO_2 / $\text{La}_2\text{Ni}_{0.8}\text{Fe}_{0.2}\text{MnO}_6$ /Spiro-MeOTAD/Au, (3) glass/FTO/ ZrO_2 / $\text{La}_2\text{NiMnO}_6$ /Spiro-MeOTAD/Au, (4) glass/FTO/ ZrO_2 / $\text{La}_2\text{Ni}_{0.8}\text{Fe}_{0.2}\text{MnO}_6$ /Spiro-MeOTAD/Au and investigated their photovoltaic characteristics.

2. Experiment

2.1. Materials and samples preparation

The $\text{La}_2\text{NiMnO}_6$ (LMNO) and $\text{La}_2\text{Ni}_{0.8}\text{Fe}_{0.2}\text{MnO}_6$ (LMNO(Fe)) double perovskite oxide nanopowders were synthesized by glycine nitrate combustion method ($G/N = 0.55$) using corresponding salts according to the procedure described in [19]. The obtained materials were mixed with acetic acid, terpineol, ethyl cellulose and ethanol to obtain homogeneous pastes as specified in [20]. The pastes were sonicated in ultrasonic bath several times and deposited by screen-printing onto FTO conductive glass substrates (Solaronix, 2×2 cm) with subsequent annealing at 500°C for 1 hour to form thin layers for SEM and optical measurements. LMNO and LMNO(Fe)-based homogeneous pastes were then used as precursors for spin coating perovskite light absorbing layers in the process of PSC device fabrication [21].

2.2. Device fabrication

Schematic representation of the PSC architecture is illustrated in Fig. 1. The electron transport layers (ETLs) were fabricated using TiO_2 and ZrO_2 materials. For this purpose, we used commercially available TiO_2 nanoparticles (Degussa-P25) and ZrO_2 nanoparticles prepared by dehydration of co-precipitated hydroxides under hydrothermal conditions. The method was described in our previous work [22]. Nanostructured TiO_2 and ZrO_2 ETLs with 200 nm thickness were deposited on conductive FTO (fluorine-doped tin oxide) glass substrates using spin-coating method at 2000 rpm for 1 min, followed by sintering at 500°C for 30 min. Next, the light absorbing active layer based on inorganic double perovskite oxide LMNO or LMNO(Fe) and a hole transport layer (HTL) based on Spiro-MeOTAD (Sigma-Aldrich) were successively deposited on the ETL surface. Fabrication of the PSCs was completed by the deposition of Au electrodes with a thickness of 50 nm using thermal evaporation. As a result, we fabricated 4 series of the PSC samples with the following architectures: (1) glass/FTO/ TiO_2 / $\text{La}_2\text{NiMnO}_6$ /Spiro-MeOTAD/Au, (2) glass/FTO/ TiO_2 / $\text{La}_2\text{Ni}_{0.8}\text{Fe}_{0.2}\text{MnO}_6$ /Spiro-MeOTAD/Au, (3) glass/FTO/ ZrO_2 / $\text{La}_2\text{NiMnO}_6$ /Spiro-MeOTAD/Au, and (4) glass/FTO/ ZrO_2 / $\text{La}_2\text{Ni}_{0.8}\text{Fe}_{0.2}\text{MnO}_6$ /Spiro-MeOTAD/Au.

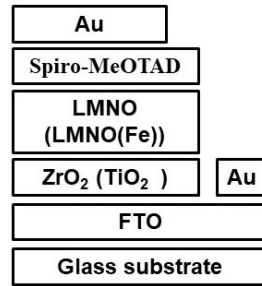


FIG. 1. Schematic representation of the PSC architecture

3. Characterization studies

XRD measurements of LMNO and LMNO(Fe) nanoparticles were provided using DRON-3M X-ray diffractometer with $\text{CuK}\alpha$ radiation ($\lambda = 1.5405 \text{ \AA}$) as the X-ray source. The elemental composition of the powders was determined by XRF on a Spectroscan GF-2 X-ray fluorescence spectrometer and EDXMA using Vega 3 Tescan scanning electron microscope with the EDAX energy dispersive analyzer. SEM images of the specially prepared perovskite layers on glass substrates were obtained by Hitachi SU8000 field-emission scanning electron microscope (FE-SEM). The optoelectronic properties of the perovskite layers were characterized using UV-Vis spectrophotometer (Shimadzu UV-3600, Japan) with an ISR-3100 integrating sphere in the wavelength range of 300 – 1400 nm.

Photovoltaic (PV) characteristics of the developed PSCs were measured under standard illumination conditions (AM1.5G , 1000 W/m^2) by recording the current-voltage (I - V) characteristics using Keithley 4200-SCS Semiconductor Characterization System (Keithley, USA) and Abet Technologies 10500 solar simulator with Xenon lamp (Abet, USA) as the light source. The PCE (η) values of the PSCs was calculated from the I - V data using the known formula:

$$\eta = \frac{J_{SC} \cdot V_{OC} \cdot FF}{P_{IN}} \cdot 100 \%, \quad (1)$$

where J_{SC} is the short-circuit current density, V_{OC} is the open-circuit voltage, FF is the fill factor and P_{IN} is the incoming light intensity.

4. Results and discussion

XRD patterns of the LMNO and LMNO(Fe) nanopowders are shown in Fig. 2. The peaks indicate the single-phase perovskite structure and the purity of all samples. The reflexes are recorded for monoclinic, rhombohedral and orthorhombic structures confirming the triple phase structure of double perovskite oxides such as $\text{La}_2\text{NiMnO}_6$ [23]. Table 1 shows the chemical composition and the crystallite size of the synthesized LMNO and LMNO(Fe) nanopowders determined by EDXMA and XRF measurements.

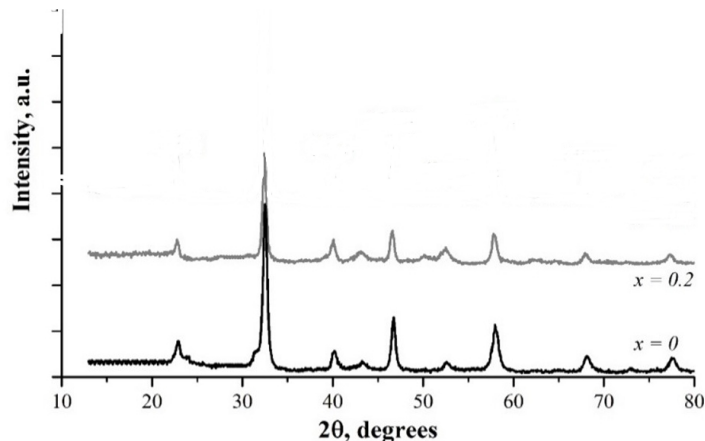


FIG. 2. XRD patterns of $\text{La}_2\text{NiMnO}_6$ and $\text{La}_2\text{Ni}_{0.8}\text{Fe}_{0.2}\text{MnO}_6$ nanopowders

TABLE 1. Chemical composition and average crystallite size for powders of the double perovskite oxides prepared

Sample	Method	Chemical composition, mol. %				Average crystallite size, nm
		La	Ni	Fe	Mn	
$\text{La}_2\text{NiFeMnO}_6$	EDXMA	52.5	25.6	0.0	21.9	18 ± 1
$\text{La}_2\text{Ni}_{0.8}\text{Fe}_{0.2}\text{MnO}_6$	EDXMA	46.7	25.4	6.6	21.3	20 ± 1
	XRF	50.9	22.2	5.7	21.2	

SEM images of thin LMNO and LMNO(Fe) layers deposited on glass substrates show porous structure of the layer surfaces (see Fig. 3). It could be seen that LMNO sample exhibits large amount of macropores, while in LMNO(Fe) their number is significantly lower. Besides that, LMNO(Fe) sample possesses more uniform surface and denser morphology which is important for light energy absorbing layer in high efficient PSCs. The decrease in pore size and the enhancement of uniformity of the LMNO(Fe) thin layer in comparison with LMNO sample can be attributed to the partial B'/B'' cation ordering in the crystal structure initiated by the introduction of Fe^{3+} ions. It is known that $\text{La}_2\text{NiMnO}_6$ is characterized by a disordered structure in which Ni^{2+} , Ni^{3+} , Mn^{3+} , Mn^{4+} cations randomly occupy B-positions whereas the introduction of Fe^{3+} ions lead to a predominant content of Ni^{2+} and Mn^{4+} ions and to their stricter placement in the lattice structure [24].

The optical measurements have shown that the band gaps for the fabricated thin perovskite layers, calculated from the Tauc plots [25], were 1.18 and 1.28 eV for LMNO and LMNO(Fe), respectively (see Fig. 4). The band gap of the synthesized LMNO(Fe) is close to the Shockley-Queisser limit of 1.34 eV, which provides the maximum power conversion efficiency for the single-junction solar cell [26]. Thus, due to the lower band gap, synthesized LMNO(Fe) double perovskite oxide can absorb larger part of solar radiation in comparison with the halide perovskite $\text{CH}_3\text{NH}_3\text{PbI}_3$ with a band gap of 1.5 – 1.6 eV, which is used in conventional PSCs [27].

Table 2 summarizes the details on the architectures of the fabricated PSCs and the PV parameters obtained. Inorganic PSCs based on both undoped and Fe^{3+} doped LNMO layers with TiO_2 ETLs exhibited *poor PV characteristics* (see Table 2). To improve the performance of LNMO-based PSCs, we used the ETLs based on very wide band-gap ZrO_2 nanostructured layers with the band gap of ~ 6 eV, which was much larger than that for the TiO_2 layer (3.2 eV). Previously we have shown that the charge transport mechanisms at the perovskite/ETL interfaces was entirely different in ZrO_2 ETL in comparison with TiO_2 ETL [22].

Figure 5 presents schematic energy band diagrams for the developed PSCs based on double perovskite LNMO(Fe) light absorbing layers with TiO_2 and ZrO_2 ETLs. It could be seen that developed PSCs have different interface electronic

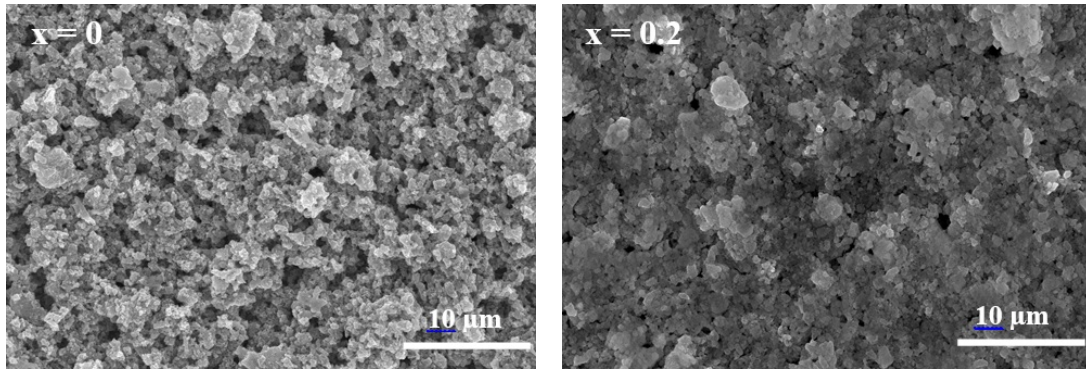


FIG. 3. SEM surface images of LMNO (left) and LMNO(Fe) (right) thin layers

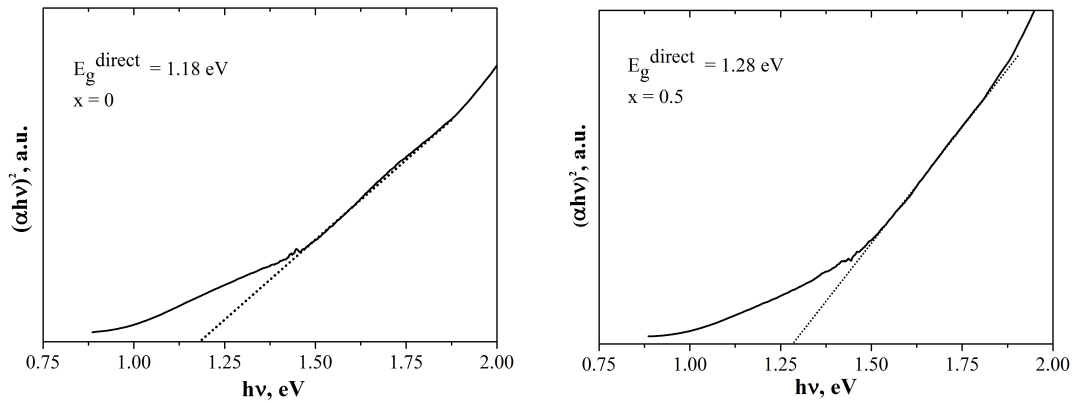


FIG. 4. Tauc plots of LMNO (left) and LMNO(Fe) (right) thin layers

TABLE 2. The architectures of inorganic PSCs and their photovoltaic characteristics under simulated AM 1.5G irradiance

	ETL	Perovskite light absorbing layer	HTL	J_{SC} , mA/cm^2	V_{OC} , mV	FF , a.u.	η , %
1	TiO_2	$\text{La}_2\text{NiMnO}_6$	Spiro-MeOTAD	1.2	470	0.4	0.22
2	TiO_2	$\text{La}_2\text{Ni}_{0.8}\text{Fe}_{0.2}\text{MnO}_6$	Spiro-MeOTAD	1.6	495	0.47	0.37
3	ZrO_2	$\text{La}_2\text{NiMnO}_6$	Spiro-MeOTAD	6.5	700	0.49	2.2
4	ZrO_2	$\text{La}_2\text{Ni}_{0.8}\text{Fe}_{0.2}\text{MnO}_6$	Spiro-MeOTAD	8.5	740	0.58	3.7

structures, although both interfaces show the spike conduction band offsets. At the $\text{TiO}_2/\text{LNMO}(\text{Fe})$ interface (Fig. 5a), the conduction band (CB) of the LMNO(Fe) perovskite is located 0.4 eV below the CB of the TiO_2 ETL. Such band energy structure reduces the efficient charge transfer across the perovskite/ETL interface to the front FTO electrode and leads to the significant decrease of the device performance. However, valence bands (VBs) structure at the LMNO(Fe)/Spiro-MeOTAD interface found to be favorable for the efficient hole transfer providing the pathways to the Au back electrode. The obtained PV parameters and the PCEs of the developed PSCs with TiO_2 ETLs were poor (see Table 2). A slight improvement of the PV parameters was observed for LMNO(Fe)-based PSCs in comparison with LMNO ones, which could be attributed to the higher light absorption ability due the larger E_g value of LMNO(Fe) perovskite material and better morphology of LMNO(Fe) ETL layer.

Incomparably higher conduction band offset is realized at the perovskite/ETL interface when using ZrO_2 ETLs (Fig. 5b). Indeed, the CB of the LMNO(Fe) perovskite absorbing layer is located 1.6 eV below the CB position of ZrO_2 ETL. Such energy band offset blocks the charge transfer across the perovskite/ETL interface. So, the alternative conductivity mechanism could be considered. In our previous publications, we reported on the successful application of the ZrO_2 ETL in the fabrication of inorganic PSCs based on the BiFeO_3 perovskite light absorbing layers [22]. It was shown that charge transfer across the $\text{BiFeO}_3/\text{ZrO}_2$ interface was quite efficient regardless the unfavorable interface electronic structure, in which the CB of the BiFeO_3 perovskite layer was located 1.1 eV below the CB of the ZrO_2 ETL.

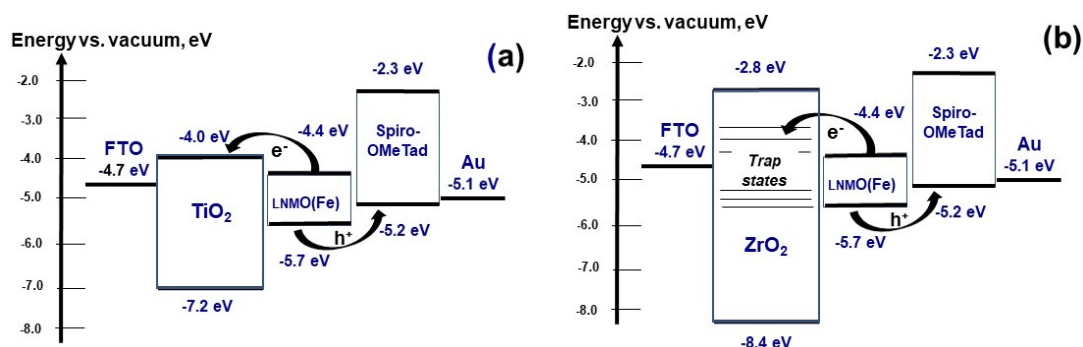


FIG. 5. Schematic energy band diagrams for the PSCs based on double perovskite LMNO(Fe) light absorption layers with ZrO_2 (a) and TiO_2 (b) ETLs

The observed effective electron transfer across perovskite/ ZrO_2 interface could be described to the hopping conduction through the localized states within the forbidden zone of ZrO_2 due to the large concentration of the nanoparticle surface defects [20]. Several publications confirmed that nanostructured layers based on very wide band gap ($E_g > 5$ eV) materials with negligible density of the electrons in the CB provide the effective transfer due to the large concentration of the surface defects in the forbidden zone. Thus, we have found that the best PCE value of 3.7 % was observed for the PCS device with glass/FTO/ ZrO_2 / $\text{La}_2\text{Ni}_{0.8}\text{Fe}_{0.2}\text{MnO}_6$ /Spiro-MeOTAD/Au architecture. The new approach for fabrication all inorganic PSCs based on double perovskite oxides with record photovoltaic parameters was developed.

5. Conclusions

Nanopowders of double perovskite oxides $\text{La}_2\text{NiMnO}_6$ and $\text{La}_2\text{Ni}_{0.8}\text{Fe}_{0.2}\text{MnO}_6$ were synthesized using glycine-nitrate combustion method and used to fabricate thin nanostructured light absorbing layers for the inorganic PSCs. XRD, SEM and optical measurements of the prepared layers revealed that the introduction of Fe^{3+} ions into the crystal structure of $\text{La}_2\text{NiMnO}_6$ material improves the structural properties of the perovskite layer and increases in the optical band gap value from 1.2 to 1.3 eV. For the first time the PSCs based on the LNMO and LNMO(Fe) double perovskite oxides with ZrO_2 -based ETLs were developed, and their photovoltaic properties were studied. Thus, we have fabricated the series of the PSCs with the following architectures: (1) glass/FTO/ TiO_2 / $\text{La}_2\text{NiMnO}_6$ /Spiro-MeOTAD/Au, (2) glass/FTO/ TiO_2 / $\text{La}_2\text{Ni}_{0.8}\text{Fe}_{0.2}\text{MnO}_6$ /Spiro-MeOTAD/Au, (3) glass/FTO/ TiO_2 / $\text{La}_2\text{NiMnO}_6$ /Spiro-MeOTAD/Au, (4) glass/FTO/ ZrO_2 / $\text{La}_2\text{Ni}_{0.8}\text{Fe}_{0.2}\text{MnO}_6$ /Spiro-MeOTAD/Au. The best performance was obtained for the LNMO(Fe)-based PSC with ZrO_2 ETL, showing PCE value of 3.7 % under AM1.5G illumination conditions. This value was significantly higher as compared to the PCE values observed for PSCs based on the TiO_2 ETLs. It was also shown that very wide-bandgap ETLs provide efficient electron transfer described by hopping transport mechanism.

References

- [1] Shubbak M.H. Advances in solar photovoltaics: Technology review and patent trends. *Renew. Sustain. Energ. Rev.*, 2019, **115**, 109383.
- [2] Green M. Photovoltaic technology and visions for the future. *Progr. Energ.*, 2019, **1** (1), 013001.
- [3] Lu H., Krishna A., et al. Compositional and interface engineering of organic-inorganic lead halide perovskite solar cells. *iScience*, 2020, **23** (8), 101359.
- [4] Tejeda A., Choy W.C.H., Deleporte E., Graetzel M. Hybrid perovskites for photovoltaics and optoelectronics. *J. Phys. D: Appl. Phys.*, 2020, **53** (7), 070201
- [5] Ansari M.I.H., Qurashi A., Nazeeruddin M.K. Frontiers, opportunities, and challenges in perovskite solar cells: a critical review. *J. Photochem. Photobiol. C: Photochem. Rev.*, 2018, **35**, P. 1–24.
- [6] Green M.A., Dunlop E.D., et al. Solar cell efficiency tables (version 58). *Prog. Photovolt.: Res. Appl.*, 2021, **29**, P. 657–667.
- [7] Park N.G. Research direction toward scalable, stable, and high efficiency perovskite solar cells. *Adv. Energy Mater.*, 2020, **10** (13), 1903106.
- [8] Bisquert J., Juarez-Perez E.J. The causes of degradation of perovskite solar cells. *J. Phys. Chem. Lett.*, 2019, **10** (19), P. 5889–5891.
- [9] Wang H.-Q., Wang S., et al. Understanding degradation mechanisms of perovskite solar cells due to electrochemical metallization effect. *Sol. Energ. Mater. Sol. Cell.*, 2021, **230**, 111278.
- [10] Schileo G., Grancini G. Lead or no lead? Availability, toxicity, sustainability and environmental impact of lead-free perovskite solar cells. *J. Mater. Chem. C*, 2021, **9**, P. 67–76.
- [11] Su P., Liu Y., et al. Pb-based perovskite solar cells and the underlying pollution behind clean energy: dynamic leaching of toxic substances from discarded perovskite solar cells. *J. Phys. Chem. Lett.*, 2020, **11**, P. 2812–2817.
- [12] Yin W.-J., Weng B., et al. Oxide perovskites, double perovskites and derivatives for electrocatalysis, photocatalysis, and photovoltaics. *Energy Environ. Sci.*, 2019, **12**, P. 442–462.
- [13] Lan C., Zhao S., et al. Investigation on structures, band gaps, and electronic structures of lead free $\text{La}_2\text{NiMnO}_6$ double perovskite materials for potential application of solar cell. *J. Alloy. Comp.*, 2016, **655**, P. 208–214.
- [14] Sheikh M.S., Ghosh D., et al. Lead free double perovskite oxides $\text{Ln}_2\text{NiMnO}_6$ (Ln = La, Eu, Dy, Lu), a new promising material for photovoltaic application. *Mater. Sci. Eng. B*, 2017, **226**, P. 10–17.

- [15] Kumar M., Raj A., Kumar A., Anshul A. Theoretical evidence of high power conversion efficiency in double perovskite solar cell device. *Opt. Mater.*, 2021, **111**, 110565.
- [16] Xu X., Zhong Y., Shao Z. Double perovskites in catalysis, electrocatalysis, and photo(electro)catalysis. *Trends Chem.*, 2019, **1** (4), P. 410–424.
- [17] Afroze S., Karim A.H., et al. Latest development of double perovskite electrode materials for solid oxide fuel cells: a review. *Front. Energ.*, 2019, **13** (4), P. 770–797.
- [18] Shi J., Gan H., Wang C., Shen Q. Fe-doping effect on magnetic properties of $\text{La}_2\text{CoMnO}_6$ ceramics prepared by plasma activated sintering. *J. Eur. Ceram. Soc.*, 2021, **41**, P. 6516–6522.
- [19] Popkov V.I., Almjashaeva O.V., et al. Magnetic properties of YFeO_3 nanocrystals obtained by different soft-chemical methods. *J. Mater. Sci. Mater. Electron.*, 2017, **28**, P. 7163–7170.
- [20] Ito S., Chen P., et al. Fabrication of screen-printing pastes from TiO_2 powders for dye-sensitized solar cells. *Prog. Photovolt.: Res. Appl.*, 2007, **15**, P. 603–612.
- [21] Nikolskaia A.B., Kozlov S.S., et al. Cation doping of $\text{La}_2\text{NiMnO}_6$ complex oxide with the double perovskite structure for photovoltaic applications. *Russ. J. Inorg. Chem.*, 2022, **67** (6), P. 921–925.
- [22] Vildanova M.F., Nikolskaia A.B., Kozlov S.S., Shevaleevskiy O.I. Charge transfer mechanisms in multistructured photoelectrodes for perovskite solar cells. *J. Phys. Conf.*, 2020, **1697** (1), 012187.
- [23] Sheikh M.S., Sakhya A.P., Dutta A., Sinha T.P. Light induced charge transport in $\text{La}_2\text{NiMnO}_6$ based Schottky diode. *J. Alloy. Comp.*, 2017, **727**, P. 238–245.
- [24] Hossain A., Atique Ullah A.K.M., Guin P.S., Roy S. An overview of $\text{La}_2\text{NiMnO}_6$ double perovskites: synthesis, structure, properties, and applications. *J. of Sol-Gel Science and Technology*, 2020, **93** (3), P. 479–494.
- [25] Tauc J., Grigorovici R., Vancu A. Optical properties and electronic structure of amorphous germanium. *Phys. Status Solidi*, 1966, **15**, P. 627–637.
- [26] Park N.-G., Segawa H. Research direction toward theoretical efficiency in perovskite solar cells. *ACS Photonics*, 2018, **5** (8), P. 2970–2977.
- [27] Yang Z., Rajagopal A., Jen A.K.Y. Ideal bandgap organic–inorganic hybrid perovskite solar cells. *Adv. Mater.*, 2017, **29** (47), 1704418.

Submitted 18 May 2022; accepted 26 May 2022

Information about the authors:

Sergey S. Kozlov – Solar Photovoltaic Laboratory, Emanuel Institute of Biochemical Physics, Russian Academy of Sciences, Kosygin St., 4, Moscow, 119334, Russia; sergeykozlov1@gmail.com

Olga V. Alexeeva – Solar Photovoltaic Laboratory, Emanuel Institute of Biochemical Physics, Russian Academy of Sciences, Kosygin St., 4, Moscow, 119334, Russia; ORCID 0000-0001-8982-3959; alexol@yandex.ru

Anna B. Nikolskaia – Solar Photovoltaic Laboratory, Emanuel Institute of Biochemical Physics, Russian Academy of Sciences, Kosygin St., 4, Moscow, 119334, Russia; anickolskaya@mail.ru

Oleg I. Shevaleevskiy – Solar Photovoltaic Laboratory, Emanuel Institute of Biochemical Physics, Russian Academy of Sciences, Kosygin St., 4, Moscow, 119334, Russia; ORCID 0000-0002-8593-3023; shevale2006@yahoo.com

Denis D. Averkiev – St. Petersburg State Electrotechnical University “LETI”, Professora Popova St., 5, St. Petersburg, 197376, Russia; swnesli2019@gmail.com

Polina V. Kozhuhovskaya – St. Petersburg State Electrotechnical University “LETI”, Professora Popova St., 5, St. Petersburg, 197376, Russia; Ioffe Physical-Technical Institute, Russian Academy of Sciences, Politekhnikeskaya St., 26, St. Petersburg, 194021, Russia; polina219017@gmail.com

Oksana V. Almjashaeva – St. Petersburg State Electrotechnical University “LETI”, Professora Popova St., 5, St. Petersburg, 197376, Russia; Ioffe Physical-Technical Institute, Russian Academy of Sciences, Politekhnikeskaya St., 26, St. Petersburg, 194021, Russia; ORCID 0000-0002-6132-4178; almjasheva@mail.ru

Liudmila L. Larina – Solar Photovoltaic Laboratory, Emanuel Institute of Biochemical Physics, Russian Academy of Sciences, Kosygin St., 4, Moscow, 119334, Russia; llarina@yahoo.com

Conflict of interest: the authors declare no conflict of interest.

Electrochemical performance of r-graphene oxide based MnO₂ nanocomposite for supercapacitor

S. Kalaiarasi^{1,2}, S. Shyamala³, M. Kavitha³, C. Vedhi³, R. R. Muthuchudarkodi³

¹Manonmaniam Sundaranar University, Tirunelveli, Tamilnadu, India

²PG and Research Department of Chemistry, A.P.C. Mahalaxmi College for Women, Thoothukudi, Tamilnadu, India

³PG and Research Department of Chemistry, V.O. Chidambaram College, Thoothukudi, Tamilnadu, India

Corresponding author: R. R. Muthuchudarkodi, muthu.rajaram@gmail.com, cvedhi23@gmail.com

ABSTRACT In this study, we improved the capacitance of carbon based reduced graphene oxide (rGO) and metal oxide based MnO₂ by preparing nanocomposites of rGO/MnO₂ nanocomposite using chemical synthesis method. The prepared nanoparticles and nanocomposites are characterized by FTIR spectroscopy, XRD, PL spectroscopy and FESEM with EDAX spectroscopy. FTIR studies disclose the characteristic chemical bonding between the respective materials. The FESEM images demonstrate that the surface structure of rGO and MnO₂ can be easily tuned by forming the composite of rGO/MnO₂ materials leading to excellent process ability of the system. The super capacitive behaviors of nanocomposites are evaluated using cyclic voltammetry and galvanostatic charge–discharge techniques. The specific capacitance of rGO/MnO₂ composite is high compared to that of MnO₂ nanoparticle. In addition, impedance measurements of the MnO₂ nanoparticles and rGO/MnO₂ electrodes are executed proposing that the rGO/MnO₂ composite electrodes are promising materials for super capacitor (186.6 Fg⁻¹).

KEYWORDS graphene oxide, cyclic voltammetry, nanocomposite, FESEM, electrochemical properties, supercapacitors

ACKNOWLEDGEMENTS The authors would like to express their gratitude to the Department of Science and Technology (FAST TRACK and FIST) in New Delhi, India for allowing them to use the CHI electrochemical workstation. The FT-IR spectra were generously provided by the PG and Research Department of Chemistry at V. O. Chidambaram College in Thoothukudi. We are grateful to the Secretary of A. P. C. Mahalaxmi College for Women, Thoothukudi.

FOR CITATION Kalaiarasi S., Shyamala S., Kavitha M., Vedhi C., Muthuchudarkodi R. R. Electrochemical performance of r-graphene oxide based MnO₂ nanocomposite for supercapacitor. *Nanosystems: Phys. Chem. Math.*, 2022, **13** (3), 320–330.

1. Introduction

Recently, great interest appeared in fabricating and utilizing novel graphene oxide–metal oxide nanocomposites for environmental remediation by the degradation and elimination of toxic organic contaminants and heavy metals, and for antibacterial applications. Compared with graphene oxide, graphene oxide–metal oxide nanocomposites show a unique structural morphology and photochemical properties which render them good candidates for water treatment projects [1]. Many research groups are working on the nanocomposite materials particularly graphene-based composite materials. Different types of graphene based composite materials are being investigated and reported for various engineering applications [2].

Supercapacitors have attracted growing interest, due to their high power density, long cycle life, and fast charging rate, which play an important role in complimenting or even replacing batteries in many applications [3–5]. Nevertheless, the low-energy density and higher production cost are still some of the major challenges for implementing supercapacitor in future application. To date, the carbon materials (activated carbon, carbon nanotubes, (CNT) and reduced graphene oxide (rGO)) [3,4,6] transition metal oxides (ruthenium dioxide (RuO₂), manganese dioxide (MnO₂), nickel oxide (NiO), cobalt oxide (Co₃O₄) [4,5,7] and conducting polymers (polypyrrole, polyaniline, PEDOT-PSS and polythiophene) [8,9] have been recognized as the most promising materials for supercapacitors. Based on literature, the carbon-based electrodes display an excellent rate of capability, good reversibility [3], and superior cyclability but suffer from low capacitance value. On the other hand, transition metal oxides and polymer-based electrodes produce high capacitance through a fast faradic reaction but have a poor rate of capability and stability [3,10].

Transition metal oxides are used in supercapacitor applications. In transition metal oxide, RuO₂ exhibits major supercapacitive performance, but it cannot be commercialized due to its high production cost and toxicity. Low cost

and high theoretical specific capacitance materials, like manganese oxide, ferrous oxide and nickel oxide have been used as electrode materials for supercapacitor [11–13]. However, the electrical conductivity of these metal oxides limits on its power density and cycling stability. Out of these metal oxides, manganese oxide is a most stable oxide and it has a number of significant applications as electrochemical material, high density magnetic storage medium, active catalyst, ion-exchange, Li–Mn–O rechargeable batteries, etc. [14]. Reduced graphene oxide has high specific surface area, which is highly desirable in catalysis, and acts as a two dimensional support for metallic nanoparticles with high dispersion [15]. In addition, it has a high adsorption capacity, defects in its structure that can generate new surface functionalities and increase the interactions with the metal nanoparticles [16, 17] and excellent mechanical properties that allow one to reach high stability and durability, increasing the lifetime of the catalyst. In this work, we report on the synthesis of nanostructured composites, consisting of manganese oxide anchored on rGO, by the one-step chemical synthesis method. The prepared samples were investigated by UV-Vis, FTIR, XRD, Field Emission Scanning Electron Microscope (FESEM) with EDAX spectroscopy and Photoluminescence spectroscopy. The electrochemical properties of these materials are evaluated by cyclic voltammetry, charge-discharge method and impedance techniques.

2. Material and methods

2.1. Material

All reagents used were of analytical grade, obtained from Merck (India) Ltd and used as received without further purification. Graphite, potassium permanganate, phosphoric acid, H₂O₂, manganese sulphate, concentrated hydrochloric acid, potassium hydroxide, sodium hydroxide and deionized water were used to synthesis of MnO₂ nanoparticles and rGO/MnO₂ nanocomposites.

2.2. Synthesis of MnO₂ nanoparticles

For the co-precipitation method, the manganese salt, manganese (II) sulphate of 0.2 M, dissolved in double distilled water with continuous stirring at a constant temperature of 80 °C. 2 M of NaOH solution was added while stirring until the pH of the solution reached 12. The stirring was continued at a constant temperature of 80 °C for 1 hour. The resulting brown precipitate was then filtered and washed with ethanol.

2.3. Synthesis of rGO/MnO₂ nanocomposite

In the present work, reduced graphene oxide (rGO) was produced using modified Hummer's method from pure graphite powder. 0.2 g of rGO was dispersed in 100 mL water by ultra-sonication up to 30 min to separate out a single sheet of graphene oxide. To synthesize in situ rGO/ MnO₂ nanocomposites, subsequently, 0.2 M (100 mL) of manganese (II) sulphate was added and sonicated for another 30 min, followed by drop wise addition of 1M potassium hydroxide solution under stirring for 1 h. This mixture was stirred well and refluxed for 2 h, which resulted in the formation of black colour reduced graphene oxide decorated MnO₂ nanocomposite. The precipitate was separated from the reaction mixture, washed several times with deionised water and followed by washing with ethanol to remove the impurities. Finally, the obtained product was dried at room temperature [18]. Fig. 1 shows that Synthesis of rGO/MnO₂ nanocomposite.

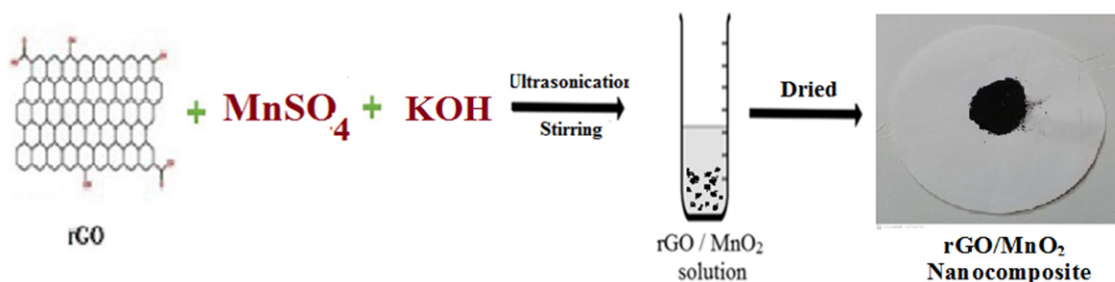


FIG. 1. Preparation method of rGO/MnO₂ nanocomposite

2.4. Characterization

Computer controlled Thermo Scientific Instrument with iD Transmission (Model P4600) was used to record the FTIR spectra, which was then followed by the KBr pellet method. Photoluminescence (PL) Spectra of the samples were recorded on a spectrofluorometer (JASCO, FP8300). The computer controlled XRD system JEOL IDX 8030 was used to record the X-ray diffraction of samples. EDAX and FESEM measurements were carried by JEOL JSM-6700F field emission scanning electron microscope. The electrochemical behaviors of nanocomposites have been investigated through CH-Instrument Inc., TX, and USA.

3. Result and discussion

3.1. FTIR analysis

The FTIR spectra disclose the chemical information and major functional groups existing in the MnO₂ nanoparticles and rGO/MnO₂ materials. Fig. 2 shows FTIR spectra of MnO₂ nanoparticles and rGO/MnO₂ nanocomposites. The broad band observed at 3421 cm⁻¹ is assigned to the symmetric stretching vibrational mode of hydroxyl groups in the MnO₂ nanoparticles and rGO/MnO₂ nanocomposites [19]. The bands at 1460.56, 1461.39, 1635.79, and 1680.42 cm⁻¹ indicate the presence of C–OH groups and water molecules in the both prepared samples. The two narrow and strong absorption bands at 642 and 540 cm⁻¹ are assigned to the pairing mode between Mn–O stretching modes. The FTIR spectrum for rGO/MnO₂ nanocomposites is depicted in Fig. 2(b) which denotes the peaks corresponding to the wave numbers 2324, and 516 cm⁻¹ denoting the presence of functional groups such as C–H, C–OH, O–Mn–O, respectively. These characteristic bands confirm the formation of rGO, MnO₂ nanoparticles and rGO/MnO₂ nanocomposites [20].

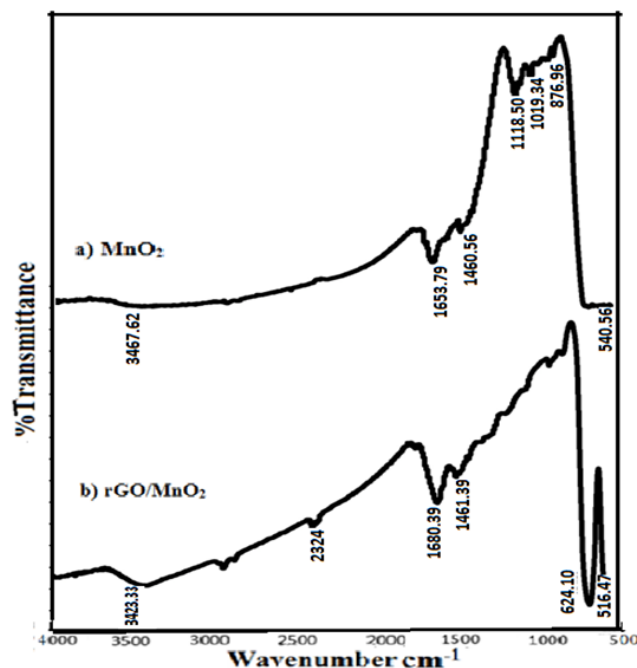


FIG. 2. FT-IR spectra of a) MnO₂ nanoparticles, b) rGO/MnO₂ nanocomposite

3.2. X-Ray diffraction analysis

The crystal structures of MnO₂ nanoparticles and rGO/MnO₂ nanocomposite are characterized by XRD. As can be seen in Fig. 3(a), all the diffraction peaks of pure MnO₂ nanoparticles indicate the tetragonal structure JCPDS (044-0141). The good crystallization is proved by its reflection peak. The XRD pattern for MnO₂ nanoparticles is depicted in the diffraction peaks at (110), (101), (211), (221) and (311) corresponding to 2θ values 29.4, 37.4, 46.0, 55.6 and 63.30. Fig. 3(b) shows the XRD patterns of rGO/MnO₂ nanocomposites. The XRD patterns of rGO/MnO₂ nanocomposite showed diffraction peaks at 29.0, 32.5, 36.1, 44.4, 58.4 and 69.90, and a phase with a rhombohedral structure was formed (JCPDS 96-500-0208) [21]. The main crystallite sizes of the rGO based metal oxide nanocomposite are calculated using the Debye–Scherrer formula (eq. (1)):

$$D = \frac{k\lambda}{\beta \cos \theta}, \quad (1)$$

where λ is the wavelength of radiation used (1.54060 Å for CuK α radiation), k is the Scherrer constant equal to 0.94, β is the full width at half maximum (FWHM) intensity of the diffraction peak for which the particle size is to be calculated, θ is the diffraction angle of the diffraction peak in question and D is the crystalline size in nanometers (nm). The average crystallite sizes of MnO₂ nanoparticles and rGO/MnO₂ nanocomposite are determined to be 47.1 and 40 nm, respectively.

3.3. FESEM and energy dispersive X-Ray analysis (EDAX)

The surface morphological studies of nanoparticles and nanocomposites were performed by FESEM analysis. The elements of deposits on MnO₂ nanoparticles and rGO/MnO₂ nanocomposite are also studied using EDAX spectrum. Figs. 4(a,b,c) and 4(a,b,c) show the FESEM image, EDAX spectrum and Elemental distribution of MnO₂ nanoparticles and rGO/MnO₂ nanocomposites. The FESEM images of MnO₂ nanoparticles are portrayed in Fig. 4(a). It is well

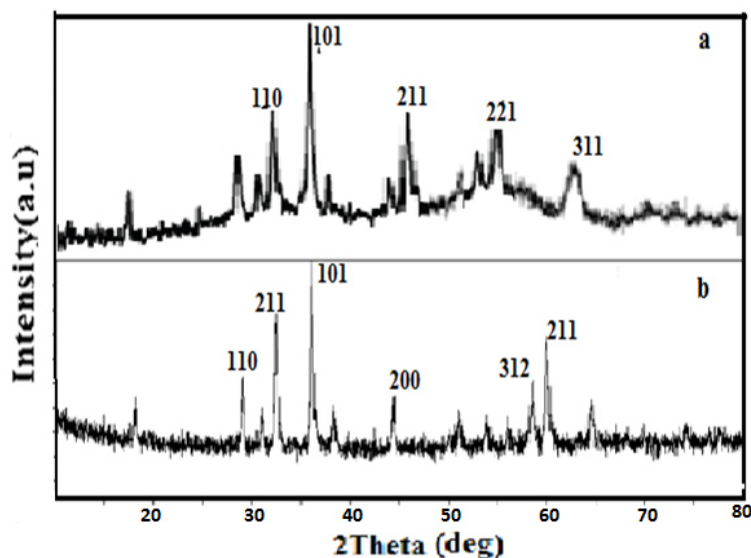


FIG. 3. XRD pattern of a) MnO₂ nanoparticles, b) rGO/MnO₂ nanocomposites

documented that the surface morphology has significant impact on the performance of nanostructure materials. The uniform distributions of grains are observed in the micrographs. The particles are nearly spherical in shape and has uniform size (one micron) [18]. The presence of atomic composition manganese (34 %) and oxygen (66 %) are confirmed as observed from the EDAX (Fig. 4(c)) spectrum. The chemical composition and product purity of the MnO₂ nanoparticle was examined by EDAX. The elemental mapping of MnO₂ nanoparticles are shown in Fig. 4(c). The highest amount of manganese (Mn) is distributed in the whole surface compared to that oxygen.

Figure 5(a) shows the surface morphologies of synthesized rGO/MnO₂ nanocomposites. It looks like the combination of flakes (sheet like structure) and spheres indicating the collaboration of rGO and MnO₂ nanocomposites [20]. The EDAX pattern of rGO/MnO₂ nanocomposites materials from Fig. 5(b) confirms that the synthesized materials show predominant peaks of C, O and Mn elemental peaks only. The respective EDAX spectra confirm the presence of carbon element along with the rGO/MnO₂ nanocomposites [22]. The elemental mapping of rGO/MnO₂ nanocomposites is shown in Fig. 5(c). There are large amount of oxygen (O) which is distributed on the surface in Fig. 5(c) compared to that carbon and manganese surface [23].

3.4. Photoluminescence study

The optical properties of MnO₂ nanoparticles, and rGO/MnO₂ nanocomposites were studied by using the photoluminescence spectra analysis. To investigate the efficient separation of charge carriers in the nanocomposites, photoluminescence (PL) spectroscopy was carried out to reveal the migration, transfer, and recombination processes of photo induced electron/hole pairs. The excitation source employed here was the 370 nm. Fig. 6(a) shows that pure MnO₂ nanoparticles have emission peak at 412 nm. However, the emission peak of the rGO/MnO₂ nanocomposite is much lower than that of the pure MnO₂ nanoparticles indicating that the addition of graphene leads to the PL quenching. The lowest recombination of the electron-hole pair is achieved by rGO/MnO₂ nanocomposites where it shows the lowest emission intensity among all. As shown in Fig. 6, the PL intensity decreases successively in the order of MnO₂ nanoparticles, and rGO/MnO₂ nanocomposites. The emissions was mostly attributed to the radiative transition between the electron and the hole recombination process [24].

3.5. Electrochemical studies

Electrochemical measurements of cyclic voltammetric studies were conducted using a CHI 650c electrochemical workstation with conventional three electrode cell at room temperature. Modified MnO₂ and rGO/MnO₂-glassy carbon electrode for comparison, was employed as the working electrode. Silver/silver chloride (Ag/AgCl) electrode acted as the reference electrode and platinum wire as the counter electrode. The electrochemical properties of the MnO₂ nanoparticles, and rGO/MnO₂ nanocomposites were investigated by means of cyclic voltammetry (CV) with potential window from 0.3 to 0.7 V at pH 7 (phosphate buffer solution). The CV curve of synthesized nanomaterials with different scan rate such as 100, 50, 30, 20, 10 and 5 mV/s are shown in Fig. 7(a–c). Strong redox behavior of metal oxides and asymmetric variation is observed during the lower scanning rate. However, beyond scan rate, nearly rectangular smooth CV loops are observed with mild redox behavior due to the presence of rGO. It is found that the current increases when the scan rate is increased, which indicates the good capacitance behavior of the nanocomposite.

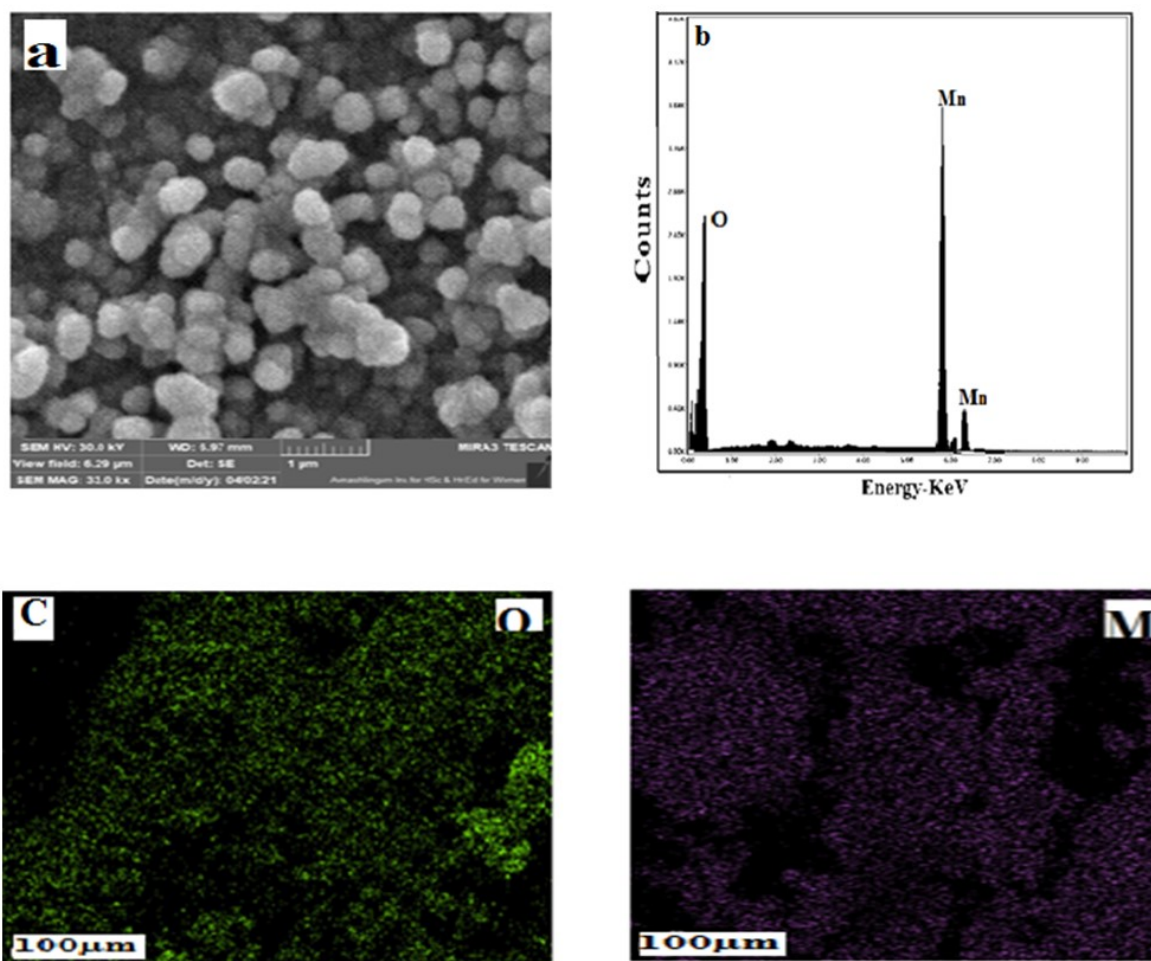


FIG. 4. a) FESEM image; b) EDAX spectrum; c) element mapping of Mn and O of the MnO₂ nanoparticles

3.6. EIS investigation of electrochemical behavior of nanoparticle and nanocomposite

The Nyquist plots of the modified nanoparticles and nanocomposites were studied using EIS. Randles' equivalent circuit model was used to fit experimental parameters such as the electron transfer resistance (R_{ct}), the solution resistance (R_s) and the double layer capacity (C_{dl}). Fig. 8 shows the real and imaginary parts of the electrochemical impedance spectra for the bare glassy carbon electrodes (GCE), MnO₂ nanoparticles, and rGO/MnO₂ nanocomposites modified GCE recorded at pH 7. The rGO/MnO₂ nanocomposites modified GCE shows small semicircular region with very high electron transfer resistance value compared to that of bare and MnO₂ nanoparticle of GCE electrode, indicating the low conductivity of the nanocomposite. These results show that the rGO/MnO₂ nanocomposites have very good electrochemical activity compared with the bare GCE. The composite could therefore be efficiently used for various electrocatalytic reactions. Table 1 shows that impedance parameters such that R_s , R_{ct} and C_{dl} values of bare, MnO₂ nanoparticles and rGO/MnO₂ nanocomposites.

TABLE 1. Impedance parameters such that R_s , R_{ct} and C_{dl} values of bare, MnO₂ nanoparticle, and rGO/MnO₂ nanocomposite

Samples	R_s (Ω)	R_{ct} (Ω cm ²)	C_{dl} (μ F cm ⁻²)
Bare GCE(Glassy Carbon Electrode)	7.928	7140	0.0014
MnO ₂ Nanoparticles	24.16	12110	0.0036
rGO/MnO ₂ Nanocomposite	15.21	34125	0.0023

The phase angle against frequency plot termed as Bode plot articulates about the capacitive character. The maximum phase angle of rGO/MnO₂ nanocomposite (73 °) strongly demonstrates the capacitive nature [25] compared to that for MnO₂ nanoparticles (71 °) as displayed in Fig. 9. Now, electrochemical performance in scale of mechanical flexibility is

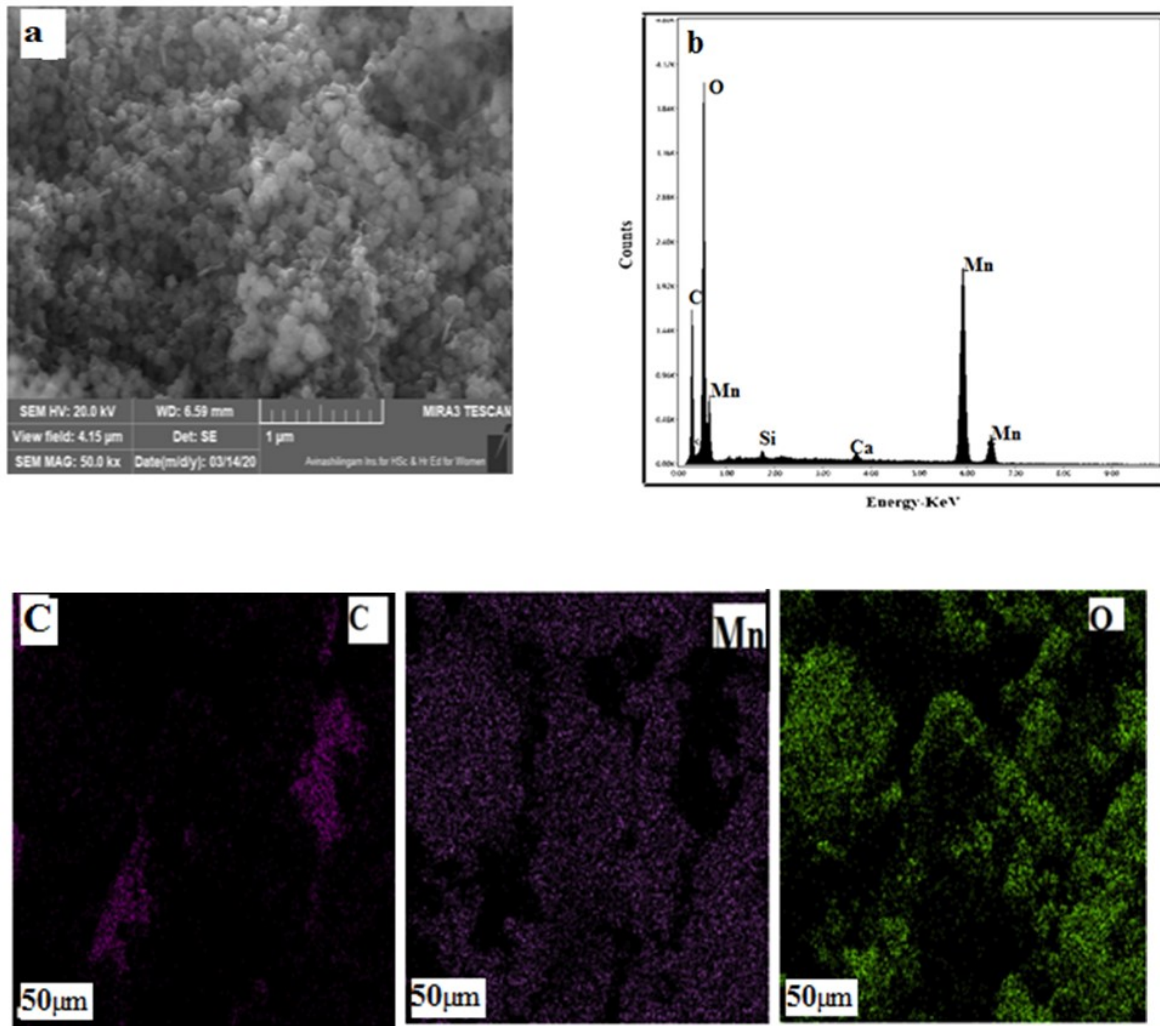


FIG. 5. a) FESEM image; b) EDAX spectrum; c) element mapping of C, Mn and O of the rGO/MnO₂ nanocomposite

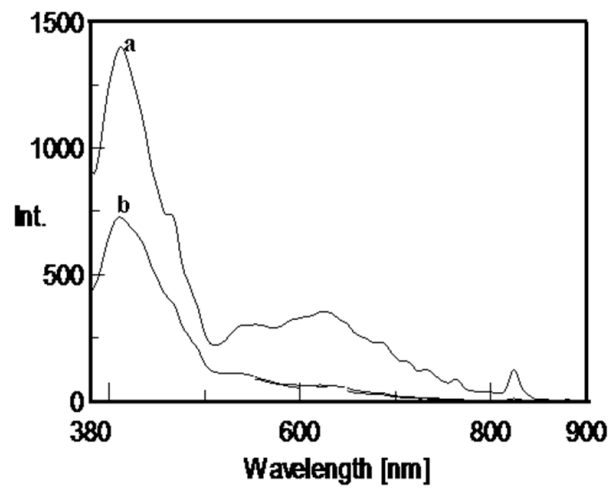


FIG. 6. PL spectrum of a) MnO₂ nanoparticles; b) rGO/MnO₂ nanocomposite

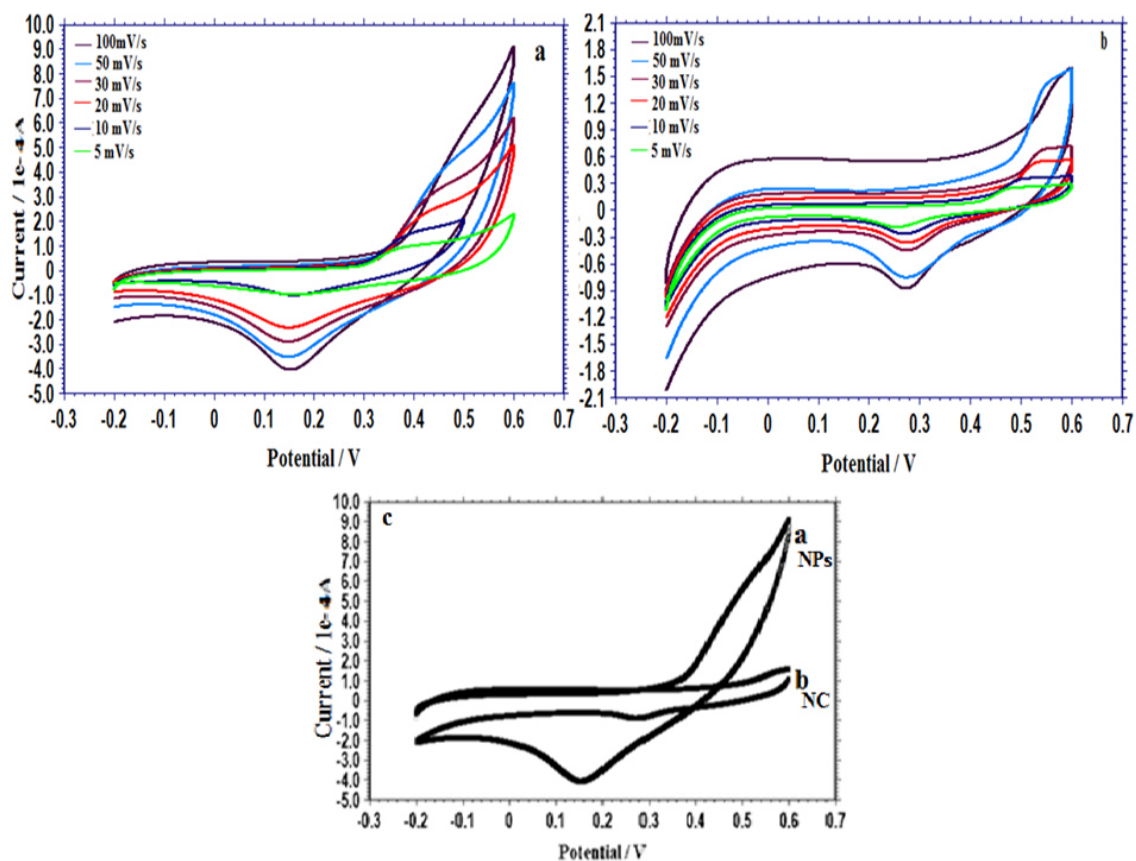


FIG. 7. Cyclic voltammetric behavior of a) MnO_2 nanoparticles; b) rGO/MnO_2 nanocomposites at different scan rate in pH 7; c) MnO_2 nanoparticles and rGO/MnO_2 nanocomposites at scan rate 100 mV/s

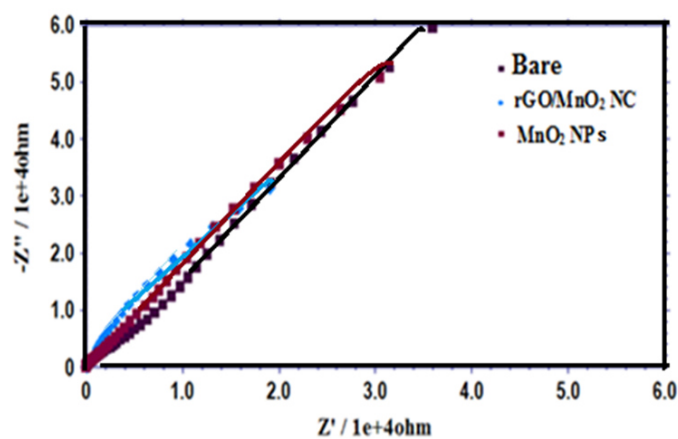


FIG. 8. Electrochemical Impedance spectra of MnO_2 nanoparticles and rGO/MnO_2 nanocomposite

an important tool to implement its application towards portable electronics. Investigation of flexibility was carried out by bending the device from 0 to 175 °.

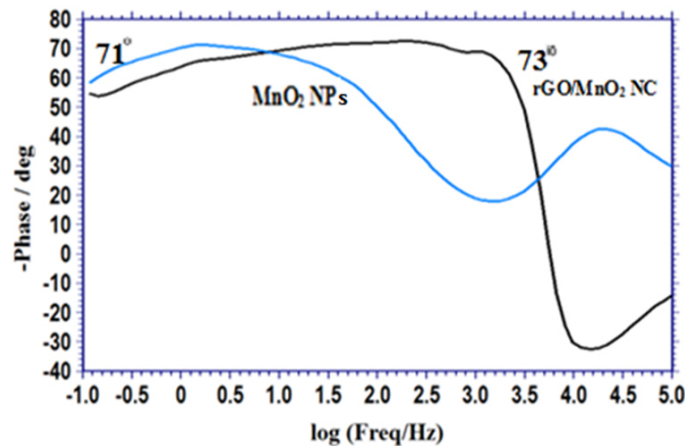


FIG. 9. Bode plot of $-$ phase angle/deg. versus $\log (f/\text{Hz})$ for MnO₂ nanoparticles and rGO/MnO₂ nanocomposite

3.7. Galvanostatic charge-discharge behaviour of the MnO₂ nanoparticle and rGO/MnO₂ nanocomposite

The galvanostatic charge-discharge method is essential for assessing supercapacitor performance and long-term stability. A formula (eq. (2)) can be used to calculate the discharge specific capacitance from the discharge curve. The galvanostatic charge-discharge behaviour of MnO₂ nanoparticles and rGO/MnO₂ nanocomposite with a variable constant current density such as 0.1, 0.3 and 0.5 Ag⁻¹ in the potential range of 0.5 to 1 is depicted in Fig. 10. Specific capacitances of the electrodes were calculated from charge-discharge curves using the following equation:

$$C_s = \frac{I\Delta t}{m\Delta V}, \quad (2)$$

where I (A) is the discharge current, Δt (s) is the discharge time, m is the mass of the electroactive material (g), and ΔV is the potential window (V). At constant current density of 0.1 Ag⁻¹, the specific capacitances obtained from charge-discharge curves of MnO₂ nanoparticles and rGO/MnO₂ nanocomposite are 92.5 and 186.5 Fg⁻¹, respectively. As a result, the rGO/MnO₂ nanocomposite has good capacitive behaviour during the charge-discharge process. The comparison results clearly show that our newly prepared nanocomposite electrode outperforms several others. One of the important factors influencing the capacitive behavior of the supercapacitor is the current density. The prepared samples' charge-discharge curves were performed at pH 7. With increasing current densities, the specific capacitance gradually decreases. This takes place due to the low utilization of electroactive materials at high discharge current densities, as ions in the electrolyte are unable to enter the active material's inner surface, leaving only the active material's outer surface.

In addition, the power density and energy density are important parameters for the investigation of the electrochemical performance of the electrochemical cells. They have been used to evaluate the performance of the hybrid rGO/MnO₂ composite electrode. The power density and energy density can be calculated from the following equations (eqs. (3) and (4)).

$$E = \frac{1}{2}C\Delta V^2, \quad (3)$$

$$P = \frac{E}{t}, \quad (4)$$

where, P (Wkg⁻¹), C (Fg⁻¹), Δ (V), t (s) and E (Whkg⁻¹) are the power density, specific capacitance, potential window of discharge, discharge time and energy density, respectively. Tables 2 and 3 show the calculated specific capacitance, energy and power density values. The plots of specific capacitance, current density, power density, and energy density can be seen in Fig. 11(a,b). Fig. 11(b) depicts the maximum power density of the rGO/MnO₂ nanocomposite versus nanoparticles. These findings support the use of MnO₂ nanoparticles and rGO/MnO₂ nanocomposite as potential materials for energy storage applications. The electrochemical stability of supercapacitors is critical for their use in practical applications.

4. Conclusion

In this study, chemical synthesis was used to successfully prepare MnO₂ nanoparticles and an rGO/MnO₂ nanocomposite. The phase purity of the synthesized nanoparticles and nanocomposites is confirmed by the X-ray diffraction pattern. FTIR is used to confirm the presence of surface functional groups on MnO₂ nanoparticles and the rGO/MnO₂

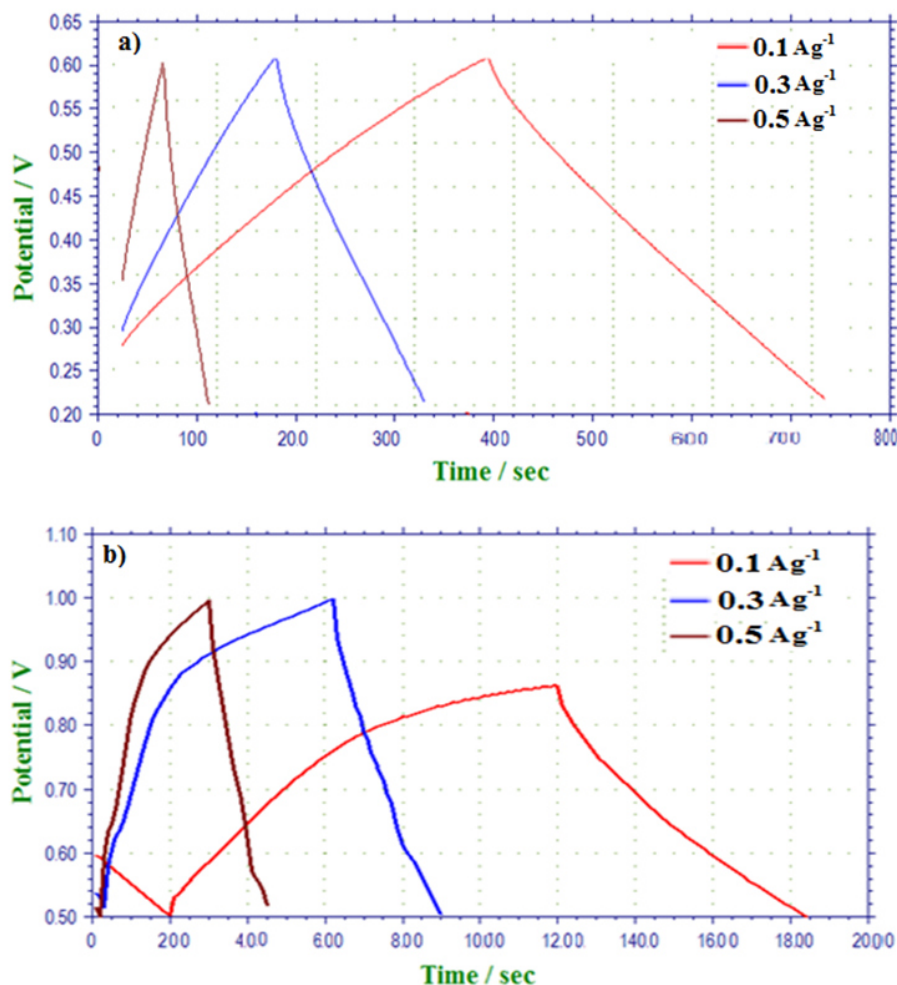


FIG. 10. Galvanostatic charge-discharge curves of a) MnO_2 nanoparticles; b) rGO/MnO_2 nanocomposite at different current densities in pH 7

TABLE 2. Various values of specific capacitance (F/g), energy (Wh/kg) and Power density (W/kg) obtained for MnO_2 nanoparticle at different current density

Current Density (Ag^{-1})	0.1	0.3	0.5
Specific capacitance (Fg^{-1})	92.5	89	85
Energy Density (Whkg^{-1})	7.4	7.12	6.8
Power Density (Wkg^{-1})	64	142.4	320

TABLE 3. Various values of specific capacitance (F/g), energy (Wh/kg) and Power density (W/kg) obtained for rGO/MnO_2 Nanocomposite at different current density

Current Density (Ag^{-1})	0.1	0.3	0.5
Specific capacitance (Fg^{-1})	186.6	180	160
Energy Density (Whkg^{-1})	22	20	17
Power Density (Wkg^{-1})	160.2	247.4	426.6

nanocomposite. The X-ray diffraction pattern confirms the phase purity of the synthesized nanoparticle and nanocomposite. FESEM analysis confirms the nanosize of MnO_2 nanoparticles and rGO/MnO_2 nanocomposite. PL spectra revealed the change of luminescence intensity in the rGO/MnO_2 nanocomposite are compared to the MnO_2 sample with almost

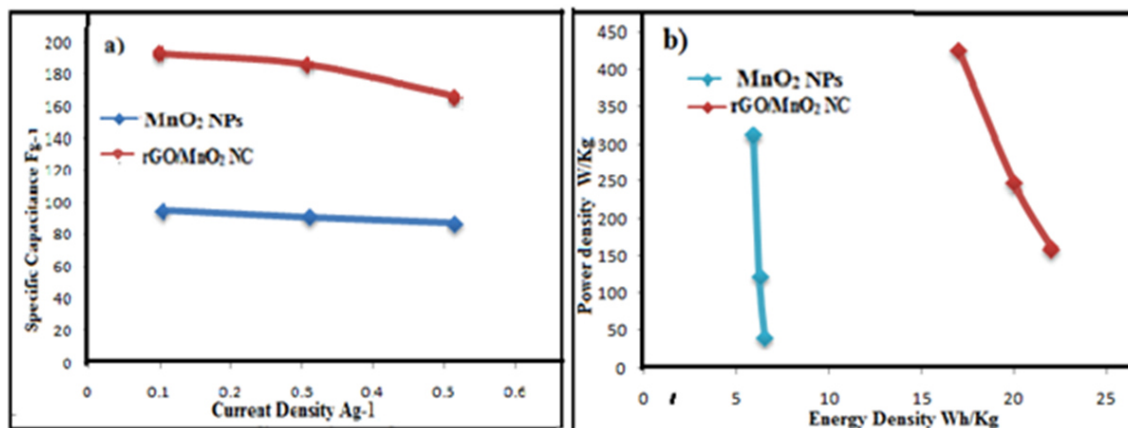


FIG. 11. a) Specific capacitances of MnO₂ nanoparticles and rGO/MnO₂ nanocomposite versus different current densities; b) Plot of power density versus energy density of MnO₂ nanoparticles and rGO/MnO₂ nanocomposite

linear decrease in excitation intensity. The specific capacitance of the rGO/MnO₂ nanocomposite was discovered to be higher than that of pure MnO₂ nanoparticles. In (phosphate buffer solution) pH 7, the two samples showed distinct capacitances at different current densities. The energy density and power density of the rGO/MnO₂ nanocomposites are higher than those of the MnO₂ nanoparticles. The nanocomposite's relatively high energy density and power density ensure that it acts as an efficient supercapacitor.

References

- [1] Li Q., Zhan Z., Jin S., Tan B. Wetttable Magnetic hyper cross linked microporous Nanoparticle as an efficient adsorbent for water treatment. *Chem. Eng. J.*, 2017, **326**, P. 109–116.
- [2] Chandra V., Park J., et al. Water dispersible magnetite reduced graphene oxide composites for arsenic removal. *ACS Nano*, 2010, **4** (7), P. 3979–3986.
- [3] Wanlu Yang, Zan Gao, et al. Synthesis of reduced graphene nanosheet/urchin-like manganese dioxide composite and high performance a super capacitor electrode. *Electrochim. Acta*, 2012, **69**, P. 112–119.
- [4] Li Wang, Yaolin Zheng, et al. Three-Dimensional Kenai Stem-Derived Porous Carbon/MnO₂ for High-Performance Supercapacitors. *Electrochim. Acta*, 2014, **135**, P. 380–387.
- [5] Wei W., Cui X., Chen W., Ivey D.G. Manganese oxide-based materials as electrochemical supercapacitor electrodes. *Chem. Soc. Rev.*, 2011, **40** (3), P. 1697–1721.
- [6] Bordjiba T., Belanger D. Development of new nanocomposite based on nanosized-manganese oxide and carbon nanotubes for high performance electrochemical capacitors. *Electrochim. Acta*, 2010, **55** (9), P. 3428–3433.
- [7] Wang H., Gao Q., Hu J. Asymmetric capacitor based on superior porous Ni–Zn–Co oxide/hydroxide and carbon electrodes. *J. Power Sources*, 2010, **195** (9), P. 2419–3046.
- [8] Snook A.G., Kao P., Best A.S. Conducting-polymer-based supercapacitor devices and electrodes. *J. Power Sources*, 2011, **196** (1), P. 1–12.
- [9] Farah Alvi, Manoj K. Ram, et al. Graphene–polyethylene dioxythiophene conducting polymer nanocomposite based supercapacitor. *Electrochim. Acta*, 2011, **56**, P. 9406–9412.
- [10] Qian Yang, Qi Li, et al. High performance graphene/manganese oxide hybrid electrode with flexible holey structure. *Electrochim. Acta*, 2014, **129**, P. 237–244.
- [11] Wei W., Cui X., Chen W., Ivey D.G. Manganese oxide-based materials as electrochemical supercapacitor electrodes. *Chemical Society Reviews*, 2011, **40**, 1697.
- [12] Hu C.C., Wu Y.T., Chang K.H. Low-Temperature Hydrothermal Synthesis of Mn₃O₄ and MnOOH Single Crystals: Determinant Influence of Oxidants. *Chemistry of Materials*, 2008, **20**, 2890.
- [13] Toupin M., Brousse T., Belanger D. Charge storage mechanism of MnO₂ electrode used in aqueous electrochemical capacitor. *Chemistry of Materials*, 2004, **16**, 3184.
- [14] Dubal D.P., Dhawale D.S., Salunkhe R.R., Pawar S.M., Lokhande C.D. A novel chemical synthesis and characterization of Mn₃O₄ thin films for supercapacitor application. *Applied Surface Science*, 2010, **256**, 4411.
- [15] Hu M., Yao Z., Wang X. Graphene-Based Nanomaterial for Catalysis. *Ind. Eng. Chem. Res.*, 2017, **56**, P. 3477–3502.
- [16] Julkapli N.M., Bagheri S. Graphene supported heterogeneous catalysts: An overview. *Int. J. Hydrogen Energy*, 2015, **40** (2), P. 948–979.
- [17] Machado B.F., Serp P. Graphene-based materials for catalysis. *Catal. Sci. Technol.*, 2012, **2** (1), P. 54–75.
- [18] Nagi M. Graphene oxide–metal oxide nanocomposites: fabrication, characterization and removal of cationic rhodamine B dye. *RSC Advances*, 2018, **8** (24), P. 13323–13332.
- [19] Farahmandjou M. Simple synthesis of new nano-sized pore structure vanadium pentoxide (V₂O₅). *Int. J. Bio-Inorg. Hybr. Nanomater.*, 2015, **4** (4), P. 243–247.
- [20] Yugambica S., Clara Dhanemozhi A., Iswariya S. Synthesis and characterization of MnO₂/rGO nanocomposite for supercapacitors. *Int. Research J. of Engineering and Technology (IRJET)*, 2017, **4** (2), P. 486–491.
- [21] Wyckoff R.W.G. The Crystal Structures of Some Carbonates of the Calcite Group. *American J. of Science*, 1920, P. 317–360.
- [22] Shihao Huang. Development of Graphene Based Nanocomposite for Supercapacitor Applications, Ph.D thesis. School of Materials Science and Engineering Faculty of Science, University of New South Wales, 2019.

- [23] Gadang Priyotomo, Siska Prifiharni, et al. A Field Study Of Atmospheric Corrosion Of Carbon Steel After Short Exposure In Palauan Ratu, West Java Province, Indonesia. *Walailak J. Sci. & Tech.*, 2021, **18** (17), 9667.
- [24] Sadiq M.J.M., Shenoy U.S., Bhat K.D. Synthesis of BaWO₄/NRGO-g-C₃N₄ nanocomposites with excellent multifunctional catalytic performance via microwave approach. *Front. Mater. Sci.*, 2018, **12**, P. 247–263.
- [25] Yadav A.A., Lokhande C.A., et al. The synthesis of multifunctional porous honey comb-like La₂O₃ thin film for supercapacitor and gas sensor applications. *J. Colloid Interface Sci.*, 2016, **484**, P.51–59.

Submitted 2 April 2022; revised 5 April 2022; accepted 28 May 2022

Information about the authors:

Senthurpandi Kalaiarasi – Research scholar (Reg. No.18222232032025), PG and Research Department of Chemistry, V. O. Chidambaram College, Thoothukudi, (Affiliated to Manonmaniam Sundaranar University, Tirunelveli, Tamilnadu, India); PG and Research Department of Chemistry, A.P.C. Mahalaxmi College for Women, Thoothukudi, Tamilnadu, India; kalaponpriya@gmail.com

Sudalaimani Shyamala – PG and Research Department of Chemistry, V.O. Chidambaram College, Thoothukudi, Tamilnadu, India; sruthsam1@gmail.com

Murugan Kavitha – PG and Research Department of Chemistry, V.O. Chidambaram College, Thoothukudi, Tamilnadu, India; Kavithamurugam25@gmail.com

Chinnapaiyan Vedhi – PG and Research Department of Chemistry, V.O. Chidambaram College, Thoothukudi, Tamilnadu, India; cvedhi23@gmail.com

Rajaram R. Muthuchudarkodi – PG and Research Department of Chemistry, V.O. Chidambaram College, Thoothukudi, Tamilnadu, India; muthu.rajaram@gmail.com, cvedhi23@gmail.com

Conflict of interest: the authors declare no conflict of interest.

Impact of sensitizer Yb and activator Tm on luminescence intensity of β -NaYF₄:Yb/Tm nanoluminophores

Sergey V. Kuznetsov^{1,a}, Sergey A. Burikov^{2,b}, Anna A. Fedyanina^{2,c}, Ekaterina A. Filippova^{2,d}, Vera Yu. Proydakova^{1,e}, Valerii V. Voronov^{1,f}, Nataliya Yu. Tabachkova^{1,g}, Pavel P. Fedorov^{1,h}, Tatiana A. Dolenko^{2,i}

¹Prokhorov General Physics Institute of the Russian Academy of Sciences, Moscow, 119991, Russia

²Department of Physics, Lomonosov Moscow State University, Moscow, 119991, Russia

^akouznetzovsv@gmail.com, ^bsergey.burikov@gmail.com, ^cfedyanechka@mail.ru,

^dfilippova.ea17@physics.msu.ru, ^evera.proydakova@gmail.com, ^fvoronov@lst.gpi.ru,

^gntabachkova@gmail.com, ^hppfedorov@yandex.ru, ⁱtdolenko@mail.ru

Corresponding author: Sergey V. Kuznetsov, kouznetzovsv@gmail.com

ABSTRACT In this study, the impact of sensitizer and activator ions concentration on the intensity of up-conversion luminescence of nanoluminophores β -NaYF₄:Yb³⁺/Tm³⁺ in dimethyl sulfoxide (DMSO) was investigated. Analysis of all luminescence spectral bands allows one to establish that the ratio of concentrations of ytterbium and thulium ions strongly effects on the luminescent properties of nanoluminophores. Increase of sensitizer concentration at constant activator concentration leads to an increase of the luminescence integral intensity. Optimal concentration of activators at fixed sensitizer concentration was determined: 2 mol.% for thulium and 18 mol.% for ytterbium. The sensitivity of each luminescence spectrum band to changes in the concentration of activators and sensitizers was explained by cross-relaxation processes in activator ions.

KEYWORDS up-conversion luminescence, nanoluminophores, rare earth elements, sensitizer, activator

ACKNOWLEDGEMENTS This research was performed according to the Development Program of the Interdisciplinary Scientific and Educational School of Lomonosov Moscow State University “Photonic and Quantum technologies. Digital medicine”. The study of the structure was carried out on the equipment of the Center Collective Use “Materials Science and Metallurgy” with the financial support of the Russian Federation represented by the Ministry of Education and Science (No. 075-15-2021-696).

FOR CITATION Kuznetsov S.V., Burikov S.A., Fedyanina A.A., Filippova E.A., Proydakova V.Yu., Voronov V.V., Tabachkova N.Yu., Fedorov P.P., Dolenko T.A. Impact of sensitizer Yb and activator Tm on luminescence intensity of β -NaYF₄:Yb/Tm nanoluminophores. *Nanosystems: Phys. Chem. Math.*, 2022, **13** (3), 331–341.

1. Introduction

Recently, nanoparticles based on various classes of chemical substances doped with ions of rare earth elements (REE) have attracted great interest due to their unique luminescent properties. In such nanoparticles, it is possible to implement up-conversion luminescence in which two or more photons with low energy turn into one photon with higher energy [1–3]. Such phosphors are used for optical imaging in biology and medicine [4–6], as optical coding elements [7], photovoltaic devices and anticounterfeiting [8], thermometry [9–12], and increasing the efficiency of solar panels [13–15].

Currently, the most effective up-conversion nanoluminophores have been developed on the basis of substances with gagarinite type crystal structure – NaYF₄ [9, 16, 17] or NaGdF₄ [5, 12, 18], which are doped with two types of ions. One (sensitizer ion) has a large absorption cross-section, and the other (activator ion) has high luminescence efficiency. The sensitizer ion absorbs the excitation energy and non-radiatively transfers it to the activator ion, which then emits up-conversion luminescence. Ytterbium ions often act as sensitizer while erbium, thulium, and holmium ions are used as activators [5, 8, 9, 12, 16–18].

The luminescent properties of nanoluminophores with REE ions are influenced by a number of factors such as intensity of exciting radiation [19–21], temperature [9–12], the ratio of concentrations of activator and sensitizer ions [5, 8, 17, 22–32], and environment of the emitting nanoparticles [33].

An increase of the sensitizer concentration leads to a significant increase of both the absorption cross-section and integral luminescence intensity [22, 23]. However, additional difficulties for the achieving the high-intensity luminescence arise from concentration quenching of luminescence [23], heating [34] and decrease of the luminescence lifetime due to the interactions between sensitizer and activator ions [24]. Luminescence concentration quenching at high concentrations of sensitizer ions can be eliminated by creating particles NaYF₄:Yb/Tm with sandwich-type multilayer architecture [23].

In this study, the concentration of sensitizer ions increased up to 60 % and the integral luminescence intensity continuously increased.

The luminescent properties of nanoluminophores with REE ions significantly depend on the concentration of activator ions. The Ho^{3+} , Tm^{3+} , and Er^{3+} ions were commonly used as activators due to cascade system of energy levels. The Yb^{3+} ions were used as sensitizers mostly often because of single excited state. In this regard, cross-relaxation processes between the ions are possible with appearance of the additional luminescence-quenching channel. As the concentration of activator ions increases accompanied by the simultaneous decrease of the distance between them the probability of excitation energy transfer to the unexcited ion increases as a result of electromagnetic interaction between them [25]. Such cross-relaxation converts both ions into intermediate state, which leads to cascade transfer of excitation energy to the vibrations of the crystal lattice [25].

The concentration of dopants (i.e., the average distance between neighboring active ions) has a great influence on the integral luminescence intensity and intensity ratio of the different peaks in the luminescence spectrum [26–32]. Increase of activator ions concentration (Er^{3+}) and probability of the cross-relaxation process (${}^4\text{S}_{3/2} + {}^4\text{I}_{15/2} \rightarrow {}^4\text{I}_{9/2} + {}^4\text{I}_{13/2}$) leads to decrease of the population of the ${}^4\text{S}_{3/2}$ level and increase of the population of the ${}^4\text{I}_{13/2}$ level [27]. Finally, the ${}^4\text{F}_{9/2}$ level is additionally populated from the ${}^4\text{I}_{13/2}$ level, which leads to increase of the intensity of the luminescence band in the red spectrum range. The probability of ${}^4\text{F}_{7/2} + {}^4\text{I}_{11/2} \rightarrow {}^4\text{F}_{9/2} + {}^4\text{F}_{9/2}$ cross-relaxation is also determined by the lifetimes of the corresponding levels and the concentration of Er^{3+} ions and affects the luminescence intensity in the red spectrum region [28]. Increase of the activator ions concentration (Er^{3+}) also leads to the increase of the probability of other cross-relaxation processes: ${}^2\text{H}_{11/2} + {}^4\text{I}_{15/2} \rightarrow {}^4\text{I}_{9/2} + {}^4\text{I}_{13/2}$ and ${}^4\text{I}_{11/2} + {}^4\text{I}_{13/2} \rightarrow {}^4\text{F}_{9/2} + {}^4\text{I}_{15/2}$ [29]. This leads to decrease of the luminescence intensity in the green spectrum region and increase of the luminescence intensity in the red spectrum region. Cross-relaxation mechanism (${}^4\text{F}_{7/2} + {}^4\text{I}_{11/2} \rightarrow {}^4\text{F}_{9/2} + {}^4\text{F}_{9/2}$) leads to the increase of the luminescence intensity in the red spectrum region relative to the luminescence in the green region at increase of the concentration of Yb^{3+} dopant ions [30]. Intensity of the luminescence bands in the blue (479 nm) and red (650 nm) spectral regions for $\text{NaYF}_4:\text{Yb}/\text{Tm}$ phosphors decreases with increasing thulium concentration from 0.1 to 2 % due to the presence of cross-relaxation processes [31]. Meanwhile, the band in the region of 800 nm turns out to be significantly less sensitive to changes of the concentration of thulium. Integral luminescence intensity, the intensity ratio of different spectral bands and the dependence of the luminescence intensity on the pump power for $\text{NaYF}_4:\text{Yb}/\text{Tm}$ phosphors are determined by the balance between the up-conversion of energy and excited state absorption dependent on dopant concentration [31].

For each crystal structure of the luminophores, the ion concentrations corresponding to maximal integral luminescence intensity were established [17,20,24,35–38]. The optimal concentrations of Yb^{3+} sensitizer and Er^{3+} activator ions for $\text{NaYF}_4:\text{Yb}/\text{Er}$ phosphors are 18 – 20 mol.% and less than 2 mol.%, respectively [36]. For $\text{NaYF}_4:\text{Yb}/\text{Tm}$ phosphors it has been demonstrated that the optimal concentration for excitation of maximal luminescence in the blue region of the spectrum is 20 – 30 mol.% for ytterbium and 0.3 mol.% for thulium [37]. Meanwhile, at least 30 mol.% ytterbium and 1 mol.% thulium are required to achieve the maximum luminescence intensity of the band in the region of 800 nm. Cross-relaxation processes at thulium concentrations larger than 2 mol.% for these phosphors already begin to significantly affect the intensity of the band in the region of 800 nm [38].

Thus, the concentrations of activator and sensitizer ions strongly impact on the luminescent properties of phosphors with REE ions. Therefore, the dependences of the nanoluminophores luminescence on the dopant ions concentrations are currently being actively investigated. However, there is a complicated problem in performing a comparative analysis and comparing the data from different authors for phosphors with nominally the same composition. The impossibility of the correct comparative analysis is caused by the fact that different authors studied nanoluminophores of the same nominal compositions prepared by different synthesis techniques from different initial chemicals. These nanoluminophores differed significantly in morphology and size. Moreover, laser radiation of various pump power density was used and only some of the most intense bands of the luminescence spectrum were analyzed.

Thus, in order to clarify the conclusions about the effect of the concentration of activators and sensitizers on the luminescent properties of up-conversion nanoluminophores, it is necessary to obtain complete luminescence spectra of nanoluminophores, differing from each other only in the concentrations of activators and sensitizers, under the same experimental conditions (intensity of excitation radiation, optical scheme of experiment etc.). Herewith, the nanoparticles should be synthesized by the same method using the same reagents.

In this article, the dependences of the intensity of the luminescence bands in spectral region 300 – 900 nm for the dispersions of $\beta\text{-NaYF}_4:\text{Yb}^{3+}/\text{Tm}^{3+}$ phosphors in dimethyl sulfoxide (DMSO) on the concentration of activator and sensitizer ions were recorded under the same experimental conditions. For this purpose, a series of samples differing in the concentration of activator and sensitizer ions were specially synthesized. As a result, the full luminescence spectra recorded under the same conditions at the same laser pumping power density were analyzed. The optimal concentration of activators at fixed sensitizer concentration is revealed, namely, it is 2 mol.% for thulium and 18 mol.% for ytterbium.

2. Materials and methods

2.1. Synthesis and characterization of the samples

Eight β -NaYF₄:Yb³⁺/Tm³⁺ nanoluminophores with different concentrations of ytterbium ions (sensitizer) and thulium (activator) were synthesised. Two series of β -NaYF₄:Yb³⁺/Tm³⁺ samples were synthesised with constant concentration of the sensitizer and varied concentration of activator and vice versa in the other series. Nanoparticles β -NaYF₄:Yb³⁺/Tm³⁺ were synthesized by the solvothermal synthesis technique in a high-boiling solvent according to the procedure described elsewhere [12, 39]. Ytterbium, thulium and yttrium acetates of purity 99.99 (Lanhit, Russia) were added to oleic acid (pure, Chimmed, Russia) and 90 % octadecene-1 (Sigma Aldrich). The reaction mixture was heated up to 130 °C under vigorous stirring under an argon atmosphere until completely dissolving of initial chemicals with preparing of ytterbium, thulium and yttrium oleates. The sub-product of reaction such as water and acetic acid were removed in vacuum. The sodium hydroxide and ammonium fluoride (chemically pure, Lanhit, Russia) were dissolved in methanol (chemically extra pure, Chimmed, Russia). Mixture of NaOH and NH₄F solutions was added to the reaction mixture with oleates at room temperature. Entire mixture was heated up to 50 – 60 °C and kept at this temperature for one hour with following removing methanol in vacuum. After removing the entire methanol, the reaction mixture was heated up to 315 °C stored for 3 hours and then cooled to 25 °C. The nanoparticle precipitate was separated from the solution by centrifugation (Eppendorf 5804 centrifuge, 6500 rpm, 5 min). The resulting nanoparticles were sequentially dispersed three times in chloroform and washed with 96 % ethanol. Suspensions of nanoparticles in DMSO (chemically pure, Chimmed, Russia) were prepared with the same concentration of 1 mg/ml according to the developed protocol: 10 ml of DMSO was added to 10 mg of β -NaYF₄:Yb/Tm nanoparticles. The resulting suspensions were sonicated at 35 kHz for 1 hour in the ultrasonic bath “GRAD 13-35”.

X-ray pattern diffraction of powders was performed on Bruker D8 diffractometer with CuK α -radiation. The typical X-ray pattern was corresponded to β -NaYF₄ crystal type (JCPDS card #16-0344, $a = 5.96$ Å, $c = 3.53$ Å, Fig. 1). Unit cell parameters of samples were evaluated by TOPAS software (Table 1).

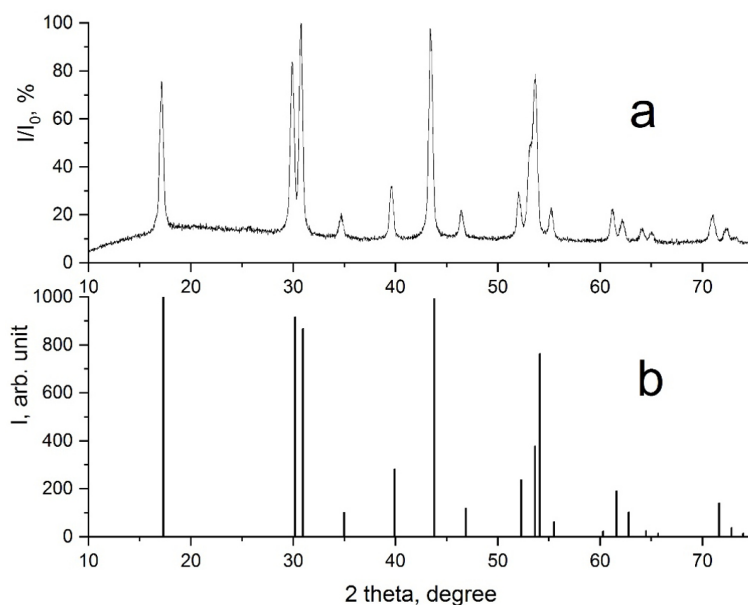


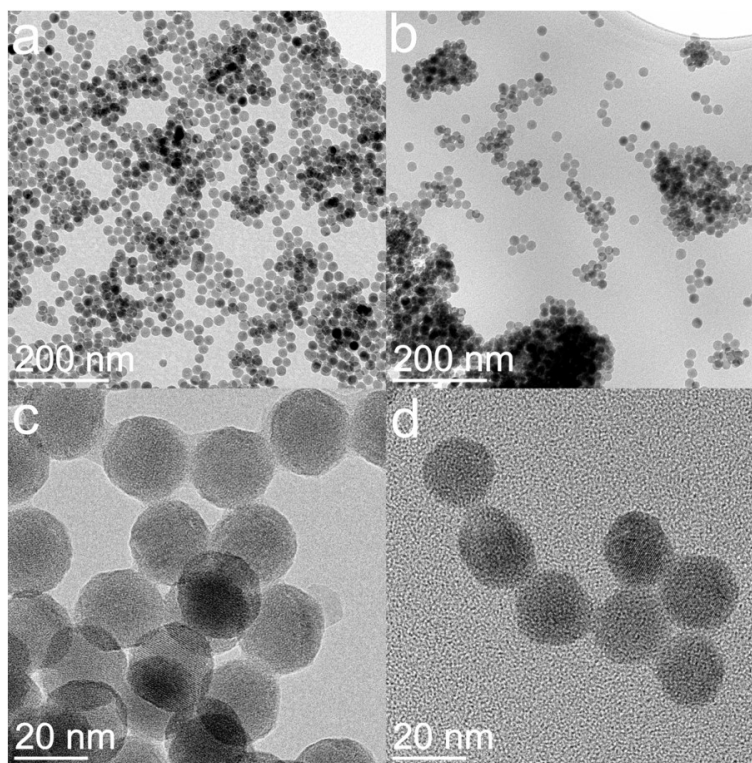
FIG. 1. X-ray pattern diffraction of β -NaYF₄:Yb(18 mol.):Tm(2 mol.) sample (a) and JCPDS # 16-0344 for β -NaYF₄ (b)

Transmission electron microscopy (TEM) was performed using JEOL JEM-2100 microscope. The particle size was estimated using the ImageJ software based on 50 particles (Table 1). TEM images of β -NaYF₄: Yb³⁺/Tm³⁺ samples are shown in Fig. 2 and Figs. A1–A3.

The nanoparticle sizes of β -NaYF₄: Yb³⁺/Tm³⁺ in DMSO suspensions were measured by dynamic light scattering (DLS) using Malvern Zetasizer Nano ZS setup (Table 1). The size distributions of nanoparticles in suspensions for several of the studied nanoluminophores are shown in Figs. A4–A6. As it follows from the obtained results, the sizes of most objects do not exceed 50 nm, which indicates that there is no significant aggregation of nanoparticles in suspensions. This is also evidenced by the observation of the colloidal stability of suspensions – for several months there was no precipitation of particles, and the luminescence intensity of complexes in suspensions did not decrease with time, which corresponds to the data we previously obtained [18].

TABLE 1. Characteristics of synthesized samples of $\beta\text{-NaYF}_4\text{:Yb}^{3+}/\text{Tm}^{3+}$

No	Composition	Unit cell parameters, Å	Size (TEM), nm	Size (DLS), nm
1	$\beta\text{-NaYF}_4\text{:Yb}(10\%)/\text{Tm}(4\%)$	$a = 5.9745(3)$ $c = 3.5196(1)$	16.7	21.2
2	$\beta\text{-NaYF}_4\text{:Yb}(14\%)/\text{Tm}(4\%)$	$a = 5.9734(4)$ $c = 3.5166(2)$	19.5	32.6
3	$\beta\text{-NaYF}_4\text{:Yb}(18\%)/\text{Tm}(4\%)$	$a = 5.9723(2)$ $c = 3.5134(1)$	22.8	38.1
4	$\beta\text{-NaYF}_4\text{:Yb}(22\%)/\text{Tm}(4\%)$	$a = 5.9717(5)$ $c = 3.5135(3)$	20.7	25.7
5	$\beta\text{-NaYF}_4\text{:Yb}(18\%)/\text{Tm}(1\%)$	$a = 5.9728(3)$ $c = 3.5153(2)$	18.9	36.4
6	$\beta\text{-NaYF}_4\text{:Yb}(18\%)/\text{Tm}(2\%)$	$a = 5.9731(3)$ $c = 3.5140(2)$	24.0	70.1
7	$\beta\text{-NaYF}_4\text{:Yb}(18\%)/\text{Tm}(4\%)$	$a = 5.9723(2)$ $c = 3.5134(1)$	22.8	50.5
8	$\beta\text{-NaYF}_4\text{:Yb}(18\%)/\text{Tm}(6\%)$	$a = 5.9707(1)$ $c = 3.5113(1)$	20.9	104.6

FIG. 2. TEM images of $\beta\text{-NaYF}_4\text{:Yb}^{3+}/\text{Tm}^{3+}$ nanoluminophores: No. 7 (left) and No. 8 (right)

2.2. Luminescent spectroscopy of $\beta\text{-NaYF}_4\text{:Yb}^{3+}/\text{Tm}^{3+}$ colloids in DMSO

A continuous diode laser with a wavelength of 980 nm (line width of 2 nm) and a pumping intensity of 205 W/cm² was used for excitation of the luminescence. Luminescence spectra were recorded in the spectral range of 300 – 900 nm at room temperature.

The samples were studied in the 90-degree geometry of the experiment in the standard quartz cuvette (10 × 10 × 50 mm). The registration system consisted of Acton 2500i monochromator (focal length 500 mm, diffraction grating 900 grooves per mm), and photomultiplier (Hamamatsu H-8259, operating in photon counting mode). A blocking interference filter was used to suppress the elastic scattering signal at the wavelength of 980 nm.

It occurs that the up-conversion luminescence in $\beta\text{-NaYF}_4\text{:Yb}^{3+}/\text{Tm}^{3+}$ samples is in accordance with the transitions scheme between the energy levels of ytterbium and thulium (Fig. 3).

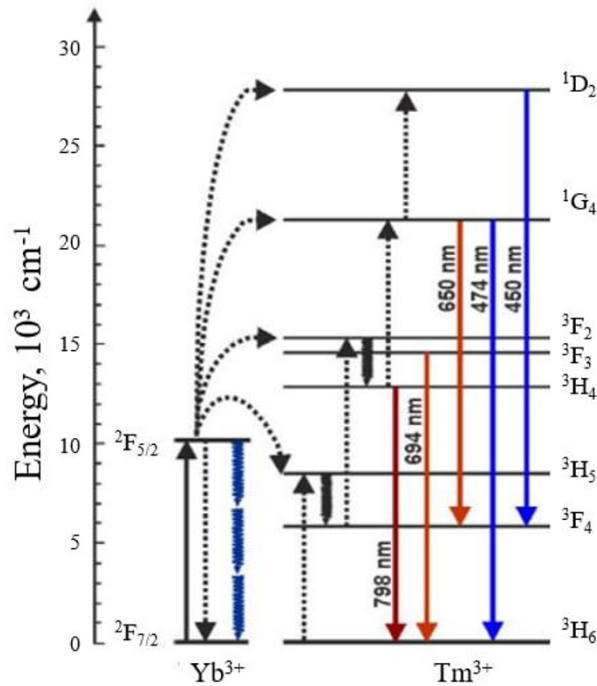


FIG. 3. Energy levels diagram and transitions demonstrating the generation of up-conversion radiation in β -NaYF₄:Yb³⁺/Tm³⁺ particles

The photon of the exciting radiation (980 nm) is absorbed by the ytterbium ion (transition ${}^2F_{7/2} \rightarrow {}^2F_{5/2}$) then the energy is transferred to the thulium ion according to transition ${}^3H_6 \rightarrow {}^3H_5$ with arising excited state. The energy of the next photon absorbed by the ytterbium ion allows the thulium ion to pass through the intermediate levels 3F_4 and 3F_2 to the level 3H_4 . From this level, radiative transition ${}^3H_4 \rightarrow {}^3H_6$ is possible with the emission of the photon with wavelength of 798 nm. Similarly (with the absorption of three or four photons), it is possible to populate levels 1G_4 and 1D_2 with radiative transitions causing up-conversion luminescence in the blue and red spectral regions (Fig. 3).

3. Results and discussion

3.1. Dependence of the intensity of up-conversion luminescence of nanoluminophores on the ratio between concentrations of activator and sensitizer

The recorded luminescence spectra for all the samples β -NaYF₄:Yb³⁺/Tm³⁺ in DMSO with the nanoparticle concentration (1 mg/ml) are presented in Fig. 4. Each spectrum contains a set of bands with various intensities corresponding to the following energy transitions: ${}^3H_4 \rightarrow {}^3H_6$ (798 nm), ${}^1G_4 \rightarrow {}^3H_6$ (474 nm), ${}^1D_2 \rightarrow {}^3F_4$ (450 nm), ${}^1G_4 \rightarrow {}^3F_4$ (650 nm), and ${}^3F_3 \rightarrow {}^3H_6$ (694 nm).

Luminescence intensity of nanoparticles with different ratio of concentrations of activator and sensitizer varies in a wide range (Fig. 4). Dependence of integral luminescence of nanoparticles on the concentration of sensitizer and activator ions is presented in Fig. 5.

Obtained results demonstrate the increase of integral luminescence at fixed activator concentration and increasing of sensitizer concentration (samples 1 – 4). Firstly, it can be explained by the fact that more energy of exciting radiation is absorbed. Secondly, it can be the result of the decrease of the average distance between activator and sensitizer ions with the increase of their concentration. Consequently, transmission of excitation from sensitizer ions to activator ions turns to be more effective.

The efficiency of energy transfer from sensitizer ions to activator ions is determined by the distance between sensitizer and activator ions (their concentrations) according to the formula [40, 41]:

$$P = \frac{1}{t_s} \left(\frac{R_0}{R} \right)^s, \quad (1)$$

where t_s is the effective lifetime of the excited state of sensitizer ion, that takes into account all the channels of deactivation except the energy transfer to activator ion; R is the distance between ions, which are involved into the energy transfer process; R_0 is the distance between ions when the rate of energy transfer equals the rate of the spontaneous decay of the excited state of sensitizer; s is the multipolar reaction index ($s = 6$ corresponds to dipole-dipole interaction, $s = 8$ – dipole-quadrupole, $s = 10$ – quadrupole-quadrupole). Increasing concentration of sensitizer ions leads to the decrease of R and the growth of efficiency of energy transfer to the activator ions.

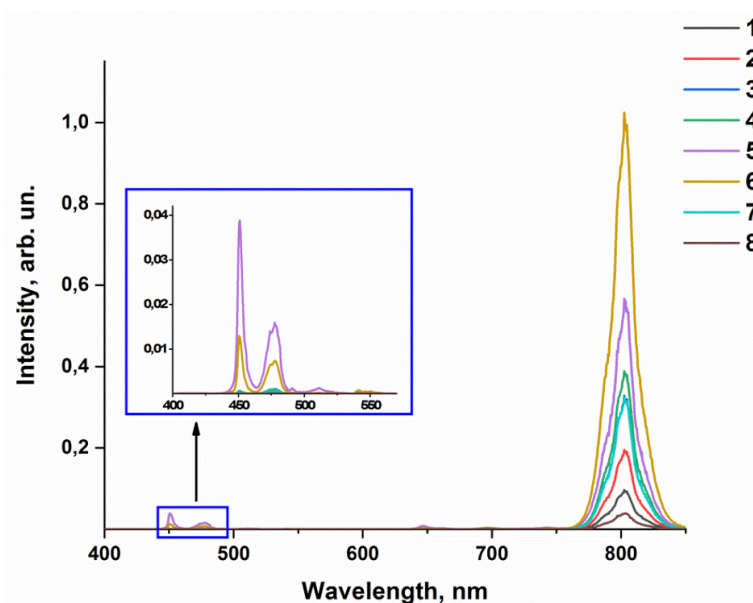


FIG. 4. Luminescence spectra of the studied samples No. 1 – 8

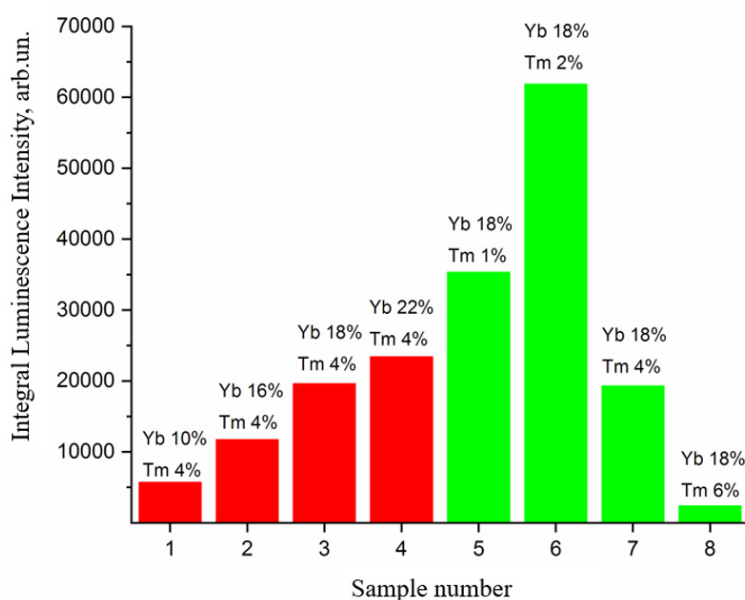


FIG. 5. Dependence of integral luminescence intensity on the concentration of sensitizer (Yb) and activator (Tm) ions

At fixed concentration of sensitizer ions (samples 5 – 8), the dependence of the luminescence intensity on the activator concentration is more complex. On the one hand, the increase of the activator concentrations leads to the increase of the luminescence intensity, since the number of luminescent centers is growing. On the other hand, the increase of the activators concentration may lead to the appearance of an additional luminescence quenching channel associated with the presence of cross-relaxation processes [17, 23]. Cross-relaxation is responsible for the concentration quenching of luminescence, since neighboring ions, one of which is in the excited state and the other in the ground state, exchange energy non-radiatively, as a rule, with subsequent relaxation of phonons [42].

Thus, there is a competition between the increase of the luminescence intensity due to the increase of the activator concentration and luminescence quenching due to cross-relaxation. This leads to the fact that there is an optimal concentration of activator ions at which the integral luminescence intensity is maximal. As it follows from the results obtained in this study, for the studied samples of $\beta\text{-NaYF}_4:\text{Yb}^{3+}/\text{Tm}^{3+}$ in DMSO such optimal concentration of Tm is 2 mol.% at the concentration of Yb 18 mol.% (Fig. 5).

It should be noted that the increase of the sensitizer concentration does not lead to deactivation of excited states due to cross-relaxation, since it requires the presence of several excited levels in the ion [23, 43].

3.2. Dependences of the intensities of the luminescence bands of nanoluminophores on the ratio of activator and sensitizer concentrations

The luminescence spectrum consists of the bands with different intensities (Fig. 4), therefore, the dependencies of the intensity on the concentration of activator and sensitizer ions for each band of the spectrum were constructed separately (Fig. 6).

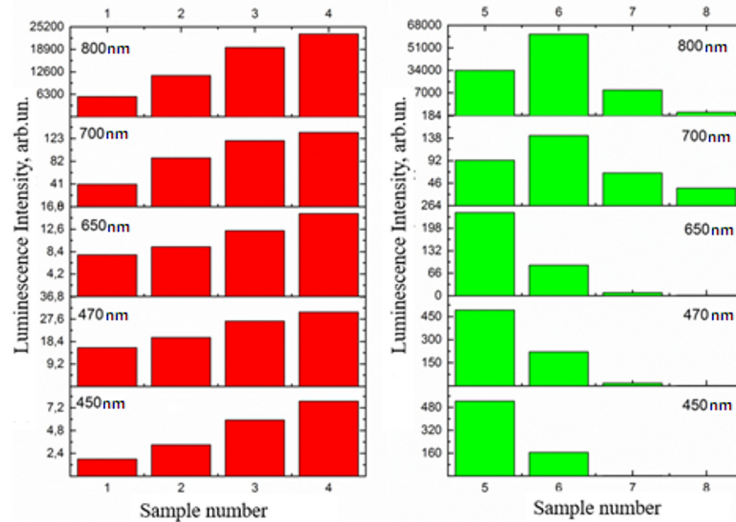


FIG. 6. Luminescence intensities of different bands while changing the concentration of sensitizer ions (left) and activator ions (right)

Samples with different sensitizer concentrations and fixed activator concentration have similar dependence, which has been previously revealed for integral intensity (Fig. 6, left). The increase of the sensitizer concentration leads to the increase of the luminescence intensity as the proportion of absorbed radiation increases and the distance between activator and sensitizers ions decreases, which causes the increase of the efficiency of energy transfer.

The results obtained for various concentrations of activator and fixed concentration of sensitizer are more complicated (Fig. 6, right). Dependences of the luminescence intensity on the concentration of the activator for the bands in the region of 700 and 800 nm qualitatively repeat the same dependences for integral intensity. Dependences of the luminescence intensity on the activator concentration for the bands in the regions of 450, 475 and 650 nm differ. The intensities of these bands decrease with the increase of the activator concentration.

Such a difference can be explained as follows. Different numbers of photons are required for excitation of the different bands of luminescence: excitation of bands in the regions of 700 and 800 nm requires two photons, 475 and 650 nm – three photons, 450 nm – four photons (Fig. 3). Therefore, bands with maximums at 450, 475 and 650 nm are more sensitive to the efficiency of cross-relaxation of excited states of activator ions.

Increasing activator concentration and decreasing average distance between ions resulted in increasing the probability of cross-relaxation. As a result, there is a monotonous decrease of the luminescence intensity of these bands with the increase of the concentration of the activator ions. It concerns especially the band in the region of 450 nm, which requires the largest number of photons for excitation. Its intensity decreases most rapidly with the increase of the concentration of activator ions (Fig. 6). Probably, the optimal value of the activator ion concentration for bands 450, 470, 650 nm corresponds to the thulium concentration of less than 1 mol.% with the fixed sensitizer concentration of 18 mol.%. At the same time, the optimal value of thulium concentration for bands with maximum in the region of 700 and 800 nm corresponds to 2 mol.%. Since the band in the region of 800 nm located in transparency tissue window makes the greatest contribution to the integral luminescence intensity (Fig. 6), the optimal value of the activator ion concentration for the integral luminescence intensity also equals 2 mol.%.

4. Conclusions

In this study, the dependences of the integral intensity and intensities of all bands of the luminescence spectra of β -NaYF₄:Yb³⁺/Tm³⁺ nanoluminophores in DMSO on the concentration of activator and sensitizer ions were investigated. In order to ensure the greatest reliability of the measured photophysical characteristics, a series of samples with different concentrations of activator and sensitizer ions were successfully synthesized. The spectra were recorded under the same optical scheme and intensity of excitation radiation.

It was established that the ratio between concentrations of ytterbium and thulium ions strongly influences on both the integral luminescence intensity and the intensity of individual spectral bands. The increase of the sensitizer concentration

at the constant concentration of the activator leads to the increase of the intensity of integral luminescence. At the fixed concentration of sensitizer ions, there is optimal activator concentration that provides the most intense luminescence. For the studied samples of $\beta\text{-NaYF}_4\text{:Yb}^{3+}/\text{Tm}^{3+}$ in DMSO, such optimal concentration of Tm is 2 mol.% at the concentration of Yb 18 mol.%.

The obtained dependences reflect the role of cross-relaxation in activator ions. Bands in the regions of 450, 475 and 650 nm are more sensitive to the efficiency of cross-relaxation because they require more photons for excitation than the bands in the regions of 700 and 800 nm.

Appendix

TEM images of the samples.

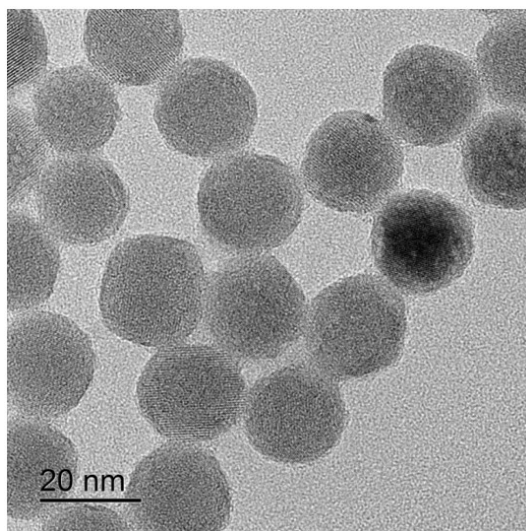


FIG. A1. TEM image of the sample No. 2

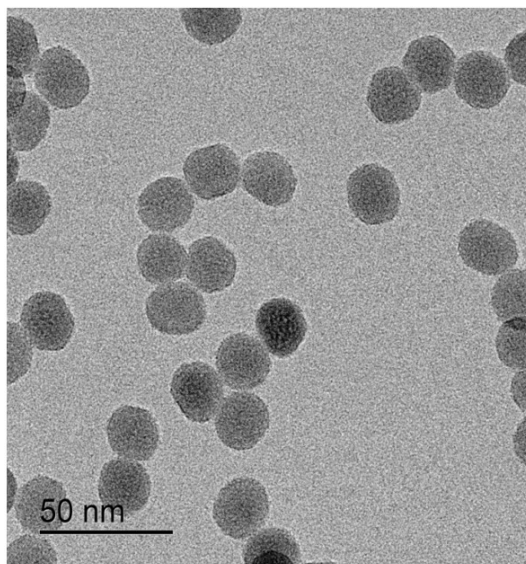


FIG. A2. TEM image of the sample No. 3

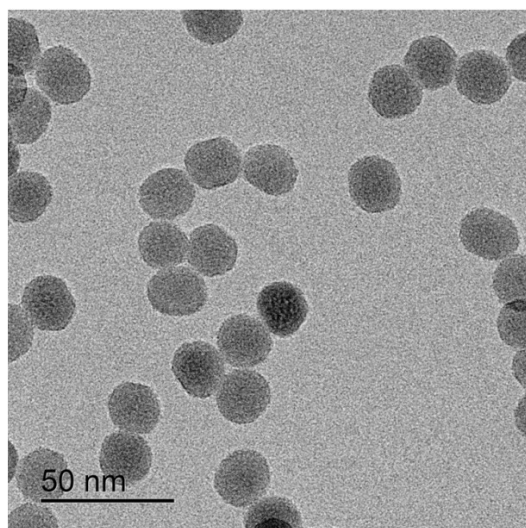


FIG. A3. TEM image of the sample No. 5

Size distribution of nanoluminophores $\beta\text{-NaYF}_4\text{:Yb}^{3+}/\text{Tm}^{3+}$ in DMSO, obtained by DLS method.

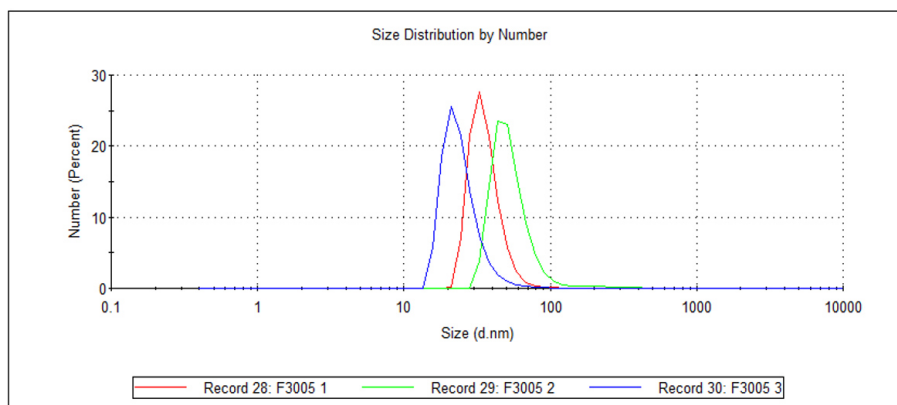


FIG. A4. Size distribution of the sample No. 2

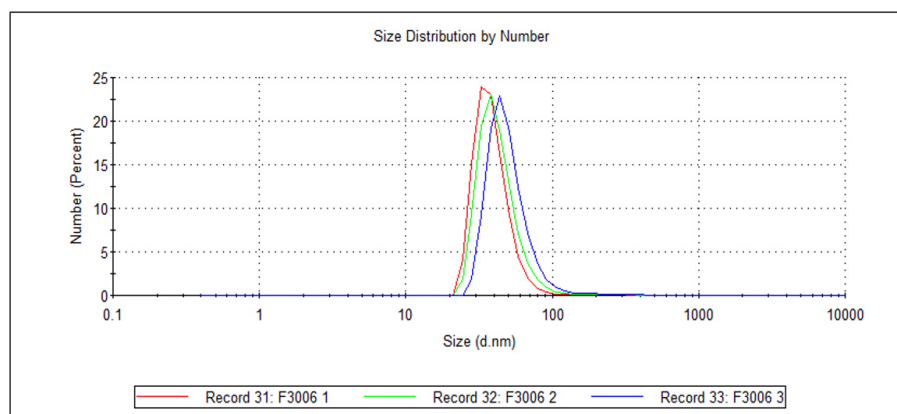


FIG. A5. Size distribution of the sample No. 3

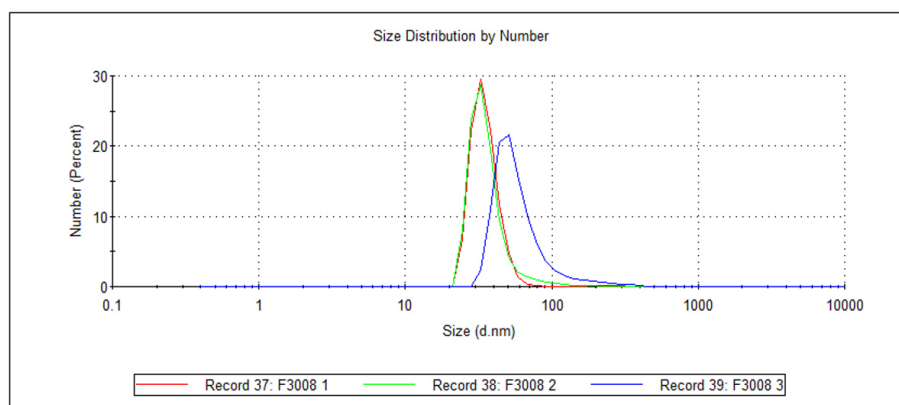


FIG. A6. Size distribution of the sample No. 5

References

- [1] Auzeil F. History of upconversion discovery and its evolution. *J. Luminescence*, 2020, **223**, 1169005.
- [2] Bloembergen N. Solid State Infrared Quantum Counters. *Phys. Rev. Lett.*, 1959, **2**, P. 84–85.
- [3] Ovsyankin V.V., Feofilov P.P. Mechanism of Summation of Electronic Excitations in Activated Crystals. *JETP Lett.*, 1966, **3**, P. 322–323.
- [4] Escudero A., Becerro A.I., et al. Rare earth based nanostructured materials: synthesis, functionalization, properties and bioimaging and biosensing applications. *Nanophotonics*, 2017, **6**, P. 881–921.
- [5] Pominova D.V., Proydakova V.Y., et al. Achieving high NIR-to-NIR conversion efficiency by optimization of Tm³⁺ content in Na(Gd,Yb)F₄: Tm upconversion luminophores. *Laser Physics Letters*, 2020, **17**, 125701.
- [6] Burikov S.A., Kotova O.D., et al. Determining the Photophysical Parameters of NaGdF₄:Eu Solid Solutions in Suspensions Using the Judd-Ofelt Theory. *JETP Lett.*, 2020, **111**, P. 525–531.
- [7] Liu Q. *Studies of optical properties of lanthanide upconversion nanoparticles for emerging applications*. Stockholm: KTH Royal Institute of Technology, 2020, 73 p.
- [8] Han S., Deng R., Xie X., Liu X. Enhancing luminescence in lanthanide-doped upconversion nanoparticles. *Angew. Chem. Int. Ed.*, 2014, **53**, P. 11702–11715.
- [9] Sarmanova O.E., Burikov S.A., et al. In Vitro Temperature Sensing with Up-Conversion NaYF₄:Yb³⁺/Tm³⁺-Based Nanocomposites: Peculiarities and Pitfalls. *Spectrochim. Acta A*, 2020, **24**, 118627.
- [10] Geitenbeek R.G., Prins P.T., et al. NaYF₄:Er³⁺, Yb³⁺/SiO₂ Core/Shell Upconverting Nanocrystals for Luminescence Thermometry up to 900 K. *J. Phys. Chem. C*, 2017, **121**, P. 3503–3510.
- [11] Jaque D., Vetrone F. Luminescence nanothermometry. *Nanoscale*, 2012, **4**, P. 4301–4326.
- [12] Pominova D., Proydakova V., et al. Temperature sensing in the short-wave infrared spectral region using core-shell NaGdF₄:Yb³⁺, Ho³⁺, Er³⁺@NaYF₄ nanothermometers. *Nanomaterials*, 2020, **10** (10), 1992.
- [13] Shalav A., Richards B.S., Green M.A. Luminescent Layers for Enhanced Silicon Solar Cell Performance: Up-Conversion. *Sol. Energy Mater. Sol. Cells*, 2007, **91**, P. 829–842.
- [14] Trupke T., Green M.A., Würfel P. Improving Solar Cell Efficiencies by Up-Conversion of Sub-Band-Gap Light. *J. Appl. Phys.*, 2002, **92**, P. 4117–4122.
- [15] Richards B.S. Enhancing the Performance of Silicon Solar Cells via the Application of Passive Luminescence Conversion Layers. *Sol. Energy Mater. Sol. Cells*, 2006, **90**, P. 2329–2337.
- [16] Hu Y., Sun Y., et al. A facile synthesis of NaYF₄:Yb³⁺/Er³⁺ nanoparticles with tunable multicolor upconversion luminescence properties for cell imaging. *RSC Adv.*, 2014, **4**, P. 43653–43660.
- [17] Pilch A., Wawrzyńczyk D., et al. The concentration dependent up-conversion luminescence of Ho³⁺ and Yb³⁺ co-doped β-NaYF₄. *J. Lumin.*, 2017, **182**, P. 114–122.
- [18] Kormshikov I.D., Voronov V.V., et al. Study of stability of luminescence intensity of β-NaGdF₄: Yb: Er nanoparticle colloids in water solution. *Nanosystems: Phys. Chem. Math.*, 2021, **12**, P. 218–223.
- [19] Liu H.C., Xu C.T., et al. Balancing power density based quantum yield characterization of upconverting nanoparticles for arbitrary excitation intensities. *Nanoscale*, 2013, **5**, P. 4770–4775.
- [20] Saleta Reig D., Grauel B., et al. Upconversion properties of SrF₂:Yb³⁺, Er³⁺ single crystals. *J. Mater. Chem. C*, 2020, **8**, P. 4093–4101.
- [21] Zhao J., Jin D., et al. Single-nanocrystal sensitivity achieved by enhanced upconversion luminescence. *Nature Nanotechnology*, 2013, **8**, P. 729–734.
- [22] Chen G., Ohulchanskyy T.Y., et al. *ACS Nano*, 2010, **4**, P. 3163–3168.
- [23] Ma C.S., Xu X.X., et al. Optimal Sensitizer Concentration in Single Upconversion Nanocrystals. *Nano Lett.*, 2017, **17**, P. 2858–2864.
- [24] Wei W., Zhang Y., et al. Cross relaxation induced pure red upconversion in activator- and sensitizer-rich lanthanide nanoparticles. *Chem. Mater.*, 2014, **26**, P. 5183–5186.
- [25] Pisarenko V.F. Rare-earth scandoborates as new laser materials. *Soros. Obrazovat. Zh.*, 1996, **11**, P. 111–116.
- [26] Li X., Shen D., et al. Successive layer-by-layer strategy for multi-shell epitaxial growth: shell thickness and doping position dependence in upconverting optical properties. *Chem. Mater.*, 2013, **25**, P. 106–112.
- [27] Liu M., GuM., et al. Multifunctional CaSc₂O₄:Yb³⁺/Er³⁺ one-dimensional nanofibers: electrospinning synthesis and concentration-modulated upconversion luminescent properties. *J. Mater. Chem. C*, 2017, **5**, P. 4025–4033.
- [28] Bai X., Song H., et al. Size-dependent upconversion luminescence in Er³⁺/Yb³⁺-codoped nanocrystalline yttria: saturation and thermal effects. *J. Phys. Chem. C*, 2007, **111**, P. 13611–13617.
- [29] Liu F., Ma E., et al. Tunable red-green upconversion luminescence in novel transparent glass ceramics containing Er:NaYF₄ nanocrystals. *The Journal of Physical Chemistry B*, 2006, **110**, P. 20843–20846.

- [30] Vetrone F., Boyer J.-C., Capobianco J.A. Significance of Yb³⁺ concentration on the upconversion mechanisms in codoped Y₂O₃:Er³⁺, Yb³⁺ nanocrystals. *J. of Applied Physics*, 2004, **96**, P. 661–667.
- [31] Misiak M., Prorok K., et al. Thulium concentration quenching in the up-converting α -Tm³⁺/Yb³⁺ NaYF₄ colloidal nanocrystals. *Optical Materials*, 2013, **35**, P. 1124–1128.
- [32] Xu D., Liu C., et al. Understanding energy transfer mechanisms for tunable emission of Yb³⁺-Er³⁺ codoped GdF₃ nanoparticles: concentration-dependent luminescence by near-infrared and violet excitation. *J. Phys. Chem. C*, 2015, **119**, P. 6852–6860.
- [33] Tie Cong, Yadan Ding, et al. Solvent-Induced Luminescence Variation of Upconversion Nanoparticles. *Langmuir*, 2016, **32** (49), P. 13200–13206.
- [34] Brites C.D.S., Kuznetsov S.V., et al. Simultaneous measurement of the emission quantum yield and local temperature: The illustrative example of SrF₂:Yb³⁺/Er³⁺ single crystals. *European J. of Inorganic Chemistry*, 2020, **2020** (17), P. 1555–1561.
- [35] Madirov E.I., Konyushkin V.A., et al. Effect of Yb³⁺ and Er³⁺ concentration on upconversion luminescence of co-doped BaF₂ single crystals. *J. Mater. Chem. C*, 2021, **9**, P. 3493–3503.
- [36] Fedorov P.P., Kuznetsov S.V., Osiko V.V. Elaboration of nanofluorides and ceramics for optical and laser applications. In *Photonic & Electronic Properties of Fluoride Materials*, Ed. A. Tressaud, K. Poepelmeier, 2016, P. 7–31.
- [37] Valenta J., Repko A., Greben M., Nižňanský D. Absolute up- and down-conversion luminescence efficiency in hexagonal Na(Lu/Y/Gd)F₄: Yb, Er/Tm/Ho with optimized chemical composition. *AIP Advances*, 2018, **8**, 075226.
- [38] Wang F., Liu X. Upconversion Multicolor Fine-Tuning: Visible to Near-Infrared Emission from Lanthanide-Doped NaYF₄ Nanoparticles. *J. of the American Chemical Society*, 2008, **30**, P. 5642–5643.
- [39] Liu J., Chen G., Hao S., Yang C. Sub-6 nm monodisperse hexagonal core/shell NaGdF₄ nanocrystals with enhanced upconversion photoluminescence. *Nanoscale*, 2017, **9**.
- [40] Clegg R.M. Chapter 1 Förster resonance energy transfer – FRET what is it, why do it, and how it's done. *Laboratory Techniques in Biochemistry and Molecular Biology*, 2009, **33**, P. 1–57.
- [41] Dexter D.L. A Theory of Sensitized Luminescence in Solids. *J. Chem. Phys.*, 1953, **21**, P. 836–850.
- [42] Bergstrand J., Liu Q.Y., et al. On the decay time of upconversion luminescence. *Nanoscale*, 2019, **11**, P. 4959–4969.
- [43] Wen S., Zhou J., et al. Advances in highly doped upconversion nanoparticles. *Nat. Commun.*, 2018, **9**, 2415.

Submitted 5 May 2022; accepted 14 June 2022

Information about the authors:

Sergey V. Kuznetsov – Prokhorov General Physics Institute of the Russian Academy of Sciences, Moscow, 119991, Russia; ORCID 0000-0002-7669-1106; kouznetzovsv@gmail.com

Sergey A. Burikov – Department of Physics, Lomonosov Moscow State University, Moscow, 119991, Russia; ORCID 0000-0003-2271-8980; sergey.burikov@gmail.com

Anna A. Fedyanina – Department of Physics, Lomonosov Moscow State University, Moscow, 119991, Russia; ORCID 0000-0001-6659-5674; fedyanechka@mail.ru

Ekaterina A. Filippova – Department of Physics, Lomonosov Moscow State University, Moscow, 119991, Russia; filippova.ea17@physics.msu.ru

Vera Yu. Proydakova – Prokhorov General Physics Institute of the Russian Academy of Sciences, Moscow, 119991, Russia; ORCID 0000-0001-8017-9175; vera.proydakova@gmail.com

Valerii V. Voronov – Prokhorov General Physics Institute of the Russian Academy of Sciences, Moscow, 119991, Russia; ORCID 0000-0001-5029-8560; voronov@lst.gpi.ru

Nataliya Yu. Tabachkova – Prokhorov General Physics Institute of the Russian Academy of Sciences, Moscow, 119991, Russia; ORCID 0000-0002-0169-5014; ntabachkova@gmail.com

Pavel P. Fedorov – Prokhorov General Physics Institute of the Russian Academy of Sciences, Moscow, 119991, Russia; ORCID 0000-0002-2918-3926; ppfedorov@yandex.ru

Tatiana A. Dolenko – Department of Physics, Lomonosov Moscow State University, Moscow, 119991, Russia; ORCID 0000-0003-2884-8241; tdolenko@mail.ru

Conflict of interest: the authors declare that they have no known competing financial interests or personal relationships that could have appeared to influence the work reported in this paper.

Evaluation of antibacterial potential of bilirubin nanoparticles against *Staphylococcus aureus* and *Escherichia coli*

Dhaval J. Kamothi¹, Vinay Kant¹, Vinod Kumar¹, Vinay G. Joshi², Rajesh Chhabra³

¹Department of Veterinary Pharmacology & Toxicology, COVS, Lala Lajpat Rai University of Veterinary and Animal Sciences, Hisar, Haryana, India

²Department of Animal Biotechnology, COVS, Lala Lajpat Rai University of Veterinary and Animal Sciences, Hisar, Haryana, India

³College Central Laboratory, COVS, Lala Lajpat Rai University of Veterinary and Animal Sciences, Hisar, Haryana, India

Corresponding author: Vinay Kant, drvinaykantluvas@gmail.com

ABSTRACT Antimicrobial resistance is a major emerging clinical and public health issue across the globe. Nanotechnology is an emerging field and developing area of scientific interest in the world. Earlier reports showed *in vivo* antibacterial activity of bilirubin. Therefore, in present study, bilirubin nanoparticles (BNP) were synthesized of ~100 – 150 nm, spherical shape and negative charge. Antibacterial activity of BNPs at different concentrations (0.03, 0.1 and 0.3 %) was evaluated by agar well diffusion method against the gram-positive i.e. *S. aureus* and gram-negative i.e. *E. coli* bacteria. Tetracycline and enrofloxacin used as positive control. Tetracycline and Enrofloxacin at different concentrations exhibited zones of inhibition against both *S. aureus* and *E. coli*. However, BNPs as well as bulk bilirubin showed no *in vitro* antibacterial effect on *S. aureus* and *E. coli*, however, testing by broth method and at higher concentration as well as against other microorganisms can be explored in future.

KEYWORDS Bilirubin nanoparticles, *S. aureus*, *E. coli*, antibacterial activity

ACKNOWLEDGEMENTS All the authors are highly thankful to the administration of Lala Lajpat Rai University of Veterinary and Animal Sciences (LUVAS), Hisar, Haryana, India for providing essential facilities and support for carrying out present study. We also acknowledge the support of SAIF, AIIMS, New Delhi for providing the facilities for TEM studies.

FOR CITATION Kamothi D. J., Kant V., Kumar V., Joshi V. G., Chhabra R. Evaluation of antibacterial potential of bilirubin nanoparticles against *Staphylococcus aureus* and *Escherichia coli*. *Nanosystems: Phys. Chem. Math.*, 2022, **13** (3), 342–348.

1. Introduction

The discovery of antibiotics is considered to be one of the most important medical achievements during the twentieth century [1]. In the years between 1930 and 1962, more than 20 new classes of antibiotics were produced, however, as a result of the evolution of new resistant bacterial strains, a major challenge has been set up against the pharmaceutical industries for the discovery of new molecules with antibacterial activity [2]. In the present scenario, an emerging major clinical and public health issue across the globe is the development of bacterial resistance to antibiotics. Indiscriminate use of antibiotics, lack of new strategies against antibacterial resistance development has mainly lead to the development of bacterial resistance to antibiotics. Microorganisms acquire the ability to produce resistance against antibacterial agents through different modifications either by inactivating them or by causing a decrease in their therapeutic efficacy. Antibiotic resistance is developed by decreased influx and increased efflux of antibiotic by microorganisms, alteration in binding target sites, production of some enzymes etc. These resistances can appear spontaneously in microorganisms through genetic modifications over a period of time. Such modifications are favored by the inappropriate use and abuse of antibiotics [2]. In the present situation, the development of new antibacterial agents is required to overcome antimicrobial resistance. Bilirubin belongs to the superfamily of tetrapyrrolic compounds, which is one of the most highly conserved groups of molecules. Bilirubin, due to its strong antioxidant, immunomodulatory and anti-inflammatory responses has gained wide attention in biomedical research [3]. Bilirubin exhibited protective effects in rat model of endotoxemia [4]. Bilirubin also showed antiviral activity when added to infected cell cultures [5]. Bilirubin levels are also elevated during conditions of sepsis, intra-abdominal abscesses from urological, gynecological or gastroenterological origins, and antiviral therapy [6]. Bilirubin has been suggested to be an effective antibacterial, but little data is available. In the previous studies, the antibacterial effects of bilirubin on gram-negative bacterial agents have been evaluated [7]. However, bilirubin did not exhibit *in vitro* antibacterial effect. The present study was proposed to synthesize bilirubin nanoparticles, as

the nanoformulations have the advantage of requiring low dosage or drug usage, nano particle size which enables better penetration of drug, increased drug solubility, sustained release property and decreased degradation of drug. On the contrary, a bulk or dissolved form of drug have large particle size, requires higher concentration to produce desired effect and increases the risk of toxicity. Therefore, to exploit the full potential of bilirubin, the present study was proposed to evaluate the antibacterial potential of bilirubin nanoparticles and its comparison with its bulk form, as such work has not been reported previously.

2. Materials and methods

2.1. Preparation of bilirubin loaded pluronic F-127 (PF-127) nanoparticles

Bilirubin (mixed isomers) and pluronic F-127 (PF-127) were purchased from Sigma Aldrich (St. Louis, Missouri, USA). Bilirubin and eudragit were dissolved in dimethyl sulfoxide (DMSO) and were stirred for 20 min on a magnetic stirrer. Thereafter, 1% Pluronic F-127 (1% PF-127) was prepared by dissolving pluronic F-127 in distilled water. After that, using a 25-gauge needle, bilirubin solution was then added dropwise into PF-127 (1%) aqueous solution and stirred for 2 h on magnetic stirrer at 1000 rpm for antisolvent precipitation and encapsulation. The suspension was further sonicated for 5 min at 4 °C. Three different concentrations of bilirubin nanoparticles i.e. 0.03% bilirubin nanoparticles [BNP (0.03%)], 0.1% bilirubin nanoparticles [BNP (0.1%)] and 0.3% bilirubin nanoparticles [BNP (0.3%)] were prepared using this method. The ratio of bilirubin to eudragit was kept at 1.0 : 0.5 for the synthesis of bilirubin nanoparticles.

2.2. Characterization of nanoparticles

2.2.1. Hydrodynamic diameter and polydispersity index (PDI) of bilirubin nanoparticles. Hydrodynamic diameter and polydispersity index (PDI) of the nanoparticles were determined by Zetasizer (Malvern, UK), as per the instructions of the instrument.

2.2.2. Zeta potential measurement of bilirubin nanoparticles. Zeta potential of the nanoparticles was determined by Zetasizer (Malvern, UK), as per the instructions of the instrument. Zeta potential measurement was carried out to determine the surface charge of the nanoparticles. For this the bilirubin nanosuspension was injected into the zeta cell with the help of 1mL disposable syringe and then the syringe plunger was gently pressed to fill the zeta cell with the nanosuspension, thereafter the zeta cell was placed in the instrument to determine the zeta potential of the bilirubin nanoparticles.

2.2.3. Transmission electron microscopy (TEM). Size and morphology of bilirubin nanoparticles were determined by transmission electron microscopy studies. TEM grid was used for the study on which the dispersed nanoparticle suspension was placed and then it was transferred to the microscope for imaging.

2.3. In vitro evaluation of antibacterial activity of bilirubin nanoparticles

Antibacterial activity of bilirubin nanoparticles at different concentrations (0.03, 0.1 and 0.3%) were evaluated against the gram-positive i.e. *Staphylococcus aureus* (*S. aureus*) (ATCC 12600) and gram-negative i.e. *Escherichia coli* (*E. coli*) (ATCC 10536) bacterial strains. These bacterial strains were gifted by the Department of Veterinary Microbiology, COVS, LUVAS, Hisar, Haryana, India. The PF-127, blank NP, 0.3% bulk bilirubin were also evaluated along with bilirubin nanoparticles for antibacterial activity. Standard antibacterial i.e. tetracycline (Cat. no. MB178, HiMedia) (at 62.5, 125, 250 µg/ml) and enrofloxacin (Cat. no. CMS8318, HiMedia) (at 31.25, 62.5, 125 µg/ml) were used as positive control to compare the efficacy of the nanoparticles. The antibacterial activity was determined on Muller–Hinton agar by the agar well diffusion method [8]. The autoclaved Muller–Hinton agar was poured (12 ml) in petri plates and smeared with overnight cultures of different bacterial strains (10^8 cfu/ml). The agar plates were allowed to solidify and, wells of 6 mm diameter were made in each plate with the help of sterile gel puncher. Thirty microlitres of bilirubin nanoparticles of different concentrations, other preparations (i.e. pluronic F-127, blank nanoparticles and 0.3% bulk bilirubin) and different dilutions of standard antibiotic (tetracycline and enrofloxacin) were poured into separate wells using a micropipette. After overnight incubation at 37 °C, the different diameters of zone of inhibition were measured to quantify the antibacterial activity. The same experiment for all was conducted in triplicate.

2.4. Statistical analysis

The values are expressed as mean \pm SEM with *n* equal to the number of replicates and calculated using GraphPad Prism v8.0.2 software program (San Diego, CA, USA).

3. Results

3.1. Characterization of synthesized bilirubin nanoparticles

The hydrodynamic diameter of the blank PF-127 nanoparticles was 87.41 ± 4.98 nm and that of bilirubin loaded nanoparticles in three different concentrations i.e. 0.03, 0.1 and 0.3% was 119.83 ± 7.28 , 121.03 ± 6.21 and 139.03 ± 6.21 nm, respectively (Fig. 1A).

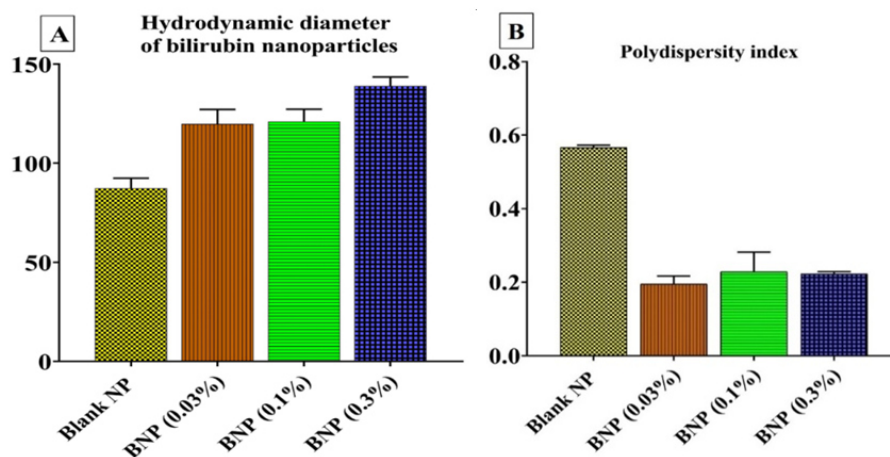


FIG. 1. (A) Hydrodynamic diameter and (B) Polydispersity index (PDI) of blank nanoparticles, and bilirubin nanoparticles (BNP) of different concentrations (0.03, 0.1, 0.3 %) ($n = 3$)

The PDI of blank PF-127 nanoparticles was 0.57 ± 0.01 , that of the bilirubin nanoparticles of three different concentrations i.e. 0.03, 0.1 and 0.3 % was 0.19 ± 0.02 , 0.23 ± 0.05 and 0.22 ± 0.01 , respectively (Fig. 1B). The zeta potential of the three different concentrations of bilirubin nanoparticles i.e. 0.03, 0.1 and 0.3 % was -11.47 ± 0.17 , -13.57 ± 0.20 and -15.43 ± 0.15 mV, respectively ($n = 3$) (Fig. 2).

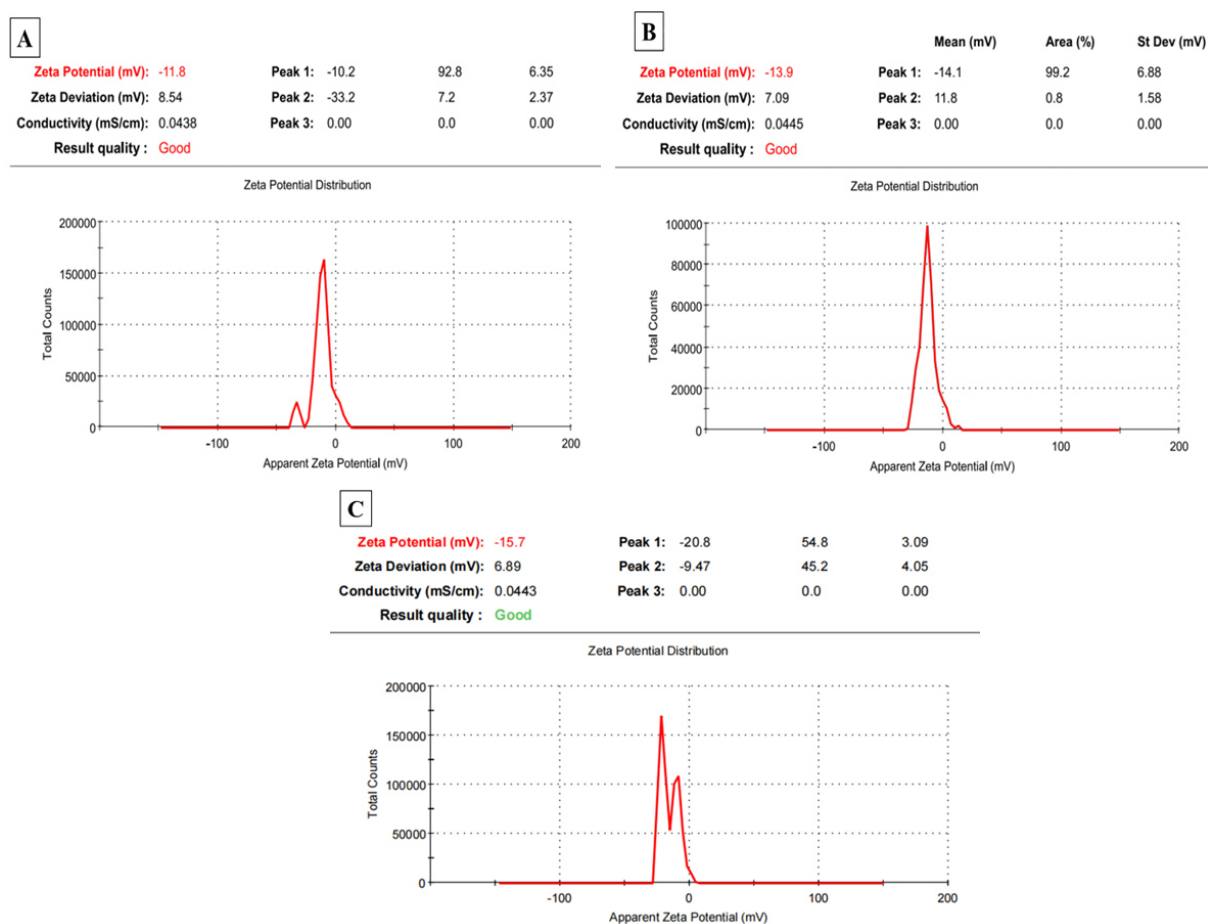


FIG. 2. Graphs showing the zeta potential of nanoparticles. (A) 0.03 % bilirubin nanoparticles, (B) 0.1 % bilirubin nanoparticles and (C) 0.3 % bilirubin nanoparticles

3.2. TEM of bilirubin nanoparticles

The representative TEM image of bilirubin nanoparticles is given in Fig. 3. The image revealed that the size of particles was in nano range. The TEM study revealed that the bilirubin encapsulated pluronic F127 nanoparticles have spherical morphology. There was no presence of agglomeration/aggregation of bilirubin nanoparticles and the size of the nanoparticles was found to be in agreement with that of the hydrodynamic diameter measured using zetasizer.

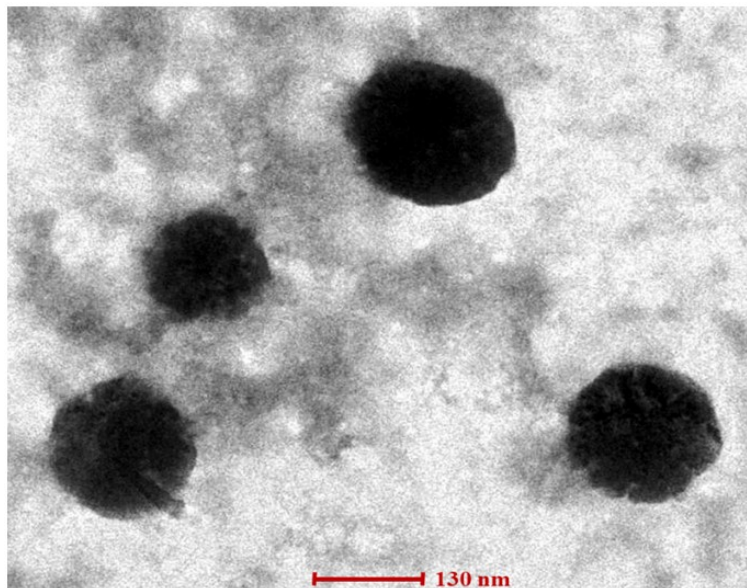


FIG. 3. TEM image showing the spherical shape of the synthesized bilirubin nanoparticles

3.3. Antibacterial effect of bilirubin nanoparticles

The representative images of zone of inhibition produced by different concentrations of antibiotics i.e. tetracycline and enrofloxacin, and different formulations i.e. pluronic F-127, blank nanoparticles, 0.3 % bulk bilirubin, bilirubin nanoparticles (0.03, 0.1 and 0.3 %) against *S. aureus* and *E. coli* is shown in Fig. 4(A). The value of zone of inhibition are presented in Fig. 4(B,C). The different concentrations of tetracycline i.e. 250, 125, 62.5 $\mu\text{g/ml}$ exhibited zones of inhibition of 22.67 ± 0.33 , 19.33 ± 0.67 and 17.33 ± 0.67 mm against *S. aureus*, and 19.00 ± 0.58 , 16.33 ± 0.33 and 13.67 ± 0.33 mm against *E. coli*, respectively. In the case of enrofloxacin, the different concentrations i.e. 125, 62.5, 31.25 $\mu\text{g/ml}$ exhibited zones of inhibition of 21.67 ± 0.88 , 19.00 ± 0.58 and 17.00 ± 0.58 mm against *S. aureus*, and 19.00 ± 0.58 , 18.00 ± 0.58 and 15.00 ± 0.58 mm against *E. coli*, respectively. Bilirubin nanoparticles and other formulations exhibited no zone of inhibition against these bacterial strains.

4. Discussion

Nanomaterials have been identified as an emerging area of research that are highly in demand for multiple practical applications. Nanoparticles provide an efficient carrier for the delivery of drugs and have a particle size ranging from 1 to 1000 nm. Polymers such as pluronic F-127 have been commonly used for encapsulation of active compounds by entrapping within the polymeric core. In our previously published work, we synthesized bilirubin nanoparticles by our novel method and the bilirubin nanoparticles were in nano range and had spherical morphology which was observed in TEM study and had negative zeta potential. The Fourier transform infrared microscopy (FTIR) of bilirubin nanoparticles showed that there was no intermolecular interaction between the bilirubin and the pluronic F127 and the entrapment of bilirubin by pluronic F127 was estimated by determining encapsulation efficiency [9]. In view of our previous work, the present study was proposed and the bilirubin nanoparticles were synthesized and characterized revealing spherical morphology of the bilirubin nanoparticles as observed in TEM study, also the hydrodynamic diameter of the bilirubin nanoparticles (120 – 140 nm) estimated by the zetasizer was in accordance with that of the TEM study and the zeta potential of the bilirubin nanoparticles was in the range of -11 to -16 mV which is in agreement with the literature value [10], considering the three different concentration of bilirubin nanoparticles.

In the *in vitro* antibacterial study, bilirubin nanoparticles (0.03, 0.1 and 0.3 %), bulk bilirubin and other prepared formulations of present study did not show antibacterial effect against *S. aureus* and *E. coli* at the tested concentrations. There is no report of evaluation of antibacterial effect of bilirubin against *S. aureus*, which has been recognized as one of the most important bacteria that cause diseases in humans, which has been tested in the present study. The earlier study has also reported that bilirubin had no antibacterial effect on *E. coli*, *Klebsiella pneumonia*, *Acinetobacter baumannii*

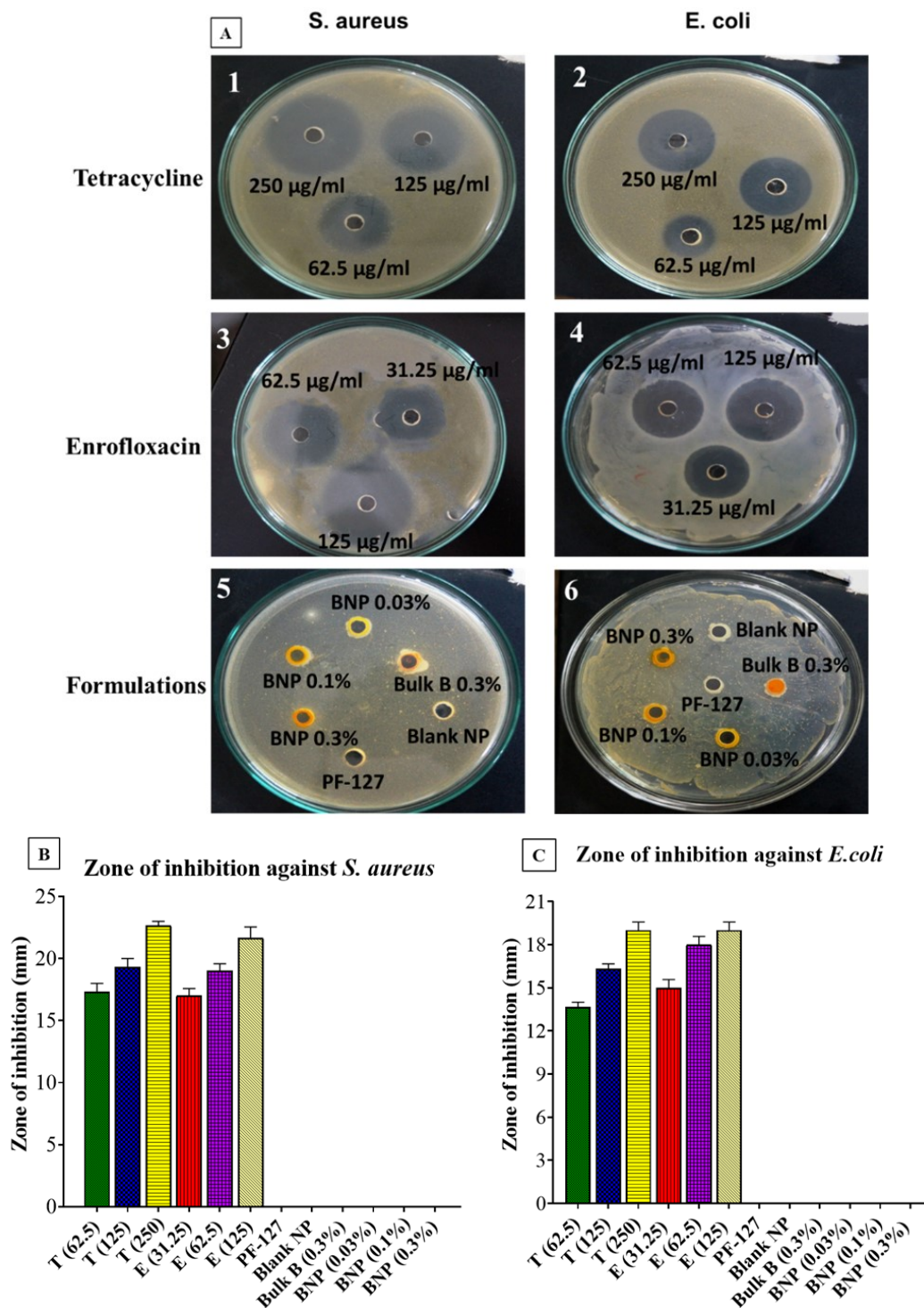


FIG. 4. (A) Images showing zone of inhibitions by tetracycline, enrofloxacin and different formulations against *S. aureus* and *E. coli*. (B–C) Zone of inhibitions of tetracycline (T; 62.5, 125 and 250 $\mu\text{g/ml}$), enrofloxacin (E; 31.25, 62.5 and 125 $\mu\text{g/ml}$) and different formulation against (B) *S. aureus* and (C) *E. coli*. Data are expressed as mean \pm SEM ($n = 3$). PF-127: (Pluronic F-127); Blank NP: (Blank nanoparticles); Bulk B 0.3%: (0.3% bulk bilirubin); BNP 0.03%: (0.03% bilirubin nanoparticles); BNP 0.1%: (0.1% bilirubin nanoparticles) and BNP 0.3%: (0.3% bilirubin nanoparticles)

and *Pseudomonas aeruginosa* [7]. In contrary to our *in vitro* antibacterial study, *in vivo* study has revealed that mice injected with *E. coli* endotoxin were protected from mortality and liver dysfunction by a single intravenous injection of bilirubin [4]. Further, it has been reported that mouse mortality caused by endotoxins is reduced in the presence of increased bilirubin levels [11]. Protective action of bilirubin against endotoxins is due to its potential of attenuating nitric oxide synthase-2 (NOS2) induction secondary to inhibition of NADPH oxidase activity, which is involved in the reduction of oxygen to form superoxide radicals [11]. These studies suggested that bilirubin might have no direct effect on endotoxins or bacteria, but attenuates the damage caused by radicals formed during bacterial infection as a result of its antioxidant potential. This might be the reason for the failure of bilirubin nanoparticles to show antibacterial activity during their *in vitro* evaluations.

In a recent study, antibacterial effect of bilirubin was evaluated against *Streptococcus agalactiae*, which is involved in early-onset neonatal sepsis [12]. The study involved a transcriptomic and proteomic assessment of *Streptococcus agalactiae* cultured in the presence/absence of bilirubin. The transcriptome analysis revealed that 19 genes were expressed/upregulated in presence of bilirubin and in case of proteomic analysis, 12 different proteins were expressed of which half were over-expressed due to the bilirubin. The expressed genes and proteins in the bacterial cells were involved in transport mechanism of sugar or toxic substance. This indicated that in presence of bilirubin, bacterial cells enhance their transport mechanism in order to eliminate the bilirubin out of the cell or increase the uptake of sugar in presence of bilirubin to compensate increased metabolic rate. In presence of bilirubin the bacterial cell showed downregulation of certain genes which are responsible for the production of N-acetyl neuramic acid synthetase NeuB, transketolase, and ornithine carbamoyltransferase leading to functional alteration of bacterial cell.

These reports indicate that the antibacterial mechanism of bilirubin can be indirect i.e. due to its antioxidant potential and ability to upregulate or downregulate certain bacterial genes and expression of bacterial proteins. Although, bilirubin having such potential, it is able to inhibit bacterial growth or exert bacteriostatic effect to a certain limit.

However, the antibacterial effect of bilirubin was evaluated in a liquid model which allowed interaction of bacteria and the bilirubin in free suspension, partially representing an *in vivo* environment. In the present study, *in vitro* antibacterial study was carried out using agar well diffusion assay. The failure of nanoparticles to diffuse through the agar might be another reason for no antibacterial activity of bilirubin nanoparticles. So, testing these nanoparticles for antibacterial activity in the broth might be a more effective approach providing better interaction between the bilirubin nanoparticles and the microbes in a suspension and their testing can also be attempted at concentrations higher than 0.3 % against more bacterial strains.

5. Conclusion

On the basis of findings of this study, it might be concluded that the synthesized spherical bilirubin nanoparticles showed no antibacterial activity against *S. aureus* and *E. coli* by the agar well diffusion method. The testing of these nanoparticles for antibacterial activity in the broth might be a more effective approach. Further, their testing for antibacterial activity at higher concentrations and against other microorganisms may be explored in the future. However, in view of searching for a novel formulation having antibacterial activity, we synthesized bilirubin nanoparticles and investigated its antibacterial effect against *S. aureus* and *E. coli*, in order to understand the effect of bilirubin nanoparticles compared to its bulk form, a novel approach which is not yet adopted and reported.

Authors' contributions

D.J.K., V.K.*, V.K. and R.C. designed the experiment. D.J.K. and V.G.J. did the synthesis and characterization studies of nanoparticles. D.J.K. and V.K.* did the *in vitro* experimentation. All authors analysed the data and contributed in writing the manuscript. V.K.* supervised the whole study.

References

- [1] World Health Organization. Antibacterial agents in clinical development: an analysis of the antibacterial clinical development pipeline, including tuberculosis. No. WHO/EMP/IAU/2017.11, World Health Organization, 2017.
- [2] Aslam B., Wang W., et al. Antibiotic resistance: a rundown of a global crisis. *Infect. Drug Resist.*, 2018, **11**, P. 1645–1658.
- [3] Lee Y., Kim H., et al. Bilirubin nanoparticles as a nanomedicine for anti-inflammatory therapy. *Angew. Chem. Int. Ed.*, 2016, **55** (26), P. 7460–7463.
- [4] Wang W. W., Smith D.L., Zucker, S. D. Bilirubin inhibits iNOS expression and NO production in response to endotoxin in rats. *Hepatology*, 2004, **40** (2), P. 424–433.
- [5] Santangelo R., Mancuso C., et al. Bilirubin: An Endogenous Molecule with Antiviral Activity in vitro. *Front. Pharmacol.*, 2012, **3**, 36.
- [6] Buyukasik Y., Akman U., et al. Evidence for higher red blood cell mass in persons with unconjugated hyperbilirubinemia and Gilbert's syndrome. *Am. J. Med. Sci.*, 2008, **335**, P. 115–119.
- [7] Terzi H.A., Kardes H., et al. The antibacterial effects of bilirubin on gram-negative bacterial agents of sepsis. *Biomed. Res.*, 2016, **27**, P. 207–209.
- [8] Perez C., Pauli M., Bazerque P. An antibiotic assay by agar-well diffusion method. *Acta Biol. Med. Exp.*, 1990, **15**, P. 113–115.
- [9] Kamothi D.J., Kant V., et al. Novel preparation of bilirubin-encapsulated pluronic F-127 nanoparticles as a potential biomaterial for wound healing. *Eur. J. Pharmacol.*, 2022, **919**, 174809.
- [10] Shaarani S., Hamid S.S., Mohd Kaus N.H. The Influence of Pluronic F68 and F127 Nanocarrier on Physicochemical Properties, *In vitro* Release, and Antiproliferative Activity of Thymoquinone Drug. *Pharmacogn. Res.*, 2017, **9** (1), P. 12–20.

- [11] Lanone S., Bloc S., et al. Bilirubin decreases nos2 expression via inhibition of NAD (P) H oxidase: implications for protection against endotoxic shock in rats. *Faseb J.*, 2005, **19** (13), P. 1890–1892.
- [12] Hansen R., Gibson S., et al. Adaptive response of neonatal sepsis-derived Group B Streptococcus to bilirubin. *Sci. Rep.*, 2018, **8** (1), 6470.

Submitted 27 January 2022; revised 21 May 2022; accepted 22 May 2022

Information about the authors:

Dhavak J. Kamothi – Department of Veterinary Pharmacology & Toxicology, COVS, Lala Lajpat Rai University of Veterinary and Animal Sciences, Hisar, Haryana, India; ORCID 0000-0003-2072-2855; kamothidhaval@gmail.com

Vinay Kant – Department of Veterinary Pharmacology & Toxicology, COVS, Lala Lajpat Rai University of Veterinary and Animal Sciences, Hisar, Haryana, India; ORCID 0000-0001-9600-4417; drvinaykantluvas@gmail.com

Vinod Kumar – Department of Veterinary Pharmacology & Toxicology, COVS, Lala Lajpat Rai University of Veterinary and Animal Sciences, Hisar, Haryana, India; drvinodk10@gmail.com

Vinay G. Joshi – Department of Animal Biotechnology, COVS, Lala Lajpat Rai University of Veterinary and Animal Sciences, Hisar, Haryana, India; ORCID 0000-0001-8872-1838; vinaygjoshi18@gmail.com

Rajesh Chhabra – College Central Laboratory, COVS, Lala Lajpat Rai University of Veterinary and Animal Sciences, Hisar, Haryana, India; rchhabra59@rediffmail.com

Conflict of interest: the authors declare there is no any potential conflict of interest related to this article.



NANOSYSTEMS:

PHYSICS, CHEMISTRY, MATHEMATICS

INFORMATION FOR AUTHORS

The journal publishes research articles and reviews, and also short scientific papers (letters) which are unpublished and have not been accepted for publication in other magazines. Articles should be submitted in English. All articles are reviewed, then if necessary come back to the author to completion.

The journal is indexed in Web of Science Core Collection (Emerging Sources Citation Index), Chemical Abstract Service of the American Chemical Society, Zentralblatt MATH and in Russian Scientific Citation Index.

Author should submit the following materials:

1. Article file in English, containing article title, the initials and the surname of the authors, Institute (University), postal address, the electronic address, the summary, keywords, MSC or PACS index, article text, the list of references.
2. Files with illustrations, files with tables.
3. The covering letter in English containing the article information (article name, MSC or PACS index, keywords, the summary, the literature) and about all authors (the surname, names, the full name of places of work, the mailing address with the postal code, contact phone number with a city code, the electronic address).
4. The expert judgement on possibility of publication of the article in open press (for authors from Russia).

Authors can submit a paper and the corresponding files to the following addresses: nanojournal.ifmo@gmail.com, popov1955@gmail.com.

Text requirements

Articles should be prepared with using of text editors MS Word or LaTeX (preferable). It is necessary to submit source file (LaTeX) and a pdf copy. In the name of files the English alphabet is used. The recommended size of short communications (letters) is 4-6 pages, research articles– 6-15 pages, reviews – 30 pages.

Recommendations for text in MS Word:

Formulas should be written using Math Type. Figures and tables with captions should be inserted in the text. Additionally, authors present separate files for all figures and Word files of tables.

Recommendations for text in LaTeX:

Please, use standard LaTeX without macros and additional style files. The list of references should be included in the main LaTeX file. Source LaTeX file of the paper with the corresponding pdf file and files of figures should be submitted.

References in the article text are given in square brackets. The list of references should be prepared in accordance with the following samples:

- [1] Surname N. *Book Title*. Nauka Publishing House, Saint Petersburg, 2000, 281 pp.
- [2] Surname N., Surname N. Paper title. *Journal Name*, 2010, 1 (5), P. 17-23.
- [3] Surname N., Surname N. Lecture title. In: Abstracts/Proceedings of the Conference, Place and Date, 2000, P. 17-23.
- [4] Surname N., Surname N. Paper title, 2000, URL: <http://books.ifmo.ru/ntv>.
- [5] Surname N., Surname N. Patent Name. Patent No. 11111, 2010, Bul. No. 33, 5 pp.
- [6] Surname N., Surname N. Thesis Title. Thesis for full doctor degree in math. and physics, Saint Petersburg, 2000, 105 pp.

Requirements to illustrations

Illustrations should be submitted as separate black-and-white files. Formats of files – jpeg, eps, tiff.



NANOSYSTEMS:

PHYSICS, CHEMISTRY, MATHEMATICS

Журнал зарегистрирован

Федеральной службой по надзору в сфере связи, информационных технологий и массовых коммуникаций

(свидетельство ПИ № ФС 77 - 49048 от 22.03.2012 г.)

ISSN 2220-8054

Учредитель: федеральное государственное автономное образовательное учреждение высшего образования

«Санкт-Петербургский национальный исследовательский университет информационных технологий, механики и оптики»

Издатель: федеральное государственное автономное образовательное учреждение высшего образования

«Санкт-Петербургский национальный исследовательский университет информационных технологий, механики и оптики»

Отпечатано в Учреждении «Университетские телекоммуникации»

Адрес: 197101, Санкт-Петербург, Кронверкский пр., 49

Подписка на журнал НФХМ

На второе полугодие 2022 года подписка осуществляется через

ОАО «АРЗИ», подписной индекс Э57385